CENTRO INTERNACIONAL DE ESTUDOS
DE DOUTORAMENTO E AVANZADOS
DA USC (CIEDUS)

TESE DE DOUTORAMENTO

# Search for flavour anomalies at LHCb: decay-time-dependent CP violation in $B_s^0 \to (K^+\pi^-)(K^-\pi^+)$ and Lepton Universality in $B^0 \to D^{(*)+} l \nu_l$

Julián García Pardiñas

ESCOLA DE DOUTORAMENTO INTERNACIONAL

PROGRAMA DE DOUTORAMENTO EN FÍSICA NUCLEAR E DE PARTÍCULAS

SANTIAGO DE COMPOSTELA

ANO 2018

USC
UNIVERSIDADE
DE SANTIAGO
DE COMPOSTELA

# DECLARACIÓN DO AUTOR/A DA TESE

**Search for flavour anomalies at LHCb:**
**decay-time-dependent CP violation in $B_s^0 \to (K^+\pi^-)(K^-\pi^+)$**
**and Lepton Universality in $B^0 \to D^{(*)+}l\nu_l$**

D. Julián García Pardiñas

Presento a miña tese, seguindo o procedemento axeitado ao Regulamento, e declaro que:

1) A tese abarca os resultados da elaboración do meu traballo.
2) De selo caso, na tese faise referencia ás colaboracións que tivo este traballo.
3) A tese é a versión definitiva presentada para a súa defensa e coincide coa versión enviada en formato electrónico.
4) Confirmo que a tese non incorre en ningún tipo de plaxio doutros autores nin de traballos presentados por min para a obtención doutros títulos.

*En Santiago de Compostela, 20 de marzo de 2018*

Asdo.
Julián García Pardiñas.

USC
UNIVERSIDADE
DE SANTIAGO
DE COMPOSTELA

# AUTORIZACIÓN DO DIRECTOR / TITOR DA TESE

**Search for flavour anomalies at LHCb:**
**decay-time-dependent CP violation in $B_s^0 \to (K^+\pi^-)(K^-\pi^+)$**
**and Lepton Universality in $B^0 \to D^{(*)+} l\nu_l$**

D. Máximo Pló Casasús

D. Juan José Saborido Silva

INFORMAN:

*Que a presente tese, correspóndese co traballo realizado por D.* ***Julián García Pardiñas****, baixo a miña dirección, e autorizo a súa presentación, considerando que reúne os requisitos esixidos no Regulamento de Estudos de Doutoramento da USC, e que como director desta non incorre nas causas de abstención establecidas na Lei 40/2015.*

*En Santiago de Compostela, 20 de marzo de 2018*

Asdo.
Máximo Pló Casasús.

Asdo:
Juan José Saborido Silva.

USC
UNIVERSIDADE
DE SANTIAGO
DE COMPOSTELA

*"The good life is one inspired by love and guided by knowledge."*

*"Do not fear to be eccentric in opinion, for every opinion now accepted was once eccentric."*

Bertrand Russell

*"Keep on beginning and failing. Each time you fail, start all over again, and you will grow stronger until you have accomplished a purpose – not the one you began with perhaps, but one you will be glad to remember."*

Anne Sullivan

USC UNIVERSIDADE DE SANTIAGO DE COMPOSTELA

USC
UNIVERSIDADE
DE SANTIAGO
DE COMPOSTELA

# *Abstract*

The Standard Model (SM) of Particle Physics is a very successful theory, but it leaves some important questions unanswered. One long-standing mystery is the so called flavour structure, consisting on the specific arrangement of fermions in three families and the connections among them. Several New Physics (NP) models predict modifications to the flavour structure and consequent deviations from the expected behaviour of sub-atomic processes. The LHCb experiment, at CERN, searches for NP by measuring the properties of B mesons decays, using B mesons produced in p-p collisions at the LHC. This thesis presents two measurements performed in LHCb that allow to test the flavour structure of the SM in different ways.

The first and main analysis corresponds to the World's first measurement of the Charge-Partity (*CP*)-violating phase $\phi_s^{d\bar{d}}$, using $B_s^0 \to (K^+\pi^-)(K^-\pi^+)$ decays. The analysis employs data collected by LHCb in 2011 and 2012. The physical motivation is the *CP* problem, corresponding to the inconsistency between the huge matter/anti-matter asymmetry in the Universe and the small *CP* asymmetry that the SM can accommodate (embedded in the flavour structure). The $B_s^0 \to K^{*0}(\to K^+\pi^-)\overline{K}^{*0}(\to K^-\pi^+)$ decay is forbidden at tree level in the SM, only proceeding via loop (penguin) diagrams. This suppression allows potential NP contributions to play a significant role. The $\phi_s^{d\bar{d}}$ phase, predicted to be approximately 0 in the SM, arises in the interference between the $B_s^0/\overline{B}_s^0$ oscillation and the decay of either a $B_s^0$ or a $\overline{B}_s^0$ to the $K^{*0}\overline{K}^{*0}$ final state. To increase the available statistics, not only the $K^{*0}(\overline{K}^{*0})$ resonance is inspected, but also several scalar, vector and tensor $K\pi$ components present in a two-dimensional $K\pi$ mass window of 750 to 1600 $\mathrm{MeV}/c^2$. A total of 19 amplitudes are studied. Given the current level of sensitivity, the same $\phi_s^{d\bar{d}}$ phase is used for all the states. A full amplitude analysis is done via an un-binned fit to the multi-dimensional decay distribution on the $B_s^0$ decay-time, three angular variables and the two $K\pi$ invariant masses. The *CP*-violating phase is measured to be $\phi_s^{d\bar{d}} = -0.10 \pm 0.13 \pm 0.14\,\mathrm{rad}$, where the first uncertainty is statistical and the second one is systematic. It is compatible with the SM prediction, within uncertainties. Many other amplitude-parameters are determined in addition. In particular, the longitudinal-polarisation fraction of the $B_s^0 \to K^{*0}\overline{K}^{*0}$ decay is found to be $f_\mathrm{L} = 0.208 \pm 0.032 \pm 0.046$, which confirms the previously measured low value and deviates from the existent expectations based on the SM.

The second analysis aims at testing the Lepton Universality. This property of the SM consists on the electro-weak couplings being the same for the three lepton families. Several deviations from this behaviour have been recently observed, the largest one corresponding to the combined measurement of $R(D)$ and $R(D^*)$ and being of 4.1 standard deviations. The $R$ observables are defined as $R(D^{(*)}) = \mathcal{B}(B \to D^{(*)}\tau\bar{\nu}_\tau)/\mathcal{B}(B \to D^{(*)}\mu\bar{\nu}_\mu)$, where $D$ is $D^0$ or $D^+$ and $D^*$ is $D^{*0}$ or $D^{*+}$. The analysis presented in this work corresponds to the first LHCb measurement of $R(D)$ using $D^+$, and is restricted to the case $\tau \to \mu\nu_\tau\bar{\nu}_\mu$ and $D^+ \to K^-\pi^+\pi^+$. A data sample collected by LHCb in 2015 is used. The measurement is done through a binned, three-dimensional, template-based fit to filtered candidates with the visible final state $K^-\pi^+\pi^+\mu^-$. Contributions from $D^{*+} \to D^+\pi^0$ to the same visible state, when the $\pi^0$ is not reconstructed, allow to measure $R(D^*)$ in combination with $R(D)$. After filtering, a total yield of about 800 000 $D^+$ candidates is found. The thesis reports the work done in this analysis, which will be continued in the future. To improve the sensitivity, the 2015 data sample will be combined for the final result with the data collected in 2016.

USC
UNIVERSIDADE
DE SANTIAGO
DE COMPOSTELA

# *Resumo*

O Modelo Estándar (ME) da Física de Partículas é unha teoría exitosa, pero deixa cuestións importantes sen resolver. Un dos interrogantes é a chamada estrutura de sabor, que consiste na organización dos fermións en tres familias e as relacións entre elas. Varios modelos de Nova Física (NF) predín modificacións á estrutura de sabor e conseguintes desviacións respecto do esperado en certos procesos sub-atómicos. O experimento LHCb, no CERN, busca NF a través de medidas en decaementos de mesóns B, os cales se producen en colisións p-p no LHC. Esta tese presenta dúas medidas feitas en LHCb, destinadas a poñer a proba a estrutura de sabor do ME de formas distintas.

A primeira e principal análise correspóndese coa primeira medida mundial da fase de violación de Carga-Paridade (*CP*) $\phi_s^{d\bar{d}}$, usando a canle $B_s^0 \to (K^+\pi^-)(K^-\pi^+)$. Úsanse datos tomados por LHCb en 2011 e 2012. A motivación física é o chamado problema de *CP*, que consiste na inconsistencia entre a grande asimetría de materia/anti-materia no Universo e a pequena asimetría de *CP* que o ME pode acomodar (grazas á estrutura de sabor). A canle $B_s^0 \to K^{*0}(\to K^+\pi^-)\overline{K}^{*0}(\to K^-\pi^+)$ está prohibida a nivel árbore no ME e só ocorre a través de diagramas de lazo (tipo pingüino). Esta supresión faina moi sensible a contribucións de NF. A fase $\phi_s^{d\bar{d}}$, que no ME é próxima a 0, orixínase na interferencia entre a oscilación $B_s^0/\overline{B}_s^0$ e o decaemento dun $B_s^0$ ou un $\overline{B}_s^0$ ó estado final $K^{*0}\overline{K}^{*0}$. Para aumentar o tamaño da mostra e mellorar a medida, non só se estuda a resonancia $K^{*0}(\overline{K}^{*0})$, senón tamén as contribucións $K\pi$ escalares, vectoriais y tensoriais presentes nunha ventá bi-dimensional de masa $K\pi$ de 750 a 1600 $\mathrm{MeV}/c^2$. Estúdanse un total de 19 amplitudes e úsase a mesma fase $\phi_s^{d\bar{d}}$ para todas elas, o que é razoable ó nivel de sensibilidade actual. Faise unha análise de amplitudes a través dun axuste ó espectro diferencial no tempo de decaemento do $B_s^0$, en tres variables angulares e nas masas invariantes $K\pi$. A fase de violación de *CP* medida é $\phi_s^{d\bar{d}} = -0.10 \pm 0.13 \pm 0.14\,\mathrm{rad}$, onde a primeira incerteza é estadística e a segunda sistemática. O resultado é compatible coa predición do ME, dentro da incerteza. Tamén se determinan moitos outros parámetros das amplitudes. En concreto, mídese unha baixa fracción de polarización lonxitudinal para a canle $B_s^0 \to K^{*0}\overline{K}^{*0}$, de $f_\mathrm{L} = 0.208 \pm 0.032 \pm 0.046$, o que confirma as medidas previas e dista das estimacións actuais basadas no ME.

A segunda análise constitúe un test da Universalidade Leptónica do ME, que consiste na igualdade de acoplos electro-débiles para as tres familias de leptóns. Recentemente, obsérvaronse varias desviacións, a maior das cales é de 4.1 desviacións estándar e corresponde á medida combinada de $R(D)$ e $R(D^*)$. Os observables $R$ defínense como $R(D^{(*)}) = \mathcal{B}(B \to D^{(*)}\tau\bar{\nu}_\tau)/\mathcal{B}(B \to D^{(*)}\mu\bar{\nu}_\mu)$, onde $D$ é $D^0$ ou $D^+$ e $D^*$ é $D^{*0}$ ou $D^{*+}$. A análise que se presenta corresponde á primeira medida de $R(D)$ usando $D^+$ en LHCb, e restrínxese ó caso con $\tau \to \mu\nu_\tau\bar{\nu}_\mu$ e $D^+ \to K^-\pi^+\pi^+$. Úsase unha mostra de datos tomada en 2015. A medida faise mediante un axuste de histogramas tri-dimensionais, baseado en plantillas, a eventos seleccionados, que teñen o estado final visible $K^-\pi^+\pi^+\mu^-$. Contribucións de $D^{*+} \to D^+\pi^0$ ó mesmo estado visible, cando o $\pi^0$ non se reconstrúe, permiten a medida de $R(D^*)$ en combinación con $R(D)$. Trala selección, obsérvanse uns 800 000 candidatos a $D^+$. A tese detalla o traballo feito na análise, que será continuada e rematada no futuro. Para mellorar a sensibilidade, a mostra de 2015 combinarase con outra de 2016 na medida final.

USC
UNIVERSIDADE
DE SANTIAGO
DE COMPOSTELA

# *Resumen*

El Modelo Estándar (ME) de la Física de Partículas es una teoría exitosa, pero deja cuestiones importantes sin resolver. Uno de los interrogantes es la llamada estructura de sabor, que consiste en la organización de los fermiones en tres familias y las relaciones entre ellas. Varios modelos de Nueva Física (NF) predicen modificaciones a la estructura de sabor y consiguientes desviaciones respecto de lo esperado en ciertos procesos sub-atómicos. El experimento LHCb, en el CERN, busca NF a través de medidas en desintegraciones de mesones B, los cuáles se producen en colisiones p-p en el LHC. Esta tesis presenta dos medidas hechas en LHCb, destinadas a poner a prueba la estructura de sabor del ME de maneras distintas.

El primer y principal análisis constituye la primera medida mundial de la fase de violación de Carga-Paridad (*CP*) $\phi_s^{d\bar{d}}$, usando el canal $B_s^0 \to (K^+\pi^-)(K^-\pi^+)$. Se usan datos tomados por LHCb en 2011 y 2012. La motivación física es el llamado problema de *CP*, que consiste en la inconsistencia entre la gran asimetría de materia/anti-materia en el Universo y la pequeña asimetría de *CP* que el ME puede acomodar (gracias a la estructura de sabor). El canal $B_s^0 \to K^{*0}(\to K^+\pi^-)\overline{K}^{*0}(\to K^-\pi^+)$ está prohibido a nivel árbol en el ME y sólo ocurre a través de diagramas de lazo (tipo pingüino). Esta supresión lo hace muy sensible a contribuciones de NF. La fase $\phi_s^{d\bar{d}}$, que en el ME es próxima a 0, se origina en la interferencia entre la oscilación $B_s^0/\overline{B}_s^0$ y la desintegración de un $B_s^0$ o un $\overline{B}_s^0$ al estado final $K^{*0}\overline{K}^{*0}$. Para aumentar el tamaño de la muestra y mejorar la medida, no sólo se estudia la resonancia $K^{*0}(\overline{K}^{*0})$, sino también las contribuciones $K\pi$ escalares, vectoriales y tensoriales presentes en una ventana bi-dimensional de masa $K\pi$ de 750 a 1600 $\mathrm{MeV}/c^2$. Se estudia un total de 19 amplitudes y se usa la misma fase $\phi_s^{d\bar{d}}$ para todas ellas, lo que es razonable al nivel de sensibilidad actual. Se hace un análisis de amplitudes a través de un axuste al espectro diferencial en el tiempo de desintegración del $B_s^0$, en tres variables angulares y en las masas invariantes $K\pi$. La fase de violación de *CP* medida es $\phi_s^{d\bar{d}} = -0.10 \pm 0.13 \pm 0.14\,\mathrm{rad}$, dónde la primera incertidumbre es estadística y la segunda sistemática. El resultado es compatible con la predicción del ME, dentro de la incertidumbre. También se determinan muchos otros parámetros de las amplitudes. En concreto, se mide una baja fracción de polarización longitudinal para el canal $B_s^0 \to K^{*0}\overline{K}^{*0}$, de $f_\mathrm{L} = 0.208 \pm 0.032 \pm 0.046$, lo que confirma las medidas previas y dista de las estimaciones actuales basadas en el ME.

El segundo análisis constituye un test de la Universalidad Leptónica del ME, que consiste en la igualdad de acoplos electro-débiles para las tres familias de leptones. Recientemente, se han observado varias desviaciones, la mayor de las cuales es de 4.1 desviaciones estándar y corresponde a la medida combinada de $R(D)$ y $R(D^*)$. Los observables $R$ se definen como $R(D^{(*)}) = \mathcal{B}(B \to D^{(*)}\tau\bar{\nu}_\tau)/\mathcal{B}(B \to D^{(*)}\mu\bar{\nu}_\mu)$, dónde $D$ es $D^0$ o $D^+$ y $D^*$ es $D^{*0}$ o $D^{*+}$. El análisis que se presenta corresponde a la primera medida de $R(D)$ usando $D^+$ en LHCb, y se restringe al caso con $\tau \to \mu\nu_\tau\bar{\nu}_\mu$ y $D^+ \to K^-\pi^+\pi^+$. Se usa una muestra de datos tomada en 2015. La medida se hace mediante un ajuste de histogramas tri-dimensionales, basado en plantillas, a eventos seleccionados, que tienen el estado final visible $K^-\pi^+\pi^+\mu^-$. Contribuciones de $D^{*+} \to D^+\pi^0$ al mismo estado visible, cuándo el $\pi^0$ no se reconstruye, permiten la medida de $R(D^*)$ en combinación con $R(D)$. Tras la selección, se observan unos 800 000 candidatos a $D^+$. La tesis detalla el trabajo hecho en el análisis, que será continuado y terminado en el futuro. Para mejorar la sensibilidad, la muestra de 2015 se combinará con otra de 2016 en la medida final.

USC
UNIVERSIDADE
DE SANTIAGO
DE COMPOSTELA

# *Acknowledgements*

I would like to express my gratitude to the Spanish Ministry of Education, Culture and Sport (MECD), for not only funding my whole PhD via a FPU grant but also funding two research stays of three months at CERN. I would also like to thank the High Energy Physics Group (GAES) of the University of Santiago de Compostela, for funding the complements of my formation, and for allowing me to develop a set of important transversal skills for research.

I want to thank my supervisors, Máximo Pló and Juan Saborido, for the fruitful conversations and advices during these years. Special thanks to the researchers Matt Kenzie and Patrick Owen, with whom I had the pleasure to collaborate and that accepted to write me the two expert's reports for the International Mention of the PhD. I would also like to thank Diego Martínez, for the interesting physics discussions and for familiarising me with a powerful software tool to improve the fitter of my main analysis. My gratitude also goes to José Ramón Pelaez and Arkaitz Rodas, for providing me with a state-of-the-art phenomenological model to deal with the scalar $k\pi$ contribution. I also want to thank the reviewers of my main analysis, specially Greig Cowan, with whom I shared very fruitful technical and physics discussions. I would also like to thank Bernardo Adeva, for introduced me for the first time to the $B_s^0 \to K^{*0}\overline{K}^{*0}$ decay, while supervising the final project of my Bachelor.

My general gratitude goes to the LHCb Collaboration, not only for giving me the essential material to develop my thesis but, also, for allowing me to grow as a researcher and boost my visibility in the international scientific community. I also want to thank the conveners and members from the Charmless working group, for their support and advice, and those from the Flavour Tagging group, for giving me experience in one of the most important tools of the experiment, during my two-year role as liaison. Special thanks to Vincenzo Vagnoni, for his help and his energetic cheering up during the last period of my PhD.

Last, but not least, I would like to thank all those who I met in Lindau, that enlightened me with their passion for research and that showed me that evolution and change is one of the best practices in science (and even in life).

# *Agradecementos*

Gustaríame primeiro agradecer ós meus pais por haberme permitido chegar ata aquí, non so co seu esforzo e apoio, senón tamén coas cualidades que herdei deles: a capacidade de traballo de miña nai e o carácter de meu pai. Gustaríame tamén agradecerlle a Bea e ós meus amigos de Vilalba (Héctor, Noel, Alberto, Daniel, Antonio, Francisco, Estéban, Adrián, Eloy ...) por tantas vivencias enriquecedoras, que complementan a vida máis alá do traballo.

Grazas tamén a todos os meus amigos e amigas de Santiago (botando a vista atrás, porque esta tese pecha a miña etapa en Santiago: María, Cristina, Miriam, Gonzalo, Antía, Marco, ...) que, aínda que os grupos se fosen desfacendo e evolucionando co paso do tempo, me permitiron vivir algúns dos mellores momentos da miña vida durante a miña etapa universitaria. Quero dar gracias especiais a María, por tantos momentos e reflexións compartidas ó longo destes anos.

Gustaríame finalmente agradecer ó grupo das comidas en Fonseca (Pablo, Álvaro, Juan, Toño, María, Eliseo, Abraham, Édgar, ...) por tanto divertimento, xeralmente axeno á física, que alegraba o día en tempos complicados.

A miña experiencia estaría incompleta sen todos e todas vós.

USC
UNIVERSIDADE
DE SANTIAGO
DE COMPOSTELA

# Contents

**Abstract** **ix**

**Acknowledgements** **xv**

**1 Introduction** **1**
1.1 First study: inspecting the Charge-Parity violation . . . 1
1.2 Second study: challenging the Lepton Universality . . . 3
1.3 The work process . . . 3

**2 Physical motivation** **7**
2.1 Overview of the Standard Model of particles . . . 8
2.2 Flavour physics in the Standard Model . . . 10
2.3 Challenging the Standard Model in a two-front way . . . 11
2.3.1 First analysis: measurement of the CP-violating phase $\phi_s^{s\bar{d}d}$ . . . 11
2.3.1.1 Types of CP violation . . . 11
2.3.1.2 The $B_s^0 \to K^{*0}\overline{K}^{*0}$ decay . . . 12
2.3.1.3 Extension to other $B_s^0 \to (K^+\pi^-)(K^-\pi^+)$ decays . . . 13
2.3.2 Second analysis: measurement of the $R(D^{(*)+})$ ratios . . . 14
2.3.2.1 Hints of lepton non-universality . . . 15
2.3.2.2 Measuring $R(D^+)$ at LHCb . . . 16
2.4 Beyond the Standard Model alternatives . . . 17

**3 Phenomenology of the $B_s^0 \to (K^+\pi^-)(K^-\pi^+)$ decay** **19**
3.1 Time dependence and CP violation . . . 19
3.2 Decay distributions at $t = 0$. . . . 21
3.2.1 Angular dependence . . . 22
3.2.2 Mass dependence . . . 24
3.2.2.1 Model of the scalar $K\pi$ mass amplitude . . . 25
3.2.2.2 Model of the vector and tensor $K\pi$ mass amplitudes . . . 28

**4 Phenomenology of the $\overline{B}^0 \to D^{(*)+}l\bar{\nu}_l$ decays** **29**
4.1 Signal, normalisation and background species . . . 29
4.1.1 Signal channels . . . 30
4.1.2 Normalisation channels . . . 30
4.1.3 Background channels . . . 30
4.1.3.1 Feed-down . . . 30
4.1.3.2 Double-charm . . . 30
4.1.3.3 Combinatorial . . . 31
4.1.3.4 Misidentification . . . 31
4.2 Discriminant variables . . . 31
4.3 Form factors used in simulation . . . 32

**5 Experimental conditions** **33**
5.1 Flavour physics at the Large Hadron Collider . . . 33
5.2 The LHCb detector . . . 35
5.2.1 Detection principles . . . 35
5.2.2 Vertex detector . . . 36
5.2.3 Tracking stations . . . 38
5.2.4 RICH detectors . . . 38
5.2.5 Calorimeter system . . . 39
5.2.6 Muon chambers . . . 40
5.2.7 Trigger system . . . 40

**6 Tools and techniques** **43**
6.1 Simulation tools . . . 43
6.2 Computing tools . . . 44
6.2.1 Boosted Decision Tree . . . 44
6.2.2 Gradient Boost Reweigher . . . 45
6.2.3 Task parallelisation using a GPU . . . 45
6.3 Mathematical techniques . . . 46
6.3.1 Splines . . . 46
6.4 Analysis techniques . . . 46
6.4.1 Method of the ${}_s\mathcal{W}eights$ . . . 46
6.4.2 Normalisation weights . . . 47
6.4.3 Flavour tagging . . . 48
6.4.4 Machine-learning-based acceptance correction . . . 49
6.4.5 Legendre moments . . . 50
6.4.6 Charged particle isolation techniques . . . 51
6.4.7 Neutral particle isolation techniques . . . 51

**7 Measurement of the $\phi_s$ phase in $B_s^0 \to (K^+\pi^-)(K^-\pi^+)$** **53**
7.1 Data samples . . . 53
7.2 Event selection . . . 55
7.2.1 Pre-selection and BDT . . . 55
7.2.2 PID, mass vetoes and multiple candidates . . . 56
7.2.2.1 PID requirements . . . 56
7.2.2.2 Mass Vetoes . . . 59
7.2.2.3 Multiple Candidates . . . 59
7.2.3 Selection efficiencies . . . 59
7.2.4 Four-body-mass fit and sWeights . . . 59
7.2.4.1 Model used for fitting . . . 59
7.2.4.2 Mass fit results . . . 62
7.3 Flavour tagging . . . 66
7.4 Production Asymmetry . . . 68
7.5 Decay-time resolution . . . 70
7.6 Acceptance effects . . . 72
7.6.1 Study of correlations between acceptance variables . . . 72
7.6.2 Models used in the generation of the MC samples . . . 73
7.6.3 Decay-time acceptance . . . 74
7.6.4 Angular and invariant mass acceptance . . . 75
7.6.4.1 Normalization weights . . . 76
7.6.4.2 Acceptance for plotting and toy MC generation . . . 76
7.7 Flavour-tagged time-dependent amplitude fit . . . 79

7.7.1 Model used for fitting . . . 79
7.7.2 Setup of the fit . . . 80
7.7.3 Implementation of the fit using GPUs . . . 81
7.7.4 Fit results . . . 82
7.8 Checks of the model . . . 87
7.8.1 Comparison between the two simulation samples . . . 87
7.8.2 TD-fitter validation with simulated $B_s^0 \to K^{*0}\bar{K}^{*0}$ data . . . 87
7.8.3 Fit in a narrow $K\pi$ mass window . . . 89
7.8.4 Higher wave contributions: distributions of Legendre moments . . . 89
7.8.5 Toy MC study of the main fitter . . . 90
7.8.5.1 Approximations . . . 90
7.8.5.2 Generation step . . . 95
7.8.5.3 Fitting step . . . 96
7.8.5.4 Results . . . 98
7.8.6 Likelihood profiles . . . 100
7.8.7 Exclusive fit to 2012 data . . . 100
7.8.8 Exclusive fit to the high $K\pi$ mass region . . . 103
7.9 Systematic uncertainties . . . 107
7.9.1 Yield of the 4-body-mass-model components . . . 107
7.9.2 Shape of the 4-body-mass-model components . . . 107
7.9.3 Correlations in the sWeights . . . 108
7.9.4 Bias of the time-dependent amplitude fit . . . 110
7.9.5 Meson-radius parameter in Blatt-Weisskopf functions . . . 110
7.9.6 Central mass and width of the $K\pi$-mass-dependent amplitudes . . . 112
7.9.7 Scalar $K\pi$-mass dependent amplitude . . . 113
7.9.8 Angular-momentum barrier factors . . . 116
7.9.9 High $K\pi$-mass vector resonances . . . 117
7.9.10 Normalisation weights . . . 120
7.9.11 Decay-time acceptance: Monte Carlo statistics . . . 122
7.9.12 Decay-time acceptance: configuration of knots . . . 122
7.9.13 Data/Monte Carlo acceptance correction . . . 126
7.9.14 Angular and $K\pi$-mass resolution . . . 130
7.9.15 Time-resolution calibration model . . . 133
7.9.16 Data/Monte Carlo time-resolution correction . . . 135
7.9.17 Production asymmetry . . . 137
7.9.18 Summary of the systematic uncertainties . . . 139
7.10 Summary . . . 144

**8 Measurement of the $R(D^{(*)+})$ ratios using $\overline{B}^0 \to D^+ l\bar{\nu}_l$ decays** **147**
8.1 Data samples . . . 147
8.2 Event selection . . . 148
8.2.1 Pre-selection requirements . . . 148
8.2.2 Particle identification . . . 148
8.2.3 Decay kinematics and topology . . . 150
8.2.4 Isolation from charged particles . . . 151
8.2.5 Isolation from neutral particles . . . 154
8.2.5.1 Resolved neutral pions . . . 154
8.2.5.2 Analysis of neutral cones . . . 155
8.2.5.3 Combined neutral isolation . . . 157
8.2.6 Fit to the filtered $M(K\pi\pi)$ distribution . . . 159
8.3 Multi-dimensional templates . . . 161

8.3.1 Monte Carlo templates . . . 161
8.3.2 Data templates . . . 161
8.4 Fit and sensitivity studies . . . 163
8.4.1 Setup of the fit . . . 163
8.4.2 Optimisation of the binning . . . 163
8.4.3 Toy Monte Carlo studies and sensitivity estimation . . . 164
8.4.4 Effect of the Monte Carlo sample size on the sensitivity . . . 164
8.5 Summary and future of the analysis . . . 167

**9 Conclusions** **169**

**10 Resumo da tese en galego** **171**
10.1 Introdución . . . 171
10.2 Motivación teórica . . . 171
10.2.1 Fenomenoloxía da desintegración $B_s^0 \to (K^+\pi^-)(K^-\pi^+)$ . . . 172
10.2.2 Fenomenoloxía das desintegracións $\overline{B}^0 \to D^{(*)+}l\bar{\nu}_l$ . . . 173
10.3 Condicións experimentais . . . 174
10.4 Análise da desintegración $B_s^0 \to (K^+\pi^-)(K^-\pi^+)$ . . . 175
10.5 Análise das desintegracións $\overline{B}^0 \to D^{(*)+}l\bar{\nu}_l$ . . . 176
10.6 Conclusións . . . 179

**Appendix A Measurement of $\phi_s$: pull distributions of the physical parameters** **181**

**Appendix B Measurement of $\phi_s$: systematic studies on the normalisation weights** **195**

**References** **201**

USC UNIVERSIDADE DE SANTIAGO DE COMPOSTELA

# List of Abbreviations

| | |
|---|---|
| **USC** | **U**niversidade de **S**antiago de **C**ompostela |
| **CERN** | **C**onseil **E**uropéen pour la **R**echerche **N**ucléaire |
| **LHC** | **L**arge **H**adron **C**ollider |
| **LHCb** | **L**arge **H**adron **C**ollider **b**eauty |
| **QCD** | **Q**uantum **C**hromo**d**ynamics |
| **HEP** | **H**igh **E**nergy **P**hysics |
| **SM** | **S**tandard **M**odel |
| **NP** | **N**ew **P**hysics |
| **CP** | **C**harge **P**arity |
| **LU** | **L**epton **U**niversality |
| **BDT** | **B**oosted **D**ecision **T**ree |
| **FT** | **F**lavour **T**agging |
| **MC** | **M**onte **C**arlo |
| **PID** | **P**article **ID**entification |
| **PDF** | **P**robability **D**ensity **F**unction |

USC UNIVERSIDADE DE SANTIAGO DE COMPOSTELA

USC
UNIVERSIDADE
DE SANTIAGO
DE COMPOSTELA

# Chapter 1

# Introduction

The discovery of the Higgs boson in 2012 [1, 2] at the Large Hadron Collider (LHC) [3] closed the chapter of the Standard Model (SM) of Particle Physics. This has brought us to another point in history where our theory succeeds in predicting our most inmediate observables, but fails to explain several more general phenomena (e.g. the existence of dark matter and dark energy) and is not able to answer several fundamental questions (e.g. why do the particles have their specific properties). The next step is moving forward towards a more complete theoretical model, and many alternative ones have been developed over the last decades. Given the absence of a clear prevalence of any of them, the ball lies now in the court of the experimentalists to find the signatures of New Physics (NP) that point the way ahead. The LHC is able to provide a unique insight in this sense, offering a vast amount of different decay processes to study, in which NP can be involved. While the direct detection of new particles is essential to completely determine their properties, it is restricted to those particles light enough to be created with a given proton collision energy. On the contrary, arbitrarily heavy particles can contribute via quantum processes to the properties of a given decay, and be indirectly observed via precision measurements. This last direction is of main importance in the current scenario, where the mass scale of the new particles is not well known, and can extend to very large values.

The LHCb[1] experiment [4], at CERN[2], is specialized on indirect searches by studying proton-proton collisions at the LHC, and this thesis covers two different precision measurements carried out within this experiment. Among the list of unsolved mysteries in particle physics, one of crucial importance concerns the so called flavour structure, consisting on the properties and relations between the three families of quarks and leptons. In the SM, this structure is determined by the interaction of these particles with the Higgs boson. Not only there is no prediction for these interactions (they are obtained from experimental measurements) but flavour physics is also directly linked to several current theoretical problems (see Sect. 2.4). As will be explained below, this thesis focusses in addressing two of these problems, one related to the Charge-Parity violation and the other one to the Lepton Universality. The LHCb experiment provides a broad view of the flavour sector by studying decays of hadrons containing the heaviest possible quark, the botton/beauty (b) one[3], which are mediated by inter and intra-family quark transitions. An overview of the SM, its flavour structure and possible extensions is presented in Sect. 2. The LHCb detector is described in Sect. 5.

## 1.1 First study: inspecting the Charge-Parity violation

The first and main analysis of this thesis focuses in one of the aforementioned theoretical problems related to flavour, the search for potential new sources of Charge-Parity (CP) violation in the quark sector. This long-standing topic is motivated by the currently observed huge matter-antimatter

[1] Large Hadron Collider beauty.
[2] The European Laboratory for Particle Physics.
[3] The top/truth (t) quark decays too fast to be able to hadronise.

asymmetry in the Universe, which is not expected from the evolution in time of the assumed initial symmetric situation, unless some very specific conditions are satisfied [5]. One of these conditions is the existence of processes that violate CP (break the symmetry between particles and antiparticles) at much larger rates than those predicted by the SM, which only originate from the interactions of the Higgs with the quarks.

LHCb has unique capabilities to study CP violation in decays of the $B_s^0$ meson. This is due to the fact that this particle oscillates in time between the flavour eigenstates $B_s^0$ and $\overline{B}_s^0$ with high frequency, and the LHCb vertex locator (VELO) provides an excellent resolution on the meson flight distance (and consequently the decay time) which allows to resolve this oscillation. When both the $B_s^0$ and $\overline{B}_s^0$ mesons decay to a set of particles which constitute a CP eigenstate[4], the interference between the involved processes leads to a decay time-dependent CP asymmetry that can be parameterised in terms of a phase, $\phi_s$, that depends on the particular decay channel. This phase is only sensitive to NP involved in the mixing process if the decay occurs at tree-level in the SM. This is the case for $\bar{b} \to \bar{s}c\bar{c}$ transitions ($B_s^0 \to J/\psi K^+K^-$ and $B_s^0 \to J/\psi \pi^+\pi^-$), and the corresponding phase, $\phi_s^{c\bar{c}}$, has been measured by several experiments [6–9], obtaining results compatible with the SM. On the contrary, transitions like $\bar{b} \to \bar{s}s\bar{s}$ and $\bar{b} \to \bar{s}d\bar{d}$ occur at loop level in the SM, and new particles involved in the decay process can also modify the value of the phase, which is predicted to be close to 0 in the SM. The $\phi_s^{s\bar{s}}$ phase was measured by LHCb using $B_s^0 \to \phi\phi$ decays [10], reporting a value $\phi_s^{s\bar{s}} = -0.17 \pm 0.15$ which is consistent with the SM expectation.

This thesis presents the first measurement of the CP-violating phase $\phi_s^{d\bar{d}}$. The decay mode[5] $B_s^0 \to K^*(892)^0\overline{K}^*(892)^0$, that gives access to this phase, is considered a golden channel in the search for NP involving CP violation [11–17]. This condition comes from the fact that it can be easily detected experimentally, particularising to the $K^{*0} \to K^+\pi^-$ and $\overline{K}^{*0} \to K^-\pi^+$ subsequent decays, from its inherent sensitivity to NP and from the possibility to precisely control the uncertainty on the SM expectation for the $\phi_s^{d\bar{d}}$ phase when information from the U-spin related channel $B^0 \to K^{*0}\overline{K}^{*0}$ is added. The $B_s^0 \to K^{*0}\overline{K}^{*0}$ decay was discovered by LHCb based on the analysis of 35 pb$^{-1}$ of data collected in 2010 in $pp$ collisions at $\sqrt{s} = 7$ TeV [18] and an updated analysis, still with a too small data sample to attempt a measurement of $\phi_s^{d\bar{d}}$, was done by LHCb using 1 fb$^{-1}$ of data collected in 2011 at $\sqrt{s} = 7$ TeV [19]. Both analyses were performed by a team of researchers from the Experimental High Energy Physics Group (known in Spanish as GAES) of the Universidade de Santiago de Compostela.

The study of this thesis is based on a sample of 3 fb$^{-1}$ (full LHC Run 1 data), composed of the 1 fb$^{-1}$ of data collected in 2011 and 2 fb$^{-1}$ of data collected in 2012 at $\sqrt{s} = 8$ TeV. In an attempt to increase the available statistics, this analysis does not only restrict itself to the $B_s^0 \to K^{*0}\overline{K}^{*0}$ decay, but studies a set of quasi-two-body channels of the form $B_s^0 \to (K^+\pi^-)_{j_1}(K^-\pi^+)_{j_2}$, where $j_1$ and $j_2$ are the angular momentum of the $K\pi$ pairs, that are assumed to share the same $\phi_s^{d\bar{d}}$ phase. The $K\pi$ pairs are required to have an invariant mass in the range from 750 MeV/$c^2$ to 1600 MeV/$c^2$, where three angular momentum components contribute: a scalar one ($j = 0$), dominated by the $K_0^*(1430)^0$, the $K_0^*(800)^0$ and a non-resonant component; a vector one ($j = 1$), dominated by the $K^{*0}$; and a tensor one ($j = 2$), dominated by the $K_2^*(1430)^0$. This enlarged phase-space gives a factor $\sim 4$ times more statistics than a narrow window of 150 MeV/$c^2$ around the $K^{*0}$ pole. However, this comes at the prize of having to deal with a combination of a large number of decay amplitudes, which is not a CP eigenstate as a whole but a sum of CP eigenstates with different eigenvalues. These states need to be disentangled to measure $\phi_s^{d\bar{d}}$, and this implies a multi-dimensional study where not only the decay-time is considered, but also the angular distribution of the decay products and the dependence on the $K^+\pi^-$ and $K^-\pi^+$ invariant

[4] A CP eigenstate is a quantum state that does not change under a CP transformation.

[5] Hereafter, the notation $K^{*0}$ refers to the $K^*(892)^0$ resonance.

masses. The phenomenological model used in this analysis for the $B_s^0 \to (K^+\pi^-)(K^-\pi^+)$ decay distribution is described in Sect. 3.

## 1.2 Second study: challenging the Lepton Universality

The second study of this thesis aims at testing one of the postulates of the SM that lacks any kind of fundamental explanation but only comes from experimental observation, the so called Lepton Universality (LU). In the SM, the electroweak bosons ($W^\pm$ and $Z$) couple with equal strength to the three families of leptons, and the only difference in their transition processes comes from their different masses (so from the interaction with the Higgs boson). However, in the last few years, some deviations from this behaviour have been observed when comparing $b \to s\mu\mu$ versus $b \to see$ loop-level transitions [20, 21], at the order of $2\sigma$ from the SM, and $b \to c\tau\nu$ versus $b \to cl\nu$ (with $l \in \{e, \mu\}$) tree-level transitions [22], at the order of $4\sigma$. These kind of measurements involve ratios of branching fractions, denoted as $R$, which are very clean both from the theoretical and the experimental viewpoint, by largely cancelling the uncertainties from QCD computations and from efficiency and reconstruction effects, respectively. This thesis focuses on studying the tree-level transitions, and aims at improving the precision of the World's combined measurements by analysing new complementary data.

The $4\sigma$ deviation observed in tree-level transitions corresponds to the combined measurement of the $R(D)$ and $R(D^*)$ ratios, defined as $R(D^{(*)}) = \mathcal{B}(\overline{B} \to D^{(*)}\tau\overline{\nu}_\tau)/\mathcal{B}(\overline{B} \to D^{(*)}l\overline{\nu}_l)$, with $l \in \{e, \mu\}$. This is a unified notation that combines the cases with neutral and charged $D^{(*)}$ mesons since, by applying isospin relations, the equalities $R(D) = R(D^0) = R(D^+)$ and $R(D^*) = R(D^{*0}) = R(D^{*+})$ hold. The deviations in $R(D)$ and $R(D^*)$ were first observed in the $B$ factories [23]. Afterwards, in 2015, LHCb did its first measurement of $R(D^{*+})$ [24] with the 3 fb$^{-1}$ of data from the Run 1, focusing on the muonic decay of the tau, $\tau^- \to \mu^-\overline{\nu}_\mu\nu_\tau$. A $2.1\sigma$ anomaly was found, in the same direction than the one from the $B$ factories. The second LHCb measurement of $R(D^{*+})$ came in 2017 [25], also using the full Run 1 data but this time focusing on the hadronic decay of the tau, $\tau^- \to \pi^-\pi^+\pi^-(\pi^0)\nu_\tau$.

The second part of this thesis aims at performing the first LHCb measurement of $R(D^+)$ and a new measurement of $R(D^{*+})$, focusing in both cases on the muonic decay of the tau and using 2 fb$^{-1}$ of data taken in 2015 and 2016 at $\sqrt{s} = 13$ TeV. The charm mesons are reconstructed through the decays $D^+ \to K^-\pi^+\pi^+$ and $D^{*+} \to D^+\pi^0$. The phenomenology of the involved decays is explained in Sect. 4. The basis of the analysis is finished and described in this thesis, but some work is still to be done and the analysis is expected to be completed in the next months.

## 1.3 The work process

I have been working for the whole period of my Ph.D. in the $B_s^0 \to (K^+\pi^-)(K^-\pi^+)$ analysis, being the main author, designing the strategy for the analysis and implementing all its parts (below summarised) except the event selection and background subtraction, which was carried out by a postdoctoral researcher currently at the University of Cambridge. During the last year, I have been working in parallel in the $R(D^{(*)+})$ analysis, which I started together with people from the Universities of Zürich and Milano. In this case, I have been in charge of the signal isolation and the study of backgrounds, so that the two analyses complement each other in my formation as a data analyst, not only from a physics viewpoint but also with respect to experimental tools and methods. The most relevant techniques used in these analyses, some of them original and designed by me, are described in Sect. 6.

The analysis of $B_s^0 \to (K^+\pi^-)(K^-\pi^+)$ decays to measure $\phi_s^{d\bar{d}}$ starts with a two-step signal isolation, consisting on the application of a set of specifically designed requirements followed by the subtraction of the remaining background in a data-driven way. A phenomenological

model of the angular, $K\pi$ invariant mass and decay-time distribution of signal events must be constructed and implemented in software. The parameterisation of the $K\pi$ spectrum deserves special attention, specifically for the less-known scalar component, where the controversial $K_0^*(800)^0$ resonance may contribute (see the *"Note on Scalar Mesons below 2 GEV"* in [26] for details). In developing the phenomenological model I used some of the experience I had gained during the first months of my Ph.D., when I did a contribution to an analysis aimed at measuring polarisation fractions and CP asymmetries in $B_s^0 \to J/\psi \overline{K}^{*0}$ decays [27], with $J/\psi \to \mu^+\mu^-$ and $\overline{K}^{*0} \to K^-\pi^+$. My work in that analysis, which is not covered in this document, consisted in a model-independent study of the $K\pi$ invariant mass spectrum up to high masses, and a study of a potential contribution from the $K_2^*(1430)^0$ resonance. On top of the theoretical decay model, in order to access the time-dependent CP asymmetry in $B_s^0 \to (K^+\pi^-)(K^-\pi^+)$, the initial flavour of the decaying beauty meson ($B_s^0$ or $\overline{B}_s^0$) has to be identified. This is done in LHCb via the so called Flavour Tagging (FT) algorithms, that need to be inserted into the analysis framework. The skills that I developed working with these tools allowed me to be appointed as contact person between the LHCb group in charge of FT development and optimisation and the analysis group devoted to charmless $B$ decays. This two-year position allowed me to increase my experience in the sector. Other detector effects that must be taken into account in the $B_s^0 \to (K^+\pi^-)(K^-\pi^+)$ analysis are the efficiency variation as a function of the analysis variables, known as acceptance, and the resolution. In particular, the decay-time resolution is of main importance since it directly impacts the sensitivity on the $\phi_s^{d\bar{d}}$ phase. To measure this phase together with the CP conserving parameters describing the different amplitudes involved in the decay, a fit to the background-subtracted data sample with the designed model has to be performed. The high dimensionality of the analysis variables and the large number of parameters to be measured would make this fit very slow for normal CPUs, so a new framework was developed to do it using Graphics Processor Units (GPUs). In this respect, I participated in the creation of a new software package to do High Energy Physics analyses on these devices [28], and designed a set of specific tools to be used in the $B_s^0 \to (K^+\pi^-)(K^-\pi^+)$ analysis. The work is finished by doing some checks of the employed methods and estimating the systematic uncertainties on the measured parameters. All the analysis procedure is described in Sect. 7.

The challenges of the $R(D^{(*)})$ measurement are significantly different from those of the previous study, starting from the fact that, in this case, part of the information from the final state is not available due to the missing neutrinos. The main goal is to distinguish the tauonic $\overline{B}^0 \to D^{(*)+}\tau\overline{\nu}_\tau$ modes from the muonic $\overline{B}^0 \to D^{(*)+}\mu\overline{\nu}_\mu$ modes and from several background components. The analysis process starts by designing a set of requirements on data to remove as much background as possible. As a new element with respect to the previous study in this thesis, several tools that look for extra charged and neutral tracks in the events are used with the aim of isolating the signal against backgrounds from partially reconstructed decays. The yield of the different signal and background components is obtained from a 3-dimensional binned template fit to data, using kinematic variables that are sensitive to the effect of missing a different number of neutrinos and to the change in phase space due to the $\tau/\mu$ mass difference. In this way, the next step after the selection is to obtain the templates for the different components, which is done using simulated samples for some modes and background-enriched control data samples for others. The fitting framework has to be developed and checked. The previous steps, that constitute the basis of the analysis, have been finished and are documented in Sect. 8. In order to do the final measurement, some work needs to be done after the PhD thesis, focusing on fitting the data, applying some corrections to the templates to account for small mis-modellings and estimating the reconstruction and selection efficiencies. Finally, the different systematic uncertainties need to be evaluated.

Apart from data analysis, I have done a small instrumentation project in silicon detectors for High Energy Physics, in the framework of the GAES contribution to the construction of the

new pixel-based VELO for the future LHCb detector upgrade. I participated in several test-beam campaigns that were carried out in the Super Proton Synchrotron (SPS) at CERN, aimed at characterising the behaviour of new chip prototypes. Posteriorly, I analysed some of the data taken in those campaigns. In particular, I studied the potential electronic noise induced by the so called Fast Oscillator of the TimePix3 readout chips [29]. This oscillator, which has a frequency of 640 MHz, provides a time-of-arrival measurement with a 1.56 ns step size. If it was removed, the time step size would increase to 25 ns. I found the noise to be negligible at the operation conditions, which supports the utilisation of this feature.

The main conclusions of the projects covered in this thesis and the prospects for the future are written in Sect. 9. Finally, a summary of the thesis in Galician language is presented in Sect. 10.

USC
UNIVERSIDADE
DE SANTIAGO
DE COMPOSTELA

# Chapter 2

# Physical motivation

Particle dynamics is currently best described in the framework of relativistic Quantum Field Theory (QFT). In this framework, particles are described as probability fields, defined in the four-dimensional space-time together with an extra coordinate for the spin of the particle. The different types of fields (particles) are defined by a specific set of absolute couplings (interactions) with other fields and the magnitude of the spin. According to this last quantity, particles are categorised as fermions, if the spin is half-integer, or as bosons, if the spin is integer. Fermions are typically known as matter constituents and bosons as interaction mediators. The property of the spin and its correlation with the spacial coordinates leads to the existence of several different possible states for each particle field. In particular, in the case of fermions, two different states are possible according to their chirality: right-handed or left-handed. A parity (P) transformation changes from one state to the opposite. Additionally, each field can be two-folded with respect to the sign of the charges, which leads to the concept of anti-particles. The particle and anti-particle states can be exchanged by a Charge-Parity (CP) transformation.

The Standard Model (SM) of particles corresponds to the collection of the currently known different types of particles, together with the couplings among them. These couplings are considered to be the consequence of a few number of fundamental interactions, directly related to mathematical symmetries present in nature. When the model is input with a limited set of parameters for some fundamental couplings (that have to be determined from data), it can predict the properties of a large number of different microscopic phenomena. Even if the predictions have so far been checked to be very accurate in almost all the particle-laboratory experiments, the model is known to lack several crucial ingredients. For example, it does not include any description of gravity, and does not contain any particle candidates for the dark matter and dark energy that are considered to exist in the Universe. Additionally, the fact that several parameters need to be input to the model implies that there is no fundamental understanding of their nature. In general, new particle components and/or new symmetries can exist in nature. If this is the case, they will cause some deviations in the properties of specific phenomena with respect to the SM expectations.

One of the unexplained characteristics of the SM is the existence of three families of fermions, that appear to be identical copies of the same type of particles except for the different interaction with the so called Higgs boson. The property that distinguishes between members of the different families is called flavour, and the specific arrangement of the families and their interactions with the Higgs are referred to as flavour structure. This thesis presents two measurements aimed at testing the flavour structure of the SM by looking at two specially sensitive phenomena.

The particles and interactions of the SM are briefly reviewed in Sect. 2.1, and the SM flavour structure is presented in Sect. 2.2. The motivation for the first measurement of this thesis is explained in Sect. 2.3.1 and the motivation for the second analysis is explained in Sect. 2.3.2. Finally, some New Physics models that could explain several anomalies observed in flavour physics are cited and briefly commented in Sect. 2.4. For a rigurous mathematical construction of QFT and the Standard Model of particles, the reader is referred to Ref. [30].

## 2.1 Overview of the Standard Model of particles

As explained in the previous section, the fundamental particles can be classified according to their spin in either fermions or bosons. The bosons are associated in the SM to fundamental interactions, as written below.

- Photon ($\gamma$): mediator of the electromagnetic (E) interaction.
- $W^+$, $W^-$ and $Z^0$: mediators of the weak (W) interaction. For the case of the $W^\pm$ bosons, the interaction is said to proceed via charged currents and, for the case of the $Z^0$ boson, it is said to occur through a neutral current.
- Gluons ($g$): mediators of the strong (S) interaction.
- Higgs ($H$): boson that gives a mass to the particles.

The electromagnetic, weak and strong interactions are associated to the existence of so-called Gauge symmetries [30], and the corresponding mediators are referred to as Gauge bosons. The electromagnetic and the weak interactions can be unified under the so-called electroweak (EW) interaction. The electromagnetic and the strong interactions do not distinguish between left- and right-handed particles, while the weak interaction does so (it is said to violate parity).

The fermions can be sub-classified in quarks (Q) and leptons (L). The quarks experiment both the electroweak and the strong interaction, while the leptons only experiment the electroweak one. Additionally, these particles can be grouped in terms of their electric charge ($q$), in up-type and down-type particles. The list of fermions is written below.

- Up-quarks ($q = +2/3$): up ($u$), charm ($c$), top/truth ($t$).
- Down-quarks ($q = -1/3$): down ($d$), strange ($s$), bottom/beauty ($b$).
- Up-leptons ($q = 0$): electron-neutrino ($\nu_e$), muon-neutrino ($\nu_\mu$), tau-neutrino ($\nu_\tau$).
- Down-leptons ($q = -1$): electron ($e$), muon ($\mu$), tau ($\tau$).

Finally, the strong interaction makes each of the quarks exist in one of three possible states, identified by their so-called color charge. An overall scheme of the previously mentioned particles is shown in Fig. 2.1.

As introduced in the previous section, the fermions can be regrouped in three families, in such a way that the electroweak and strong interactions are equal for each family. The quark families are:

- First family: $u$, $d$.
- Second family: $c$, $s$.
- Third family: $t$, $b$.

The lepton families are:

- First family: $\nu_e$, $e$.
- Second family: $\nu_\mu$, $\mu$.
- Third family: $\nu_\tau$, $\tau$.

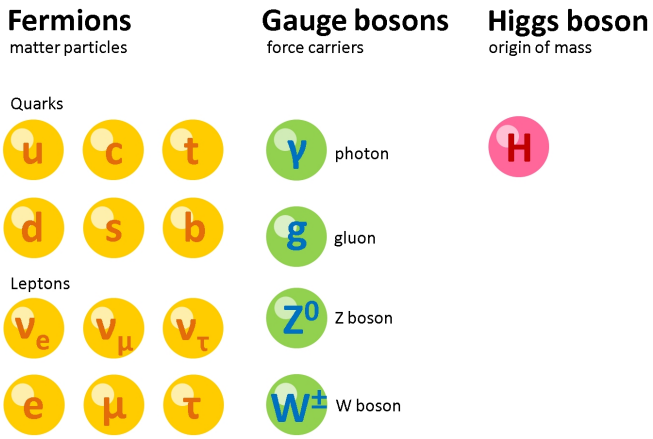



FIGURE 2.1: Particles of the Standard Model. Picture taken from http://www.u-tokyo.ac.jp.

Under this scheme, the Lagrangian of the SM, that contains the dynamics of the whole system of particles, is briefly depicted below. First, it can be decomposed in two parts:

$$\mathcal{L}_{SM} = \mathcal{L}_{SM}^{noH} + \mathcal{L}_{SM}^{H}, \tag{2.1}$$

where $\mathcal{L}_{SM}^{H}$ contains all the dynamics related to the Higgs boson and $\mathcal{L}_{SM}^{noH}$ describes all the other elements. This last term can be decomposed as:

$$\mathcal{L}_{SM}^{noH} = 3 \times \mathcal{L}_{SM}^{Q} + 3 \times \mathcal{L}_{SM}^{L} + \mathcal{L}_{SM}^{GB}, \tag{2.2}$$

where $\mathcal{L}_{SM}^{Q}$ and $\mathcal{L}_{SM}^{L}$ describe the dynamics of a given family of quarks and leptons, respectively, and $\mathcal{L}_{SM}^{GB}$ contains the dynamics of the Gauge bosons. Each of the previous contributions can be made of kinematic terms, $\mathcal{K}$, that account for the free movement of particles, and point interaction terms, $\mathcal{I}$. In the case of quarks and leptons, the Lagrangian terms can be written as:

$$\begin{aligned} \mathcal{L}_{SM}^{Q} &= \mathcal{K}_Q + \mathcal{I}_{Q,EW} + \mathcal{I}_{Q,S}, \\ \mathcal{L}_{SM}^{L} &= \mathcal{K}_L + \mathcal{I}_{L,EW}, \end{aligned} \tag{2.3}$$

where $\mathcal{K}_Q$ and $\mathcal{K}_L$ are the kinematic terms, $\mathcal{I}_{Q,EW}$ and $\mathcal{I}_{L,EW}$ contain the interactions with the EW bosons and $\mathcal{I}_{Q,S}$ contains the interaction with the gluons. In a similar way, the Lagrangian element $\mathcal{L}_{SM}^{GB}$ includes the kinematics of the gauge bosons and the interactions among them.

The so-called Higgs mechanism was proposed in the 1960s, as a way to give Lagrangian mass terms for the particles in a way that the postulated Gauge symmetries were not explicitly broken. Instead, the Higgs fields breaks the electroweak symmetry in a spontaneous way, by having a non-zero vacuum expectation value. The Higgs boson was discovered in 2012 at the LHC, by the experiments ATLAS and CMS [31, 32]. The Lagrangian term associated to the Higgs is given by:

$$\mathcal{L}_{SM}^{H} = \mathcal{K}_H + \mathcal{I}_{H,H} + \mathcal{I}_{H,EW} + \mathcal{I}_Y, \tag{2.4}$$

where

- $\mathcal{K}_H$ is the kinematic term,
- $\mathcal{I}_{H,H}$ is the self interaction term, which gives mass to the Higgs and allows for the existence of a non-zero vacuum expectation value for its field,

- $\mathcal{I}_{H,EW}$ contains the couplings to the $W^{\pm}$ and $Z^0$ bosons and allows to give them masses once the symmetry is broken,
- $\mathcal{I}_Y$ is the so-called Yukawa term, that contains the interactions with the quarks and leptons that, as in the previous case, allows to give them masses after the symmetry is broken.

It is the last term of the previous Lagrangian, $\mathcal{I}_Y$, the only one in the SM that distinguishes between the three fermion families. As will be discussed in the next section, it does not only give different masses to quarks and leptons of different flavour, but also allows for inter-family quark transitions and CP violation.

## 2.2 Flavour physics in the Standard Model

The Yukawa term introduced in Eq. 2.4 is constructed in such a way that it respects the electroweak Gauge symmetry. When it comes to the electroweak interaction, fermions act in fundamental groups that are either doublets or singlets. In particular, for each family of leptons and each family of quarks, the left-handed up- and down-type particles are grouped in a doublet, while the right-handed up- and down-type particles are considered as two independent singlets.

In the SM, the interaction of the Higgs with the fermions is divided into two parts, one for quarks and one for leptons:

$$\mathcal{I}_Y = \mathcal{I}_{Y,Q} + \mathcal{I}_{Y,L}. \tag{2.5}$$

Let's focus on the coupling to quarks, $\mathcal{I}_{Y,Q}$. As explained in Ref. [26], this term is constructed as:

$$\mathcal{I}_{Y,Q} = -Y^d_{ij}\overline{Q^I_{Li}}\phi d^I_{Rj} - Y^u_{ij}\overline{Q^I_{Li}}\epsilon\phi^* u^I_{Rj} + h.c., \tag{2.6}$$

where $i$ and $j$ label the quark families, the superscripts $d$ and $u$ respectively refer to down- and up-type particles, $Q^I_{Li}$ are left-handed doublets, $d^I_{Ri}$ and $u^I_{Ri}$ respectively refer to right-handed down- and up-type quark singlets, $\phi$ is the Higgs field, $\epsilon$ is the $2\times 2$ antisymmetric tensor, $Y^{u,d}$ are $3\times 3$ complex matrices, the bars over the quark doublets indicate the Dirac adjoints and $h.c.$ denotes the Hermitian conjugate. The superscript $I$ in the quark doublets and singlets indicates that the quark flavours in the expression above are defined in the weak-eigenstate basis. When the electroweak symmetry is spontaneously broken, $\phi$ acquires a vacuum expectation value $\langle\phi\rangle = (0, v/\sqrt{2})$ and Eq. 2.6 gives mass to the quarks. To obtain the so-called physical quarks, corresponding to the mass-eigenstates, the $Y^{u,d}$ elements have to be diagonalised by four unitary matrices, $V^{u,d}_{L,R}$, as $M^f_{diag} = V^f_L Y^f V^{f\dagger}_R (v/\sqrt{2})$, with $f \in \{u, d\}$. As a consequence, the charged-current $W^{\pm}$ interactions couple to the physical quarks, $u_{Li}$ and $d_{Li}$, with couplings given by:

$$\frac{-g}{\sqrt{2}}(\overline{u_L}, \overline{c_L}, \overline{t_L})\gamma^\mu W^+_\mu V_{CKM} \begin{pmatrix} d_L \\ s_L \\ b_L \end{pmatrix} + h.c., \tag{2.7}$$

where $g$ is the weak coupling constant, $\gamma^\mu$ are the Dirac matrices, and $V_{CKM}$ is the so-called Cabibbo-Kobayashi-Maskawa (CKM) matrix [33, 34], given by

$$V_{CKM} = V^u_L V^{d\dagger}_L = \begin{pmatrix} V_{ud} & V_{us} & V_{ub} \\ V_{cd} & V_{cs} & V_{cb} \\ V_{td} & V_{ts} & V_{tb} \end{pmatrix}. \tag{2.8}$$

The CKM matrix is $3 \times 3$ and unitary. It can be parameterised in terms of three mixing angles and a complex phase. A standard parameterisation is the following one:

$$V_{CKM} = \begin{pmatrix} c_{12}c_{13} & s_{12}c_{13} & s_{13}e^{-i\delta_{13}} \\ -s_{12}c_{23} - c_{12}s_{23}s_{13}e^{i\delta_{13}} & c_{12}c_{23} - s_{12}s_{23}s_{13}e^{i\delta_{13}} & s_{23}c_{13} \\ s_{12}s_{23} - c_{12}c_{23}s_{13}e^{i\delta_{13}} & -c_{12}s_{23} - s_{12}c_{23}s_{13}e^{i\delta_{13}} & c_{23}c_{13} \end{pmatrix}, \tag{2.9}$$

where $s_{ij} = \sin\theta_{ij}$, $c_{ij} = \cos\theta_{ij}$ and $\delta_{13}$ is the complex phase. The existence of $\delta_{13}$ constitutes the only source of CP violation in the SM. Finally, it should be noted that the quark-mixing mechanism of the SM does not contain any equivalent couplings as those above for possible flavour-changing neutral-currents.

A similar construction can be done for the leptonic case, in order to give masses to the $e$, $\mu$ and $\tau$. The original version of the SM assumed zero mass for the neutrinos. However, this was later proven not to be the case, when the neutrino oscillations were experimentally observed by the Super-Kamiokande Observatory and the Sudbury Neutrino Observatories. Even if the origin of the mass for these leptons is still being investigated, a similar mixing matrix as above can be constructed. In this case, the matrix is named Pontecorvo–Maki–Nakagawa–Sakata (PMNS) [35].

## 2.3 Challenging the Standard Model in a two-front way

As previously stated, this thesis is based on two analyses that look for effects of new contributions to flavour physics involved in two different kinds of phenomena. The first of them, explained in Sect. 2.3.1, focuses on searching for NP contributions that can help solving the so-called Charge Parity (CP) problem. The second analysis, presented in Sect. 2.3.2, aims at testing one property of the SM called Lepton Universality.

### 2.3.1 First analysis: measurement of the CP-violating phase $\phi_s^{s\bar{d}d}$

The non-zero value of the complex phase $\delta_{13}$ of the CKM matrix (see Eq. 2.9) provides the only source of CP violation in the electroweak sector of the SM. This mechanism is not enough to account for the huge matter-antimatter asymmetry observed in the Universe nowadays, and unknown additional processes should have occurred in the history of the Universe to arrive at this situation [36]. In the next section, a classification of the different ways to search for CP-violating effects in particle transitions is presented and the motivation for the particular measurement performed in this thesis is explained.

#### 2.3.1.1 Types of CP violation

The amount of CP violation in a given phenomenon is determined by comparing the measured yields for a pair of CP-conjugated processes. From a theoretical perspective, any fundamental CP-violating effect appears in the form of a complex quantum phase, as in Eq. 2.9. These phases can only be measured in interference processes, which implies that any CP-violating effect can only be detected in transitions where several amplitudes of comparable size contribute and interfere.

Historically, CP violation has been studied in three different types of processes. The definition and characteristics for each of them are presented below.

- Type 1: CP violation in the decay (also known as direct CP violation). To define this concept, let's consider the amplitude for the decay of a particle $P$ to a final state $f$, $A(P \to f)$. It is said to be CP violation in the decay if the square module of this amplitude, $|A(P \to f)|^2$, is different from the one of the CP conjugated decay, $|A(\overline{P} \to \overline{f})|^2$. To obtain a non-vanishing

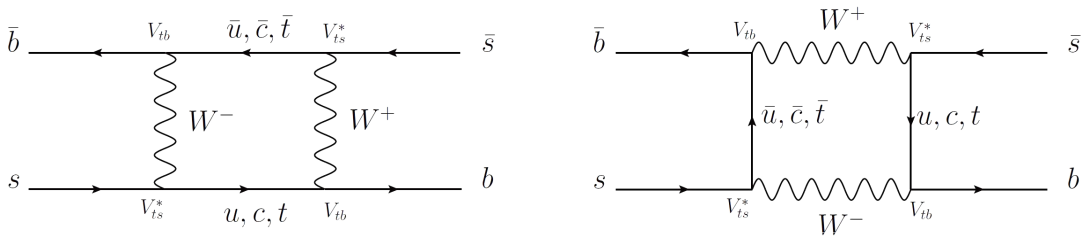



FIGURE 2.2: Leading order Feynman diagrams for the $B_s^0 - \bar{B}_s^0$ mixing in the SM.

CP violation, the decay amplitude has to be the coherent sum of two or more contributions of similar size.

- Type 2: CP violation in mixing. A neutral particle, $P^0$, can be mixed with its own anti-particle, $\overline{P}^0$, via transitions as those shown in Fig. 2.2 for the $B_s^0 - \bar{B}_s^0$ case. In Sect. 3.1, it is explained how this mixing leads to an oscillation in time between $P^0$ and $\overline{P}^0$. It is said to be CP violation in mixing if the square moduli of the transitions in both directions are different, *i.e.* $|A(P^0 \to \overline{P}^0)|^2 \neq |A(\overline{P}^0 \to P^0)|^2$. A non-vanishing CP violation in this case requires several contributions to the mixing amplitude that are similar in size.

- Type 3: CP violation in the interference between mixing and decay. In cases where the oscillating $P^0$ decays to a final state $f$ which is a CP eigenstate, *i.e.* $f = \overline{f}$, the CP conjugated neutral particle, $\overline{P}^0$, can also decay to the same state. This leads to an interference between the mixing and decay processes, that gives sensitivity to a CP violating phase denoted as $\phi$. This phase contains contributions from the phase difference in the CP-conjugated decay amplitudes and the phase difference in the CP-conjugated mixing amplitudes (see Eq. 3.9). Consequently, even if both the CP violation in the decay and in the mixing are zero (statement which only affects the moduli), this phase can still violate CP. The determination of this quantity can be done by measuring a yield asymmetry as a function of the $P^0$ decay time. Finally, when the decaying particle is a $B_s^0$ meson, the phase is denoted as $\phi_s$.

#### 2.3.1.2 The $B_s^0 \to K^{*0}\overline{K}^{*0}$ decay

The analysis presented in this thesis focuses on the CP violation arising in the interference between mixing and decay (type 3). For $b \to c\bar{c}s$ transitions, *e.g.* $B_s^0 \to J/\psi K^+K^-$ and $B_s^0 \to J/\psi \pi^+\pi^-$ decays, the weak phase $\phi_s^{c\bar{c}}$ has been measured by several experiments [7–9, 37]. The World average reported by HFLAV, $\phi_s^{c\bar{c}} = -0.021 \pm 0.031\,\text{rad}$ [37], is compatible with the Standard Model expectation of $\phi_s^{c\bar{c}} = -0.0370 \pm 0.0006$ rad [38]. The $b \to c\bar{c}s$ transitions can occur at tree level in the SM, which would hide small NP contributions to the decay process. Consequently, the $\phi_s^{c\bar{c}}$ phase is only sensitive to NP involved in the mixing process. A different scenario is found in $b \to sq\bar{q}$ transitions, that are mediated by Flavour Changing Neutral Currents (FCNC) which only proceed via loop (penguin) diagrams in the SM. In this case, potential NP contributions to the decay could also significantly affect the relevant CP-violating phase. The LHCb collaboration has measured the $\phi_s^{s\bar{s}}$ phase in $B_s^0 \to \phi\phi$ transitions [10], reporting a value of $\phi_s^{s\bar{s}} = -0.17 \pm 0.15\,\text{rad}$. This value is compatible with the corresponding SM expectation of $\phi_s^{s\bar{s}} \sim 0$ rad [39], even if the uncertainty is larger than for the measurement of $\phi_s^{c\bar{c}}$.

This thesis presents the World's first measurement of the $\phi_s^{d\bar{d}}$ phase, corresponding to $b \to sd\bar{d}$ transitions, which is done by studying $B_s^0 \to (K^+\pi^-)(K^-\pi^+)$ decays. The $B_s^0 \to K^{*0}\overline{K}^{*0}$ channel, where the $K^{*0}(\overline{K}^{*0})$ meson can decay as $K^{*0} \to K^+\pi^-(\overline{K}^{*0} \to K^-\pi^+)$, has been extensively discussed in the literature as a golden channel in the search for NP involved in CP violation [11–

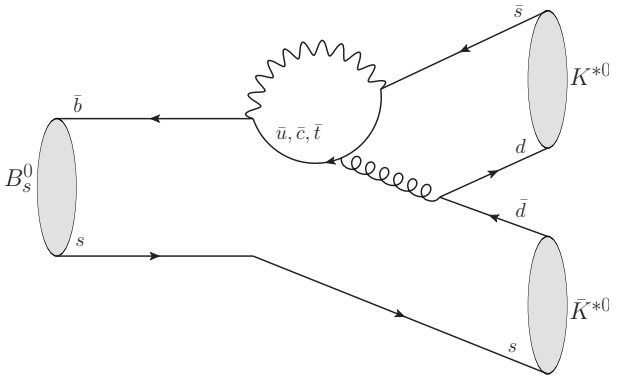



FIGURE 2.3: Leading order Feynman diagram for the $B_s^0 \to K^{*0}\overline{K}^{*0}$ decay in the SM.

17]. Apart from the high sensitivity associated to the decay via a FCNC (see Fig. 2.3 for the leading order SM diagram), this system offers the additional possibility to control higher-order SM contributions to the $\phi_s^{d\bar{d}}$ phase by studying the U-spin related channel $B^0 \to K^{*0}\overline{K}^{*0}$.

The $B_s^0 \to K^{*0}(\to K^+\pi^-)\overline{K}^{*0}(\to K^-\pi^+)$ decay was first observed by the LHCb collaboration, basing on $p$-$p$ collision data corresponding to an integrated luminosity of $35\,\text{pb}^{-1}$ at a centre-of-mass energy $\sqrt{s} = 7\,\text{TeV}$ [18]. A branching fraction and a final-state polarisation analysis were reported. An updated analysis of the decay was also performed by LHCb using $1.0\,\text{fb}^{-1}$ of data taken at $\sqrt{s} = 7\,\text{TeV}$ [19]. Both these analyses were time-integrated and no efforts were put on measuring the $\phi_s^{d\bar{d}}$ phase, given the small size of the available data samples. The updated branching fraction was measured to be $\mathcal{B}(B_s^0 \to K^{*0}\overline{K}^{*0}) = 10.8 \pm 2.1(stat.) \pm 1.4(syst.) \pm 0.6(f_d/f_s)) \times 10^{-6}$, where $f_d/f_s$ is the ratio of production fractions for a $B^0$ and a $B_s^0$. The available triple-product asymmetries were measured and found to be compatible with the SM expectations. In both analyses, the amplitude study yielded a low value for the polarisation fraction for the $B_s^0 \to K^{*0}\overline{K}^{*0}$, being the most recent measurement $f_L = 0.201 \pm 0.057(stat.) \pm 0.040(syst.)$. This value contrasts both with the theoretical expectation [40] and with the longitudinal polarisation fraction observed in the $B^0 \to K^{*0}\overline{K}^{*0}$ decay by the BaBar experiment [41], of $f_L = 0.80^{+0.12}_{-0.13}$. A tantalising question is whether this deviation can be related to a set of flavour anomalies recently found in $b \to sll$ transitions (see Sect. 2.4 for more details). Many NP models that have been proposed to solve those anomalies also predict effects in $b \to sqq$ transitions. All these considerations add an extra interest to the time-dependent study of the $B_s^0 \to K^{*0}\overline{K}^{*0}$ decay.

#### 2.3.1.3 Extension to other $B_s^0 \to (K^+\pi^-)(K^-\pi^+)$ decays

The analysis presented in this thesis expands the original scope of measuring the $\phi_s^{d\bar{d}}$ phase in $B_s^0 \to K^{*0}\overline{K}^{*0}$, by determining an average of this phase over an ensemble of $B_s^0 \to (K^+\pi^-)(K^-\pi^+)$ modes that include the $B_s^0 \to K^{*0}\overline{K}^{*0}$. The motivation for this approach is two-folded. First, the two previous LHCb analyses showed a large scalar $K\pi$ contribution below the $K^{*0}$ peak, entangled with it and consequently impossible to properly isolate. To accurately understand and measure the contribution from this component, an extension of the phase-space region under scrutiny was desirable. The second motivation comes from the fact that, even using the full Run 1 dataset ($1.0\,\text{fb}^{-1}$ recorded in 2011 at $\sqrt{s} = 7\,\text{TeV}$ and $2.0\,\text{fb}^{-1}$ recorded in 2012 at $\sqrt{s} = 8\,\text{TeV}$), the $B_s^0 \to K^{*0}\overline{K}^{*0}$ expected yield would not be enough for a relatively accurate determination of $\phi_s^{d\bar{d}}$. When combining the need to solve this problem with the consideration that the CP-violating phase for several other $B_s^0 \to (K^+\pi^-)(K^-\pi^+)$ decays can be assumed to be the same at the

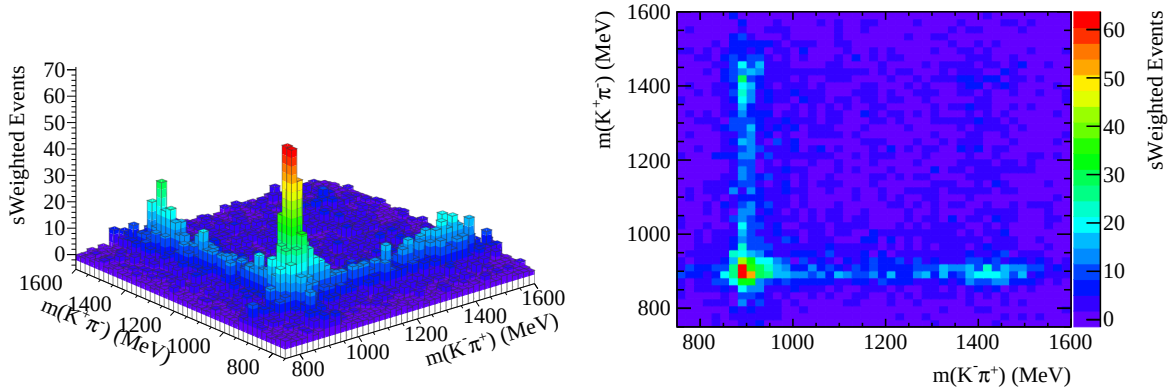



FIGURE 2.4: Two-dimensional background-subtracted distribution for the two $K\pi$ invariant masses, shown from two different perspectives. The dominant resonances at $m(K^{\pm}\pi^{\mp}) = 892\,\mathrm{MeV}/c^2$ and $m(K^{\pm}\pi^{\mp}) = 1430\,\mathrm{MeV}/c^2$ are clearly visible.

current level of sensitivity, a reasonable approach to increase the available data sample consists on studying several modes altogether as a signal channel. Following this approach, the analysis in this thesis studies a phase-space region corresponding to a two-dimensional $K\pi$ mass window from 750 to 1600 $\mathrm{MeV}/c^2$ (to be compared with a window of 150 $\mathrm{MeV}/c^2$ around the $K^{*0}$ mass, used in the previous analyses). This mass range approximately extends from the $K\pi$ production threshold to below the production threshold for the charm resonances.

When using an angular momentum basis, a particular decay of a $B_s^0$ meson to a $(K^+\pi^-)(K^-\pi^+)$ final state can be identified by three quantum numbers: the angular momentum of the $K^+\pi^-$ pair, $j_1$, the angular momentum of the $K^-\pi^+$ pair, $j_2$, and the helicity of the $K\pi$ pairs, $h$. Focusing on a given $K\pi$ pair, contributions from $j \in \{0, 1, 2\}$ are expected. Resonances with $j > 2$ are not taken into account in this analysis since their nominal mass falls outside the $K\pi$ mass range and any residual contributions are assumed to be too small to significantly affect the results. In Sect. 7.8.4, a potential contribution from the $K_3^*(1780)^0$ resonance is studied and found to be compatible with zero. As will be explained in Sect. 3.2.2, the scalar ($j = 0$) term contains possible contributions from the $K_0^*(800)^0$ and $K_0^*(1430)^0$ resonances and from a non-resonant (NR) component. For simplicity, the scalar term is overall denoted as $(K\pi)_0^*$. The vector ($j = 1$) component is dominated by the $K_0^*(892)^0$ (denoted by $K^{*0}$ in many places of this document) and the tensor one ($j = 2$) is dominated by the $K_2^*(1430)^0$. The two-dimensional signal-data distribution on the two $K\pi$ invariant masses is shown in Fig. 2.4. The three possible angular arrangements per $K\pi$ pair give a total of $3 \times 3 = 9$ decays to study, which have a different number of polarisation amplitudes allowed by angular-momentum-conservation rules (see Sect. 3.2.1 for details). The list of the decay amplitudes considered in the analysis is written in Table 2.1. The time-dependent study of these decays does not only provide the measurement of the $\phi_s^{d\bar{d}}$ phase, but also the determination of many amplitude parameters, most of them measured here for the first time. The resulting information could also be used to study QCD[1] phenomenology in this system. For example, differences in the decay amplitudes for modes related by a $j_1 j_2 \leftrightarrow j_2 j_1$ transformation, in the case of $j_1 \neq j_2$, provide information about the physical difference associated to the expectator quark (see Fig. 2.3) ending up in $K\pi$ pairs with different angular momentum configurations.

### 2.3.2 Second analysis: measurement of the $R(D^{(*)+})$ ratios

As explained in Sect. 2.1, the SM predicts equal couplings of the electroweak bosons to the three lepton families, the only differences being related to the interactions with the Higgs boson. This

[1]Quantum chromodynamics (QCD) is the theoretical field that studies the properties of the strong interaction.

TABLE 2.1: Quasi-two-body decay channels and corresponding polarisation amplitudes contributing to the $B_s^0 \to (K^+\pi^-)(K^-\pi^+)$ final state in the $K\pi$ mass window from 750 to 1600 $\mathrm{MeV}/c^2$. The different contributions are identified by the spin $j_1$ ($j_2$) of the $K^+\pi^-$ ($K^-\pi^+$) pair and the helicity $h$. In cases where more than one amplitude contributes, the polarisations are defined as being longitudinal, parallel, or perpendicular, which are then denoted by $0$, $\parallel$ and $\perp$ respectively, following the definitions given in Ref. [26]. The subscripts 1 and 2 in the parallel and perpendicular helicities of the tensor-tensor component denote different spin states leading to a parallel or a perpendicular configuration.

| Decay | Mode | $j_1$ | $j_2$ | Allowed values of $h$ |
|---|---|---|---|---|
| $B_s^0 \to (K^+\pi^-)_0^*(K^-\pi^+)_0^*$ | scalar-scalar | 0 | 0 | 0 |
| $B_s^0 \to (K^+\pi^-)_0^*\overline{K}^*(892)^0$ | scalar-vector | 0 | 1 | 0 |
| $B_s^0 \to K^*(892)^0(K^-\pi^+)_0^*$ | vector-scalar | 1 | 0 | 0 |
| $B_s^0 \to (K^+\pi^-)_0^*\overline{K}_2^*(1430)^0$ | scalar-tensor | 0 | 2 | 0 |
| $B_s^0 \to K_2^*(1430)^0(K^-\pi^+)_0^*$ | tensor-scalar | 2 | 0 | 0 |
| $B_s^0 \to K^*(892)^0\overline{K}^*(892)^0$ | vector-vector | 1 | 1 | 0, $\parallel$, $\perp$ |
| $B_s^0 \to K^*(892)^0\overline{K}_2^*(1430)^0$ | vector-tensor | 1 | 2 | 0, $\parallel$, $\perp$ |
| $B_s^0 \to K_2^*(1430)^0\overline{K}^*(892)^0$ | tensor-vector | 2 | 1 | 0, $\parallel$, $\perp$ |
| $B_s^0 \to K_2^*(1430)^0\overline{K}_2^*(1430)^0$ | tensor-tensor | 2 | 2 | 0, $\parallel$ 1, $\perp$ 1, $\parallel$ 2, $\perp$ 2 |

condition is known as Lepton Universality (LU). From a more general perspective, there is no fundamental reason to assume it should hold in nature. Recently, several experimental hints of LU violation have been observed, and many efforts are ongoing to help elucidating the nature of those deviations. In the next sections, the overall experimental situation is reviewed and the motivation for the specific analysis performed in this thesis is presented.

#### 2.3.2.1 Hints of lepton non-universality

Lepton Universality is typically studied by measuring ratios of branching fractions, denoted as $R$. These observables are very clean from both a theoretical and an experimental viewpoint. In the first case, a good fraction of the uncertainties associated to the computation of hadronic form factors cancel out in the ratio. In the second case, many efficiency effects also cancel out when dividing the branching fractions. Even if some deviations of the order of $2\sigma$ have been observed in the $\mu/e$ case [42, 43], the most striking deviations have been found when comparing the third (tauonic) family with the lighter ones. In the last case, the World average for the combined measurement of the $R(D)$ and $R(D^*)$ observables deviates $4.1\sigma$ with respect to the SM expectation. The $R(D)$ and $R(D^*)$ ratios are defined as

$$R(D^{(*)}) = \frac{\mathcal{B}(B \to D^{(*)}\tau\overline{\nu}_\tau)}{\mathcal{B}(B \to D^{(*)}l\overline{\nu}_l)}, \tag{2.10}$$

where $D$ refers to either $D^0$ or $D^+$, $D^*$ refers to either $D^*(2007)^0$ or $D^*(2010)^+$, and $l \in \{e, \mu\}$. For simplicity, the $D^*(2007)^0$ or $D^*(2010)^+$ resonances are referred to as $D^{*0}$ and $D^{*+}$ throughout this document. A graphical summary of the performed measurements in this system can be found in Fig. 2.5. While the $B$ factories have measured both $R(D)$ and $R(D^*)$ and studied muons and electrons, LHCb has only measured $R(D^*)$, using $D^{*+}$ and without considering electrons. Two complementary measurements have been performed by LHCb, one using the muonic decay of the $\tau$, $\tau \to \mu\nu_\tau\overline{\nu}_\mu$ [44], and the other one using the hadronic decay of the $\tau$, $\tau \to \pi^+\pi^-\pi^-(\pi^0)\nu_\tau$ [25].

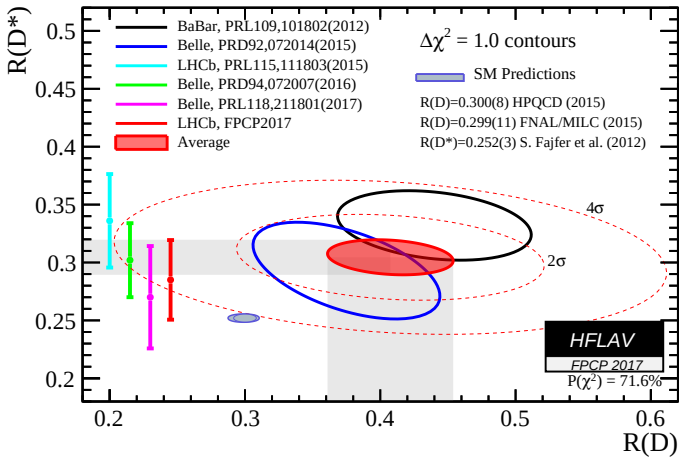



FIGURE 2.5: World average for the combined measurement of $R(D)$ and $R(D^*)$.

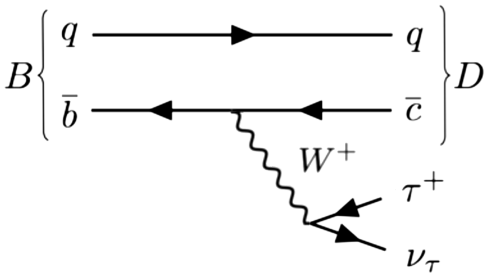



FIGURE 2.6: Leading-order Feynman diagram for the considered tauonic $B$ decays in the SM. The creation of a $D^-$ corresponds to the case $q = d$.

Additional measurements of either $R(D)$ and $R(D^*)$ can be combined with the current World average and help to shed light on the ultimate nature of the observed deviations.

#### 2.3.2.2 Measuring $R(D^+)$ at LHCb

The second analysis of this thesis primarily aims at measuring for the first time in LHCb the $R(D)$ ratio, using $D^{+2}$ and comparing the tauonic decay with the muonic one. The leading-order Feynman diagram for the $\overline{B}^0 \to D^+\tau\overline{\nu}_\tau$ decay in the SM is shown in Fig. 2.6. The expected value for the ratio of branching fractions with respect to the muonic decay, $R(D) \sim 0.3$ [45, 46], deviates from unity due to the difference in mass between the $\tau$ and the $\mu$.

This analysis restricts to the case where $D^+ \to K^-\pi^+\pi^+$ and $\tau \to \mu\nu_\tau\overline{\nu}_\mu$. Consequently, the visible final state in LHCb is $K^-\pi^+\pi^+\mu^-$. This state is the same as in the first LHCb measurement of $R(D^*)$ [44], which implies that several similar strategies can be used. However, the kinematic distributions and the contributions from several background sources are different, and need to be specifically studied. One extra feature of the analysis is that the decays of the form $\overline{B}^0 \to D^{*+}l\overline{\nu}_l$, where $D^{*+} \to D^+\pi^0$ can also contribute to the same visible final state when the $\pi^0$ is not reconstructed. This offers the possibility to determine the $R(D^*)$ ratio, using $D^{*+}$, together with the $R(D)$ ratio. The SM prediction for the $D^*$ case is $R(D^*) = 0.252 \pm 0.003$ [47]. With the previous considerations, the analysis presented in this thesis can determine an ellipsis in the two-dimensional plot shown in Fig. 2.5.

[2]The charge conjugate of $D^+$, $D^-$, is implicitely included in the analysis.

## 2.4 Beyond the Standard Model alternatives

As introduced in Sect. 2.3.2.1, several experimental observations point to Lepton-Universality-violating effects, that can be related to potential NP that predominantly couples to the third lepton generation. Since the $b \to c\tau\nu$ transitions involved in such anomalies proceed at tree level in the SM, the expected contribution from NP would be relatively large, possibly pointing to new (non-Yukawa) interactions at the TeV scale. Several models have been proposed to explain these kind of anomalies. One possibility would be the existence of a new vector boson, $W'^{\pm}$, similar to the SM $W^{\pm}$ boson, but with a greater mass, and with couplings of varying strengths to different leptons and quarks. Another candidate would be a new, non-SM, charged Higgs. This particle was proposed in minimal extensions of the SM [48], that are part of broader theoretical frameworks such as supersymmetry [49]. Finally, another feasible solution might be leptoquarks [50]: hypothetical particles with both electric and color (strong) charges that allow transitions from quarks to leptons and vice versa. For more information on potential NP models see Ref. [51].

An independent set of deviations has been found in $b \to sll$ transitions, which correspond to FCNC that are suppressed in the SM. Examples of these deviations are those observed in the angular distributions of $B^0 \to K^{*0}\mu^+\mu^-$ decays [52] and in the $\mu/e$ LU-violating observables $R(K)$ [42] and $R(K^*)$ [43]. The different experimental inputs have been combined in global fits by theorists [53–56], finding common patterns and a certain tendency towards non-SM scenarios. Some NP models that contain a new $Z'$ boson [57] or leptoquarks are consistent with the results from the fits. Composite Higgs models, where the Higgs boson is considered to be a bound state of new strong interactions, are also possible [58]. Interestingly, several of these models also predict effects in $b \to sqq$ transitions. The results of the first analysis presented in this thesis can consequently be used by theorists in the near future to constrain those NP models.

Since the size of potential NP causing deviations in tree-level $b \to c\tau\nu$ transitions would be much larger than that of possible new contributions to loop-level $b \to sll$ decays, a combined explanation of both phenomena is not straightforward from a theoretical perspective. However, there have been several efforts in this sense, and some of the proposed models consider either leptoquarks [59–61] or a triplet of massive vector bosons, coupled predominantly to third generation fermions [62]. A recent study of the set of theoretical ingredients needed for a combined explanation of both phenomena and a comparison of different possible NP models can be found in Ref. [63].

USC
UNIVERSIDADE
DE SANTIAGO
DE COMPOSTELA

# Chapter 3

# Phenomenology of the $B_s^0 \to (K^+\pi^-)(K^-\pi^+)$ decay

In this chapter, the phenomenological model that I have constructed to describe the $B_s^0 \to (K^+\pi^-)(K^-\pi^+)$ distributions and measure the $\phi_s^{d\bar{d}}$ phase via a fit to data is described. For this channel, the background can be effectively separated from the signal sample (see Sect. 7.2), so there is no need to include a background component in the model. The chosen approach is to do a full amplitude analysis by performing a partial-wave decomposition of the decay rate that takes into account the evolution with the $B_s^0$ decay time. Apart from the CP-violating parameters, all the involved amplitudes are to be determined from data, since most of them have not been measured before. The lack of information for this channel on the $K\pi$ mass dependence for $K\pi$ pairs of spin-0 motivates the use of a form factor which is also fitted to data. In the following sections, the structure of the model is explained.

## 3.1 Time dependence and CP violation

Let's consider the decay of a $B_s^0$ meson into the final state $(K^+\pi^-)(K^-\pi^+)$. The time-dependent differential decay rate is given by

$$\frac{d\Gamma}{dt} \propto |\mathcal{A}(t)|^2, \tag{3.1}$$

where $\mathcal{A}(t)$ is a time-dependent amplitude that, in the $K\pi$ mass window under consideration, can be decomposed into a sum of the 19 polarisation amplitudes written in Table 2.1:

$$\mathcal{A}(t) = \sum_f \mathcal{A}_f(t). \tag{3.2}$$

Due to $B_s^0$-$\overline{B}_s^0$ mixing, the time evolution of these amplitudes is described by

$$\mathcal{A}_f(t) = g_+(t)\mathcal{A}_f(0) + \eta_f \frac{q}{p} g_-(t)\bar{\mathcal{A}}_f(0), \tag{3.3}$$

where $\mathcal{A}_f(0)$ and $\bar{\mathcal{A}}_f(0)$ denote amplitudes defined at $t = 0$. The $\eta_f$ factors take the value $\pm 1$ depending on the behaviour of the polarisation state under parity and will be discussed in the next section, while $p$ and $q$ are complex parameters containing the physics of the mixing. The time dependent functions $g_\pm(t)$ can be written as

$$g_\pm(t) = \frac{1}{2} e^{-im_{B_s}t} e^{-\frac{\Gamma_s}{2}t} \left( e^{i\frac{\Delta m_s}{2}t} e^{-\frac{\Delta\Gamma_s}{4}t} \pm e^{-i\frac{\Delta m_s}{2}t} e^{\frac{\Delta\Gamma_s}{4}t} \right), \tag{3.4}$$

where $\Gamma_s$ and $\Delta\Gamma_s$ are, respectively, the width average and the width difference of the two $B_s^0$ mass eigenstates, and $\Delta m_s$ is their mass difference. The present measured values for those parameters can be found in Table 3.1.

| Parameter | Value |
|---|---|
| $\Gamma_s$ | $0.6625 \pm 0.0018$ ps$^{-1}$ |
| $\Delta\Gamma_s$ | $0.090 \pm 0.005$ ps$^{-1}$ |
| $\Delta m_s$ | $17.757 \pm 0.021$ ps$^{-1}$ |

TABLE 3.1: Measured values for the $B_s^0$ mixing and decay parameters, obtained from HFLAV[64]. The correlation between $\Gamma_s$ and $\Delta\Gamma_s$ is $\rho = -0.082$.

Assuming negligible CP violation in the mixing [65] we can write $|q/p| = 1$, and so the parametrisation $q/p = e^{-i\phi_M}$ can be used, where $\phi_M$ is the mixing phase. The time-dependent decay rate of the $B_s^0$ meson can then be written as [17]

$$\frac{d\Gamma}{dt} \propto \sum_{i,j} e^{-\Gamma_s t} \times \left[ a_{ij} \cosh\left(\frac{1}{2}\Delta\Gamma_s t\right) + b_{ij} \sinh\left(\frac{1}{2}\Delta\Gamma_s t\right) + c_{ij} \cos\left(\Delta m_s t\right) + d_{ij} \sin\left(\Delta m_s t\right) \right] \tag{3.5}$$

where

$$\begin{aligned} a_{ij} &= \mathcal{A}_i(0)\mathcal{A}_j^*(0) + \eta_i\eta_j\bar{\mathcal{A}}_i(0)\bar{\mathcal{A}}_j^*(0) \\ b_{ij} &= -(\eta_j e^{i\phi_M}\mathcal{A}_i(0)\bar{\mathcal{A}}_j^*(0) + \eta_i e^{-i\phi_M}\bar{\mathcal{A}}_i(0)\mathcal{A}_j^*(0)) \\ c_{ij} &= \mathcal{A}_i(0)\mathcal{A}_j^*(0) - \eta_i\eta_j\bar{\mathcal{A}}_i(0)\bar{\mathcal{A}}_j^*(0) \\ d_{ij} &= -i(\eta_j e^{i\phi_M}\mathcal{A}_i(0)\bar{\mathcal{A}}_j^*(0) - \eta_i e^{-i\phi_M}\bar{\mathcal{A}}_i(0)\mathcal{A}_j^*(0)). \end{aligned} \tag{3.6}$$

The time-dependent decay rate of a $\overline{B}_s^0$ meson can be obtained from Eq. 3.5 making the changes $c_{ij} \to -c_{ij}$ and $d_{ij} \to -d_{ij}$.

To clearly identify the CPV terms involved in the process, the polarisation amplitudes at $t = 0$ can be separated into a CP conserving complex amplitude, $A_f(0)$, a direct CP asymmetry, $\Delta_{dir,f}^{CP}$ and a CP violating weak phase, $\phi_{D,f}$, as follows:

$$\begin{aligned} \mathcal{A}_f(0) &= \sqrt{1 - \Delta_{dir,f}^{CP}}\, e^{-i\phi_{D,f}} A_f(0) \\ \bar{\mathcal{A}}_{\bar{f}}(0) &= \sqrt{1 + \Delta_{dir,f}^{CP}}\, e^{i\phi_{D,f}} A_f(0). \end{aligned} \tag{3.7}$$

The inverse transformations are:

$$\begin{aligned} \Delta_{dir,f}^{CP} &= \frac{|\bar{\mathcal{A}}_{\bar{f}}(0)|^2 - |\mathcal{A}_f(0)|^2}{|\bar{\mathcal{A}}_{\bar{f}}(0)|^2 + |\mathcal{A}_f(0)|^2}, \\ \phi_{D,f} &= \frac{1}{2}[\arg\left(\bar{\mathcal{A}}_{\bar{f}}(0)\right) - \arg\left(\mathcal{A}_f(0)\right)], \\ A_f(0) &= \frac{1}{\sqrt{2}}\sqrt{|\mathcal{A}_f(0)|^2 + |\bar{\mathcal{A}}_{\bar{f}}(0)|^2}\exp\left[\frac{1}{2}\left(\arg\left(\mathcal{A}_f(0)\right) + \arg\left(\bar{\mathcal{A}}_{\bar{f}}(0)\right)\right)\right]. \end{aligned} \tag{3.8}$$

The CP violating phase associated to the interference between mixing and decay, for each state, is then defined as

$$\phi_{s,f} = \phi_M - 2\phi_{D,f}. \tag{3.9}$$

Since the same source of CP violation is assumed for all the decays under study (reasonable approximation given the current level of sensitivity), the conditions $\phi_{s,f} = \phi_s^{d\bar{d}}$ and $\Delta_{dir,f}^{CP} = \Delta_{dir}^{CP}$ are imposed. The direct CP asymmetry can be translated into a more commonly used parameter,

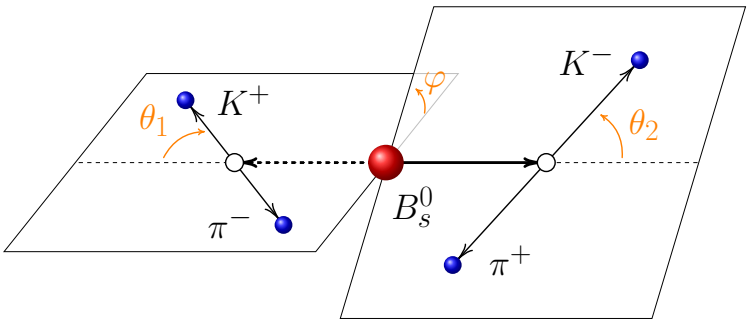



FIGURE 3.1: Definition of angles in the helicity basis. Taking the example of a $B_s^0 \to Q_1 Q_2$ decay (this analysis uses $B_s^0 \to SS$, $B_s^0 \to SV$, $B_s^0 \to VS$, $B_s^0 \to VV$, $B_s^0 \to ST$, $B_s^0 \to TS$, $B_s^0 \to VT$, $B_s^0 \to TV$ and $B_s^0 \to TT$), with each final-state quasi-two-body meson decaying to pseudoscalars ($Q_1 \to K^+\pi^-$ and $Q_2 \to K^-\pi^+$), $\theta_1$ ($\theta_2$) is defined as the angle between the directions of motion of $K^+$ ($K^-$) in the $Q_1$ ($Q_2$) rest frame and $Q_1$ ($Q_2$) in the $B_s^0$ rest frame, and $\varphi$ as the angle between the plane defined by $K^+\pi^-$ and the plane defined by $K^-\pi^+$ in the $B_s^0$ rest frame.

$|\lambda|$, as:

$$|\lambda| = \frac{\sqrt{1 + \Delta_{dir}^{CP}}}{\sqrt{1 - \Delta_{dir}^{CP}}}. \tag{3.10}$$

The measurement of the $\phi_s^{d\bar{d}}$ and $|\lambda|$ parameters is the main goal of this analysis.

The part of the decays mediated by the strong interaction, including the final hadronisation process, is contained in the CP conserving amplitudes, $A_f(0)$. These terms are discussed in detail in the next section.

## 3.2 Decay distributions at $t = 0$.

An angular analysis is needed to separate the states with $\eta_f = 1$ from the states with $\eta_f = -1$ in Eq. 3.6. The three helicity angles $\theta_1$, $\theta_2$ and $\varphi$ are defined in Fig. 3.1. Additionally, to separate the different resonant and non resonant components, the two 2-body invariant masses, $m_1 \equiv M(K^+\pi^-)$ and $m_2 \equiv M(K^-\pi^+)$, have to be included in the analysis. The time dependent differential decay rate of a $B_s^0$ meson is then

$$\frac{d^6\Gamma}{dt\, d\Omega} \propto |\mathcal{A}(t, \cos\theta_1, \cos\theta_2, \varphi, m_1, m_2)|^2 \cdot \Phi_4(m_1, m_2), \tag{3.11}$$

where $\Omega$ stands for the five-dimensional space spanned by the 3 helicity angles and the 2 invariant masses, and $\Phi_4$ is the 4-body phase space defined in Sect. 3.2.2.

The angular and mass dependence of the decay rate (apart from the phase-space factor) comes from the CP-averaged amplitudes introduced in Eq. 3.7. In the quasi-two-body approach, those amplitudes can be decomposed as

$$\begin{aligned} A_h^{j_1 j_2}(0, \cos\theta_1, \cos\theta_2, \varphi, m_1, m_2) = \\ A_h^{j_1 j_2} \cdot \Theta_h^{j_1 j_2}(\cos\theta_1, \cos\theta_2, \varphi) \cdot [\mathcal{M}_{j_1}(m_1) \cdot \mathcal{M}_{j_2}(m_2) \cdot \mathcal{F}_h^{j_1 j_2}(m_1, m_2) \cdot \mathcal{N}_h^{j_1 j_2}], \end{aligned} \tag{3.12}$$

where $j_1$ and $j_2$ stand for the the spin of the $K^+\pi^-$ and the $K^-\pi^+$ pair, respectively, and the index $h$ identifies the helicity state. Following Table 2.1 the $h$ index takes the value 0 if $j_1 = j_2 = 0$; the values $\{0, \|, \perp\}$ if $(j_1, j_2) \in \{(1,1), (1,2), (2,1)\}$; and the values $\{0, (\|1), (\|2), (\perp 1), (\perp 2)\}$ if $j_1 = j_2 = 2$. The angular dependence is contained in the functions $\Theta_h^{j_1 j_2}$, described in Sect. 3.2.1.

The mass dependence appears in the $\mathcal{M}_j$ amplitudes, the angular momentum barrier factors, $\mathcal{F}_h^{j_1 j_2}$, and the normalisation factors, $\mathcal{N}_h^{j_1 j_2}$, described in Sect. 3.2.2, Sect. 3.2.2.1 and Sect. 3.2.2.2. Finally, the complex amplitudes $A_h^{j_1 j_2}$ are constant parameters containing the CP-averaged physics of the decays, and are measured in the final fit together with the CPV parameters. The normalisation of these amplitudes is treated in Sect. 7.7.2.

### 3.2.1 Angular dependence

The amplitudes listed in Table 2.1 and written in Eq. 3.12 are expressed in the so called amplitude transversity basis. However, the angular distribution is most easily obtained working first in the amplitude helicity basis, where each state is identified by the quantum numbers $j_1$, $j_2$ and $m$. For the considered decay channels, $j_1$ and $j_2$ can take the value 0 for a scalar, 1 for a vector and 2 for a tensor, and $m$ can take any integer value from $-M(j_1, j_2)$ to $M(j_1, j_2)$, where $M(j_1, j_2) = 1/2(|j_1 + j_2| - |j_1 - j_2|)$. Following [17], the equivalent of Eq. 3.12 in the amplitude helicity basis, omitting the masses to simplify the notation, can be written as

$$A_m^{j_1 j_2}(0, \cos\theta_1, \cos\theta_2, \varphi) = A_m^{j_1 j_2} N Y_{j_1}^{-m}(\theta_1, -\varphi) Y_{j_2}^{m}(\pi - \theta_2, 0), \tag{3.13}$$

where $Y_l^m$ are spherical harmonics, $A_m^{j_1 j_2}$ are constant terms and $N$ is a normalization constant.

These amplitudes have now to be rotated into the transversity basis, where the states with the same $j_1$ and $j_2$ are labelled by the index $h$. The amplitudes $A_0^{j_1 j_2}$ are the same in the two basis, for all $j_1$ and $j_2$. The transversity amplitudes with $h \neq 0$ for $(j_1, j_2) \in \{(1,1), (1,2), (2,1)\}$ are given by

$$A_\parallel^{j_1 j_2} = \frac{1}{\sqrt{2}}\left(A_{+1}^{j_1 j_2} + A_{-1}^{j_1 j_2}\right), \qquad A_\perp^{j_1 j_2} = \frac{1}{\sqrt{2}}\left(A_{+1}^{j_1 j_2} - A_{-1}^{j_1 j_2}\right), \tag{3.14}$$

while for $j_1 = j_2 = 2$ are given by

$$A_{\parallel 1}^{22} = \frac{1}{\sqrt{2}}\left(A_{+1}^{22} + A_{-1}^{22}\right), \qquad A_{\perp 1}^{22} = \frac{1}{\sqrt{2}}\left(A_{+1}^{22} - A_{-1}^{22}\right), \tag{3.15}$$

$$A_{\parallel 2}^{22} = \frac{1}{\sqrt{2}}\left(A_{+2}^{22} + A_{-2}^{22}\right), \qquad A_{\perp 2}^{22} = \frac{1}{\sqrt{2}}\left(A_{+2}^{22} - A_{-2}^{22}\right). \tag{3.16}$$

After applying the amplitude rotation from the helicity to the transversity basis, the angular functions $\Theta_h^{j_1 j_2}$, introduced in Eq. 3.12, are obtained from the corresponding combination of the spherical harmonics in Eq. 3.13. The factor $N$ is chosen to verify the following normalisation condition:

$$\int_{-1}^{+1}\int_{-1}^{+1}\int_{0}^{2\pi} |\Theta_h^{j_1 j_2}(\cos\theta_1, \cos\theta_2, \varphi)|^2 \; \mathrm{d}(\cos\theta_1)\; \mathrm{d}(\cos\theta_2)\; \mathrm{d}\varphi = 1. \tag{3.17}$$

Table 3.2 contains the list of the 19 resulting angular functions.

Finally, from the properties of these functions under parity transformations, it can be inferred that the factor $\eta_f \equiv \eta_h^{j_1 j_2}$, introduced in Eq. 3.3, is given by:

$$\eta_h^{j_1 j_2} = (-1)^{j_1 + j_2}\eta_h, \tag{3.18}$$

where $\eta_h = +1$ for longitudinal ($\{0\}$) and parallel ($\{\parallel, \parallel_1, \parallel_2\}$) polarisations, and $\eta_h = -1$ for perpendicular ($\{\perp, \perp_1, \perp_2\}$) polarisations.

| $j_1$ | $j_2$ | $h$ | $Y_{\ell_1}^{m_1}(\theta_1,-\varphi)Y_{\ell_2}^{m_2}(\pi-\theta_2,0)$ | $\Theta_{j_1 j_2 h}(\cos\theta_1,\cos\theta_2,\varphi)$ |
|---|---|---|---|---|
| 0 | 0 | 0 | $\sqrt{\pi}Y_0^0Y_0^0$ | $\frac{1}{2\sqrt{2\pi}}$ |
| 0 | 1 | 0 | $\sqrt{\pi}Y_0^0Y_1^0$ | $-\frac{\sqrt{3}}{2\sqrt{2\pi}}\cos\theta_2$ |
| 1 | 0 | 0 | $\sqrt{\pi}Y_1^0Y_0^0$ | $\frac{\sqrt{3}}{2\sqrt{2\pi}}\cos\theta_1$ |
| 0 | 2 | 0 | $\sqrt{\pi}Y_0^0Y_2^0$ | $\frac{\sqrt{5}}{4\sqrt{2\pi}}(3\cos^2\theta_2-1)$ |
| 2 | 0 | 0 | $\sqrt{\pi}Y_2^0Y_0^0$ | $\frac{\sqrt{5}}{4\sqrt{2\pi}}(3\cos^2\theta_1-1)$ |
| 1 | 1 | 0 | $\sqrt{\pi}Y_1^0Y_1^0$ | $-\frac{3}{2\sqrt{2\pi}}\cos\theta_1\cos\theta_2$ |
| 1 | 1 | $\parallel$ | $\frac{\sqrt{\pi}}{\sqrt{2}}(Y_1^{-1}Y_1^{+1}+Y_1^{+1}Y_1^{-1})$ | $-\frac{3}{4\sqrt{\pi}}\sin\theta_1\sin\theta_2\cos\varphi$ |
| 1 | 1 | $\perp$ | $\frac{\sqrt{\pi}}{\sqrt{2}}(Y_1^{-1}Y_1^{+1}-Y_1^{+1}Y_1^{-1})$ | $-i\frac{3}{4\sqrt{\pi}}\sin\theta_1\sin\theta_2\sin\varphi$ |
| 1 | 2 | 0 | $\sqrt{\pi}Y_1^0Y_2^0$ | $\frac{\sqrt{15}}{4\sqrt{2\pi}}\cos\theta_1(3\cos^2\theta_2-1)$ |
| 1 | 2 | $\parallel$ | $\frac{\sqrt{\pi}}{\sqrt{2}}(Y_1^{-1}Y_2^{+1}+Y_1^{+1}Y_2^{-1})$ | $\frac{3\sqrt{5}}{4\sqrt{\pi}}\sin\theta_1\sin\theta_2\cos\theta_2\cos\varphi$ |
| 1 | 2 | $\perp$ | $\frac{\sqrt{\pi}}{\sqrt{2}}(Y_1^{-1}Y_2^{+1}-Y_1^{+1}Y_2^{-1})$ | $i\frac{3\sqrt{5}}{4\sqrt{\pi}}\sin\theta_1\sin\theta_2\cos\theta_2\sin\varphi$ |
| 2 | 1 | 0 | $\sqrt{\pi}Y_2^0Y_1^0$ | $-\frac{\sqrt{15}}{4\sqrt{2\pi}}(3\cos^2\theta_1-1)\cos\theta_2$ |
| 2 | 1 | $\parallel$ | $\frac{\sqrt{\pi}}{\sqrt{2}}(Y_2^{-1}Y_1^{+1}+Y_2^{+1}Y_1^{-1})$ | $-\frac{3\sqrt{5}}{4\sqrt{\pi}}\sin\theta_1\cos\theta_1\sin\theta_2\cos\varphi$ |
| 2 | 1 | $\perp$ | $\frac{\sqrt{\pi}}{\sqrt{2}}(Y_2^{-1}Y_1^{+1}-Y_2^{+1}Y_1^{-1})$ | $-i\frac{3\sqrt{5}}{4\sqrt{\pi}}\sin\theta_1\cos\theta_1\sin\theta_2\sin\varphi$ |
| 2 | 2 | 0 | $\sqrt{\pi}Y_2^0Y_2^0$ | $\frac{5}{8\sqrt{2\pi}}(3\cos^2\theta_1-1)(3\cos^2\theta_2-1)$ |
| 2 | 2 | $\parallel 1$ | $\frac{\sqrt{\pi}}{\sqrt{2}}(Y_2^{-1}Y_2^{+1}+Y_2^{+1}Y_2^{-1})$ | $\frac{15}{4\sqrt{\pi}}\sin\theta_1\cos\theta_1\sin\theta_2\cos\theta_2\cos\varphi$ |
| 2 | 2 | $\perp 1$ | $\frac{\sqrt{\pi}}{\sqrt{2}}(Y_2^{-1}Y_2^{+1}-Y_2^{+1}Y_2^{-1})$ | $i\frac{15}{4\sqrt{\pi}}\sin\theta_1\cos\theta_1\sin\theta_2\cos\theta_2\sin\varphi$ |
| 2 | 2 | $\parallel 2$ | $\frac{\sqrt{\pi}}{\sqrt{2}}(Y_2^{-2}Y_2^{+2}+Y_2^{+2}Y_2^{-2})$ | $\frac{15}{16\sqrt{\pi}}\sin^2\theta_1\sin^2\theta_2\cos(2\varphi)$ |
| 2 | 2 | $\perp 2$ | $\frac{\sqrt{\pi}}{\sqrt{2}}(Y_2^{-2}Y_2^{+2}-Y_2^{+2}Y_2^{-2})$ | $i\frac{15}{16\sqrt{\pi}}\sin^2\theta_1\sin^2\theta_2\sin(2\varphi)$ |

TABLE 3.2: Functions containing the angular dependence of the amplitudes, as introduced in Eq. 3.12.

### 3.2.2 Mass dependence

As previously explained, three $K\pi$ components are considered to contribute in the studied region of the phase space, corresponding to an angular momentum, $j$, equal to 0, 1 and 2. Their physical nature is discussed below and the phenomenological parameterisation of the corresponding two-body mass amplitudes, $\mathcal{M}_j(m)$, is described in Sect. 3.2.2.1 and Sect. 3.2.2.2. The remainder of this section is used to describe the mass dependence of the phase-space element, the angular momentum barrier factors and the normalisation terms.

- **Scalar ($j = 0$) component.**

  The $K_0^*(1430)^0$ resonance dominates in the mass region under study, together with a low mass structure whose nature has been extensively discussed in relation to the existence of the controversial $K_0^*(800)^0$ resonance. A scalar non-resonant (NR) component has also been considered in several analysis, either alone or in combination with the $K_0^*(800)^0$ resonance. This lack of understanding makes it difficult to parameterise the scalar $K\pi$ mass amplitude.

  On a technical level, approaches based on an isobar model ($K_0^*(800)^0$ + $NR$ + $K_0^*(1430)^0$) present problems of non-unitarity and are not expected to work for wide structures such as the $K_0^*(800)^0$. A common approach, solving the problem of unitarity, is the so called LASS parameterisation [66]. It combines the $K_0^*(1430)^0$ resonance with a contact term. However, it also presents its own shortcomings and may not be accurate enough within the whole $K\pi$ mass range used in this analysis. For example, this parameterisation neglects the inelastic effects that appear over the $K\eta$ mass threshold ($\sim 1050\,\mathrm{MeV}/c^2$).

  In an attempt to solve the problems of the previous models, this analysis uses the parameterisation presented in a recent phenomenological study of the $K\pi$ scattering amplitude up to $1600\,\mathrm{MeV}/c^2$ [67]. The amplitude is obtained in that study by fitting the $K\pi$ scattering data available up to date, imposing consistency with forward dispersion relations and with three threshold sum rules. In Sect. 3.2.2.1, we describe this scattering amplitude and develop a form factor to transform it into a decay amplitude.

- **Vector ($j = 1$) component.**

  The vector component is highly dominated by the $K^*(892)^0$ resonance. Additional contributions may come from the $K^*(1410)^0$ and the $K^*(1680)^0$ resonances (outside the mass range but with a large width). However, given that similar analyses have found their contributions to be small (see e.g. [68]) and taking into account the low sensitivity of the fit on them due to limited statistics, they are not included in the nominal model of this analysis. The $K^*(892)^0$ resonance is parameterised using a spin-1 relativistic Breit Wigner function, described in Sect. 3.2.2.2. When studying systematics, the $K^*(1410)^0$ and the $K^*(1680)^0$ are included in the model using an isobar approach (see Sect. 7.9.9), with a linear combination of three relativistic Breit Wigner functions. The isobar model is justified in this case since these resonances present a small overlapping.

- **Tensor ($j = 2$) component.**

  Only the $K_2^*(1430)^0$ resonance is assumed to contribute in the nominal $K\pi$ mass window. It is parameterised with a spin-2 relativistic Breit Wigner function, described in Sect. 3.2.2.2.

The phase space factor introduced in Eq. 3.11 depends on the two 2-body invariant masses, $m_1$ and $m_2$, as follows:

$$\Phi_4(m_1, m_2) = q(m_1) \cdot q(m_2) \cdot p(m_1, m_2), \tag{3.19}$$

where $q$ denotes the momentum of the $K$ or the $\pi$ in the corresponding $K\pi$ rest frame and $p$ denotes the momentum of one of the $K\pi$ pairs in the $B_s^0$ rest frame. These momenta are

| $l$ | $B_l(p, p_0)$ |
|---|---|
| 0 | 1 |
| 1 | $\sqrt{\frac{1+(p_0 d)^2}{1+(pd)^2}}$ |
| 2 | $\sqrt{\frac{9+3(p_0 d)^2+(p_0 d)^4}{9+3(pd)^2+(pd)^4}}$ |

TABLE 3.3: Blatt-Weisskopf functions up to $l = 2$. The $d$ parameter, characterising the size of the decaying particle, is set to 1.6 $\text{GeV}^{-1}$ and is varied when studying systematics.

constructed as follows:

$$\begin{aligned} q(m) &= \frac{\sqrt{(m^2 - (M(K) + M(\pi))^2)(m^2 - (M(K) - M(\pi))^2)}}{2m} \\ p(m_1, m_2) &= \frac{\sqrt{(M(B_s^0)^2 - (m_1 + m_2)^2)(M(B_s^0)^2 - (m_1 - m_2)^2)}}{2M(B_s^0)} \end{aligned} \tag{3.20}$$

We use the values $M(K) = 493.667$ MeV/$c^2$, $M(\pi) = 139.57018$ MeV/$c^2$ and $M(B_s^0) = 5366.77$ MeV/$c^2$ [69] for the masses of the involved mesons.

The angular momentum barrier factors that appear in Eq. 3.12 are constructed as follows:

$$\begin{aligned} \mathcal{F}_h^{j_1 j_2}(m_1, m_2) = &\left[ B_L(p(m_1, m_2), \tilde{p}_0) \left( \frac{p(m_1, m_2)}{\tilde{p}_0} \right)^L \right] \\ \cdot &\left[ B_{j_1}(q(m_1), \tilde{q}_0) \left( \frac{q(m_1)}{\tilde{q}_0} \right)^{j_1} \right] \cdot \left[ B_{j_2}(q(m_2), \tilde{q}_0) \left( \frac{q(m_2)}{\tilde{q}_0} \right)^{j_2} \right], \end{aligned} \tag{3.21}$$

where $B_l$ are the Blatt-Weisskopf functions for an angular momentum $l$ as defined in Table 3.3, $\tilde{p}_0(\tilde{q}_0)$ corresponds to $p(q)$ evaluated at the nominal mass of the $K^*(892)^0$ resonance (here $\tilde{p}_0$ and $\tilde{q}_0$ are sterile normalisation constants), and $L$ is the orbital angular momentum between the two $K\pi$ pairs, which in general depends on $j_1$, $j_2$ and $h$. Angular momentum conservation rules impose $|j_1 - j_2| \leq L \leq j_1 + j_2$. We adopt the usual approach of choosing the minimum allowed value for $L$, as it is supposed to dominate in decays where a relatively small amount of energy is released. Therefore, we set $L = |j_1 - j_2|$ and the angular momentum barrier factors become independent of $h$. Larger values of $L$ are explored when doing systematic studies (see Sect. 7.9.8).

Finally, the complex normalisation factors $\mathcal{N}_h^{j_1 j_2}$ are given by

$$|\mathcal{N}_h^{j_1 j_2}|^{-2} = \int\int dm_1\, dm_2\, |\mathcal{M}_{j_1}(m_1)|^2 \cdot |\mathcal{M}_{j_2}(m_2)|^2 \cdot (\mathcal{F}_h^{j_1 j_2}(m_1, m_2))^2 \cdot \Phi_4(m_1, m_2), \tag{3.22}$$

$$\arg(\mathcal{N}_h^{j_1 j_2}) = -\arg(\mathcal{M}_{j_1}(M(K^*(892)))) - \arg(\mathcal{M}_{j_2}(M(K^*(892)))), \tag{3.23}$$

where the range of the mass integrals corresponds to the mass window under study. The modulus of the normalisation factor ensures that the relation between the square moduli of the physical amplitudes, $A_h^{j_1 j_2}$, corresponds to the relation between the fractions of each polarisation state in the mass window. The phase of the $\mathcal{N}_h^{j_1 j_2}$ factor imposes the convention that the phase differences between physical amplitudes are evaluated at the $K^{*0}$ pole.

#### 3.2.2.1 Model of the scalar $K\pi$ mass amplitude

In the quasi two-body approximation (assuming independence between the $K^+\pi^-$ and the $K^-\pi^+$ pairs from the viewpoint of the strong interaction), and considering that the two body decay

is predominantly elastic, Watson's theorem [70] holds approximately, implying that the global phase shift of the two-body decay process should follow that of the $K\pi$ scattering amplitude, $\mathcal{M}_0^{\rm scat}(m)$. This allows us to use the parameterisation for the phase of the scalar $K\pi$ scattering amplitude developed in Ref [67]. Since we aim at describing a decay, we stick to the isospin-$1/2$ component and neglect the isospin-$3/2$ one, also covered in that publication. In Sect. 3.2.2.1.1, the parameterisation of the scattering amplitude is copied down for completeness.

There is no reason for the modulus of the amplitude of the decay process to be the same as the one of the scattering amplitude. The decay amplitude is also expected to present a channel-dependent behaviour and there are no phenomenological predictions available for the $B_s^0 \to (K^+\pi^-)(K^-\pi^+)$ decay. The approach followed in this analysis consists on obtaining the shape directly from data, substituting the scattering modulus by an effective form factor, $F(m)$. Therefore, the mass dependent amplitude is constructed as:

$$\mathcal{M}_0(m) = F(m) \cdot \exp\left[i \arg\left(\mathcal{M}_0^{scat}(m)\right)\right], \quad F(m) \in \Re_{>0}. \tag{3.24}$$

In order to reduce parameter correlations, the form factor is parameterised using a 4th-order expansion in Chebyshev polynomials, $T_i(x)$, as follows:

$$F(m) = 1 + \sum_{i=1}^{4} c_i^{mass} \cdot T_i(X(m)), \tag{3.25}$$

where $X(m) = (m - 1175\,\mathrm{MeV}/c^2)/425\,\mathrm{MeV}/c^2$, $X(m) \in [-1, 1]$, and where the Chebyshev polynomials are

$$\begin{array}{lll} T_0(x) = 1, & T_1(x) = x, & T_2(x) = 2x^2 - 1, \\ T_3(x) = 4x^3 - 3x, & T_4(x) = 8x^4 - 8x^2 + 1, & T_5(x) = 16x^5 - 20x^3 + 5x. \end{array}$$

The $c_i^{mass}$ coefficients are floated in the full time-dependent fit to data. Their resulting values can be found in Table 7.20. The coefficients decrease with the order of the polynomial term. The expansion is truncated at fourth order since adding an extra term would not significantly affect the result and the size of the fifth coefficient is of the order of its statistical uncertainty.

**3.2.2.1.1 Scattering amplitude** The parameterisation of the scalar $K\pi$ mass amplitude presented in Ref. [67] is defined separately for two mass regions, below and above the $K\eta$ production threshold (we use $M(\eta) = 547\,\mathrm{MeV}/c^2$). This distinction obeys to the fact that starting from this mass value the amplitude stops being completely elastic, and the parameterisation has to accommodate some inelastic effects. Below, the expressions for the two ranges are written. All the involved parameters are fixed to the values collected in Table 3.4. It should be noted that within this parameterisation the mass is expressed in $\mathrm{GeV}/c^2$.

| Parameter | Value | Parameter | Value |
|---|---|---|---|
| $s_{Adler}$ | 0.236 GeV$^2$ | $\alpha$ | 1.15 |
| $s_0$ | 1.21 GeV$^2$ | $e_1$ | 1 |
| $B_0$ | 0.411 | $e_2$ | 0.184 |
| $B_1$ | 0.162 | $a$ | $-5.20$ GeV$^{-2}$ |
| $\phi_0$ | $-0.19$ GeV$^{-1}$ | $b$ | 7.60 GeV$^{-4}$ |
| $\phi_1$ | 5.03 GeV$^{-3}$ | $c$ | $-1.73$ GeV$^{-2}$ |
| $\sqrt{s_{r1}}$ | 1.401 GeV | $G_1$ | 0.497 GeV |
| $\sqrt{s_{r2}}$ | 1.817 GeV | $G_2$ | 0.28 GeV |

TABLE 3.4: Parameters of the scalar $K\pi$ scattering amplitude presented in Ref. [67].

- Elastic region, $m \leq (M(K) + M(\eta))$.

  The elastic scattering amplitude is constructed as follows:

$$\mathcal{M}_0^{scat}(m) = \frac{1}{\cot \delta_0^{1/2}(m) - i}, \tag{3.26}$$

  where

$$\cot \delta_0^{1/2}(m) = \frac{m}{2q(m^2 - s_{Adler})}(B_0 + B_1\omega(y(m))). \tag{3.27}$$

  The $\omega$ function is parameterised as:

$$\omega(y(m)) = \frac{\sqrt{y(m)} - \alpha\sqrt{y_0 - y(m)}}{\sqrt{y(m)} + \alpha\sqrt{y_0 - y(m)}}, \tag{3.28}$$

  with

$$y(m) = \left(\frac{m^2 - \Delta_{K\pi}}{m^2 + \Delta_{K\pi}}\right)^2, \qquad \Delta_{K\pi} = M(K)^2 - M(\pi)^2, \qquad y_0 \equiv y(\sqrt{s_0}). \tag{3.29}$$

- Inelastic region, $m > (M(K) + M(\eta))$.

  The amplitude in the inelastic region is parameterised as:

$$\mathcal{M}_0^{scat}(m) = \frac{S_0^b(m)S_1^r(m)S_2^r(m)}{2i}. \tag{3.30}$$

  The non resonant term above, $S_0^b$(m), is constructed as follows:

$$S_0^b(m) = \exp[2iq_\eta(m)(\phi_0 + \phi_1 q_\eta^2(m))], \tag{3.31}$$

  where the $q_\eta(m)$ momentum variable is computed as

$$q_\eta(m) = \frac{\sqrt{(m^2 - (M(K) + M(\eta))^2)(m^2 - (M(K) - M(\eta))^2)}}{2m}. \tag{3.32}$$

  The resonant terms, $S_1^r(m)$ and $S_2^r(m)$, have the following structure:

$$S_n^r(m) = \frac{s_{rn} - m^2 + i(P_n(m) - Q_n(m))}{s_{rn} - m^2 - i(P_n(m) + Q_n(m))}, \qquad \text{for } n \in \{1, 2\}, \tag{3.33}$$

  with

$$\begin{aligned}
P_1(m) &= (s_{r1} - m^2)\beta + e_1 G_1 \frac{p_1(q(m))}{p_1(q(\sqrt{s_{r1}}))} \frac{q(m) - q(M(K) + M(\eta))}{q(\sqrt{s_{r1}}) - q(M(K) + M(\eta))}, \\
Q_1(m) &= (1 - e_1)G_1 \frac{p_1(q(m))}{p_1(q(\sqrt{s_{r1}}))} \frac{q_\eta(m)}{q_\eta(\sqrt{s_{rq}})}\Theta_{\eta K}(m), \\
P_2(m) &= e_2 G_2 \frac{p_2(q(m))}{p_2(q(\sqrt{s_{r2}}))} \frac{q(m) - q(M(K) + M(\eta))}{q(\sqrt{s_{r2}}) - q(M(K) + M(\eta))}, \\
Q_2(m) &= (1 - e_2)G_2 \frac{p_2(q(m))}{q_2(q(\sqrt{s_{r2}}))} \frac{q_\eta(m)}{q_\eta(\sqrt{s_{r2}})}\Theta_{\eta K}(m)
\end{aligned} \tag{3.34}$$

  and

$$p_1(x) = 1 + ax^2 + bx^4, \qquad p_2(x) = 1 + cx^2, \tag{3.35}$$

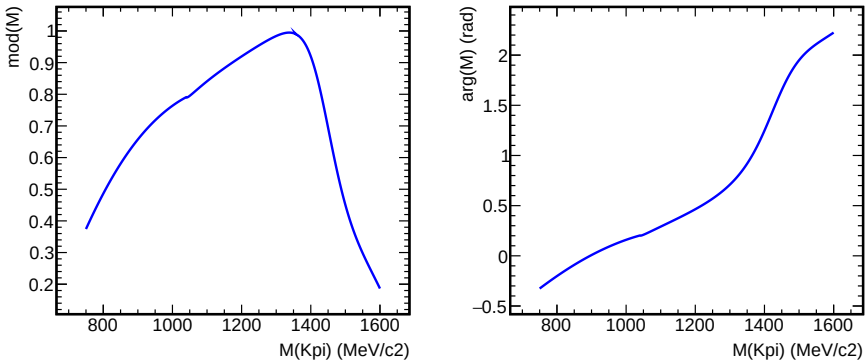



FIGURE 3.2: Mass dependence of the scalar $K\pi$ scattering amplitude presented in Ref. [67], separated in (left) modulus and (right) phase.

| Parameter | $K^*(892)^0$ | $K_2^*(1430)^0$ |
|---|---|---|
| $M$ [ MeV/$c^2$ ] | 895.81 | 1432.4 |
| $\Gamma$ [ MeV ] | 47.4 | 109 |

TABLE 3.5: Nominal mass and width [69] of the vector and tensor resonances considered in the default fitting model.

$$\Theta_{\eta K}(m) = \Theta(m - (M(K) + M(\eta))). \tag{3.36}$$

Finally, continuity at threshold is fulfilled by imposing $\beta \equiv 1/\delta_0^{1/2}(M(K) + M(\eta))$.

The mass lineshapes, for modulus and phase, of the resulting scattering amplitude are shown in Fig. 3.2. As previously explained, only the phase shape is used, while the modulus is substituted by an effective form factor.

#### 3.2.2.2 Model of the vector and tensor $K\pi$ mass amplitudes

The vector and tensor $K\pi$ mass amplitudes are parameterised using relativistic Breit Wigner functions, which correspond to the $K^*(892)^0$ and $K_2^*(1430)^0$ resonances. These functions are defined as follows:

$$\mathcal{M}_j(m) = \frac{m_j \Gamma_j}{m_j^2 - m^2 - i m_j \Gamma_j(m)}, \tag{3.37}$$

where $m_j$ and $\Gamma_j$ are the nominal mass and width of the corresponding resonance ($K^*(892)$ for $j = 1$ and $K_2^*(1430)$ for $j = 2$) and $\Gamma_j(m)$ is the so called running width, defined as

$$\Gamma_j(m) = \Gamma_j \left(\frac{q(m)}{q_0}\right)^{2j+1} \frac{m_j}{m} B_j(q(m), q_0)^2, \tag{3.38}$$

with $q_0 = q(m_j)$. The values of the nominal masses and widths for the two resonances are written in Table 3.5. These parameters are fixed during fitting.

# Chapter 4

# Phenomenology of the $\overline{B}^0 \to D^{(*)+} l \bar{\nu}_l$ decays

In this chapter, the model used to measure the $R(D^{(*)+})$ ratios via a fit to data is explained. It follows a significantly different approach from the one used in the $B_s^0 \to (K^+\pi^-)(K^-\pi^+)$ analysis, as explained below.

- The interest of this second analysis does not rely on studying the quantum amplitudes contributing to the decay, but on measuring the overall yield.
- In this case, the selection does not allow to get a background-free sample to fit, due to irreducible components, thus several background components need to be accounted for during fitting.
- The multi-dimensional distribution for each decay is not treated analytically, but in terms of histogram-like templates.
- Many of the decay distributions have already been measured and, consequently, realistic matrix elements were employed to simulate Monte Carlo samples, that can be used to obtain some of the templates.

In the following sections, the different decay modes considered in the fitting model are described, the set of discriminant variables used to distinguish among them is discussed and a theory-motivated correction to the simulated samples is presented.

## 4.1 Signal, normalisation and background species

The $R(D^+)$ ratio is obtained in this analysis as:

$$R(D^+) = \frac{N(\overline{B}^0 \to D^+ \tau \bar{\nu}_\tau)}{N(\overline{B}^0 \to D^+ \mu \bar{\nu}_\mu)} \cdot \frac{\epsilon(\overline{B}^0 \to D^+ \mu \bar{\nu}_\mu)}{\epsilon(\overline{B}^0 \to D^+ \tau \bar{\nu}_\tau)} \cdot \frac{1}{\mathcal{B}(\tau \to \mu \nu_\tau \overline{\nu}_\mu)}, \tag{4.1}$$

with $D^+ \to K^-\pi^+\pi^+$ and $\tau \to \mu\nu_\tau\overline{\nu}_\mu$, and where $N$ denotes the observed yield and $\epsilon$ the corresponding efficiency. The most directly measurable quantity is the so called raw ratio, $R_{raw}(D^+)$, defined as:

$$R_{raw}(D^+) = \frac{N(\overline{B}^0 \to D^+ \tau \bar{\nu}_\tau)}{N(\overline{B}^0 \to D^+ \mu \bar{\nu}_\mu)}. \tag{4.2}$$

Since both the tauonic and muonic decays share the same visible final state, $K^-\pi^+\pi^+\mu$, the yield of each component can be measured through a fit to the data distribution in a set of discriminant variables. Additional contributions to the same visible final state can come from $\overline{B}^0 \to D^{*+} l \bar{\nu}_l$ decays, with $D^{*+} \to D^+\pi^0$ and $l \in \{\tau, \mu\}$, if the neutral pion is not reconstructed. Those

components can also be measured in the fit, allowing for the extra determination of $R(D^{*0})$, computed as:

$$R(D^{*+}) = \frac{N(\overline{B}^0 \to D^{*+}\tau\bar{\nu}_\tau)}{N(\overline{B}^0 \to D^{*+}\mu\bar{\nu}_\mu)} \cdot \frac{\epsilon(\overline{B}^0 \to D^{*+}\mu\bar{\nu}_\mu)}{\epsilon(\overline{B}^0 \to D^{*+}\tau\bar{\nu}_\tau)} \cdot \frac{1}{\mathcal{B}(\tau \to \mu\nu_\tau\overline{\nu}_\mu)}, \tag{4.3}$$

with the subsequent decays of the $D^{*+}$ and the $\tau$ as described above. The raw ratio in this case is:

$$R_{raw}(D^{*+}) = \frac{N(\overline{B}^0 \to D^{*+}\tau\bar{\nu}_\tau)}{N(\overline{B}^0 \to D^{*+}\mu\bar{\nu}_\mu)}. \tag{4.4}$$

Finally, apart from the previous modes, there are several contributing backgrounds to the same visible final state that also need to be measured in the fit to data. All the species involved are described below.

### 4.1.1 Signal channels

Both the $\overline{B}^0 \to D^+\tau\bar{\nu}_\tau$ and the $\overline{B}^0 \to D^{*+}\tau\bar{\nu}_\tau$ are considered as signal modes for the measurements of $R(D^+)$ and $R(D^{*+})$, respectively. However, since there is no previous LHCb measurement of $R(D^+)$, the selection and fit strategy of this analysis focus on the $\overline{B}^0 \to D^+\tau\bar{\nu}_\tau$ channel. On top of the visible final state, three neutrinos are missed in the two signal modes, and a neutral pion is also missed in the $D^{*+}$ case.

### 4.1.2 Normalisation channels

The $\overline{B}^0 \to D^+\mu\bar{\nu}_\mu$ and the $\overline{B}^0 \to D^{*+}\mu\bar{\nu}_\mu$ are considered to be the normalisation channels for the measurements of $R(D^+)$ and $R(D^{*+})$, respectively. They have the same visible final state than the signal modes, but present different kinematic distributions and have only one missing neutrino, instead of three.

### 4.1.3 Background channels

The considered background components are briefly described below.

#### 4.1.3.1 Feed-down

Alternative modes where the charm meson is a higher-mass resonance, generically denoted as $B \to D^{**} l\bar{\nu}_l$, with $l \in \{\mu, \tau\}$, can contribute if the charm meson decays as $D^{**} \to D^+ X$, where $X$ refers to extra particles that are not reconstructed. These contributions can be reduced by using tools for isolation against events with extra charged or neutral particles.

#### 4.1.3.2 Double-charm

The double-charm background has the form $B \to D^+ H_c(\to l\bar{\nu}_l X')X$, where $H_c$ is a charm hadron, $X$ and $X'$ are possibly existent non-reconstructed particles and $l \in \{\mu, \tau\}$. This background is specially dangerous since the kinematic distributions on the fit variables are quite similar to those of the signal.

#### 4.1.3.3 Combinatorial

Incorrect associations of a $D^+$ with a muon that comes from a different event can happen during reconstruction. This contribution is studied on a control data sample made of same-sign $D^{\pm}\mu^{\pm}$ candidates, that correspond to random combinations of well identified particles.

#### 4.1.3.4 Misidentification

The data sample can contain background events in which a hadron is misidentified as a muon. This background can be studied in a control data sample composed of events that fulfil the same selection criteria as the nominal dataset but are required not to have any associated hits in the muon chambers.

## 4.2 Discriminant variables

The same three variables used in the first LHCb measurement of $R(D^*)$ are used for the baseline of this analysis. They are primarily aimed at separating the $\overline{B}^0 \to D^+\tau\overline{\nu_\tau}$ signal channel from the $\overline{B}^0 \to D^+\mu\overline{\nu_\mu}$ normalisation channel, that differ in the number of missing neutrinos and in the mass of the lepton. The three kinematic variables are defined in the $B^0$ rest frame. They are described below.

- The squared missing mass, $M^2_{miss}$. For the muonic case, this mass is the one from the neutrino, so it is approximately zero. The missing mass takes a range of positive values for the tauonic case.
- The energy of the final-state muon, $E^{*1}_\mu$. The $E^*_\mu$ is softer for the tauonic case and harder for the muonic case.
- The squared invariant mass of the lepton system, $q^2$. This quantity takes a range of positive values, starting from $q^2 = m^2_\tau$ for the tauonic case and from $q^2 = m^2_\mu \ll m^2_\tau$ for the muonic case.

Since these variables are defined in the rest frame of the $B^0$ meson, the momentum of this particle needs to be determined in order to perform the boost transformation from the laboratory system. It is not possible to perform a full reconstruction of this momentum because there are some missing neutrinos in the final state. In the $B$ factories, this quantity can be obtained by measuring the momentum of the other $B^0$ meson coming from the $\Upsilon(4S)$ decay, and applying momentum conservation rules. Since this is not possible in LHCb, an approximated computation that makes use of the information from the partial reconstruction of the signal decay is used instead, following Ref. [44]. In particular, the proper velocity of the $B^0$ meson along the $z$-axis is approximated by the proper velocity of the visible part of the decay. In terms of momentum, this implies

$$(p_B)_z = \frac{m_B}{m_{vis}}(p_{vis})_z, \tag{4.5}$$

where $vis$ refers to the system of the visible particles. This approximation is based on the fact that the $B^0$ boost along the $z$-axis is much larger than the boost of the decay products in the $B^0$ frame. The remaining components of the $B^0$ momentum can be obtained by using the unit vector from the PV to the SV, which corresponds to the direction of the three-momentum. In particular, the momentum module is given by

$$|p_B| = \frac{m_B}{m_{vis}}(p_{vis})_z\sqrt{1+\tan^2\alpha}, \tag{4.6}$$

[1] The superscript $*$ denotes that this variable is defined in the rest frame of the $B^0$ meson.

where $\alpha$ is the angle between the unit vector and the $z$-axis. As explained in Ref. [44], a $18\%$ resolution on the $B^0$ momentum is achieved using this method, which allows to resolve the signal and normalisation decay distributions.

In Sect. 8.4, it will be shown that these variables provide a good sensitivity for the measurement of the $R(D^{(*)+})$ ratios. However, in order to further improve the measurement, these variables are planned to be combined with some sensitive others in the period after the PhD thesis.

## 4.3 Form factors used in simulation

Both the electroweak and the strong interactions contribute to the $\overline{B}^0 \to D^{(*)+} l \bar{\nu}_l$ decays, with $l \in \{\mu, \tau\}$. The electroweak part can be exactly computed from theory but the strong part does not admit a perturbative treatment in the corresponding energy regime, which means that it has to be accounted for via effective form factors. In general, the differential decay rate for these transitions can be written as [71]:

$$\frac{d\Gamma_l}{dq^2} \propto p^*_{D^{(*)+}} q^2 \left(1 - \frac{m_l^2}{q^2}\right)^2 \left[(|H_+|^2 + |H_-|^2 + |H_0|^2)\left(1 + \frac{m_l^2}{2q^2}\right) + \frac{3m_l^2}{2q^2}|H_s|^2\right], \tag{4.7}$$

where $q^2$ is the squared invariant mass of the leptonic system, $p^*_{D^{(*)+}}$ is the linear momentum of the $D^{(*)+}$ meson in the $\overline{B}^0$ rest frame, $m_l$ is the lepton mass, and $|H_+|$, $|H_-|$, $|H_0|$ and $|H_s|$ are form factors that depend on $q^2$. In the particular case of the $D^+$ meson, the form factors $|H_\pm|$ are zero. The term $m_l^2/q^2$ is negligible for the $l = \mu$ case.

The parameterisation of the hadronic form factors depends on the specific phenomenological model that is employed. The so-called CLN method [72], that relies on the Heavy Quark Effective Theory (HQET), is the one used for event generation in LHCb. However, recent studies [73, 74] have shown that this approach can be problematic, and a more accurate description is desirable. The so-called BCL formalism [75] is considered to be a good alternative. Consequently, the simulation samples used in this analysis are corrected in order to use the BCL parameterisation, as explained in Sect. 8.3.1.

# Chapter 5

# Experimental conditions

## 5.1 Flavour physics at the Large Hadron Collider

The European Laboratory for Particle Physics (CERN[1]) was founded in 1954 in an attempt to internationalise the research for nuclear Physics after the Second World War. This combined effort would allow for a transparent and safe way to do research in this field and at the same time for a handful of human and economical resources. With time, the interests of CERN moved from nuclear to particle physics, taking advantage of the improved technology that allowed to study subatomic processes of increasing energy. The CERN's first accelerator was the Synchrocyclotron, which was closed after 33 years of service in 1990. It was followed by the Proton Synchrotron (PS), in 1959, the Intersecting Storage Rings (ISR), in 1971, and the Super Proton Synchrotron (SPS), in 1976. The ISR was the first hadron collider, and it was shut-down in 1984. Both the PS and the SPS continued operating and were used as pre-accelerators for the Large Electron-Positron Collider (LEP), which started operation in 1984. The LEP experiments showed that just three families of fermions exist, and confirmed the Standard Model with very good precision. The LEP was shut-down in 2000, and it was followed by the Large Hadron Collider (LHC), the most complex scientific instrument ever built. This accelerator, which occupies the 27 Km tunnel of the previous LEP, produced its first high energy collisions in 2010. The two analyses described in this thesis are based on data from proton-proton collisions at the LHC produced during the years 2011, 2012 and 2015. A scheme of the full LHC acceleration complex, which involves several other systems not mentioned in this text, is shown in Fig. 5.1. More information on the LHC can be found in Ref. [76].

There are four main experiments placed at four interaction points of the LHC: LHCb (for Large Hadron Collider beauty), ATLAS (A Toroidal LHC ApparatuS), CMS (Compact Muon Solenoid) and ALICE (A Large Ion Collider Experiment).

- LHCb is aimed at studying flavour physics in beauty and charm hadron decays. This experiment will be described in detail below, since it constitutes the framework for the work presented in this thesis.
- ATLAS and CMS are General Purpose Detectors (GPD), devoted to the direct search for new particles. Their most famous achievement up to date is the discovery of the Higgs boson in 2012 [31, 32].
- ALICE studies the formation and properties of a new state of mater, the Quark-Gluon Plasma (QGP), in heavy-ion collisions.

The LHCb experiment was originally conceived to do precision measurements of CP-violation and to study rare decays in the beauty-meson system. With time, it evolved towards a search for signatures of New Physics involved in flavour transitions, and showed large flexibility to expand its research program beyond the original scope. Some of LHCb's most significant

[1] CERN stands for Conseil Européen pour la Recherche Nucléaire.

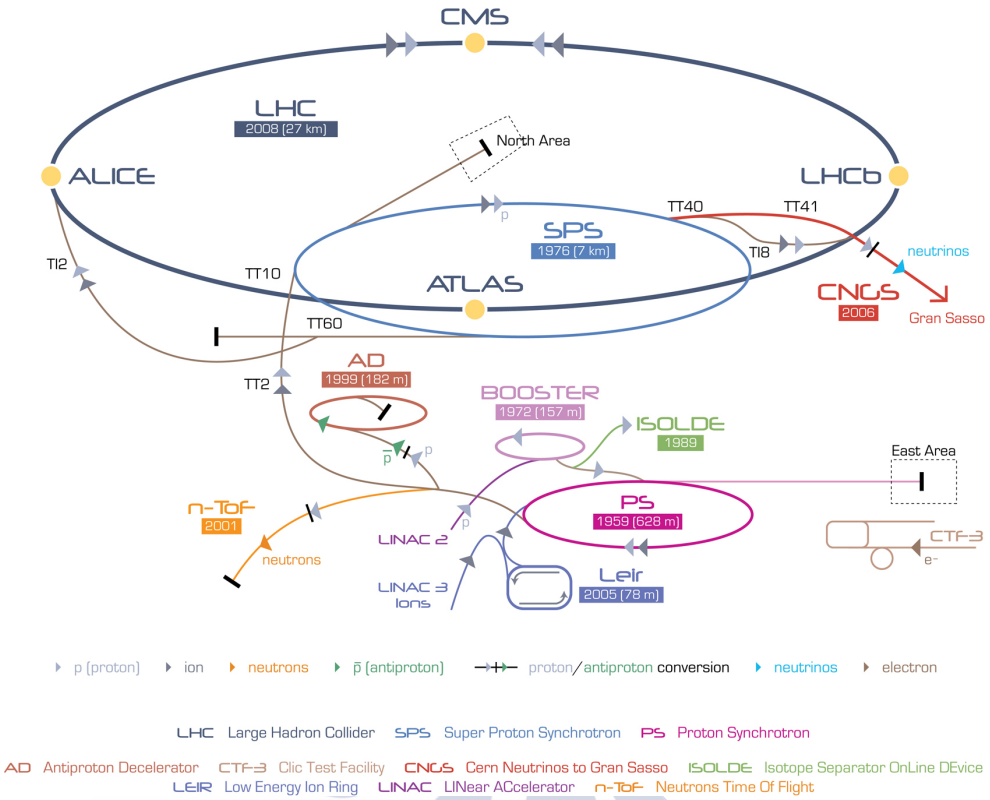



FIGURE 5.1: Full acceleration complex of the LHC [77].

achievements are: the discovery of the ultra-rare decay $B_s^0 \to \mu^+\mu^-$ [78–81], the first single-experiment observation of charm mixing [82], the most precise measurements of both the CKM angle $\gamma$ [83] and the $B_s^0$ CP-violating phase $\phi_s$ [84, 85], and the first discovery of pentaquark states [86]. With respect to the research topics, the measurement of the $\phi_s^{d\bar{d}}$ phase, presented in this thesis, follows one of the historical lines in LHCb. On the other side, the analysis of Lepton Universality in semileptonic decays corresponds to a recent new line in the experiment, driven by the observation of several anomalies in this sector.

The main competitors of LHCb are the so called $B$-factories: the BaBar experiment, which ran from 1998 to 2008, and the Belle experiment, which operated from 1999 to 2010. They produced neutral $B$ mesons in pairs, using electron-positron collisions at a center-of-mass energy corresponding to the $\Upsilon(4S)$ mass, via the decay $\Upsilon(4S) \to B^0\overline{B}^0$. The proton-proton collisions at the LHC provide much more statistics via large hadronic cross-sections, not only for the $B^0$ but also for other beauty hadrons like the $B_s^0$. This allows for the study of the rare decay $B_s^0 \to K^{*0}\overline{K}^{*0}$. In addition, LHCb's excellent vertexing and tracking performances provide enough accuracy in the determination of the $B_s^0$ decay time to resolve the fast oscillation of the $B_s^0$ meson (not possible in the $B$-factories). Consequently, the time-dependent analysis of $B_s^0 \to K^{*0}\overline{K}^{*0}$ needed to measure $\phi_s^{d\bar{d}}$ is so far exclusive to LHCb. On the other side, the $B$-factories' cleaner environment and the possibility to constrain the signal-$B$ kinematics using information from the other $B$ meson (given their coherent production via the $\Upsilon(4S)$ resonance) allow for a very good reconstruction of the decay kinematics even in the case of missing particles. This is specially important in decays with neutrinos, as is the case for the second analysis of this thesis, which focuses on $\overline{B}^0 \to D^+\tau\bar{\nu}_\tau$ and $\overline{B}^0 \to D^+\mu\bar{\nu}_\mu$. Even with a more difficult event reconstruction, LHCb can still profit from a larger cross-section and this experiment will be playing the major role in the determination of $R(D^{(*)})$ in the upcoming years.

The long-term plan for the LHC is to keep on accumulating data at the same center-of-mass

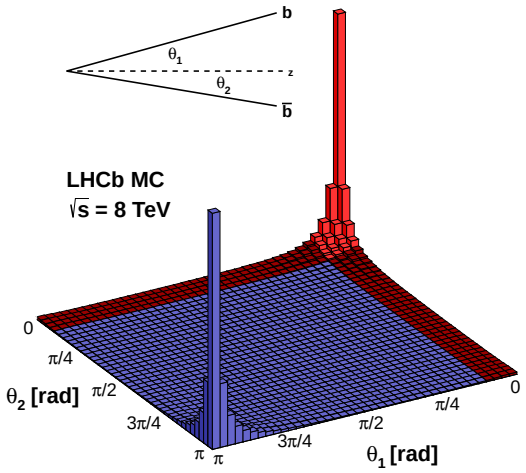



FIGURE 5.2: Production angle for the $b\bar{b}$ pairs [87].

energy than now but with a higher intensity, which aims at producing considerably larger data samples. This puts the focus on the kind of analyses performed in this thesis, where more data directly translates into more sensitivity to the possible effects from New Physics. However, the increase in intensity will require improved detectors, that resist the higher radiation doses and offer good performances in a more noisy environment. The Experimental High Energy Physics Group of the University of Santiago de Compostela is involved in the project for the upgrade of the vertex detector of LHCb, that will be replaced in 2019. As explained in the introduction of this thesis, I took a small part in this project by participating in test-beam campaigns at CERN, aimed at studying the behaviour of new silicon-pixel prototypes, and posteriorly analysed some of the data taken in those campaigns.

The following sections of this chapter are devoted to the description of the LHCb detector and its main components. A focus is put on the impact of the LHCb performance on the two analyses presented in this thesis.

## 5.2 The LHCb detector

### 5.2.1 Detection principles

In contrast to the other 3 main experiments at CERN, which have a barrel-like structure, LHCb is a singe-arm forward spectrometer with an angular coverage from approximately 15 mrad to 300 (250) mrad in the bending (non-bending) plane. This structure is motivated by the large boost along the beam axis of the $b$ quarks produced in the $p$-$p$ collision, as represented in Fig. 5.2. The two quarks of a $b\bar{b}$ pair are emitted in the same cone, either towards LHCb or in the opposite direction. Consequently, a single-arm spectrometer does not lead to loss of information from the other quark if a $b$ particle is detected. The use of the whole LHCb cavern to study the events in only one side allows to maximise the performance of the reconstruction process. A schematic view of the LHCb detector is shown in Fig. 5.3. A right-handed coordinate system is defined with $z$ along the beam axis into the detector, and $y$ and $x$ along the vertical and horizontal directions, respectively.

After a $b$ quark is produced in the $p$-$p$ interaction point, denoted by primary vertex (PV), it hadronises and then flies a distance of the order of 1 cm. Afterwards, it decays in the so

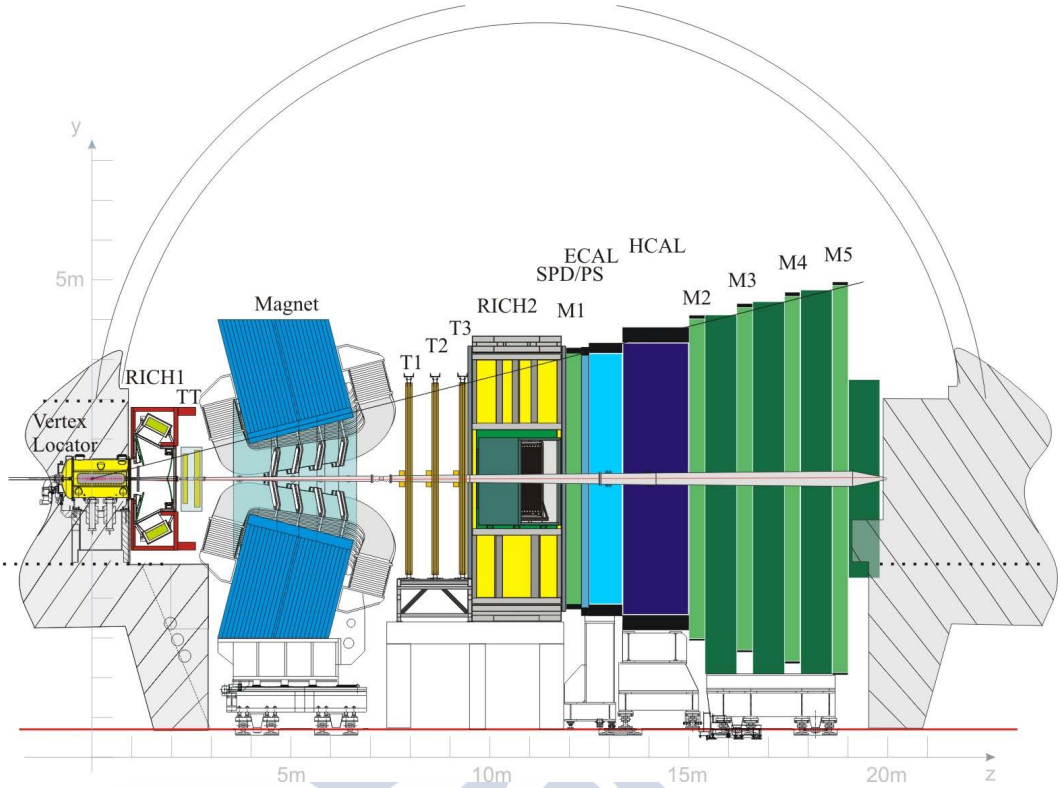



FIGURE 5.3: Structure of the LHCb detector [87] (lateral view).

called secondary vertex (SV). The VErtex LOcator (VELO) sub-detector provides a very accurate determination of these vertices. The products of the decay travel along the detector and the charged ones are deflected in the horizontal axis by a magnetic field of 4 Tm. The tracking system of LHCb is constituted by a first tracking station upstream the magnet, the Tracker Turicensis (TT), and three stations after the magnet, the T1, T2 and T3. In order to discriminate between pions, kaons and protons, two Ring Imaging CHerenkov (RICH) detectors are placed upstream and downstrem of the magnet. After the tracking stations and the RICH detectors, an electromagnetic calorimeter (ECAL) detects and stops electrons and photons. The hadrons traverse this sub-detector and are later stopped in a hadronic calorimeter (HCAL). The only charged particles that survive after the HCAL are the muons, which are detected and tracked in the muon chambers, M1-M5. The neutrinos scape the spectrometer without leaving any signature in it, given their very low interaction rate. A scheme of the different particle interactions in the LHCb detector is shown in Fig. 5.4. Apart from the description of different sub-detectors, which is provided below in this chapter, detailed information on them can be found in [88–91].

A small part of the information from the LHCb sub-detectors is used as input for a trigger system. In later stages (for a more refined trigger and for the posterior event selection), the combined vertexing, tracking and particle identification (PID) information is used to reconstruct and isolate the signal decays. The LHCb sub-detectors and the trigger system are described below. More information can be found in Ref. [4, 93].

### 5.2.2 Vertex detector

The VELO aims at measuring with high precision the production and decay vertices of the $B$ mesons (and occasionally their decay products), by measuring the charged tracks using silicon sensors. This implies detection sensitivity in a region very close to the beam line, with the potential danger of high radiation damage.

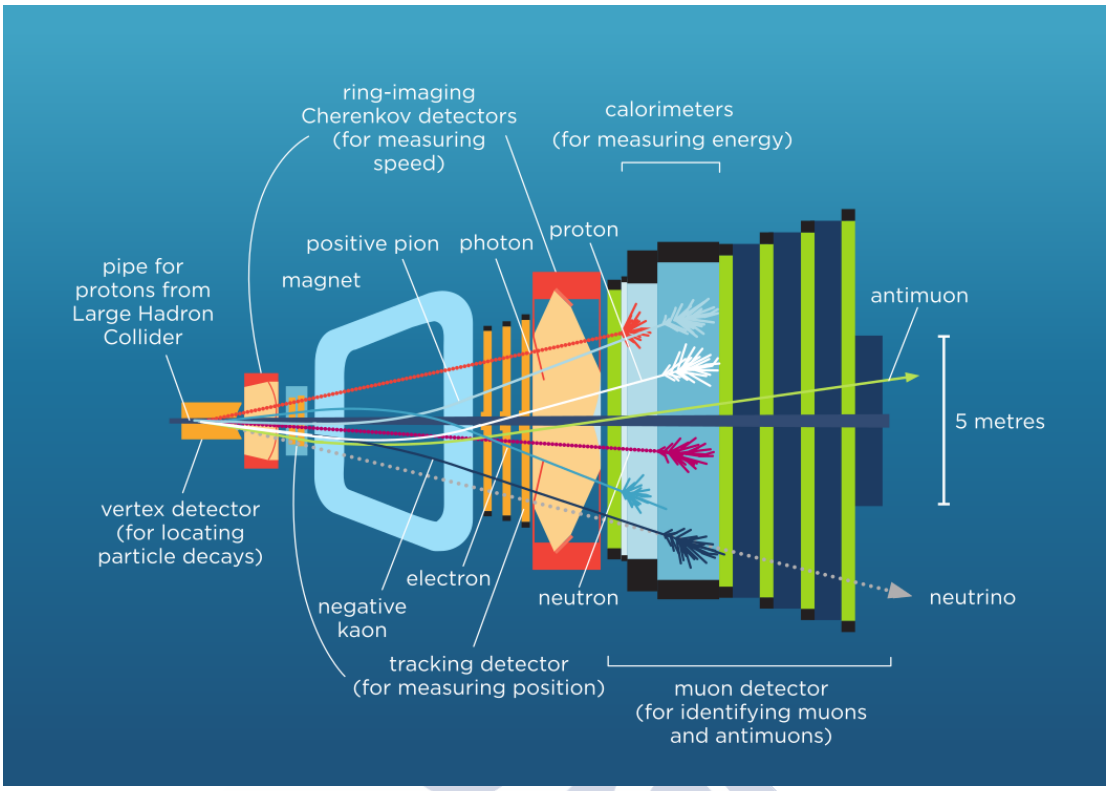


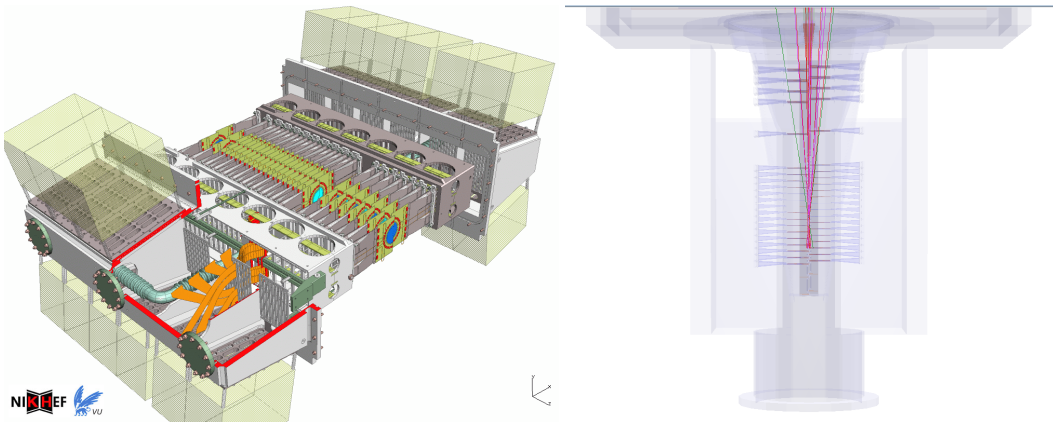

FIGURE 5.4: Scheme of the different particle interactions in the LHCb detector [92], as viewed from the top.

The chosen arrangement for the VELO consists of 42 silicon modules placed along the beam, each providing a measurement of the position in the transverse plane in polar coordinates, thanks to the so called $R$ and $\Phi$ sensors. When operating, the sensors are as close as 8 mm from the interaction point in the radial direction. For detector safety, the modules are retracted in the horizontal direction during injection of the LHC beams. The structure of the VELO is shown in Fig. 5.5. As previously stated, the GAES group is involved in the construction of the new pixel-based vertex detector for the LHCb upgrade.

The VELO allows for an excellent resolution on the impact parameter (IP) of a track with respect to the PV of $\sigma_{\text{IP}} = (15 + 29/p_{\text{T}}[\text{GeV}])\ \mu\text{m}$, where $p_{\text{T}}$ is the momentum component in the transverse plane. This is crucial for a good determination of the $B_s^0$ decay time, required for the measurement of the $\phi_s^{d\bar{d}}$ phase. Specifically, the decay time in the rest frame of the $B_s^0$ can be expressed in terms of the reconstructed decay length (measured in the VELO), $l$, the momentum, $p$, and the mass, $m$, of the meson in the LHCb rest frame, as $t = ml/p$. The decay time resolution can be expressed in terms of the decay-length uncertainty, $\sigma_l$, and the momentum uncertainty, $\sigma_p$, as

$$\sigma_t^2 = \left(\frac{m}{p}\right)^2 \sigma_l^2 + \left(\frac{t}{p}\right)^2 \sigma_p^2, \tag{5.1}$$

where the term depending on $\sigma_l$ is dominant. The decay time resolution varies with the topology of the specific $B_s^0$ decay mode, but is of the order of $\sim 45$ fs. The excellent VELO resolution is also important in the kinematic reconstruction of the $\overline{B}^0 \to D^+\tau\overline{\nu}_\tau$ and $\overline{B}^0 \to D^+\mu\overline{\nu}_\mu$ decays, in order to obtain the flight direction of the $B^0$ meson (from the PV to the SV).



(a) (b)

FIGURE 5.5: (a) Arrangement of the VELO detector, including the mechanism used to separate the modules in case of unstable beams [94], and (b) simulation of a $p-p$ collision inside the VELO [95].

### 5.2.3 Tracking stations

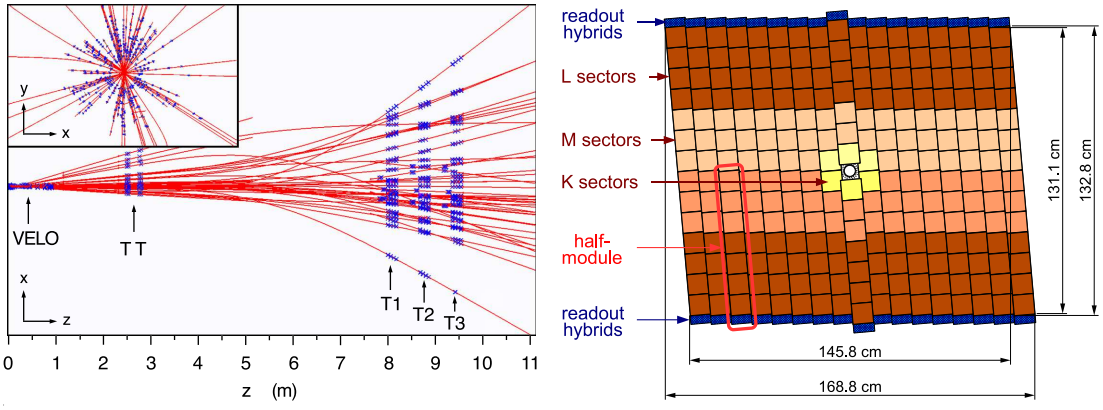
The tracking system of LHCb allows to determine the momentum of charged particles, by measuring the curvature of their tracks due to the magnetic field. The sign of their charge can also be inferred from the direction of the curvature. Less deflected tracks, which travel closer to the beam-pipe, are more difficult to study and require better spacial resolution.

As previously stated, the tracking system is composed of four stations: the TT, upstream of the magnet, and the T1-T3, downstream of the magnet. A representation of the charged particle interaction with these elements is shown in Fig. 5.6(a). The stations have a planar geometry and use two different technologies. Silicon microstrip sensors are employed in the TT and in the region close to the beam-pipe of stations T1-T3, collectively denoted as Inner Tracker (IT), whereas straw tubes are used for the outer parts of these stations, denoted as Outer Tracker (OT). The IT was constructed by the University of Santiago de Compostela in collaboration with the University of Laussane (LPHE). Each of the four silicon-based tracking stations is composed of four detection layers in a $x-u-v-x$ arrangement, with vertical strips in the two $x$ layers and strips rotated by an angle of $-5°$ and $+5°$ in the $u$ and $v$ layers, respectively. For illustration, the layout of the $v$-like TT layer is shown in Fig. 5.6(b). The three OT stations are also composed of four detection layers arranged in a $x-u-v-x$ configuration.

The relative momentum resolution achieved with the whole tracking system, $\Delta p/p$, varies from $0.5\%$ at low momentum to $1\%$ at $p = 200\,\mathrm{GeV}/c$. These values translate into excellent resolutions for different kinematic quantities (such as invariant masses and angular variables) that are used in the analyses presented in this thesis.

### 5.2.4 RICH detectors

The identification of different types of charged hadrons (pions, kaons and protons) in LHCb is based on the phenomenon known as Cherenkov radiation. This process occurs when a charged particle passes through a certain medium faster than light does, which originates the emission of a light cone whose radius depends on the speed of the particle. When this information is combined with the particle's momentum, the mass (and thus the identity) of the particle can be determined. A good hadron identification over a large momentum range is crucial for the physics program of the LHCb experiment.




(a) (b)

FIGURE 5.6: (a) Display of the reconstructed tracks in a typical event, with the assigned hits in the VELO and the tracking stations. (b) Layout of a $v$-like TT detection layer. Both pictures are taken from Ref. [4].

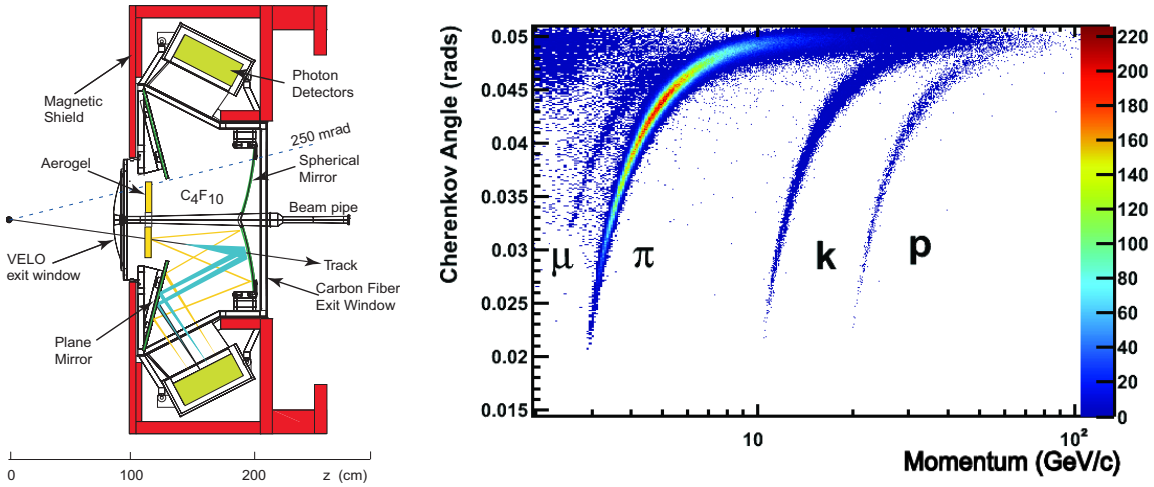
Two detectors based on Cherenkov radiation are used in LHCb, with the aim of covering different regions of particle momenta by using radiator media with different refractive indices. The RICH1, upstream of the magnet, provides particle identification at low momentum, from 2 to 60 $\mathrm{GeV}/c$. It covers the full LHCb acceptance and uses Aerogel and $C_4F_{10}$ as radiators. The RICH2 detector is placed downstream of the magnet, and focuses on particles with high momentum, from 15 to 100 $\mathrm{GeV}/c$. It's acceptance is limited to the low-angle region (where there are mostly high-momentum particles) and it uses $CF_4$ as radiator. Both RICH detectors employ mirrors to reflect the radiation onto an array of hybrid photon detectors (HPDs), that measure the positions of the emitted Cherenkov photons. For illustration, the layout of the RICH1 detector is shown in Fig. 5.7(a), and the reconstructed Cherenkov angle as a function of the particle momentum in the $C_4F_{10}$ radiator is shown in Fig. 5.7(b).

Good charged-hadron-identification is achieved by combining the information from the two RICH detectors. For instance, it is possible to identify kaons with an efficiency of $\sim 95\%$ and a $\pi \to K$ mis-identification probability of $\sim 5\%$. This high performance allows to efficiently suppress the backgrounds from hadron mis-identification in the two analyses presented in this thesis.

### 5.2.5 Calorimeter system

Calorimeters are aimed at determining the energy of particles by making them interact with an absorber material. Particles deposit all their kinetic energy in the form of a particle shower, which is identified and characterised in the calorimeter. Electrons and photons are detected in electromagnetic calorimeters (via electromagnetic interactions) while hadrons are detected in hadronic calorimeters (via nuclear interactions). Apart from measuring the energy, an appropriate configuration of calorimeters can also provide electron, photon and hadron identification.

The LHCb calorimeter system is composed of four elements: a Scintillating Pad Detector (SPD), a Preshower (PS), an electromagnetic calorimeter (ECAL) and a hadronic calorimeter (HCAL). The SPD determines whether arriving particles are charged or neutral. Between the SPD and the PS, there is a lead converter with a thickness of 2.5 radiation lengths ($X_0$), that originates a preshower if the traversing particle is an electron or a photon. Consequently, the PS can determine the electromagnetic character of the particle (distinguishing electrons from charged hadrons and photons from neutral hadrons). The ECAL has a scintillator/lead sampling structure with a total thickness of 25 $X_0$. The HCAL is a sampling device made of iron and scintillating




(a) (b)

FIGURE 5.7: (a) Layout of the RICH1 detector [4]. (b) Reconstructed Cherenkov angle as a function of particle momentum in the $C_4F_{10}$ radiator [90].

tiles. Its thickness is limited to 5.6 nuclear interaction lengths due to space constraints. All the calorimeters are divided in cells to allow the measurement of the energy-deposit position in the transverse plane.

The calorimeters are used in LHCb to provide information for the hardware-based trigger (see Sect. 5.2.7). They also contribute to the particle identification, together with the RICH and the muon chambers. Finally, the calorimeter system allows for the reconstruction of photons. This information is used to isolate signal events from others with extra neutral particles in the $R(D^+)$ analysis presented in this thesis.

### 5.2.6 Muon chambers

Muons are relatively weakly interacting particles that can traverse the calorimeter system only leaving a fraction of their energy. Consequently, they can be distinguished from charged hadrons or electrons by detecting their presence in the most downstream region of the spectrometer.

The LHCb muon detection system is composed of five stations (M1-M5), equipped predominantly with Multi Wire Proportional Chambers, except in the highest rate region of M1, where triple Gas Electron Multiplier detectors are used. Stations M2 to M5 are placed downstream of the calorimeters and are interleaved with iron absorbers. Station M1 is placed in front of the calorimeters. The association of hits in the muon stations around the extrapolated trajectory of a track reconstructed in the tracking system allows to asses the muonic character of the track.

The detection of muons is used for particle identification in the two analyses of this thesis. Even if the muon information can also be used in LHCb with trigger purposes, no muonic trigger lines are used in the $R(D^+)$ analysis, to avoid imposing extra kinematic requirements on the signal muons which could decrease the sensitivity of the measurement.

### 5.2.7 Trigger system

The frequency of bunch crossings in LHCb is 40 MHz, which leads to about 10 MHz of events with some particles inside the acceptance of the detector. The event rate that can be recorded is limited by the offline computing capacity to about 2 KHz. A trigger system is thus required to select the decays of interest as efficiently as possible while reducing the event rate to the allowed value of 2 KHz.

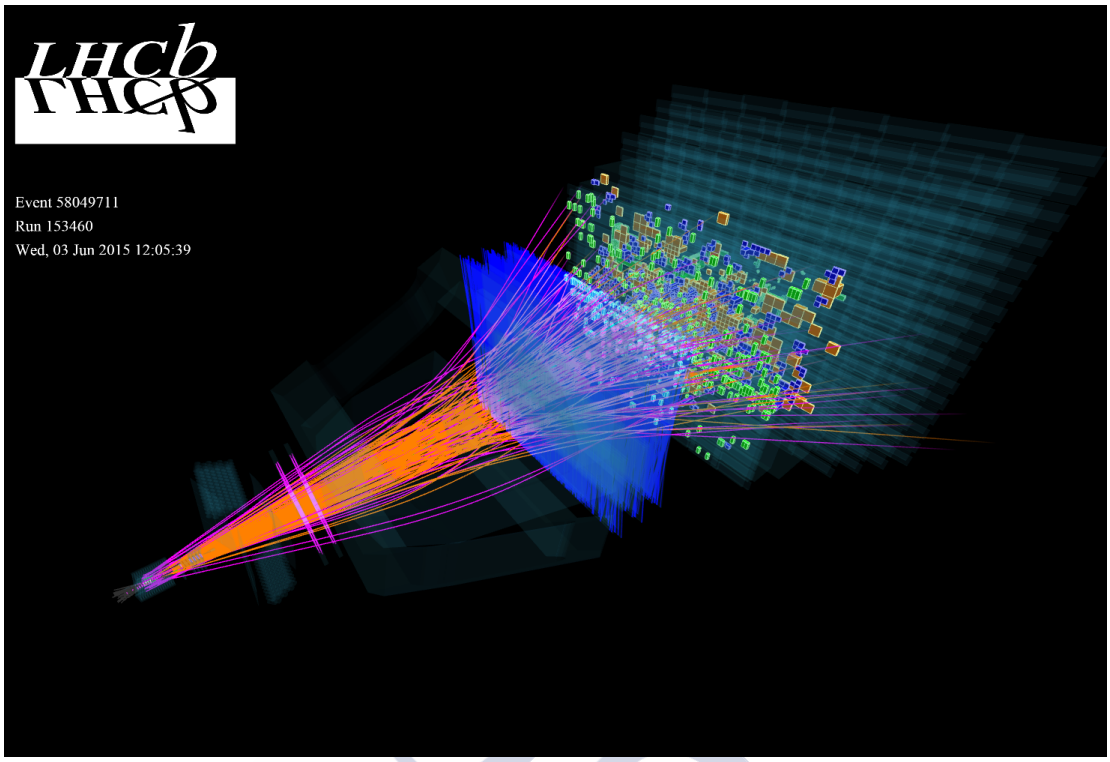



FIGURE 5.8: Typical fully reconstructed event in LHCb [96].

The LHCb trigger system consists of two levels: Level-0 (L0) and High Level Trigger (HLT). The L0 is implemented in hardware and makes decisions using the information from the calorimeter and muon systems. It reduces the event rate to 1 MHz. The HLT is a software application that runs in an event-filter farm. It is divided in two sub-levels. In the first sub-level (HLT1), a partial event reconstruction is performed and the event rate is reduced to a few tens of KHz. The second sub-level (HLT2) performs a complete event reconstruction and outputs the 2 KHz that are recorded for later offline processing. A typical fully-reconstructed event is shown in Fig. 5.8.

Two key features of $B$ decays that are used in triggering are the high transverse momentum of the daughter particles and the large impact parameter of their tracks with respect to the proton-proton interaction vertex (motivated by the large $B$ lifetime). Triggered events can be classified according to the object that fulfilled the required criteria. An event is classified as Trigger on Signal (TOS) if the trigger objects that are associated to the signal candidate are sufficient to trigger the event. An event is classified as Trigger Independent on Signal (TIS) if it has been triggered by trigger objects that are not associated with the signal. There can be events classified as TOS and TIS simultaneously.

The two analyses presented in this thesis use the L0 Hadron trigger line, that imposes a requirement on the highest-transverse-energy cluster in the HCAL. The HLT lines employed are adapted to the topology and kinematics of the considered decays. In particular, the $R(D^+)$ analysis uses a specifically designed HLT2line, aimed at minimising the biases in the measurement. This line was not available in Run 1, which motivates that only Run 2 data are used for this analysis.

USC
UNIVERSIDADE
DE SANTIAGO
DE COMPOSTELA

# Chapter 6

# Tools and techniques

Since the two analyses presented in this thesis share several specific tools and techniques, and to improve the clarity of the whole document, a brief description of the main employed methods is presented in this chapter. There are three new techniques that I have developed during the work in this thesis, and that could be useful for future analyses. They are explained in Sect. 6.2.3, Sect. 6.4.4 and Sect. 6.4.7.

## 6.1 Simulation tools

The imperfect process of event detection and reconstruction in LHCb modifies the corresponding physical distributions. To understand and parameterise these effects, LHCb uses simulations of fully reconstructed events corresponding to the decays of interest for a given analysis. Those simulated datasets, denoted as full Monte Carlo (MC) samples, can be compared to the distributions of the physical model used in generation to study the deviations.

In the simulation, proton-proton collisions are generated using PYTHIA [97] with a specific LHCb configuration [98]. Decays of particles are described by EVTGEN [99], in which final-state radiation is generated using PHOTOS [100]. The interaction of the generated particles with the detector, and its response, are implemented using the GEANT4 toolkit [101, 102] as described in Ref. [103]. The process of generation and reconstruction takes a considerable amount of computing time and is done centrally in LHCb. Time constraints and the fact that the available resources are shared among all the analysts limit the amount of data that can be simulated for a given analysis. Indeed, the limited size of the simulation samples originates the largest systematic uncertainty in the measurement of $\phi_s^{d\bar{d}}$. This factor has also been the main source of systematic uncertainty in the LHCb measurement of $R(D^*)$ [44], that sets the basis for the analysis aimed at measuring $R(D^+)$ presented in this thesis.

In the two analyses of this thesis, full Monte Carlo samples are used to describe the acceptance (variable-dependent efficiency) and resolution effects, obtain templates and compare the expected distributions of different decays under study. In general, the simulation describes accurately the interaction of the particles with the LHCb detector. In the few known cases where there is a small mis-modelling in the Monte Carlo, a data-driven correction is applied (see for example Sect. 7.9.13).

Apart from the full Monte Carlo, the two analyses presented in this thesis make use of simplified simulations, that only describe the distributions for the relevant variables under study and that are denoted as toy Monte Carlo. These simulations are generated with the models used to fit the data and mainly serve to perform checks of the analysis method. For the study of $B_s^0 \to (K^+\pi^-)(K^-\pi^+)$ decays, a new generator was constructed to perform fast event generation in parallel on a Graphics Processing Unit (see Sect. 6.2.3).

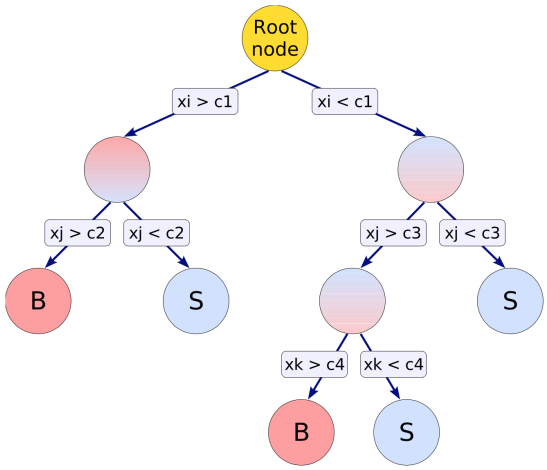



FIGURE 6.1: Illustrative example of a decision tree.

## 6.2 Computing tools

### 6.2.1 Boosted Decision Tree

Machine-learning-based tools for Multivariate Analysis (MVA) are very useful in data mining for high energy physics (HEP), since they provide accurate and automated solutions. These tools are trained on prototype data samples to identify patterns that are common to other independent samples, based on the fact that they correspond to the same phenomena. Using this information, the tools can perform different tasks. Two typical kinds of problems are:

- Classification. In this case, the aim is to separate two classes of data, typically signal versus background, and the output of the MVA tools is binary. The classification problem is treated below in this section.
- Regression. In this case, the goal is to predict exact values for a given sample and the output from the tool is continuous. An example of this kind of problems is treated in the next section.

The use of MVA tools for classification improves with respect to the classical unidimensional approach, since the discrimination power can be significantly increased by combining different variables while accounting for correlations among them. The Decision Trees constitute a common type of classifier based on machine learning. As illustrated in Fig. 6.1, a tree is composed of consecutive sets of questions (nodes), with only two possible answers per question and in such a way that each question depends on the previous answers. The final verdict is reached after a given maximum number of nodes. The training of a Decision Tree consists on the optimisation of the node criterion by maximising the separation gain between nodes. Since a single tree is not a strong classifier, a combination of many trees is typically used. The analyses in this thesis make use of a common combination scheme called Boosted Decision Tree (BDT). Within this scheme, misclassified events are weighted higher so that future learners concentrate on them.

A BDT provides an output variable which takes low values for events in one of the samples and high values for events in the other. The classification is done by imposing an adequate requirement on that variable. The performance of the classifier is evaluated with the Receiver Operating Characteristic (ROC) curve, that shows the background rejection as a function of the signal efficiency. The best classifier in a set can be identified by the largest area under the curve. One possible problem of these classifiers is the overtraining, which consists on learning statistical fluctuations instead of differences between the underlying patterns. One way to check that there

is no overtraining is to split the prototype data into training and test samples and observe if the performance of the classifier when evaluated in both of them is similar.

In the two analyses of this thesis, a BDT is used to separate signal from combinatorial background events. It is also used to develop a new tool for isolation against background with neutral particles for the $R(D^+)$ analysis (see Sect. 6.4.7). More information on the BDT tools used in this thesis can be found in Ref. [104].

### 6.2.2 Gradient Boost Reweigher

One typical problem of HEP analyses is how to reweight an event data sample such that its multidimensional distribution in a given set of variables mimics that of a different data sample. This is for example the case of developing a correction for Monte Carlo data using distributions from control data samples. The re-weighting can be treated as a regression problem (see previous section) and approached using MVA tools based on machine learning.

In this thesis, the Gradient Boost Reweighter (`GBReweighter`) tool presented in Ref. [105] is used. In a first step, the tool is input with two data samples, the original and the target ones, defined in terms of the variables of interest. A training is performed where the `GBReweighter` learns the differences between the two samples in the multi-dimensional space. In a second step, the tool is requested to predict a set of event weights that, if applied to the original sample, its multidimensional distribution in the considered variables mimics that of the target sample.

The `GBReweighter` is used in the analysis aimed at measuring $\phi_s^{d\bar{d}}$ in two different manners. First, it is employed as usual to reweight the Monte Carlo and correct it for small mis-modellings. Second, it is used in an original way, to develop a new method for acceptance correction, as explained in Sect. 6.4.4.

### 6.2.3 Task parallelisation using a GPU

There are some sets of processes that, when performed in series, can take large amounts of time but, if divided in independent tasks that are done in parallel, can be performed much faster. While a typical Central Processing Unit (CPU) has of the order of 10 cores to perform parallel tasks, a Graphics Processing Unit can have of the order of 1000. This feature makes GPUs specially suitable to perform parallelisable tasks that involve a huge computational load.

From a technical viewpoint, doing computations on a GPU requires an input/output interface to pass data from/to a normal CPU (used for global managing purposes), and a piece of code containing the required operations programmed in a language which is understandable by the GPU. To parallelise a given task, it is needed to identify the individual elements on which it can be divided (number of events in a data sample, elements of an array ...), program the routine to be performed on each element and design a way to combine the outputs at the end.

For the particular work of this thesis, several NVIDIA-branded GPUs from the local computing cluster of Santiago's group were used. The software framework provided by NVIDIA for parallel working is called CUDA [106], and it allows to use a C-like programming language for the code to be run in the GPU, called CUDA C. The data management in the CPU is done via python instructions, using the PyCUDA [107] interface. On top of this, the recently developed software package Ipanema [28] is used, to profit from a set of specific tools designed to do HEP analysis using GPUs. I personally contributed to the development of this package.

The parallelisation using GPUs is employed in the $B_s^0 \to (K^+\pi^-)(K^-\pi^+)$ analysis, given the huge computational requirements associated to the high dimensionality of the problem. The parallel computation is used in fits, event generation and multidimensional integration, for which I adapted the tools in the Ipanema package and developed some new ones.

## 6.3 Mathematical techniques

### 6.3.1 Splines

The splines are piece-wise polynomial functions. They are very versatile to describe complicated shapes and at the same time have a simple mathematical structure.

To construct a spline function that depends on one variable, $x$, it is necessary to define a set of knots (interval delimiting positions), $t_i$, and the maximum degree of the polynomial, $d$. The knots must be defined in non-descending order, $t_i \leq t_{i+1}$, and the number of them, $k$, can be freely chosen. Additionally, continuity and smoothness conditions must be imposed to the function at the knots. These conditions are automatically fulfilled if the spline function, $S(x)$, is constructed as a linear combination of the so called basis splines (B-splines), $B_{i,d}(x)$:

$$S(x) = \sum_{i=1}^{k+d-1} \alpha_i B_{i,d}(x), \tag{6.1}$$

where $\alpha_i$ are constant coefficients. The B-splines are constructed as:

$$\begin{aligned} B_{i,0}(x) &= \begin{cases} 1, \text{ for } t_i \leq x < t_{i+1}, \\ 0, \text{ otherwise,} \end{cases} \\ B_{i,k}(x) &= \frac{x - t_i}{t_{i+k} - t_i} B_{i,k-1}(x) + \frac{t_{i+k+1} - x}{t_{i+k+1} - t_{i+1}} B_{i+1,k-1}(x), \text{ for } k > 0. \end{aligned} \tag{6.2}$$

For mathematical consistency, the original set of knots, referred to as internal knots, need to be supplemented with $d$ extra points on the left, whose position is set to be the same as the first internal knot, and with $d$ extra points on the right, with the same position as the last internal knot. For more detailed information on splines see Ref. [108].

A spline function is used in this thesis to describe the decay-time-dependent acceptance of $B_s^0 \to (K^+\pi^-)(K^-\pi^+)$ decays. The mathematical simplicity of the splines allows to compute analytically the integrals on the decay time that appear in the normalisation of the probability density function (PDF) used in the main fit. The analytical integration is much faster than a numerical one, hence the fit performance is optimised using this method.

## 6.4 Analysis techniques

### 6.4.1 Method of the ${}_s\mathcal{W}eights$

The method of the ${}_s\mathcal{W}eights$ [109] is aimed at isolating a given species of a data sample, by removing other contributions in a statistical way. The technique uses the information of the one-dimensional distribution of the different components in a discriminant variable. This information is processed by a tool which assigns either positive or negative weights (${}_s\mathcal{W}eights$) to the events in the data sample, according to their position in the discriminant variable axis, in such a way that all the contributions except the chosen one are effectively cancelled. This method allows to study the distributions of a single species in a given set of variables that have to be uncorrelated to the one used for the sWeighting procedure.

The method of the ${}_s\mathcal{W}eights$ is used in the analysis of $B_s^0 \to (K^+\pi^-)(K^-\pi^+)$ decays to remove the remaining background after event selection, allowing to perform the time-dependent fit on a signal data sample. The technique is also used in the $R(D^+)$ analysis, to select specific components in control data samples.

### 6.4.2 Normalisation weights

A typical method in HEP analyses consists on measuring some physical observables of a decay by performing a maximum likelihood fit to a signal data sample. The model used in the fit has to account for any acceptance effects present in data. In the case of highly-dimensional acceptances, it is a non-trivial task to find analytical functions that can describe the effects while properly accounting for the correlations among the variables. The method of the normalisation weights, first presented in Ref. [110], offers an alternative way to deal with the acceptance in those cases. Instead of functions, it only makes use of constant quantities (weights) that automatically account for the correlations among the acceptance variables.

A probability density function for a signal model can typically be written as follows:

$$\mathcal{P}(\vec{x}) = \frac{\sum_i F_i(\vec{\lambda})\, G_i(\vec{x})\, \epsilon(\vec{x})}{\sum_j F_j(\vec{\lambda}) \int dx'\, G_j(\vec{x'})\, \epsilon(\vec{x'})}, \tag{6.3}$$

where the numerator is the unnormalised model, the denominator is the normalisation factor, the model is composed of a sum of terms indexed by $i$ ($j$), $\vec{\lambda}$ denotes the physical observables that are floated in the fit, $\vec{x}$ denotes the variables of the model ($\int dx'$ denotes a multidimensional integral) and $\epsilon(\vec{x})$ is the acceptance. The associated logarithmic likelihood for a signal data sample is:

$$\begin{aligned}
\log L &= \sum_{ev=1}^{N_{events}} \log \frac{\sum_i F_i(\vec{\lambda})\, G_i(\vec{x_{ev}})\, \epsilon(\vec{x_{ev}})}{\sum_j F_j(\vec{\lambda}) \int dx'\, G_j(\vec{x'})\, \epsilon(\vec{x'})} \\
&= \sum_{ev=1}^{N_{events}} \log \frac{\sum_i F_i(\vec{\lambda})\, G_i(\vec{x_{ev}})}{\sum_j F_j(\vec{\lambda}) \int dx'\, G_j(\vec{x'})\, \epsilon(\vec{x'})} + \sum_{ev=1}^{N_{events}} \log \epsilon(\vec{x_{ev}}) \\
&= \log L_{NW} + \sum_{ev=1}^{N_{events}} \log \epsilon(\vec{x_{ev}}).
\end{aligned} \tag{6.4}$$

The fit process consists on maximising the log likelihood with respect to the parameters of interest:

$$\frac{\partial \log L}{\partial \lambda_i} = 0,\ \forall \lambda_i. \tag{6.5}$$

Since the acceptance does not depend on the physical parameters, it follows:

$$\frac{\partial}{\partial \lambda_i} \left( \sum_{ev=1}^{N_{events}} \log \epsilon(\vec{x_{ev}}) \right) = 0 \tag{6.6}$$

and hence the corresponding contribution to the log likelihood can be omitted.

The normalisation weights, $\xi_i$, are defined as:

$$\xi_i \equiv \int dx\, G_i(\vec{x})\, \epsilon(\vec{x}). \tag{6.7}$$

They can be computed from a full Monte Carlo sample, changing the integral by a sum over the reconstructed events:

$$\xi_i \propto \sum_{ev=1}^{N_{events}} \frac{G_i(\vec{x_{ev}})}{\mathcal{P}^{gen}_{MC}(\vec{x_{ev}})}, \tag{6.8}$$

where $\mathcal{P}^{gen}_{MC}(\vec{x})$ is the generation model used in Monte Carlo. If the normalisation weights are computed in this way and inserted in the normalisation of the probability density function, the model for fitting is complete without the need for a functional form of the acceptance.

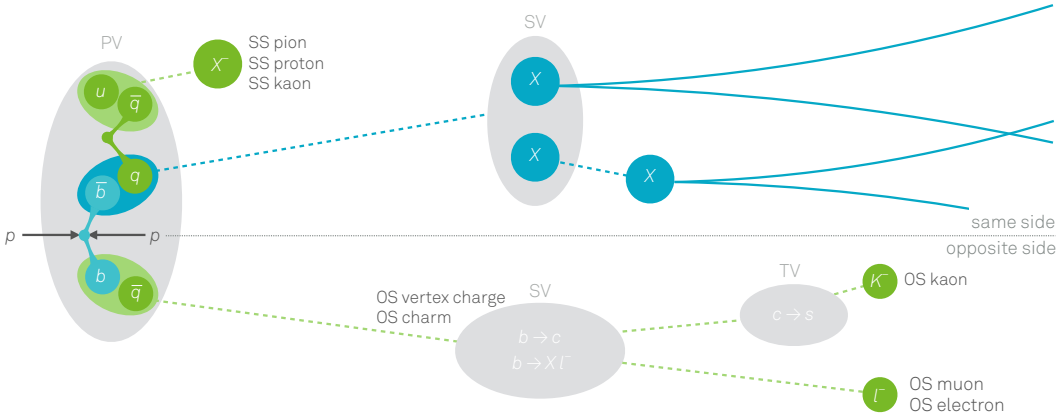



FIGURE 6.2: Scheme of the same-side and opposite-side FT algorithms [87].

The method of the normalisation weights is used in the main fit of the analysis aimed at measuring the $\phi_s^{d\bar{d}}$ phase. It serves to account for the effect of the five-dimensional part of the acceptance that depends on invariant masses and decay angles. Since this method does not provide any parametric function for the acceptance, alternative approaches are used for plotting of the model distributions, generation of toy Monte Carlo samples and specific checks. One final remark on the use of normalisation weights in this analysis is that a couple of modifications have to be made to the simple case presented in Eq. 6.3. First, an additional decay-time-dependent acceptance (factorised with respect to the rest of the acceptance) is taken into account analytically. This slightly modifies the signal PDF. Second, some nuisance parameters are included in the part of the model that describes the dependence on the invariant masses and that goes into the normalisation weights. These parameters are floated in the fit, which makes it necessary to recompute the normalisation weights per fit step.

### 6.4.3 Flavour tagging

The $B_s^0$ ($\overline{B}_s^0$) mesons oscillate in time between $B_s^0/\overline{B}_s^0$ flavours before decaying. Hence, it is not possible to know the initial flavour of the beauty meson by only looking at the products of its decay. To accomplish this task, the LHCb experiment uses the so called flavour-tagging (FT) algorithms, which analise information related to the $B_s^0$ ($\overline{B}_s^0$) production process. Apart from using the FT tools in the project of this thesis, I gained some extra experience in this procedure by holding a 2-year position of liaison between the LHCb working group dedicated to the development of FT and the working group devoted to the study of charmless $b$ decays (of which the $B_s^0 \to (K^+\pi^-)(K^-\pi^+)$ is an example).

At the LHC, $b$ quarks are predominantly produced in $b\bar{b}$ pairs. In a typical signal event, one will hadronise to produce the $B_s^0$ meson while the other $b$ quark will hadronise and decay independently. Taking advantage of this effect, two types of FT algorithms are used in LHCb: same-side (SS) taggers, based on information from accompanying particles associated to the signal-$B_s^0$ hadronisation process, and opposite-side (OS) taggers, based on information from particles produced in the decay of the other $b$ quark. An scheme of the two kinds of taggers is shown in Fig. 6.2.

Each tagging algorithm provides for every event a tagging decision, $q$, and an estimated mistag probability, $\eta_{\text{tag}}$. The tagging decision takes the value $1$ for $B_s^0$, $-1$ for $\overline{B}_s^0$ and $0$ for untagged events. To obtain the true (calibrated) mistag probability for a $B_s^0$ ($\overline{B}_s^0$) meson, $\omega(\bar{\omega})$, the estimated mistag probability is calibrated on flavour-specific control channels. The following

linear functions are used in the calibration:

$$\begin{aligned}\omega^{\mathrm{T}}(\eta^{\mathrm{T}}_{tag}) &= \left(p^{\mathrm{T}}_0 + \frac{\Delta p^{\mathrm{T}}_0}{2}\right) + \left(p^{\mathrm{T}}_1 + \frac{\Delta p^{\mathrm{T}}_1}{2}\right)(\eta^{\mathrm{T}}_{tag} - \langle\eta^{\mathrm{T}}_{tag}\rangle),\\ \bar{\omega}^{\mathrm{T}}(\eta^{\mathrm{T}}_{tag}) &= \left(p^{\mathrm{T}}_0 - \frac{\Delta p^{\mathrm{T}}_0}{2}\right) + \left(p^{\mathrm{T}}_1 - \frac{\Delta p^{\mathrm{T}}_1}{2}\right)(\eta^{\mathrm{T}}_{tag} - \langle\eta^{\mathrm{T}}_{tag}\rangle),\end{aligned} \tag{6.9}$$

where T denotes a specific tagger, $\langle\eta^{\mathrm{T}}_{tag}\rangle$ is the mean $\eta^{\mathrm{T}}_{tag}$ of the data sample under study, $p^{\mathrm{T}}_{(0,1)}$ correspond to calibration parameters averaged over $B^0_s$ and $\overline{B}^0_s$, and $\Delta p^{\mathrm{T}}_{(0,1)}$ account for $B^0_s$ /$\overline{B}^0_s$ asymmetries in the calibration. The tagging efficiency, $\epsilon_{\mathrm{tag}}$, denotes the fraction of events with a non-zero tagging decision. The FT performance is characterised by the tagging power, defined as $\epsilon_{\mathrm{eff}} = \epsilon_{\mathrm{tag}}(1-2\omega)^2$.

In the project of this thesis, the flavour-tagging algorithms are used in the analysis of $B^0_s \to (K^+\pi^-)(K^-\pi^+)$ decays, as a key ingredient in the measurement of the $\phi_s^{d\bar{d}}$ phase.

### 6.4.4 Machine-learning-based acceptance correction

There are several statistical methods to study particle decays that require working with acceptance-corrected distributions. A usual approach for this correction consists on parameterising the acceptance with an analytical function and weighting the events by the inverse of that function. However, if the number of variables in the acceptance is large, it can be difficult to find a function that takes into account all the correlations among the variables. I have designed and implemented a new method to study the acceptance and correct data for it, using a machine-learning-based technique.

As explained in Sect. 6.2.2, the `GBReweighter` tool has to be trained with an original and a target data samples, using their distributions on a set of variables of interest, $\vec{x}$. The tool predicts per-event weights that, if applied to the original sample, the corresponding multi-dimensional distribution on the given variables matches that of the target sample. Let's consider the particular case where the original sample is a full Monte Carlo, $\mathcal{F}(\vec{x})$, and the target is a simulated sample generated with the same decay model but with perfect efficiency, known as generator-level Monte Carlo, $\mathcal{G}(\vec{x})$. The two samples are related by the acceptance[1], $\epsilon(\vec{x})$:

$$\mathcal{F}(\vec{x}) = \mathcal{G}(\vec{x})\,\epsilon(\vec{x}). \tag{6.10}$$

When the `GBReweighter` is trained with these conditions, it constructs a weighting function, $w(\vec{x})$, such that

$$w(\vec{x})\,\mathcal{F}(\vec{x}) = \mathcal{G}(\vec{x}). \tag{6.11}$$

By comparing the two previous equations, we obtain $w(\vec{x}) = 1/\epsilon(\vec{x})$. If the full Monte Carlo distribution properly covers the full phase-space under consideration, the tool can be used to predict weights for any other decay channel in that region and, consequently, correct it for acceptance.

A proof of concept of this new method was done in the analysis of $B^0_s \to (K^+\pi^-)(K^-\pi^+)$ (for which it was developed), using a combined full Monte Carlo sample of $B^0_s \to K^{*0}\overline{K}^{*0}$ and pure phase-space $B^0_s \to K^+\pi^-K^-\pi^+$ decays, and the corresponding generator-level Monte Carlo sample. A six-dimensional space is considered, composed of two invariant masses ($M(K^+\pi^-)$ and $M(K^-\pi^+)$), three angular variables ($\cos\theta_1$, $\cos\theta_2$ and $\varphi$) and the $B^0_s$ decay time ($t$). Since the acceptance drops to 0 at very low decay times, and the reweighting would not be able to work in that case, the variable-space is restricted to the region with $t > 0.5$ ps for this study. The projections of the full and generator-level Monte Carlo distributions are shown in Fig. 6.3,

[1] Resolution effects are neglected in this study.

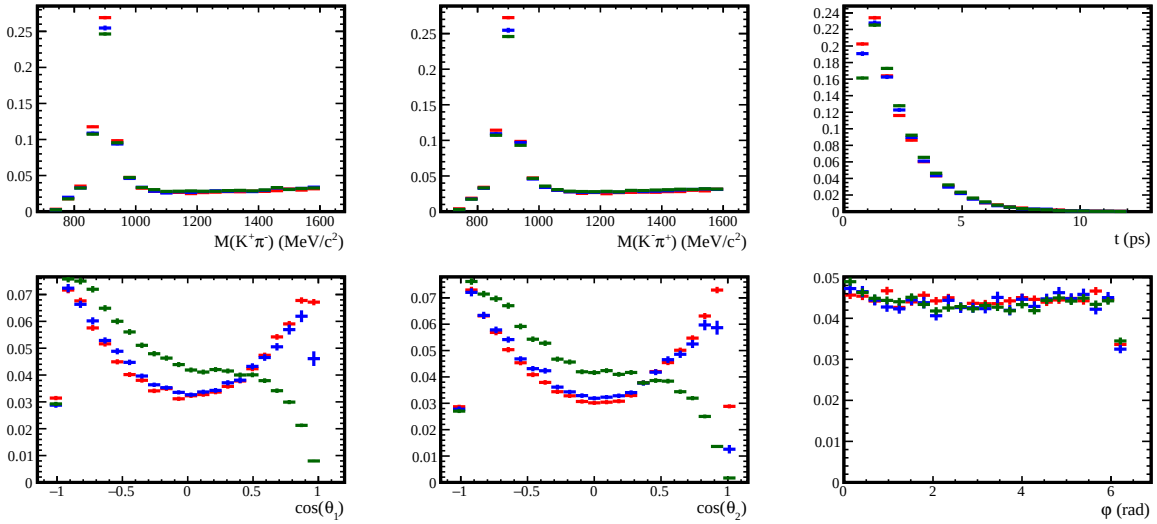



FIGURE 6.3: Check on simulated data of the machine-learning-based acceptance-correction method described in the text. Two training samples, a full Monte Carlo dataset (green line) and a generator-level one (red line), are used to train the `GBReweighter` tool. This tool is used afterwards to re-weight the full Monte Carlo, in order to obtain an acceptance corrected sample (blue line).

together with those of the acceptance-corrected full Monte Carlo. It can be seen that the corrected distributions essentially follow those of the generator-level Monte Carlo, as expected.

Since this method is not further tested yet, it is only used for a specific check of the $B_s^0 \to (K^+\pi^-)(K^-\pi^+)$ analysis (the one described in the next section). The `GBReweighter` trained on Monte Carlo with the previous configuration is used to correct signal data for acceptance. This technique has a high potential to be used in future analyses.

### 6.4.5 Legendre moments

The maximum angular momentum involved in certain decay processes can be inferred by considering a mathematical expansion of the decay angular distribution in terms of Legendre polynomials, and measuring the moments of the expansion using a decay data sample [111].

Let's consider the quasi-two-body decay $B_s^0 \to (K^+\pi^-)(K^-\pi^+)$ and focus on the first pair of charged hadrons, $K^+\pi^-$. Being $\theta_1$ the angle between the direction of motion of the $K^+$ in the $K^+\pi^-$ rest frame and the direction of motion of the $K^+\pi^-$ pair in the $B_s^0$ rest frame (as defined in Fig. 3.1), the decay angular distribution can be written as

$$\frac{dN}{d\,\cos\theta_1} = \sum_{l=0}^{l^{max}} \langle P_l \rangle P_l(\cos\theta_1), \tag{6.12}$$

where $l$ depends on the relative angular momentum between the $K^+$ and the $\pi^-$, $j_1$, the Legendre polynomials are denoted by $P_l(\cos\theta_1)$ and $\langle P_l \rangle$ are the Legendre moments. These moments are made from products of two $j_1$ eigenstates, such that $l = j_1 + j_1'$ being $j_1$ and $j_1'$ the angular momenta of the two states. Consequently, if the maximum angular momentum of a state is $j_1^{max}$, the maximum $l$ is $l^{max} = 2j_1^{max}$, and the moments with $l > 2j_1^{max}$ are zero.

Mathematically, the Legendre moments can be computed as

$$\langle P_l \rangle = \int d\,\cos\theta_1' \frac{dN}{d\,\cos\theta_1'} P_l(\cos\theta_1'). \tag{6.13}$$

For a relatively large data sample, the integral can be approximated by a sum over the events. It should be noted that the method is only valid for a background-subtracted and acceptance-corrected data sample. A way to set up the data accordingly consists on using per-event weights, $w_i$, that correspond to the product of the ${}_s\mathcal{W}eights$ introduced in Sect. 6.4.1 and the acceptance-correction weights introduced in Sect. 6.4.4. In this case, the Legendre moments can be computed as

$$\langle P_l \rangle = \sum_{i=1}^{N} w_i \, P_l(\cos\theta_{1,i}). \tag{6.14}$$

If these moments are computed in bins of a given variable, the maximum angular momentum contributing to the decay can be studied as a function of that variable.

The method explained in this section is used in the analysis of $B_s^0 \to (K^+\pi^-)(K^-\pi^+)$ decays to discard a possible contribution from a spin-3 component in the two $K\pi$ pairs (the treatment for $K^-\pi^+$ is equivalent to the one for $K^+\pi^-$).

### 6.4.6 Charged particle isolation techniques

Many decay data samples contain background contributions originating from partially reconstructed decays. By looking for extra reconstructible particles in the event and studying their connection with the signal candidate, those backgrounds can be reduced.

A tool aimed at studying extra charged particles was developed for the first LHCb measurement of the $R(D^*)$ ratio [44]. A BDT was trained to determine whether a given track originates from the signal $B$ meson (associated track) or from elsewhere (un-associated track). The input variables provided to the BDT corresponded to several properties of the track and the properties of the candidate decay with a vertex fitted to include the track under consideration. The training was done using associated tracks from simulated $B \to D^{**}\mu\overline{\nu}_\mu$ decays, with $D^{**} \to D^{*+}X$, and un-associated tracks from simulated $\overline{B}^0 \to D^{*+}\mu\overline{\nu}_\mu$ events, with the signal decay excluded.

The previously described tool is also used in the analysis of this thesis aimed at measuring $R(D^{(*)+})$, in order to suppress different background components.

### 6.4.7 Neutral particle isolation techniques

Apart from the isolation against events with extra charged tracks, treated in the previous section, isolation against events with extra neutral pions and photons can also help to reduce backgrounds from partially reconstructed decays.

During the work in this thesis, I developed a tool for neutral isolation to be used for the $R(D^{(*)+})$ measurement, that could be later exported to other analyses. The tool fundamentally bases on the information that can be retrieved from photons detected in the LHCb calorimeter system. The photon energy is determined from the total cluster energy in the ECAL and the reconstructed energy deposit in the PS. The photon direction is derived from an assumed origin for the photon and the energy-weighted position of the photon candidate. In a second step, neutral pions with low transverse momenta can be reconstructed as pairs of well-separated photons, in which case they are referred to as resolved neutral pions. Due to the finite ECAL granularity, photon pairs from the decay of a sufficiently-high-momentum $\pi^0$ can not be resolved as individual clusters. Those so-called merged $\pi^0$ candidates are not considered in the study of this thesis.

The developed tool combines two pre-processed sources of information from neutral candidates to provide a final decision per event. The first source comes from resolved neutral pions. A BDT is trained to distinguish between true and fake additional $\pi^0$ that are associated to each event during reconstruction. The second source of information corresponds to a combination of photon candidates that are identified during reconstruction and happen to be inside a geometrical

cone of a given opening angle around a signal track. The information from these so-called neutral cones is obtained from a previously developed tool in LHCb [112]. In this case, a second BDT is trained to distinguish cones that do contain neutral particles created in the considered decay and others that only contain fake photons and/or photons coming from other sources. Finally, the output from the two BDTs is combined into a single classifier.

When training the BDTs, the true neutral candidates are obtained from simulated $\overline{B}^0 \to D^{*+}(\to D^+\pi^0)\mu^-\overline{\nu}_\mu$ decays and the fake candidates are taken from simulated $\overline{B}^0 \to D^+\mu^-\overline{\nu}_\mu$ decays. The reconstruction process associates many resolved neutral pions per event, only some of which (one in this case) can be true. Additionally, the true neutral candidates are not always contained in the associated neutral cones. In order to solve this problem, I developed some truth-matching algorithms to select true simulation candidates for the training of the two BDTs. Finally, the combination of the two classifiers into a single one is optimised using simulation events without the neutral-candidate truth-matching applied.

As previously introduced, this tool was developed for the second analysis in this thesis and used with the aim of isolating $\overline{B}^0 \to D^+ l\overline{\nu}_l$ decays, where $l \in \{\mu, \tau\}$. The construction and the performance of the different classifiers is presented in Sect. 8.2.5. The overall performance is found to be lower than the one for the charged isolation, due to the low LHCb efficiency in the reconstruction of photons and neutral pions. Future improvements in these efficiencies would allow to improve the performance of this tool.

USC UNIVERSIDADE DE SANTIAGO DE COMPOSTELA

# Chapter 7

# Measurement of the $\phi_s$ phase in $B_s^0 \to (K^+\pi^-)(K^-\pi^+)$

This section explains the method and the results of the first and main analysis of this thesis. The employed data samples are described in Sect. 7.1 and the event selection, needed to obtain a background-subtracted signal sample, is explained in Sect. 7.2. As introduced in previous chapters, the $B_s^0/\overline{B}_s^0$ separation at production time is essential for the measurement of $\phi_s^{d\bar{d}}$, for which the flavour tagging is used as explained in Sect. 7.3. The determination of the $B_s^0$ production asymmetry, also needed in the process, is reviewed in Sect. 7.4. The deviations in the data distributions with respect to the ideal model presented in Sect. 3, which are due to the detection, reconstruction and event selection processes, are studied in Sect. 7.5 and Sect. 7.6. The final model used for fitting, together with the implementation of the fit and the obtained results, are presented in Sect. 7.7. A list of the checks performed to the analysis method is written in Sect. 7.8 and the computation of systematic uncertainties for the measured parameters is described in Sect. 7.9. Finally, the conclusions of the study are presented in Sect. 7.10.

## 7.1 Data samples

The full Run I dataset consisting of $1.1$ fb$^{-1}$ of data with $\sqrt{s} = 7$ TeV taken in 2011 and $2.0$ fb$^{-1}$ of data with $\sqrt{s} = 8$ TeV taken in 2012 is used in this analysis. During the event reconstruction, so as to improve the resolution on the $B_s^0$ decay time, the `DecayTreeFitter` (DTF) [113] algorithm was used. While the traditional method to fit a decay tree is 'leaf-by-leaf', starting from the downstream vertices and propagating the information upstream, the `DecayTreeFitter` takes a complete decay chain, parameterises it in terms of vertex positions, decay lengths and momentum parameters, and then fits these parameters simultaneously, taking into account the relevant constraints. In this analysis, the $B_s^0$ candidates are constrained to originate from their associated PV.

The trigger lines used are listed in Table 7.1. Due to a residual kinematic dependence on whether the event is triggered by `L0Hadron` or not, the analysis is performed in 4 different categories dependent on the year, 2011 vs 2012, and the L0 trigger, `L0Global TIS` vs `(L0Hadron TOS & not L0Global TIS)`. For simplicity, the last trigger category is denoted by `L0Hadron TOS`. The LHCb data are pre-selected in a centralised way by considering the overlap between different specific sets of requirements, denoted as stripping lines. The stripping line used in this analysis is `StrippingBetaSBs2K0stK0stNominalLine`.

The Monte Carlo samples listed in Table 7.2 are used with different purposes, as indicated in the table. In specific signal studies of this analysis that require a good statistical coverage of the full phase-space under consideration, not only the pure phase-space $B_s^0 \to K^+\pi^-K^-\pi^+$ MC is used but a combination of this sample with the $B_s^0 \to K^*(892)^0\overline{K}^*(892)^0$ MC. This allows to increase the simulation sample size in the $K^{*0}$ mass region, where the phase-space distribution takes low values but the signal data peaks.

| **L0 Any of:** |
|---|
| L0Global TIS |
| L0Hadron TOS |
| **Hlt1:** |
| Hlt1TrackAllL0 TOS |
| **Hlt2 Any of:** |
| Hlt2Topo2BodyBBDT TOS |
| Hlt2Topo3BodyBBDT TOS |
| Hlt2Topo4BodyBBDT TOS |

TABLE 7.1: Trigger lines used in this analysis.

| Sample | Utilisation |
|---|---|
| $B_s^0 \to K^*(892)^0 \overline{K}^*(892)^0$ | Signal study |
| $B_s^0 \to K^*(892)^0 \overline{K}^*(892)^0$, large CPV | Check of the model |
| $B^0 \to K^*(892)^0 \overline{K}^*(892)^0$ | Background study |
| $B_s^0 \to K^*(892)^0 \overline{K}^*(1430)^0$ | Signal study |
| $B_s^0 \to K^*(1430)^0 \overline{K}^*(1430)^0$ | Signal study |
| $B_s^0 \to K^+\pi^- K^-\pi^+$ Phase Space | Signal study |
| $B_s^0 \to K^*(892)^0 \phi(1020)$ | Background study |
| $B^0 \to K^*(892)^0 \phi(1020)$ | Background study |
| $B^0 \to K^*(892)^0 \rho(770)^0$ | Background study |
| $\Lambda_b^0 \to pK^-\pi^+\pi^-$ | Background study |
| $\Lambda_b^0 \to p\pi^-\pi^+\pi^-$ | Background study |

TABLE 7.2: List of Monte Carlo samples used.

## 7.2 Event selection

The event selection is constituted of some pre-selection requirements, followed by a BDT trained against combinatorial background, PID requirements, mass vetoes and, finally, an sWeighting procedure using a four-body-mass fit. The process is described in the next sub-sections.

### 7.2.1 Pre-selection and BDT

The requirements of the stripping line are provided in Table 7.3. After the stripping, there is a loose pre-selection developed for this analysis which keeps 97% of the signal whilst removing 25% of the background. The corresponding requirements are listed in Table 7.4.

| | |
|---|---|
| **$B_s^0$ Cuts** | |
| $B_s^0$ (DIRA) | $> 0.99$ |
| $B_s^0$ (Vertex $\chi^2$/dof) | $< 15$ |
| $B_s^0$ (IP $\chi^2$) | $< 25$ |
| $\sum p_{\mathrm{T}}$ (daughters) | $> 5000$ MeV |
| **$K^{*0}$ Cuts** | |
| $K^{*0}$ (Vertex $\chi^2$/dof) | $< 9$ |
| $K^{*0}$ ($p_T$) | $> 900$ MeV |
| **$K^{\pm}/\pi^{\pm}$ Cuts** | |
| $K^{\pm}/\pi^{\pm}$ ($p_T$) | $> 500$ MeV |
| $K^{\pm}/\pi^{\pm}$ (IP $\chi^2$) | $> 9$ |
| $K^{\pm}/\pi^{\pm}$ (Track Ghost Prob) | $< 0.8$ |
| $K^{\pm}$ (PIDK) | $> 2.0$ |
| $\pi^{\pm}$ (PIDK) | $< 0.0$ |

TABLE 7.3: Stripping requirements. In the table, DIRA stands for direction angle and corresponds to the cosine of the angle between the momentum direction of a particle and the direction from its production vertex to its decay vertex. Track Ghost Prob is the probability for the track of being fake. PIDX, with X being a given type of particle, is the difference in log likelihoods for a particle of being of type X against being a pion.

| | |
|---|---|
| **$B_s^0$ Cuts** | |
| $B_s^0$ (Vertex $\chi^2$/dof) | $< 12$ |
| $B_s^0$ decay time | $> 0$ |
| **$K^{\pm}/\pi^{\pm}$ Cuts** | |
| $K^{\pm}/\pi^{\pm}$ (Track $\chi^2$/dof) | $< 4$ |
| $K^{\pm}/\pi^{\pm}$ (IsMuon) | False |
| **Mass Cuts** | |
| $m(B_s^0)$ | $5000 < m < 5800$ MeV |
| $m(K^{\pm}\pi^{\mp})$ | $750 < m < 1600$ MeV |

TABLE 7.4: Pre-selection requirements.

After the pre-selection, a BDT is used to reject the combinatorial background.

**7.2.1.0.1 BDT training** The training sample used for the signal is the $B_s^0 \to K^*(892)^0\overline{K}^*(892)^0$ Monte Carlo. The background training sample is obtained using data from the upper mass side-band for which $m(K^+\pi^-K^-\pi^+) > 5500$ MeV/$c^2$. The $k$-fold cross-validation ($k$CV) method [114] is used to avoid overtraining. The training dataset is split into $k = 4$ samples and subsequently 4 BDTs are trained using the $k-1$ subsets as the training sample and the remaining subset for testing and evaluation. In this way there is a large training sample but each event is evaluated with a BDT that it was not used to train, thus avoiding overtraining. The training is performed separately for the 2011 and 2012 samples, resulting in 8 BDTs in total, although each event is only ever evaluated with a single BDT.

The input variables used for the training are:

1. $p_{\rm T}$ of the $B_s^0$ candidate and both $K^{*0}$ candidates.
2. maximum and minimum $p_T$ of the $K^\pm$ and $\pi^\pm$ daughters.
3. $\eta$ of the $B_s^0$ candidate and both $K^{*0}$ candidates.
4. maximum and minimum $\eta$ of the $K^\pm$ and $\pi^\pm$ daughters.
5. $DIRA$ of the $B_s^0$ candidate.
6. vertex $\chi^2$ of the $B_s^0$ candidate.

The distributions of the input variables for one sub-sample are shown in Fig. 7.1. The BDT output distributions are shown in Fig. 7.2

**7.2.1.0.2 BDT cut optimization** A cut on the output value of the BDT is used to reject combinatorial background. The optimisation procedure uses a figure of merit defined as,

$$FOM = \frac{S}{\sqrt{S+B}}, \tag{7.1}$$

where $S$ and $B$ are the number of expected signal and background events as defined below. The number of expected signal events are calculated from MC and renormalised from a fit to the data before any BDT cut is applied. The number of background events is estimated from a fit to the data in the upper mass side-band ($5600$ MeV/$c^2 < m(B_s^0) < 5800$ MeV/$c^2$) which is then extrapolated into the signal region. The distributions for the optimisation fit (which is used to estimate both the number of signal and background events before any BDT cut is applied) are shown in Fig. 7.3. The optimisation is performed separately for the 2011 and 2012 data samples. The output of the optimisation scans are shown in Fig. 7.4. The optimal cut values were found to be $> 0.02$ for 2011 and $> 0.03$ for 2012.

### 7.2.2 PID, mass vetoes and multiple candidates

The next sub-sections describe the used PID requirements against mis-ID background and the mass vetoes against alternative particle combinations. The treatment of multiple candidates is also described.

#### 7.2.2.1 PID requirements

Peaking backgrounds from sources other than the signal decay in which one of the daughters is misidentified have to be considered. Specifically, decays originating from a $B^0$ in which a kaon is misidentified as a pion, such as the $B^0 \to K^{*0}\rho^0$ decay, are problematic since they tend to peak in the signal region. Relatively tight PID requirements are applied on both the kaons and pions

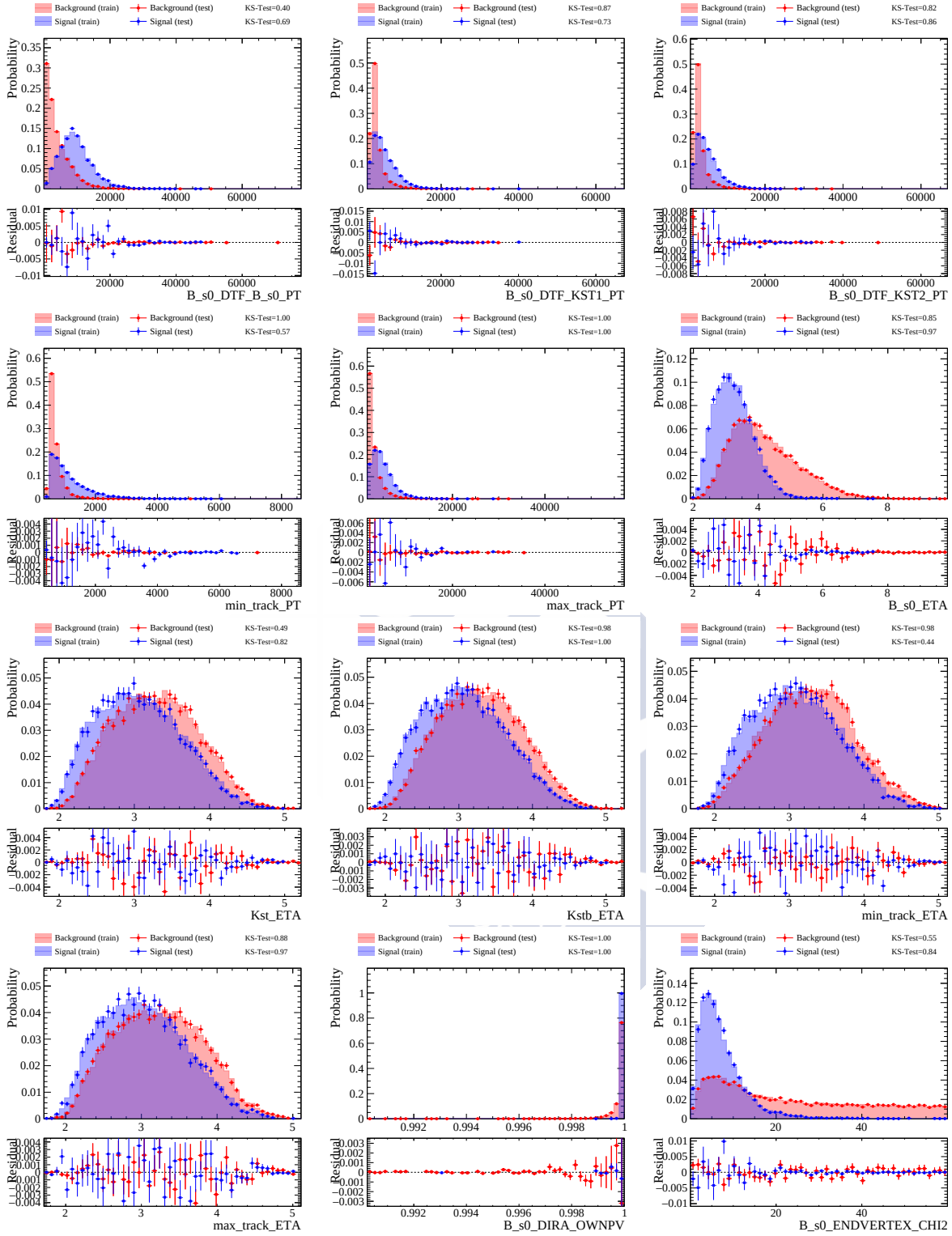



FIGURE 7.1: BDT training input variables.

in order to remove or suppress the peaking background contributions. It has been found that backgrounds in which a kaon is misidentified as a pion are much less problematic as they peak away from the signal and subsequently can be subtracted in the 4-body mass fit using the sWeight technique.

Because the PID variables are poorly modelled in MC, the distributions of the PID response

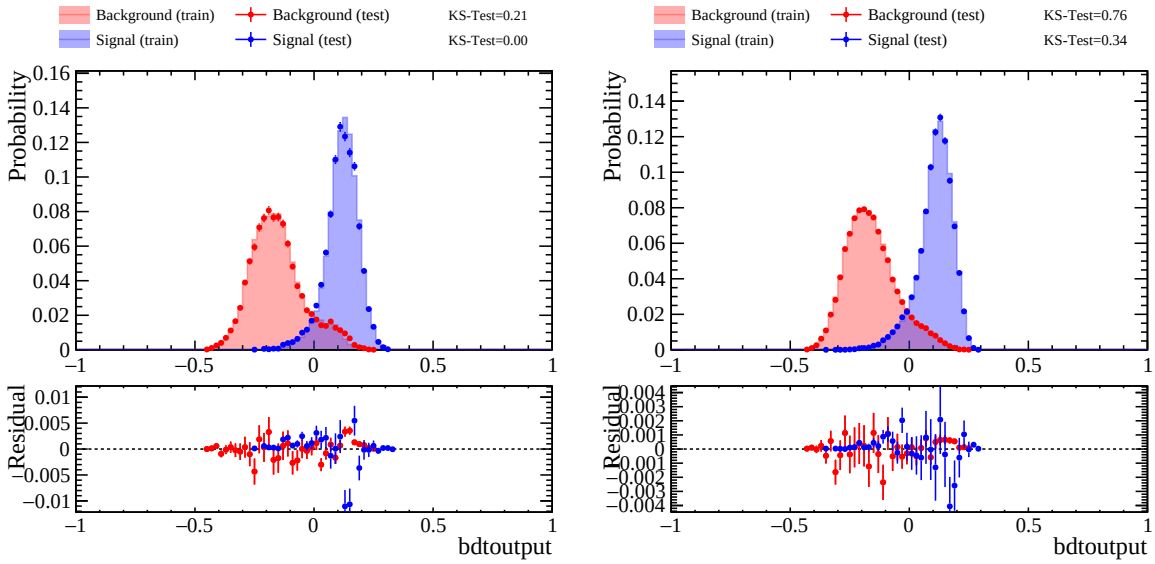



FIGURE 7.2: BDT output distributions for the 2011 (left) and 2012 (right) trainings.

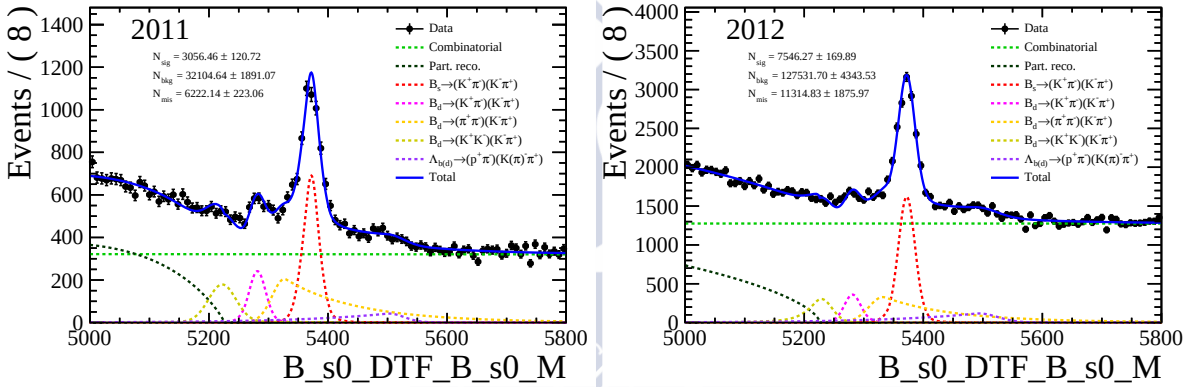



FIGURE 7.3: Fits to the data in 2011 (left) and 2012 (right) before any BDT cut is applied. These fits are used to extract the expected number of signal and background events (in the signal region) in order to optimise the BDT cut.

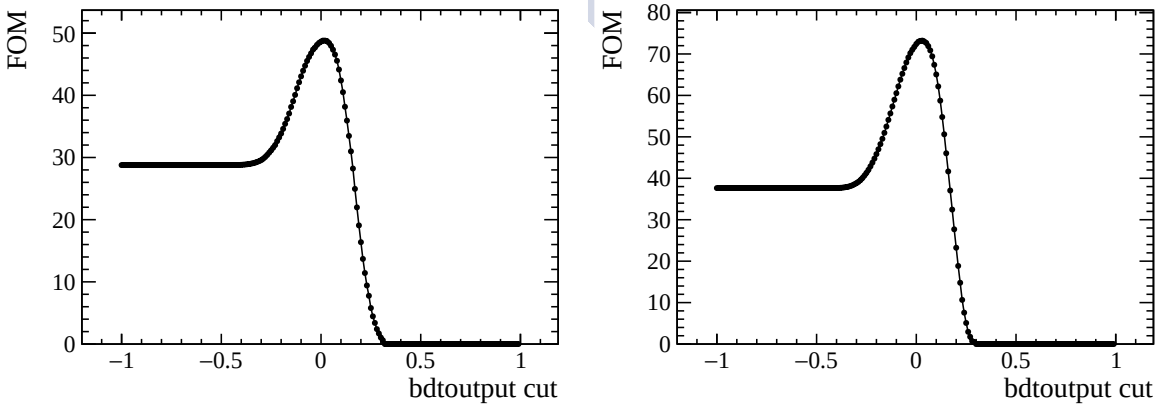



FIGURE 7.4: Distribution of the figure of merit as a function of the BDT cut value for the 2011 (left) and 2012 (right) data samples.

are corrected using the `PIDGen` package which is an LHCb customisation of the `Meerkat`

package [115]. From here on any cuts on PID refer to the transformed distributions. The $ProbNN$ PID variables, as defined in Ref. [116], are used and the following requirements are applied:

- **Kaons** - both kaons are required to fulfil $ProbNNk > 0.2$ and $ProbNNk \times (1 - ProbNNpi) > 0.3$
- **Pions** - both pions are required to fulfil $ProbNNpi > 0.2$ and $ProbNNpi \times (1 - ProbNNk) > 0.3$

#### 7.2.2.2 Mass Vetoes

To remove alternative combinations of well-identified final-state particles, several mass vetoes are applied to the relevant invariant mass distributions. A mass window of $\pm 30\,\mathrm{MeV}/c^2$ around the known $D^0$ mass is vetoed on the $m(K^+K^-)$ distribution to eliminate the contribution from $D^0(\to K^+K^-)\pi^+\pi^-$. A requirement of $m(K^+K^-\pi^\pm) > 2100\,\mathrm{MeV}/c^2$ is applied to veto 3-body decays originating from charm resonances. The resulting 2-body and 3-body invariant mass distributions are shown in Fig. 7.5 for the $B_s^0 \to K^{*0}\overline{K}^{*0}$ MC, the $B_s^0 \to (K^+\pi^-)(K^-\pi^+)$ phase space MC and the data. It can be seen that there are no resonant components in the data after the vetoes.

In addition, a specific cut is applied to further suppress contributions from $B^0 \to \rho K^{*0}$. Events are vetoed if the $m(K\pi\pi\pi)$ invariant mass is within $\pm 30\ \mathrm{MeV}/c^2$ of the $B^0$ mass and if the relevant kaon fulfills the pion ID cuts. Similarly contributions from $\Lambda_b^0 \to p\pi^-K^-\pi^+$ are vetoed by removing events which have $m(pK^-\pi^+\pi^-)$ within $\pm 35\ \mathrm{MeV}/c^2$ of the $\Lambda_b^0$ mass if the relevant kaon fulfills $ProbNNp > 0.2$.

#### 7.2.2.3 Multiple Candidates

If any event has multiple candidates which pass all of the selection requirements detailed above then one candidate is chosen at random and the others are removed. This removes 1.43% of candidates.

### 7.2.3 Selection efficiencies

For illustration, the selection efficiencies for each data and Monte Carlo sample are shown in Fig. 7.6.

### 7.2.4 Four-body-mass fit and sWeights

The 4-body-mass spectrum is fitted to provide *sWeights* for the signal candidates. A simultaneous extended maximum likelihood fit is performed to the data which is split into four categories dependent on the year (2011, 2012) and the L0 trigger decision (either `L0Global TIS` or `L0Hadron TOS`). The model used for the fit is explained below.

#### 7.2.4.1 Model used for fitting

There are several components used in the fit. Many of the shapes are obtained from previous fits to the MC distributions, the results of which are shown in Fig. 7.7. These distributions are not reweighted using PID efficiencies but it has been seen that these shapes vary negligibly when different PID cuts are applied and therefore it was considered unnecessary. Many of the

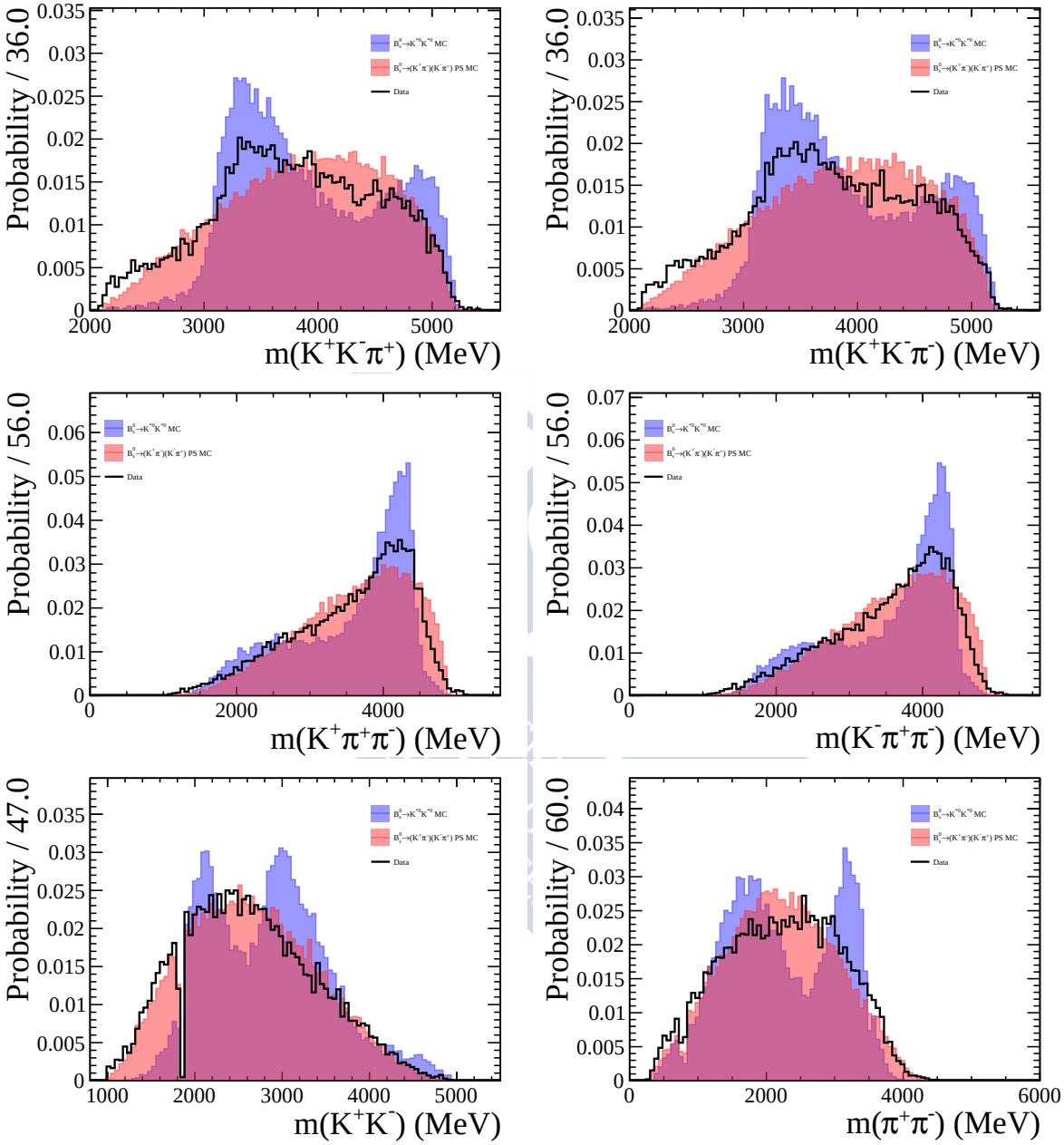



FIGURE 7.5: 2 and 3-body mass combinations for events which pass the BDT, PID and mass veto requirements. The $B_s^0 \to K^{*0}\overline{K}^{*0}$ MC is shown in blue, the $B_s^0 \to (K^+\pi^-)(K^-\pi^+)$ phase space MC is shown in red and the data are shown in black.

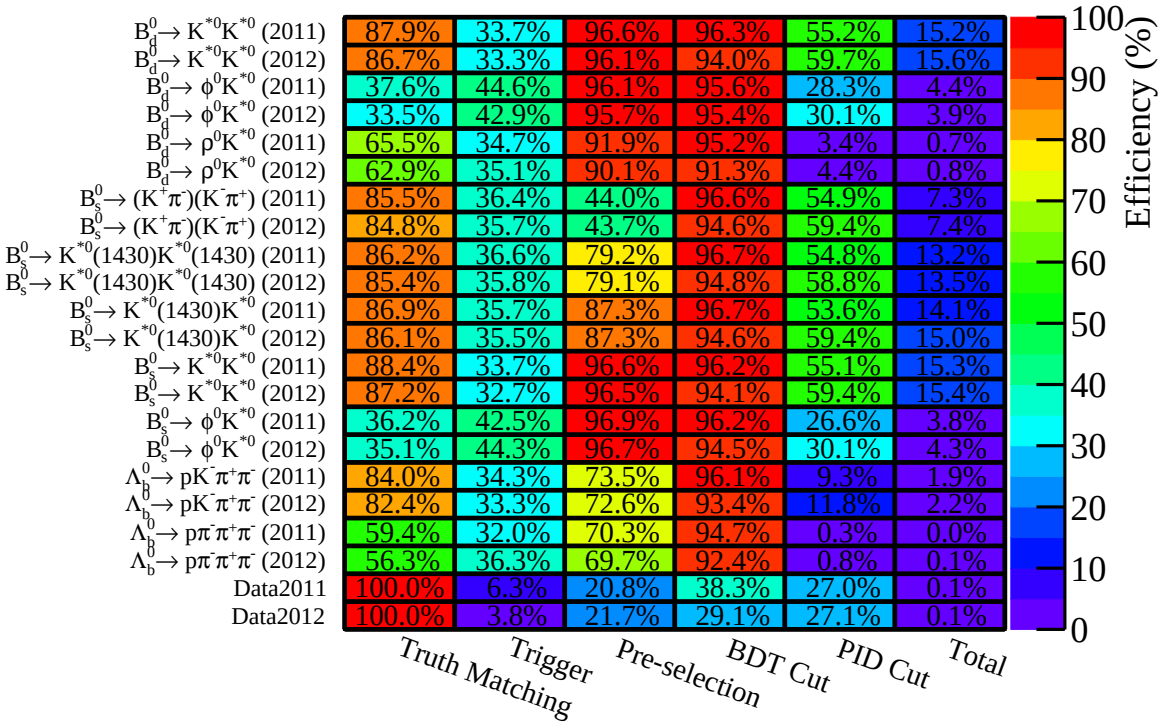



FIGURE 7.6: Selection efficiencies.

components are modelled using an *Ipatia* function [117]:

$$I(m,\mu,\sigma,\lambda,\zeta,\beta,a_1,a_2,n_1,n_2) \propto \begin{cases} \frac{A}{(B+m-\mu)^{n_1}}, & \text{if } m-\mu < -a_1\sigma \\ \frac{C}{(D+m-\mu)^{n_2}}, & \text{if } m-\mu > a_2\sigma \\ ((m-\mu)^2+\delta^2)^{\frac{1}{2}\lambda-\frac{1}{4}} e^{\beta(m-\mu)} K_{\lambda-\frac{1}{2}}(\alpha\sqrt{(m-\mu)^2+\delta^2}), & \text{otherwise,} \end{cases} \tag{7.2}$$

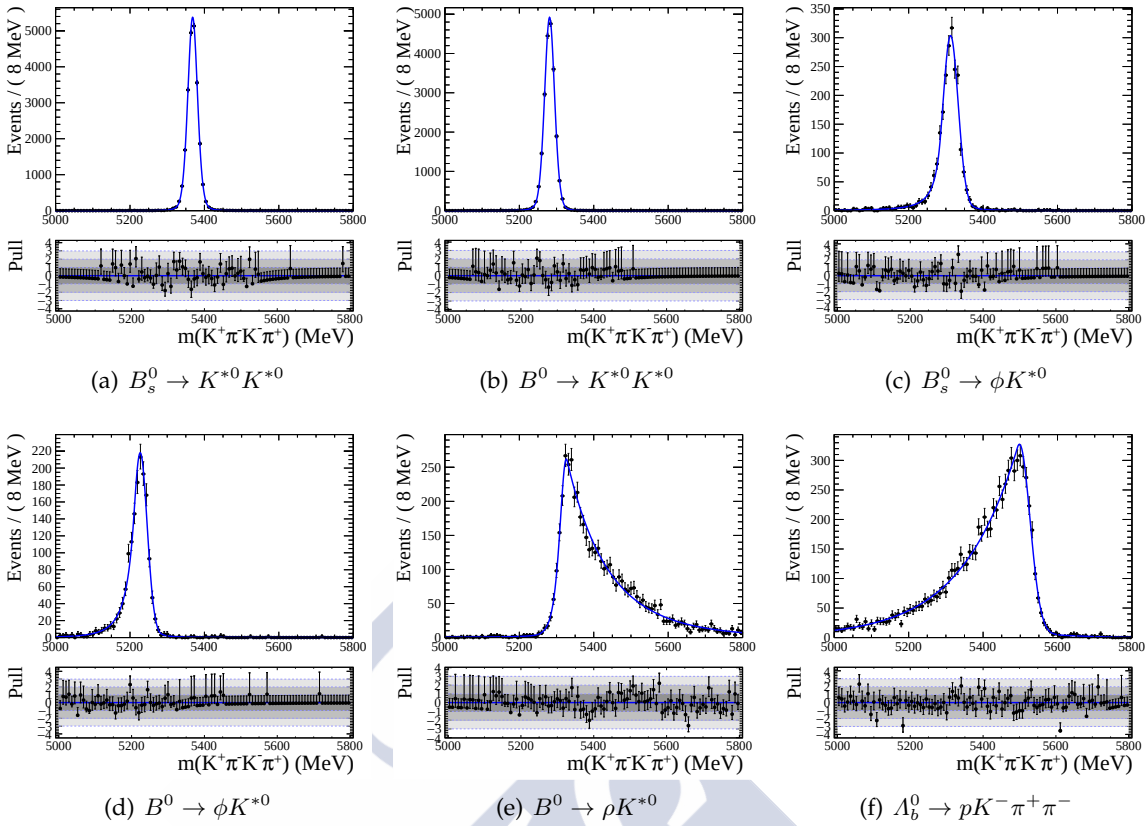
where $K_\nu(z)$ is the modified Bessel function of the second kind, $\delta \equiv \sigma\sqrt{\frac{\zeta K_\lambda(\zeta)}{K_{\lambda+1}(\zeta)}}$, $\alpha \equiv \frac{1}{\sigma}\sqrt{\frac{\zeta K_{\lambda+1}(\zeta)}{K_\lambda(\zeta)}}$, and $A$, $B$, $C$ and $D$ are obtained by imposing continuity and differentiability. The parameters $\zeta$ and $\beta$ are fixed to zero in our case.

The components used in the four-body-mass fit are the following ones.

- $\mathbf{B_s^0 \to (K^+\pi^-)(K^-\pi^+)}$. This is the signal component. The shape is modelled as an *Ipatia* distribution. The tail parameters are fixed from a fit to the MC (shown in Fig. 7.7(a)) whilst the mean and width are allowed to float when fitting the data.

- $\mathbf{B^0 \to (K^+\pi^-)(K^-\pi^+)}$. This is equivalent to the signal decay but originates from a $B^0$ instead of a $B_s^0$. The shape is modelled, as above, with an *Ipatia* function in which the tail parameters are fixed from a fit to MC (shown in Fig. 7.7(b)) whilst the width is allowed to float when fitting the data. The mass difference between the $B_s^0$ and $B^0$ mesons is fixed to its known value.

- $\mathbf{B_s^0 \to (K^+K^-)(K^-\pi^+)}$. This is background, originating from a $B_s^0$, in which one kaon is mis-identified as a pion. The shape is modelled, as above, with an *Ipatia* function in which the parameters are fixed from a fit to MC (shown in Fig. 7.7(c)).




(a) $B_s^0 \to K^{*0}K^{*0}$ (b) $B^0 \to K^{*0}K^{*0}$ (c) $B_s^0 \to \phi K^{*0}$

(d) $B^0 \to \phi K^{*0}$ (e) $B^0 \to \rho K^{*0}$ (f) $\Lambda_b^0 \to pK^-\pi^+\pi^-$

FIGURE 7.7: Fits to the MC samples in the $K^+\pi^-K^-\pi^+$ hypothesis.

- $\mathbf{B^0 \to (K^+K^-)(K^-\pi^+)}$. This is background, originating from a $B^0$, in which one kaon is mis-identified as a pion. The shape is modelled, as above, with an *Ipatia* function in which the parameters are fixed from a fit to MC (shown in Fig. 7.7(d)).
- $\mathbf{B^0 \to (\pi^+\pi^-)(K^-\pi^+)}$. This is background in which one pion is mis-identified as a kaon. The shape is modelled, as above, with an *Ipatia* function in which the parameters are fixed from a fit to MC (shown in Fig. 7.7(e)).
- $\mathbf{\Lambda_b^0 \to (p\pi^-)(K^-\pi^+)}$. This is background in which one proton is mis-identified as a kaon. The shape is modelled as a double Crystal-Ball function in which the parameters are fixed from a fit to MC (shown in Fig. 7.7(f)).
- **Partially reconstructed background**. This accounts for contributions from any partially reconstructed decays. The shape is modelled with an Argus function [118] in which the cut-off is set to the $B_s^0$ mass minus the neutral pion mass.
- **Combinatorial background**. An exponential function is used to model the combinatorial background. The shape parameter is allowed to vary when fitting.

#### 7.2.4.2 Mass fit results

The shape of each component is required to be the same for each fit category, apart from the combinatorial slope which is independent in each category. The yields of each component are allowed to float independently in each category. The relative yield of the $B_s^0 \to \phi K^{*0}$ background is constrained to be a fraction, $f$, of the $B^0 \to \phi K^{*0}$ background according to their

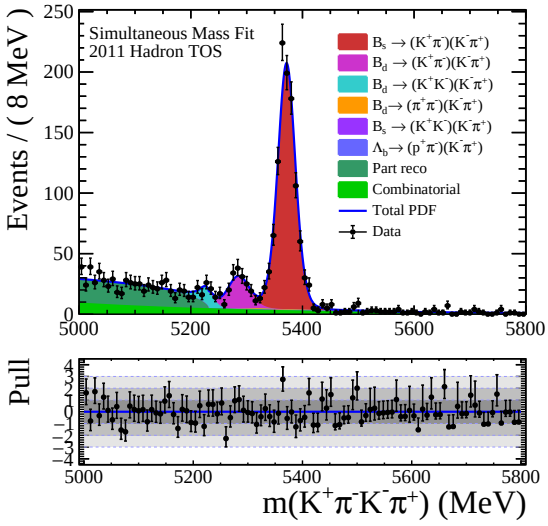
| Parameter | Value | Error |
|---|---|---|
| bd2kstkst_mu | 5285.2952 | ±1.0338 |
| bd2kstkst_sigma | 21.2208 | ±1.5069 |
| bd2kstkst_y_GlobalTIS2011 | 122.2012 | ±15.9057 |
| bd2kstkst_y_GlobalTIS2012 | 287.8914 | ±26.7279 |
| bd2kstkst_y_HadronTOS2011 | 166.5297 | ±17.5181 |
| bd2kstkst_y_HadronTOS2012 | 436.3018 | ±33.8590 |
| bd2phikst_mu | 5228.5574 | ±2.7340 |
| bd2phikst_sigma | 13.0513 | ±2.9799 |
| bd2phikst_y_GlobalTIS2011 | 22.4655 | ±11.6473 |
| bd2phikst_y_GlobalTIS2012 | 58.6005 | ±25.2003 |
| bd2phikst_y_HadronTOS2011 | 66.0711 | ±16.1131 |
| bd2phikst_y_HadronTOS2012 | 133.7962 | ±34.2152 |
| bkg_exp_p1 | −0.0029 | ±0.0003 |
| bkg_y_GlobalTIS2011 | 400.5674 | ±60.7893 |
| bkg_y_GlobalTIS2012 | 1086.7839 | ±131.1808 |
| bkg_y_HadronTOS2011 | 376.9191 | ±68.3313 |
| bkg_y_HadronTOS2012 | 946.0972 | ±142.0729 |
| bs2kstkst_mu | 5371.5365 | ±0.2469 |
| bs2kstkst_sigma | 17.5838 | ±0.2446 |
| bs2kstkst_y_GlobalTIS2011 | 749.3370 | ±29.0087 |
| bs2kstkst_y_GlobalTIS2012 | 1905.6968 | ±46.6212 |
| bs2kstkst_y_HadronTOS2011 | 1045.2979 | ±33.8802 |
| bs2kstkst_y_HadronTOS2012 | 2379.4475 | ±52.0349 |
| part_reco_c | −4.3374 | ±1.2845 |
| part_reco_p | 0.5491 | ±0.0539 |
| part_reco_y_GlobalTIS2011 | 311.6391 | ±43.8144 |
| part_reco_y_GlobalTIS2012 | 781.2398 | ±94.3142 |
| part_reco_y_HadronTOS2011 | 434.4483 | ±48.0235 |
| part_reco_y_HadronTOS2012 | 1052.2546 | ±97.6931 |
| yield_ratio_bd2rhokst_o_bd2phikst | 0.2022 | ±0.0300 |
| yield_ratio_bs2phikst_o_bd2phikst | 0.0293 | ±0.0080 |
| yield_ratio_lb2pkpipi_o_bd2phikst | 0.1580 | ±0.1534 |

TABLE 7.5: Central values and uncertainties from the 4-body-mass fit.

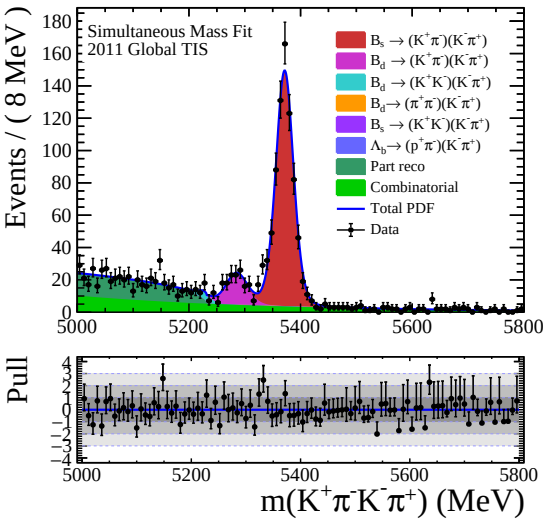
known branching fractions and the known value of $f_s/f_d$, $f = (0.029 \pm 0.008)$, using a Gaussian constraint. These are assumed to have the same efficiency which is a reasonable assumption given they have the identical final state. Similarly, the $B^0 \to \rho K^{*0}$ background is Gaussian constrained to the appropriate fraction of $B^0 \to \phi K^{*0}$ using their known branching fractions and the relative efficiencies as computed from MC after calibration using `PIDGen`, $f = (0.20 \pm 0.03)$. The relative yield of $\Lambda_b^0 \to p\pi^- K^- \pi^+$ to $B^0 \to \phi K^{*0}$ is allowed to float but required to be the same in each category.

The results of the fit to the data in each category, and the sum over all categories, are shown in Fig. 7.8. The best fit parameters resulting from the 4-body-mass fit are shown in Table 7.5. An overall signal yield of $6080 \pm 83$ events is measured.

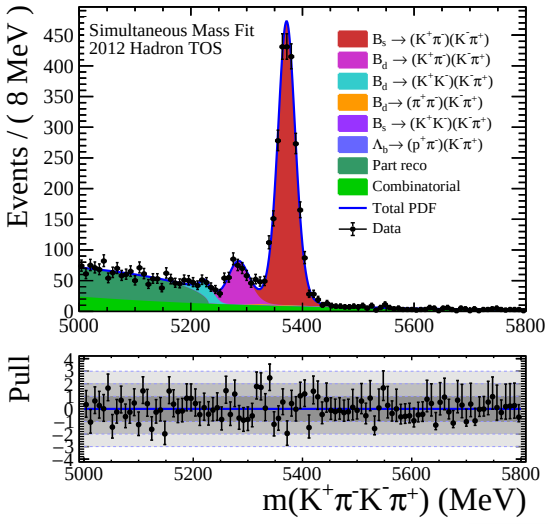
The plots shown in Fig. 7.9 compare the sWeighted data distributions with those of the $B_s^0 \to K^{*0}\overline{K}^{*0}$ MC for each BDT training variable, as a check of the whole selection procedure. They show a quite good level of agreement.



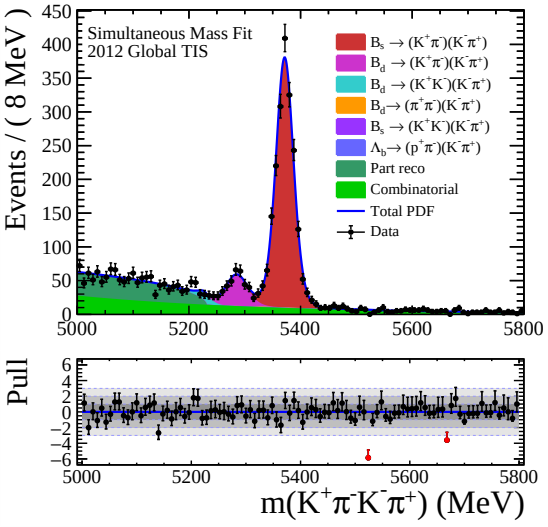

(a) 2011 L0Hadron TOS.



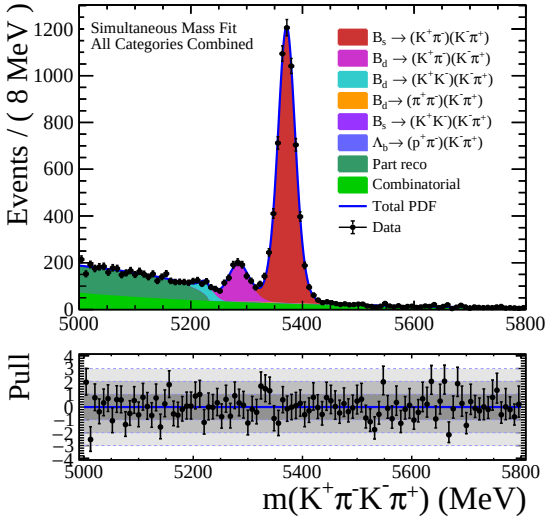

(b) 2011 L0Global TIS.



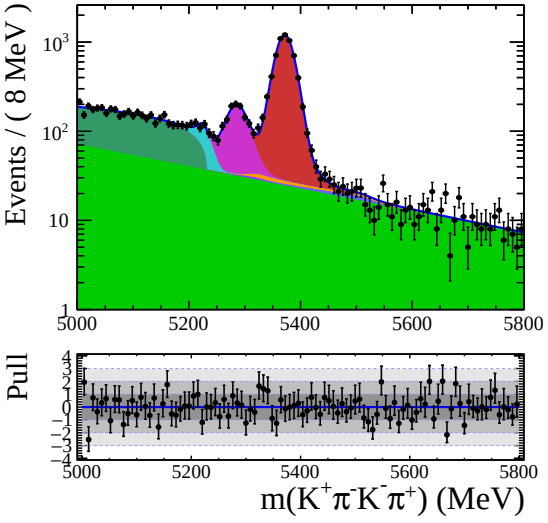

(c) 2012 L0Hadron TOS.




(d) 2012 L0Global TIS.




(e) All Categories Combined.




(f) All Categories Combined (log).

FIGURE 7.8: Four-body-mass fit for each category and for all categories combined.

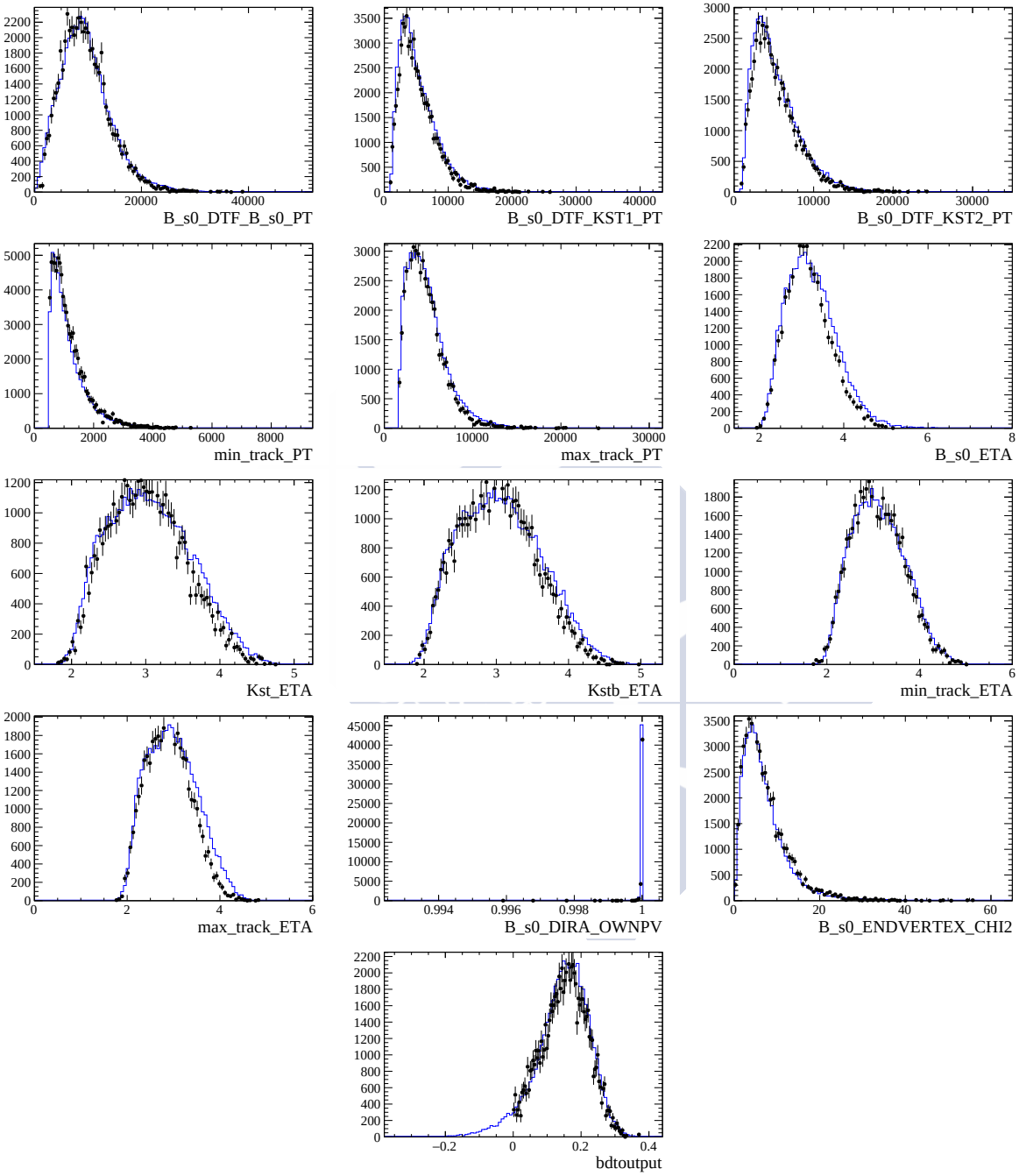



FIGURE 7.9: Comparison of the sWeighted data distributions and $B_s^0 \to K^{*0}\overline{K}^{*0}$ MC distributions for each of the BDT training variables and the BDT response itself.

## 7.3 Flavour tagging

For this analysis, both opposite-side (OS) and same-side (SS) tagging algorithms are employed (see Sect. 6.4.3 for details on the flavour tagging at LHCb). The combination of the OS-electron, OS-muon, OS-vertex charge and OS-kaon algorithms [119] is used as the nominal OS tagger. The neural network SS kaon (SSK) tagger [120] is used in this analysis as the nominal SS tagger. The estimated-mistag-probability distributions of the tagged sWeighted events for the nominal OS and SS taggers are shown in Fig. 7.10.

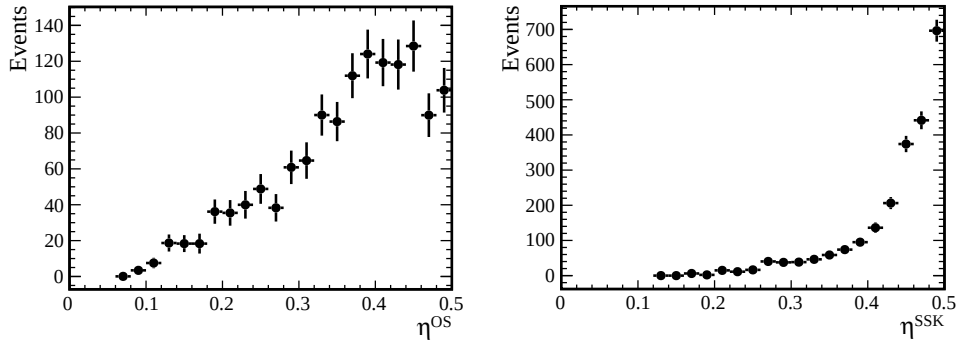



FIGURE 7.10: Estimated-mistag-probability distributions of the sWeighted data, for the OS combination and the neural network SS kaon tagging algorithms.

Ignoring acceptance and resolution effects, the multi-dimensional spectrum of data with flavour tagging, $S_{FT}$, can be written as a linear combination of the time dependent differential decay rates (see Eq. 3.11) of beauty mesons with flavour $B_s^0$ and $\bar{B}_s^0$ at $t = 0$:

$$\begin{aligned} S_{FT} &= (1+\Delta_{prod}) \cdot P^{OS}(q^{OS}) \cdot P^{SSK}(q^{SSK}) \cdot \frac{d\Gamma^6(B_s^0)}{dt\, d\Omega} \\ &+ (1-\Delta_{prod}) \cdot \bar{P}^{OS}(q^{OS}) \cdot \bar{P}^{SSK}(q^{SSK}) \cdot \frac{d\Gamma^6(\bar{B}_s^0)}{dt\, d\Omega}. \end{aligned} \tag{7.3}$$

Above, $\Delta_{prod}$ is the production asymmetry, which is computed in Sect. 7.4. The terms $P^X(q^X)$ and $\bar{P}^X(q^X)$ are defined for an $X$ tagger as:

$$\begin{aligned} P^X(q^X) &= \begin{cases} 1-\omega^X(\eta^X) & \text{for } q^X = \;\; 1, \\ 1 & \text{for } q^X = \;\; 0, \\ \omega^X(\eta^X) & \text{for } q^X = -1, \end{cases} \\ \bar{P}^X(q^X) &= \begin{cases} \bar{\omega}^X(\eta^X) & \text{for } q^X = \;\; 1, \\ 1 & \text{for } q^X = \;\; 0, \\ 1-\bar{\omega}^X(\eta^X) & \text{for } q^X = -1, \end{cases} \end{aligned} \tag{7.4}$$

where $\omega^X(\eta^X)$ and $\bar{\omega}^X(\eta^X)$ are the corrected mistag probabilities for a $B_s^0$ and a $\bar{B}_s^0$ meson, as defined in Eq. 6.9. The expression in Eq. 7.3 holds as long as the OS and the SS taggers are uncorrelated. This hypothesis is consistent with the absence of visible correlations between the $\eta^{OS}$ and $\eta^{SSK}$ variables when looking at the two-dimensional distribution of data shown in Fig. 7.11.

The flavour tagging calibration parameters are gaussian constrained during fitting to the values written in Table 7.6. The mean estimated mistag probabilities, $\langle \eta^X \rangle$, are extracted from the tagged sWeighted data and fixed during fitting. Their values are also written in Table 7.6.

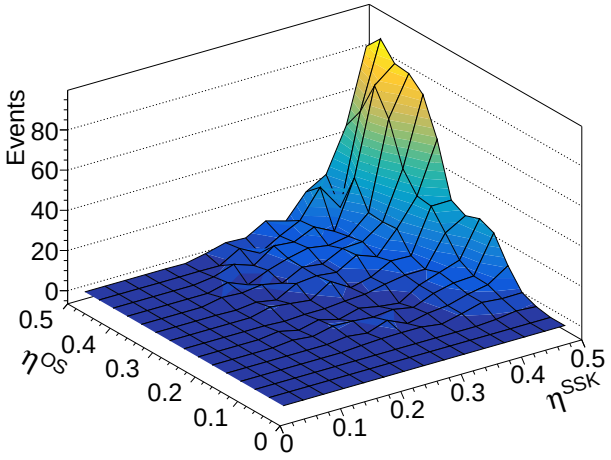



FIGURE 7.11: Two-dimensional distribution of the sWeighted data on the OS and SS estimated mistag probabilities.

| Parameter | OS Combination | NNet SSK |
|---|---|---|
| $p_0^X - \langle\eta^X\rangle$ | $0.0062 \pm 0.0044$ | $0.0070 \pm 0.0052$ |
| $\Delta p_0^X/2$ | $0.007 \pm 0.0006$ | $-0.0082 \pm 0.0019$ |
| $\langle\eta^X\rangle$ | $0.3529$ | $0.4353$ |
| $p_1^X$ | $0.982 \pm 0.035$ | $0.925 \pm 0.085$ |
| $\Delta p_1^X/2$ | $0.033 \pm 0.006$ | $-0.016 \pm 0.026$ |

TABLE 7.6: Central values for the parameters used in the calibration of the mistag probabilities. With the exception of $\langle\eta^X\rangle$, they are taken from the calibrations performed by the flavour tagging group of LHCb, namely from Ref. [121] for the OS Combination and from Ref. [120] for the NNet SSK. A new calibration, based on a specific decay mode, is not developed for this analysis since no optimal calibration sample is available, in terms of high statistics and kinematic similarity to our channels.

This way of constructing the multi-dimensional spectrum allows to combine the information from the two taggers, during fitting. The final calibration parameters, as measured in the time-dependent fit, can be found in Table 7.20. An effective tagging power of $5.15 \pm 0.14\%$ is computed for the sample under study. Details of the tagging performance can be found in Table 7.7.

| Tagging algorithm | $\epsilon_{\text{tag}}$ [%] | $\epsilon_{\text{eff}}$ [%] |
|---|---|---|
| SS | $62.0 \pm 0.7$ | $1.63 \pm 0.21$ |
| OS | $37.1 \pm 0.7$ | $3.70 \pm 0.21$ |
| Combination | $75.6 \pm 0.6$ | $5.15 \pm 0.14$ |

TABLE 7.7: Tagging performance obtained after recalibration during the time-dependent fit, for each tagger (inclusive categories) and for their combination.

| Bin | $p_{\rm T}$ ( GeV/$c$) | $\eta$ | Weight $f_i$ | $\Delta_{\rm prod}(B_s^0)$ |
|---|---|---|---|---|
| 1 | ( 2, 4) | (3.0,5.0) | $0.0656 \pm 0.0038$ | $-0.1475 \pm 0.0895 \pm 0.0192$ |
| 2 | ( 4, 8) | (3.5,4.5) | $0.1256 \pm 0.0051$ | $-0.0471 \pm 0.0513 \pm 0.0112$ |
| 3 | ( 4, 8) | (2.5,3.5) | $0.2120 \pm 0.0066$ | $0.0376 \pm 0.0467 \pm 0.0083$ |
| 4 | ( 8,12) | (3.5,4.5) | $0.0391 \pm 0.0028$ | $0.0582 \pm 0.0537 \pm 0.0053$ |
| 5 | ( 8,12) | (2.5,3.5) | $0.2759 \pm 0.0073$ | $0.0370 \pm 0.0332 \pm 0.0051$ |
| 6 | (12,30) | (3.5,4.5) | $0.0054 \pm 0.0011$ | $-0.0339 \pm 0.0750 \pm 0.0095$ |
| 7 | (12,30) | (2.5,3.5) | $0.1911 \pm 0.0060$ | $-0.0333 \pm 0.0309 \pm 0.0040$ |
| 8 | ( 8,30) | (2.2,2.5) | $0.0853 \pm 0.0041$ | $-0.0351 \pm 0.0485 \pm 0.0059$ |

TABLE 7.8: Fraction of $B_s^0 \to (K^+\pi^-)(K^-\pi^+)$ events and production asymmetry in bins of $B_s^0$ transverse momentum and pseudo-rapidity, for the nominal $K\pi$ mass window. The first uncertainty of the production asymmetry is statistical and the second one is systematic, as written in Ref. [122].

## 7.4 Production Asymmetry

The production rates of $b$ and $\bar{b}$ hadrons in $pp$ collisions are not expected to be identical, therefore this effect has to be considered when computing $CP$ asymmetries. The production asymmetry for $B_s^0$ mesons is defined as

$$\Delta_{\rm prod} \equiv \frac{\sigma(\overline{B}_s^0) - \sigma(B_s^0)}{\sigma(\overline{B}_s^0) + \sigma(B_s^0)}\,, \tag{7.5}$$

where $\sigma$ stands for the corresponding production cross-section. This asymmetry was measured by LHCb in $pp$ collisions at $\sqrt{s} = 7$ TeV by means of a time-dependent analysis of $B_s^0 \to D_s^-\pi^+$ decays [122]. To correct for the different kinematics of $B_s^0 \to D_s^-\pi^+$ and $B_s^0 \to (K^+\pi^-)(K^-\pi^+)$ decays, the $B_s^0$ production asymmetries reported in table 4 of Ref. [122] in bins of $B_s^0$ transverse momentum and pseudo-rapidity are reweighted according to

$$\Delta_{\rm prod} \equiv \sum_{\text{Bins i}} f_i \Delta_{\rm prod,i}, \tag{7.6}$$

where $f_i$ is the fraction of $B_s^0$ events in bin $i$ computed by summing over the sWeights obtained in Sect. 7.2.4. The $B_s^0$ production asymmetries and weights are listed in Table 7.8. Using these values, the following effective $B_s^0$ production asymmetry is obtained:

$$\Delta_{\rm prod} = -0.0047 \;\pm\; 0.0178\,(\text{stat.}) \;\pm\; 0.0066\,(\text{syst.}). \tag{7.7}$$

For comparison, this quantity is also computed in a narrow $K\pi$ mass window of 150 MeV/$c^2$ around the $K^*(892)^0$ peak. The weights in this case can be found in Table 7.9, and the corresponding production asymmetry is:

$$\Delta_{\rm prod}^{\rm narrow} = -0.0065 \;\pm\; 0.0185\,(\text{stat.}) \;\pm\; 0.0066\,(\text{syst.}). \tag{7.8}$$

The systematic uncertainty quoted in the previous results is taken directly from Ref. [122].

| Bin | $p_{\mathrm{T}}$ ( GeV/$c$) | $\eta$ | Weight $f_i$ |
|---|---|---|---|
| 1 | ( 2, 4) | (3.0,5.0) | 0.0846 $\pm$ 0.0079 |
| 2 | ( 4, 8) | (3.5,4.5) | 0.1284 $\pm$ 0.0096 |
| 3 | ( 4, 8) | (2.5,3.5) | 0.2230 $\pm$ 0.0127 |
| 4 | ( 8,12) | (3.5,4.5) | 0.0315 $\pm$ 0.0047 |
| 5 | ( 8,12) | (2.5,3.5) | 0.2792 $\pm$ 0.0139 |
| 6 | (12,30) | (3.5,4.5) | 0.0050 $\pm$ 0.0023 |
| 7 | (12,30) | (2.5,3.5) | 0.1803 $\pm$ 0.0111 |
| 8 | ( 8,30) | (2.2,2.5) | 0.0679 $\pm$ 0.0069 |

TABLE 7.9: Fraction of $B_s^0 \to (K^+\pi^-)(K^-\pi^+)$ events in bins of $B_s^0$ transverse momentum and pseudo-rapidity, for a narrow $K\pi$ mass window (150 $\mathrm{MeV}/c^2$ around the $K^*(892)^0$ peak).

## 7.5 Decay-time resolution

The resolution of the $B_s^0$ decay-time measurement significantly affects the accuracy of the determination of the $\phi_s^{d\bar{d}}$ phase, thus it has to be characterised and accounted for. The time resolution performance has been checked not to vary significantly with the trigger requirements, and it is thus only studied in two categories, corresponding to the 2011 and 2012 data taking conditions.

The combination of the phase space $B_s^0 \to K^+\pi^-K^-\pi^+$ and the vector-vector $B_s^0 \to K^{*0}\bar{K}^{*0}$ simulation samples is used to characterise the time resolution performance, by comparing the reconstructed decay time, $t_{rec}$, with the generated decay time, $t_{gen}$, of truth-matched events.

The overall effective time resolutions (just for illustration, not used in the time-dependent fit) can be obtained by fitting the $t_{rec} - t_{gen}$ distribution of the simulation samples with the following double-gaussian function:

$$R^{eff}(t) = f_{t,1} \cdot \frac{1}{\sqrt{2}\sigma_{t,1}} e^{-\left(\frac{t}{\sqrt{2}\sigma_{t,1}}\right)^2} + (1 - f_{t,1}) \cdot \frac{1}{\sqrt{2}\sigma_{t,2}} e^{-\left(\frac{t}{\sqrt{2}\sigma_{t,2}}\right)^2}. \tag{7.9}$$

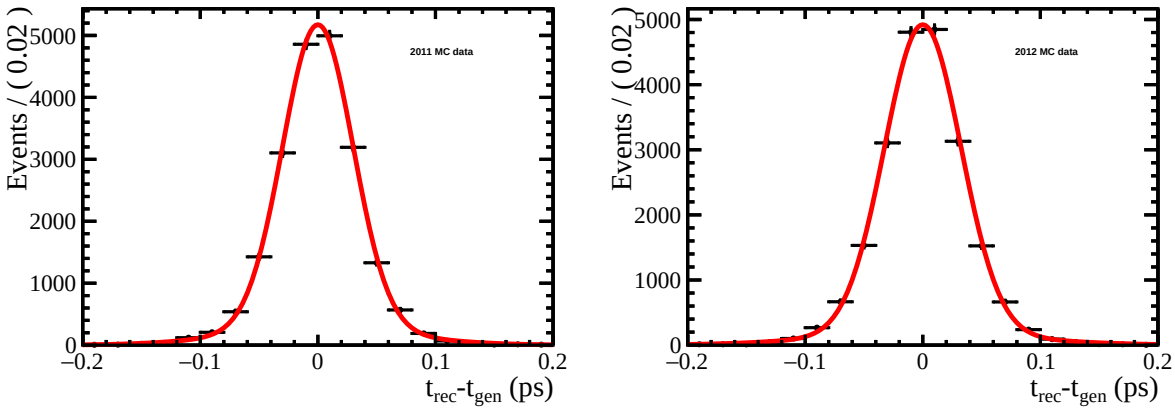



FIGURE 7.12: Plots corresponding to the fit of the double-gaussian effective resolution function to the 2011 and 2012 simulation samples.

| Parameter | 2011 sample | 2012 sample |
|---|---|---|
| $f_{t,1}$ | $8.87253e-01 \pm 1.27204e-02$ | $9.13499e-01 \pm 1.20264e-02$ |
| $\sigma_{t,1}$ [ps] | $2.99194e-02 \pm 3.56771e-04$ | $3.25476e-02 \pm 3.85014e-04$ |
| $\sigma_{t,2}$ [ps] | $7.17935e-02 \pm 2.94564e-03$ | $8.44978e-02 \pm 5.15992e-03$ |

TABLE 7.10: Parameters obtained in the fit of the double-gaussian effective resolution function to the 2011 and 2012 simulation samples.

The plots corresponding to the fits for the two year categories are shown in Fig. 7.12. The measured parameters are listed in Table 7.10. Following the method presented in Sect.9 of Ref. [123], the effective time resolutions corresponding to the double-gaussian functions can be computed to be

$$\begin{aligned} \sigma_t^{eff}(2011) &= 35.44 \pm 0.22\,\text{fs}, \\ \sigma_t^{eff}(2012) &= 37.52 \pm 1.33\,\text{fs}. \end{aligned} \tag{7.10}$$

This values are slightly below the typical decay-time resolutions in LHCb due to already-known small mis-modelling effects in simulation. Systematic uncertainties due to this simulation/data difference are evaluated in Sect. 7.9 and found to be very small.

As the time resolution is known to be non constant, specifically varying with the decay time itself, the time resolution function used in the main fitter is constructed as a function of the estimated decay-time error, $\delta_t$, computed per-event during the reconstruction process. A single gaussian model is used in this case,

$$R(t,\delta_t) = \frac{1}{\sqrt{2}\sigma_t(\delta_t)} e^{-\left(\frac{t}{\sqrt{2}\sigma_t(\delta_t)}\right)^2}, \tag{7.11}$$

where the width, $\sigma_t$, is related to $\delta_t$ through a linear calibration function,

$$\sigma_t(\delta_t) = p_0^{\sigma_t} + p_1^{\sigma_t} \cdot (\delta_t - \langle\delta_t\rangle), \tag{7.12}$$

with $\langle\delta_t\rangle$ being the mean estimated decay-time error for the dataset under consideration. This last parameter is computed to be $\langle\delta_t\rangle = 0.0283\,\text{ps}$ for the 2011 Monte Carlo sample and $\langle\delta_t\rangle = 0.0286\,\text{ps}$ for the 2012 Monte Carlo sample.

So as to obtain the calibration parameters $p_0^{\sigma_t}$ and $p_1^{\sigma_t}$, the simulation samples are divided in 20 equal-statistics bins in $\delta_t$, and a fit is performed in each of them to the $t_{rec} - t_{gen}$ distribution, using Eq. 7.11 with a constant width. The scatter-plot of $\sigma_t$ versus $\delta_t$ is fitted afterwards using the calibration function in Eq. 7.12. The plots corresponding to this last fit are shown in Fig. 7.13. The resulting calibration parameters are written in Table 7.11. These values are inserted afterwards in the main time-dependent fit via gaussian constraints (accounting for their correlations). The final calibration parameters, as retrieved by the time-dependent fit, are shown in Table 7.20.

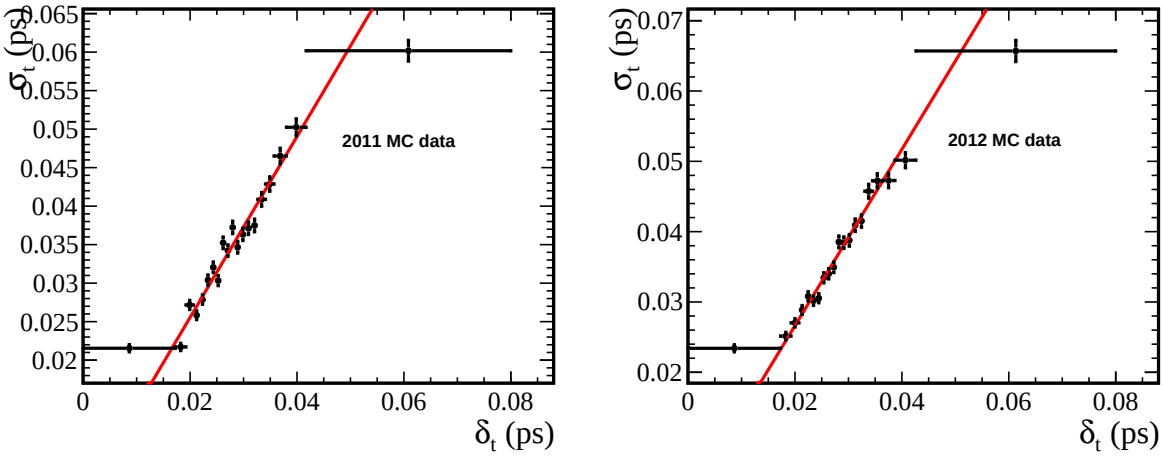



FIGURE 7.13: Fits to the $\sigma_t$ vs $\delta_t$ scatter plots using the linear calibration function in Eq. 7.12, for the 2011 and 2012 simulation samples.

| Parameter | 2011 sample | 2012 sample |
|---|---|---|
| $p_0^{\sigma_t}$ $[ps]$ | $0.0353 \pm 0.0003$ | $0.0375 \pm 0.0003$ |
| $p_1^{\sigma_t}$ | $1.1749 \pm 0.0514$ | $1.2541 \pm 0.0566$ |

TABLE 7.11: Parameters obtained in the fit to the $\sigma_t$ vs $\delta_t$ scatter plot using the linear calibration function in Eq. 7.12, for the 2011 and 2012 simulation samples. The correlation between $p_0^{\sigma_t}$ and $p_1^{\sigma_t}$ is found to be $36.9\%$ for 2011 and $41.2\%$ for 2012.

## 7.6 Acceptance effects

The LHCb detection and event reconstruction processes, together with the selection procedure, induce in data an efficiency which varies with the angles, the 2-body invariant masses and the decay time. This acceptance is evaluated using a combination of the pure phase-space $B_s^0 \to K^+\pi^-K^-\pi^+$ MC and the vector-vector $B_s^0 \to K^{*0}\bar{K}^{*0}$ MC.

The correlation between the decay-time and the rest of the variables for the acceptance is studied in Sect. 7.6.1 and found to be small. This motivates the approach followed in this analysis of factorising the acceptance as:

$$\epsilon(t,\Omega) \simeq \epsilon_t(t)\,\epsilon_\Omega(\Omega), \tag{7.13}$$

where $\epsilon_t(t)$ is a decay-time-dependent acceptance, described in Sect. 7.6.3, and $\epsilon_\Omega(\Omega)$ is a kinematic acceptance (depending on angles and invariant masses), explained in Sect. 7.6.4. This approach is checked not to induce any appreciable biases when fitting a Monte Carlo sample (see Sect. 7.8.2).

To obtain the shape of the acceptance, the combined distribution of truth-matched events is divided, via per-event weights, by a linear combination of the two generation models, that are described in Sect. 7.6.2.

In order to account for possible differences with the run period and with the L0 trigger line, the acceptance is studied separately in the four categories written in Table 7.12.

| Category | Run period | L0 trigger line |
|---|---|---|
| 1 | 2011 | L0Global TIS |
| 2 | 2011 | L0Hadron TOS & not L0Global TIS |
| 3 | 2012 | L0Global TIS |
| 4 | 2012 | L0Hadron TOS & not L0Global TIS |

TABLE 7.12: Definition of the categories used in the study of the acceptance effects.

### 7.6.1 Study of correlations between acceptance variables

In order to obtain the correlation between the different variables in the acceptance, a study is performed using the combination of the pure phase-space $B_s^0 \to K^+\pi^-K^-\pi^+$ MC and the vector-vector $B_s^0 \to K^{*0}\bar{K}^{*0}$ MC, weighted by the inverse of the combined generation model. The linear correlation matrix is evaluated by computing the Pearson product-moment correlation coefficients. It is shown in Table 7.13.

| Variable | $M(K^+\pi^-)$ | $M(K^-\pi^+)$ | $cos(\theta_1)$ | $cos(\theta_2)$ | $\varphi$ | $t$ |
|---|---|---|---|---|---|---|
| $M(K^+\pi^-)$ | 1 | 0.04 | 0.07 | 0.01 | -0.01 | 0.05 |
| $M(K^-\pi^+)$ | | 1 | -0.02 | 0.08 | 0.01 | 0.02 |
| $cos(\theta_1)$ | | | 1 | -0.04 | 0.02 | 0.04 |
| $cos(\theta_2)$ | | | | 1 | -0.05 | 0.01 |
| $\varphi$ | | | | | 1 | -0.03 |
| $t$ | | | | | | 1 |

TABLE 7.13: Linear correlation matrix for the variables in the acceptance.

As previously said, the linear correlation between the decay-time and the other variables is found to be small, specifically $\leq 5\%$. As an extra check, the time acceptance found in simulation for five equal-size bins in each of the mass and angular variables is plotted in Fig. 7.14. No significant variations are found in any of the cases.

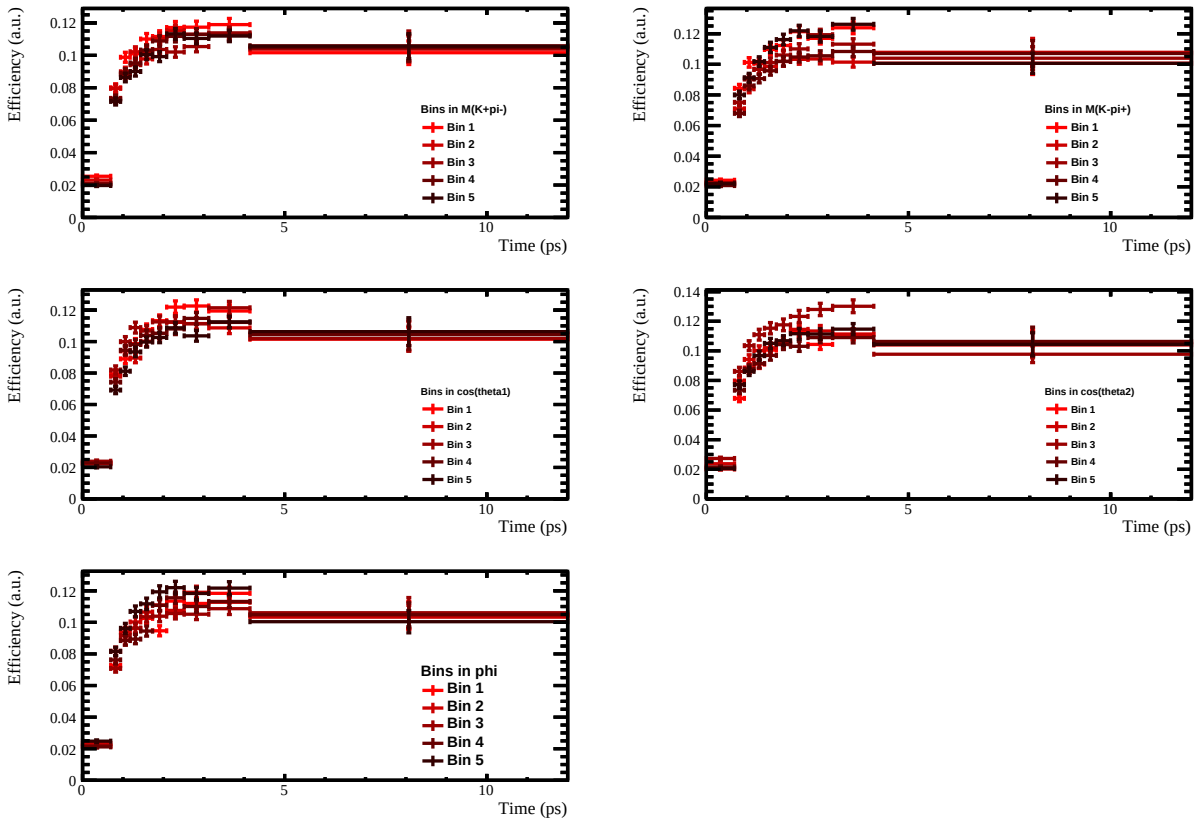



FIGURE 7.14: Time acceptance found in simulation for five equal-size bins in each of the mass and angular variables.

### 7.6.2 Models used in the generation of the MC samples

The $B_s^0 \to K^{*0}\bar{K}^{*0}$ MC model corresponds to a flavour untagged version of the expression presented in Eq. 7.3. The parameters of the amplitudes used in generation are written in Table 7.14. All CP-violating terms are set to 0.

| Parameter | Value |
|---|---|
| $f_L^{VV}$ | $1/1.36 = 0.735$ |
| $f_\parallel^{VV}$ | $0.18/1.36 = 0.132$ |
| $f_\perp^{VV}$ | $1 - f_L^{VV} - f_\parallel^{VV} = 0.133$ |
| $\delta_0^{VV}$ | $0$ |
| $\delta_\parallel^{VV}$ | $0.5$ |
| $\delta_\perp^{VV}$ | $0.5 + \pi = 3.642$ |

TABLE 7.14: Amplitude parameters of the $B_s^0 \to K^{*0}\bar{K}^{*0}$ Monte Carlo model, expressed in terms of polarisation fractions and amplitude phases.

The invariant-mass-dependent part of the $B_s^0 \to K^{*0}\bar{K}^{*0}$ model, described in Appendix D of Ref.[124], can be written as

$$PDF_{VV}^{gen} \propto \left| \frac{\sqrt{m_1 \Gamma_{K^{*0}}(m_1)}}{m_{K^{*0}}^2 - m_1^2 - i m_{K^{*0}} \Gamma_{K^{*0}}(m_1)} \right|^2 \cdot \left| \frac{\sqrt{m_2 \Gamma_{K^{*0}}(m_2)}}{m_{K^{*0}}^2 - m_2^2 - i m_{K^{*0}} \Gamma_{K^{*0}}(m_2)} \right|^2 \cdot q(m_{B_s^0}, m_1, m_{K^{*0}}) \cdot q(m_{B_s^0}, m_{K^{*0}}, m_2), \quad (7.14)$$

| Parameter | Value |
|---|---|
| $m_{B_s^0}$ | 5366.77 MeV/$c^2$ |
| $m_{K^{*0}}$ | 896 MeV/$c^2$ |
| $\Gamma_{K^{*0}}$ | 50.3 MeV |
| $m_K$ | 493.67 MeV/$c^2$ |
| $m_\pi$ | 139.57018 MeV/$c^2$ |
| $d_1$ | 3 GeV $^{-1}$ |

TABLE 7.15: Parameters in the mass-dependent terms of the $B_s^0 \to K^{*0}\bar{K}^{*0}$ and pure phase-space $B_s^0 \to K^+\pi^-K^-\pi^+$ MC generation models, as defined in Sect. 3.2.2.

where $\Gamma_{K^{*0}}(m)$ is the running width of a spin-1 relativistic Breit-Wigner, according to Eq. 3.38 and the particle momenta $q$ are constructed using the expression in Eq. 3.20.

The generation model of the pure phase-space $B_s^0 \to K^+\pi^-K^-\pi^+$ MC has a flat distribution on the three angular variables. The dependence on the invariant masses is given by:

$$PDF_{PhSp}^{gen} \propto q(m_{B_s^0}, m_1, m_2) \cdot q(m_1, m_K, m_\pi) \cdot q(m_2, m_K, m_\pi). \tag{7.15}$$

The parameters used in the previous mass-dependent expressions are written in Table 7.15.

In both generation models, the time evolution of the two $B_s^0$ mass eigenstates is taken into account. The average decay width and the decay width difference are respectively set to $\Gamma_s = 0.6614$ ps$^{-1}$ and $\Delta\Gamma_s = 0.091$ ps$^{-1}$.

The combined generation model is obtained by doing a linear combination of the two MC models, according to the number of events generated (either accepted or not) for each sample, $N_{VV}^{gen}$ and $N_{PhSp}^{gen}$, as:

$$PDF_{Comb}^{gen} = \frac{1}{N_{VV}^{gen} + N_{PhSp}^{gen}} \left( N_{VV}^{gen} \cdot PDF_{VV}^{gen} + N_{PhSp}^{gen} \cdot PDF_{PhSp}^{gen} \right). \tag{7.16}$$

### 7.6.3 Decay-time acceptance

The one-dimensional time-dependent acceptance can be easily parameterised with an analytical function. This allows for the possibility to compute analytically the time-integrals of the signal model, which are needed for normalisation purposes. Since analytical integration is much faster than the numerical approaches, the fitting time can be significantly reduced. However, the integration of the time-dependent terms in Eq. 3.5, convolved with a gaussian resolution function and multiplied by the decay-time acceptance, can be extremely time consuming if the acceptance function is not simple. To accurately model the shape of the acceptance while only using polynomial functions, a parameterisation based on splines is chosen for this analysis. The integrals are computed using the expressions presented in Ref. [125].

The specific function used for the acceptance is a linear combination of cubic B-splines, obtained using the expressions in Sect. 6.3.1 for the particular case $d = 3$. The number of knots is conveniently chosen to be 6. Their positions are assigned to the quantiles of the decay-time distribution of the combined simulation sample, corresponding to the points 0, 0.9, 1.3, 2, 3 and 12 ps. With this configuration, the acceptance can be written as:

$$\epsilon_t(t) = \sum_{i=1}^{8} c_i b_i(t), \tag{7.17}$$

where $b_i(t)$ are the B-splines and $c_i$ are free coefficients to be determined. To obtain these coefficients, a fit to the decay-time distribution of truth-matched simulated events, weighted by the inverse of the combined generation model, is done separately on each of the categories defined in Table 7.12. The fit pushes the $c_1$ and $c_2$ parameters to 0, so they are fixed to this value. The overall normalisation of the acceptance function is established by setting $c_3 = 1$. With the previous conditions, there are five remaining parameters to be determined in the fits to simulated data. The resulting parameters for the four categories can be found in Table 7.16, and the plots of the corresponding fits in Fig. 7.15.

| Coef. | Category 1 | Category 2 | Category 3 | Category 4 |
|---|---|---|---|---|
| $c_4$ | $1.205 \pm 0.137$ | $1.035 \pm 0.137$ | $1.279 \pm 0.142$ | $1.012 \pm 0.126$ |
| $c_5$ | $1.299 \pm 0.096$ | $1.342 \pm 0.109$ | $1.312 \pm 0.097$ | $1.22 \pm 0.094$ |
| $c_6$ | $1.672 \pm 0.154$ | $0.396 \pm 0.09$ | $1.57 \pm 0.15$ | $0.733 \pm 0.102$ |
| $c_7$ | $0.757 \pm 0.094$ | $2.584 \pm 0.21$ | $1.038 \pm 0.108$ | $1.382 \pm 0.12$ |
| $c_8$ | $0.93 \pm 0.08$ | $0.018 \pm 0.001$ | $1.003 \pm 0.085$ | $0.282 \pm 0.038$ |

TABLE 7.16: Coefficients of the B-splines used for the time-dependent acceptance, obtained from fits to the simulated data samples.

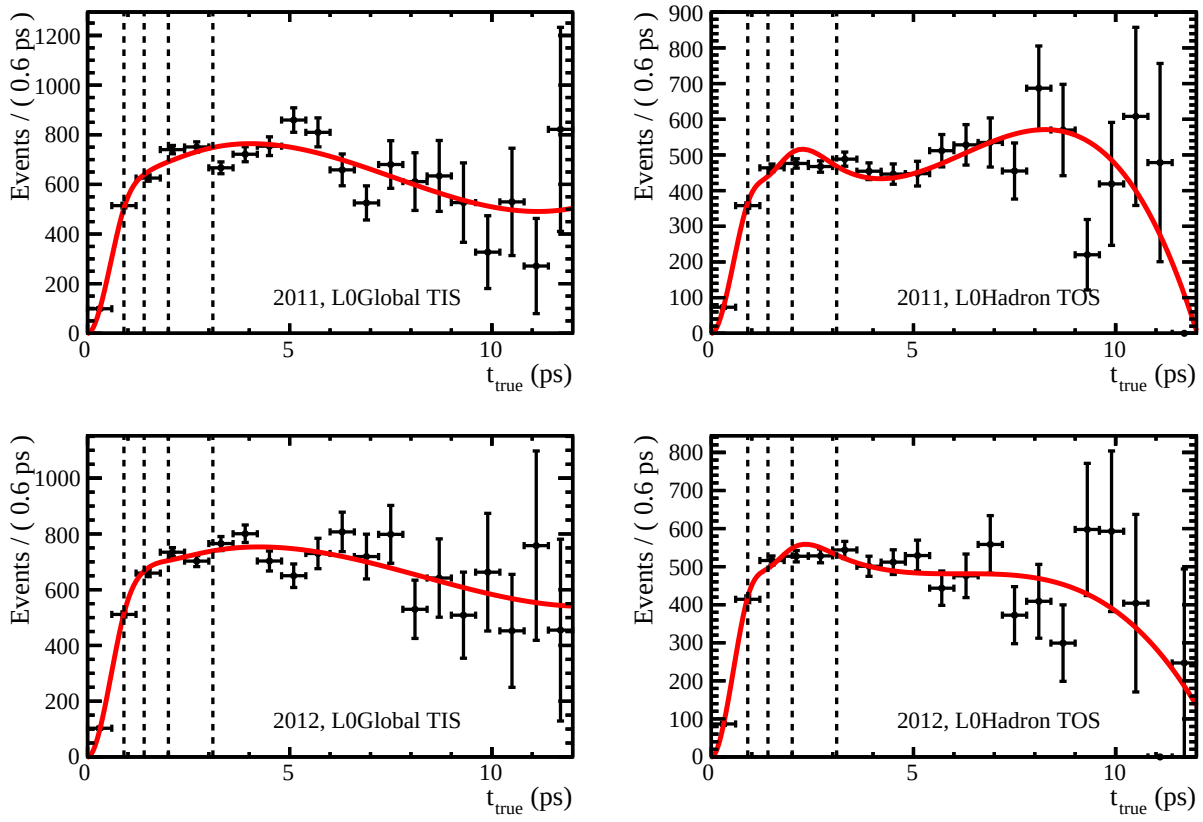



FIGURE 7.15: Spline-based function describing the time-dependent acceptance in the four considered categories, obtained from fits to the simulated data samples. The vertical dashed lines correspond to the position of the knots.

### 7.6.4 Angular and invariant mass acceptance

The method of the normalisation weights, explained in Sect. 6.4.2, is used to include the five-dimensional angular and invariant-mass acceptance in the fit. This allows to automatically

account for all the correlations among the variables. However, as this method does not provide a functional form of the acceptance, alternative approaches are used to plot the fit results and for toy MC studies, as explained in Sect. 7.6.4.2. Additionally, a machine-learning-based approach is used for a check, as explained in Sect. 7.8.4.

#### 7.6.4.1 Normalization weights

The equivalent to Eq. 6.7 for this analysis is:

$$\xi_{ij} = \int d\Omega \; F_{ij}(\Omega) \cdot \epsilon_\Omega(\Omega), \tag{7.18}$$

where the indices $i$ and $j$ run over the 19 polarisation states, $\xi_{ij}$ are the normalisation weights and $F_{ij}(\Omega)$ are functions that contain the dependence of the model components on the angles and masses. The $F_{ij}(\Omega)$ functions are defined in Eq. 7.29 and are complex valued, which implies that the normalisation weights are also complex valued. There is a total of 190 normalisation weights[1] that can be different from each other.

The normalisation weights are computed separately in each category by doing a sum over the events in the combined Monte Carlo sample:

$$\xi_{ij} \propto \sum_{ev=1}^{N_{events}} \frac{F_{ij}(\Omega_{ev})}{\mathrm{PDF}^{gen}_{Comb}(\Omega_{ev})}, \tag{7.19}$$

where $\mathrm{PDF}^{gen}_{Comb}$ is the combined generation model, described in Sect. 7.6.2. Since the $F_{ij}(\Omega)$ contain the model dependence on the $K\pi$ masses and the $c_i^{mass}$ parameters of the scalar mass-dependent amplitude are floated in the fit (see Sect. 3.2.2.1), the normalisation weights are functions of $c_i^{mass}$. This is taken into account during fitting, by computing the normalisation weights per fit iteration, as explained in Sect. 7.7.3.

#### 7.6.4.2 Acceptance for plotting and toy MC generation

An effective functional form of the kinematic acceptance can be constructed by assuming a complete factorisation on the angular and invariant-mass variables:

$$\epsilon^{fact}_\Omega(\Omega) = \epsilon^{fact}_m(m_1) \cdot \epsilon^{fact}_m(m_2) \cdot \epsilon^{fact}_{\cos\theta}(\cos\theta_1) \cdot \epsilon^{fact}_{\cos\theta}(\cos\theta_2) \cdot \epsilon^{fact}_\varphi(\varphi). \tag{7.20}$$

This parameterisation neglects the correlations among the variables, but is in general good enough to plot the model distributions and for toy Monte Carlo studies. The invariant mass acceptance, $\epsilon_m$, is parameterised using a linear function:

$$\epsilon^{fact}_m(m) = 1 + p_1 \cdot m. \tag{7.21}$$

For the acceptance in $\cos\theta$, a combination of Chebyshev polynomials up to order 5 is employed:

$$\epsilon^{fact}_{\cos\theta}(\cos\theta) = T_0(\cos\theta) + \sum_{i=1}^{5} k_i \cdot T_i(\cos\theta). \tag{7.22}$$

The Chebyshev polynomials, $T_i(x)$, are defined in Sect. 3.2.2.1. Finally, the acceptance in $\varphi$ is checked to be essentially flat.

[1] The number 190 arises when counting once the diagonal terms ($i = j$) and half the off-diagonal terms ($i \neq j$), *i.e.* $19 + 1/2(19^2 - 19) = 190$.

The parameters of the different components of the factorised acceptance are obtained by fitting the combined Monte Carlo sample, weighted by the inverse of the combined generation model, separately in the four year and trigger categories. For $\epsilon_m^{fact}$, a simultaneous fit is done of the $m_1$ and $m_2$ distributions, and $\epsilon_{\cos\theta}^{fact}$ is similarly obtained through a simultaneous fit of the $\cos\theta_1$ and $\cos\theta_2$ distributions. The resulting parameters can be found in Table 7.17 and the plots of the fits to simulated data are shown in Fig. 7.16 and Fig. 7.17.

| Parameter | Category 1 | Category 2 | Category 3 | Category 4 |
|---|---|---|---|---|
| $p_1$ | $-0.000156$ | $-9.38e-05$ | $-0.000345$ | $-0.000296$ |
| $k_1$ | $-0.471$ | $-0.457$ | $-0.487$ | $-0.457$ |
| $k_2$ | $-0.506$ | $-0.306$ | $-0.476$ | $-0.257$ |
| $k_3$ | $0.0284$ | $-0.063$ | $0.0388$ | $-0.0414$ |
| $k_4$ | $-0.00788$ | $-0.0856$ | $-0.0348$ | $-0.0801$ |
| $k_5$ | $0.0254$ | $0.0219$ | $0.00502$ | $0.000155$ |

TABLE 7.17: Parameters of the factorised acceptance, obtained from fits to simulated data, for each of the categories defined in Table 7.12.

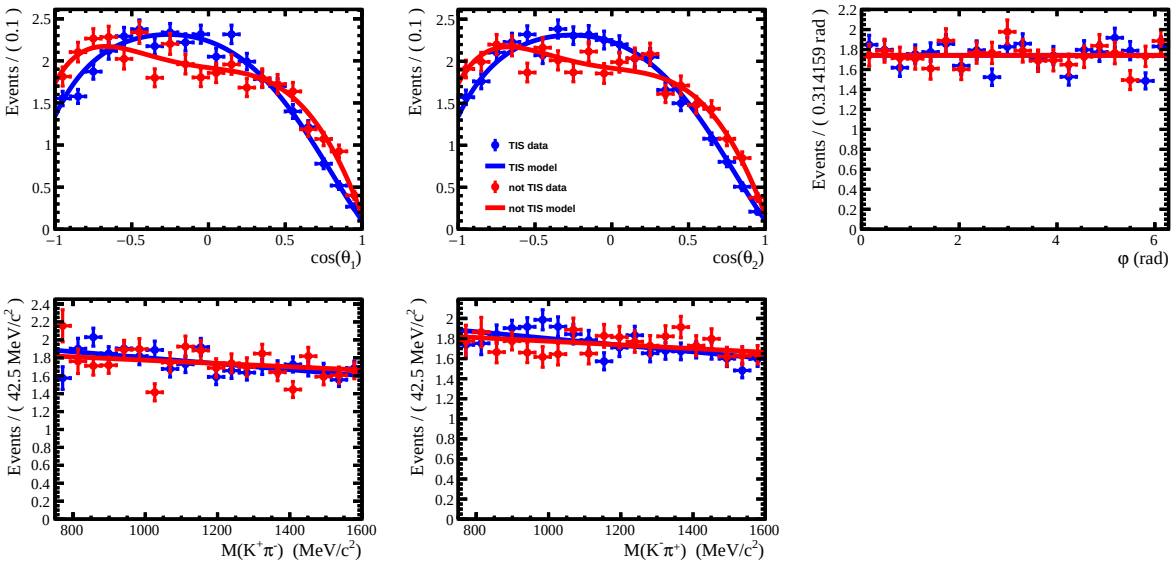



FIGURE 7.16: Fits to the acceptance distributions obtained from simulation, for the 2011 sample.

The factorised acceptance is found to be sufficiently good when plotting the model in phase-space regions that are not very large, so that correlations don't play a significant role. This acceptance is for example used in Sect. 7.8.2 and Sect. 7.8.3, where the model phase-space is restricted to a $K\pi$ mass window of $\pm 150$ MeV$/c^2$ around the $K^{*0}$ peak. However, it has been observed in this analysis that, when doing the plots in the nominal window, the correlations induce small deviations in the fitted model projections with respect to the data distributions. In order to get a more accurate visualisation of the nominal fit results, an alternative method is employed in this case. The combined Monte Carlo sample is weighted by the inverse of the combined generation model times the physical model resulting from the fit. This provides the equivalent of a Monte Carlo sample generated with the actual matrix element of the $B_s^0 \to (K^+\pi^-)(K^-\pi^+)$ decay. The projections of the fit model in each of the analysis variables, that can be seen in Fig. 7.18, correspond to one-dimensional histograms of the re-weighted Monte Carlo sample. To plot a wave component separately, the amplitudes of the other waves are set to 0

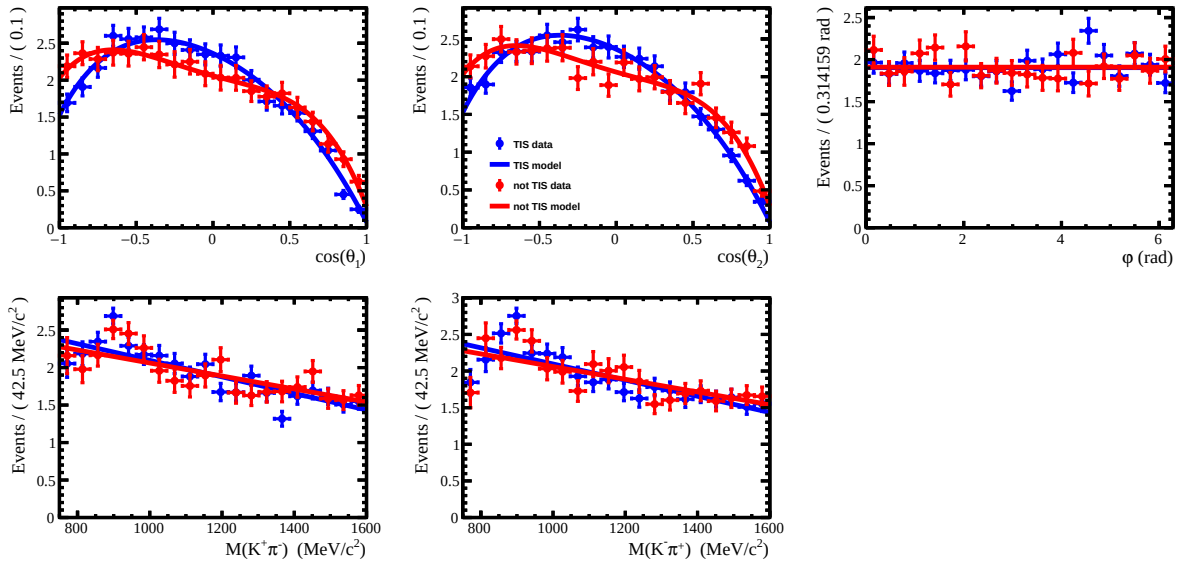



FIGURE 7.17: Fits to the acceptance distributions obtained from simulation, for the 2012 sample.

in the physical PDF used to do the re-weight. This method proves to properly account for the correlations and to remove any visible deviations with respect to the data distributions.

## 7.7 Flavour-tagged time-dependent amplitude fit

This section depicts the final model used for fitting, explains the technical implementation of the fit and presents the obtained results with the corresponding statistical uncertainties.

### 7.7.1 Model used for fitting

The multi-dimensional spectrum of data with flavour tagging, $S_{FT}(t, \Omega, q^{OS}, q^{SSK})$, is introduced in Eq. 7.3. After convolving this expression with the time-resolution function introduced in Eq. 7.11, $R(t, \delta_t)$, multiplying it by acceptance functions $\epsilon_\Omega(\Omega)$ and $\epsilon_t(t)$, and normalising it properly, it becomes a PDF which is conditional on $\delta_t$, $\eta^{OS}$ and $\eta^{SSK}$. Being $\mathcal{P}_{\delta_t}(\delta_t)$, $\mathcal{P}_{\eta^{OS}}(\eta^{OS})$ and $\mathcal{P}_{\eta^{SSK}}(\eta^{SSK})$ marginal PDFs, the full PDF describing the data sample under study can be written as:

$$\begin{aligned}\mathrm{PDF}_{\mathrm{full}}(t, \Omega, q^{OS}, q^{SSK}, \delta_t, \eta^{OS}, \eta^{SSK}) = \\ \mathrm{PDF}_{\mathrm{cond}}(t, \Omega, q^{OS}, q^{SSK}|\delta_t, \eta^{OS}, \eta^{SSK}) \cdot \mathcal{P}_{\delta_t}(\delta_t) \cdot \mathcal{P}_{\eta^{OS}}(\eta^{OS}) \cdot \mathcal{P}_{\eta^{SSK}}(\eta^{SSK}),\end{aligned} \tag{7.23}$$

where

$$\begin{aligned}&\mathrm{PDF}_{\mathrm{cond}}(t, \Omega, q^{OS}, q^{SSK}|\delta_t, \eta^{OS}, \eta^{SSK}) = \\ &\frac{R(t, \delta_t) \otimes \Big[S_{FT}(t, \Omega, q^{OS}, q^{SSK})\Big] \cdot \epsilon_\Omega(\Omega) \cdot \epsilon_t(t)}{\sum\limits_{q'^{OS}} \sum\limits_{q'^{SSK}} \int dt' \int d\Omega' \; R(t', \delta_t) \otimes \Big[S_{FT}(t', \Omega', q'^{OS}, q'^{SSK})\Big] \cdot \epsilon_\Omega(\Omega') \cdot \epsilon_t(t')}.\end{aligned} \tag{7.24}$$

The marginal PDFs factor out when fitting and can thus be omitted for this purpose. Also, the acceptance factors in the numerator of Eq. 7.24 are not needed either, as explained in Sect. 6.4.2. After removing the unnecessary elements, introducing the normalisation weights, $\xi_{ij}$, and doing some convenient term reordering, the PDF used for fitting takes the following final form:

$$\mathrm{PDF}_{\mathrm{fit}}(t, \Omega) = \frac{\sum_{\alpha=1}^{19} \sum_{\beta \leq \alpha} \Re e \left[K_{\alpha\beta}(t)\, F_{\alpha\beta}(\Omega)\right]}{\sum_{\alpha'=1}^{19} \sum_{\beta' \leq \alpha'} \Re e \left[\left(\int dt'\, K^{\mathrm{untag}}_{\alpha'\beta'}(t')\, \epsilon_t(t')\right) \xi_{\alpha'\beta'}\right]}, \tag{7.25}$$

where some of the dependences on the variables are implicit for notation simplicity, the subscript $\alpha$ ($\beta$) represents the state labels $\{j_1, j_2, h\}$ ($\{j_1', j_2', h'\}$), $K_{\alpha\beta}(t)$ contains the decay-time dependence and $F_{\alpha\beta}(\Omega)$ contains the angular and mass dependence. Both the numerator and the denominator of the PDF are constructed as a sum over 190 real terms, which arise when squaring the amplitudes decomposed in the combination of the nineteen contributing polarisation states.

The decay-time-dependent factors are constructed as

$$\begin{aligned}K_{\alpha\beta}(t) = R(t, \delta_t) \otimes \Bigg\{ e^{-\Gamma_s t} \Bigg[ \zeta_+ \left( a_{\alpha\beta} \cosh\left(\frac{1}{2}\Delta\Gamma_s t\right) + b_{\alpha\beta} \sinh\left(\frac{1}{2}\Delta\Gamma_s t\right)\right) \\ + \zeta_- \left( c_{\alpha\beta} \cos\left(\Delta m_s t\right) + d_{\alpha\beta} \sin\left(\Delta m_s t\right)\right)\Bigg]\Bigg\},\end{aligned} \tag{7.26}$$

where the $\zeta_\pm$ factors contain the flavour-tagging and production-asymmetry information (see Sect. 7.3 and Sect. 7.4) and are given by:

$$\zeta_\pm = \frac{(1 + \Delta_{\mathrm{prod}})}{2} P^{OS}(q^{OS})\, P^{SSK}(q^{SSK}) \;\pm\; \frac{(1 - \Delta_{\mathrm{prod}})}{2} \bar{P}^{OS}(q^{OS})\, \bar{P}^{SSK}(q^{SSK}). \tag{7.27}$$

The complex quantities $a_{\alpha\beta}$, $b_{\alpha\beta}$, $c_{\alpha\beta}$ and $d_{\alpha\beta}$ are defined in terms of the $CP$-averaged amplitudes, the $CP$-violating parameters and the $\eta_h^{j_1 j_2}$ factors, as

$$\begin{aligned}
a_{\alpha\beta} &= \frac{2}{1+|\lambda|^2}\left(A_\alpha A_\beta^* + \eta_\alpha\eta_\beta|\lambda|^2 A_{\bar\alpha}A_{\bar\beta}^*\right),\\
b_{\alpha\beta} &= \frac{-2|\lambda|}{1+|\lambda|^2}\left(\eta_\beta e^{i\phi_s^{d\bar d}} A_\alpha A_{\bar\beta}^* + \eta_\alpha e^{-i\phi_s^{d\bar d}} A_{\bar\alpha}A_\beta^*\right),\\
c_{\alpha\beta} &= \frac{2}{1+|\lambda|^2}\left(A_\alpha A_\beta^* - \eta_\alpha\eta_\beta|\lambda|^2 A_{\bar\alpha}A_{\bar\beta}^*\right),\\
d_{\alpha\beta} &= \frac{-2|\lambda| i}{1+|\lambda|^2}\left(\eta_\beta e^{i\phi_s^{d\bar d}} A_\alpha A_{\bar\beta}^* - \eta_\alpha e^{-i\phi_s^{d\bar d}} A_{\bar\alpha}A_\beta^*\right),
\end{aligned} \tag{7.28}$$

where the bars on the amplitude indices $\alpha$ and $\beta$ denote the $CP$ transformation of the considered final state, *i.e.* the change of quantum numbers $j_1 j_2 \to j_2 j_1$. The functions $K_{\alpha\beta}^{\rm untag}$ are obtained by summing $K_{\alpha\beta}$ over the tagging decisions and have the same expression as Eq. 7.26 but substituting $\zeta_+ \to 2$ and $\zeta_- \to 2\Delta_{\rm prod}$. The convolution with the decay-time resolution function and the integration on the decay-time that appears in the denominator of Eq. 7.25 are performed analytically, using the formalism in Ref. [125].

The angular and mass-dependent terms are constructed as

$$\begin{aligned}
F_{\alpha\beta}(\Omega) = {} & (2-\delta_{\alpha\beta})\,\Theta_h^{j_1 j_2}(\cos\theta_1,\cos\theta_2,\varphi)\,[\Theta_{h'}^{j_1' j_2'}(\cos\theta_1,\cos\theta_2,\varphi)]^*\\
& \times \Phi_4(m_1,m_2)\,\mathcal{M}_{j_1}(m_1)\,\mathcal{M}_{j_2}(m_2)\,\mathcal{M}_{j_1'}^*(m_1)\,\mathcal{M}_{j_2'}^*(m_2)\\
& \times \mathcal{F}_h^{j_1 j_2}(m_1,m_2)\,\mathcal{F}_{h'}^{j_1' j_2'}(m_1,m_2)\,\mathcal{N}_h^{j_1 j_2}\,\mathcal{N}_{h'}^{j_1' j_2'*},
\end{aligned} \tag{7.29}$$

where $\delta_{\alpha\beta}$ is the Kronecker delta and the other terms are defined in Sect. 3.2.

### 7.7.2 Setup of the fit

To avoid problems of the fitting procedure when the amplitudes are too small for a good determination of the phases, the 19 CP-averaged amplitudes described in Sect. 3.2 are written in Cartesian coordinates, i.e. as $\Re e(A_h^{j_1 j_2})$ and $\Im m(A_h^{j_1 j_2})$. The normalisation of the whole PDF and the insensitivity under a global phase transformation imply a reduction of 2 in the number of measurable parameters. To account for this reduction, the following conventions are imposed:

$$\Re e(A_0^{11}) = 1, \qquad \Im m(A_0^{11}) = 0. \tag{7.30}$$

However, for the nominal set of results, these amplitudes are transformed afterwards into wave fractions, $f_w$, polarisation fractions, $f_h^w$, and strong phases, $\delta_h^w$, given by:

$$f_w = \frac{\sum_h(\Re e^2(A_h^w) + \Im m^2(A_h^w))}{\sum_{w',h'}(\Re e^2(A_{h'}^{w'}) + \Im m^2(A_{h'}^{w'}))}, \tag{7.31}$$

$$f_h^w = \frac{\Re e^2(A_h^w) + \Im m^2(A_h^w)}{\sum_{h'}(\Re e^2(A_{h'}^w) + \Im m^2(A_{h'}^w))}, \tag{7.32}$$

$$\delta_h^w = atan\left(\frac{\Im m(A_h^w)}{\Re e(A_h^w)}\right), \tag{7.33}$$

with $w(w')$ running over the 9 decays under study (identified by $j_1 j_2$) and $h(h')$ running over the available helicities for each channel. With these definitions, it follows that

$$\sum_w f_w = 1, \qquad \sum_h f_h^w = 1, \ \forall\, w. \tag{7.34}$$

The set of measured decay parameters is then comprised of $19 - 1 = 18$ CP averaged fractions, $19 - 1 = 18$ strong phases, the CP-violating weak phase $\phi_s^{d\bar{d}}$ and a parameter that quantifies the amount of direct CP violation. This last parameter was originally taken to be the direct CP asymmetry, $\Delta_{CP}^{dir}$, and this motivates its use in some sections of this chapter. However, it was later decided to express the nominal results in terms of the $|\lambda|$ parameter, since it is more commonly used in the literature. The relation between $\Delta_{CP}^{dir}$ and $|\lambda|$ is written in Eq. 3.10.

The coefficients of the form factor describing the modulus of the scalar $K\pi$ mass amplitude (see Sect. 3.2.2.1), are floated in the fit. The rest of the parameters in the $K\pi$ mass amplitudes are fixed, and so is the production asymmetry to the value obtained in Sect. 7.4. The flavour-tagging and time-resolution calibration parameters are gaussian constrained to the values appearing in Sect. 7.3 and Sect. 7.5, respectively. Finally, the parameters $\Delta m_s$, $\Gamma_s$ and $\Delta\Gamma_s$ are gaussian constrained to the values written in Sect. 3.1. When applying the gaussian constraints, the correlation between the following pairs of parameters is taken into account: $p_0 - \langle\eta\rangle$ and $p_1$ (for OS and SSK), $p_0^{\sigma_t}$ and $p_1^{\sigma_t}$ (for 2011 and 2012), and $\Gamma_s$ and $\Delta\Gamma_s$.

Using the PDF in Eq. 7.25, an unbinned maximum likelihood fit, simultaneous in year and L0 trigger categories, is performed to the sWeighted data sample. To correct the statistical uncertainties resulting from the fit, the sWeights for each category, $\omega_{ev}^{cat}$, are renormalised as:

$$\omega_{ev}^{cat} \to \omega_{ev}^{cat} \cdot \frac{\sum_{ev'} \omega_{ev'}^{cat}}{\sum_{ev''} (\omega_{ev''}^{cat})^2}. \tag{7.35}$$

Given the complexity of the fit (which requires a huge number of computational operations), in addition to the need of floating the scalar $K\pi$ mass amplitude parameters, that forces to recompute some $K\pi$ mass integrals[2] and the normalisation weights per minimisation step, a framework has been set up to do the fit on Graphical Process Units (GPUs). To work with these machines, the very recently developed `Ipanema` [28] software package is used, expanded with some extra features needed for this analysis. Below, the fit procedure is explained from a technical viewpoint.

### 7.7.3 Implementation of the fit using GPUs

The fit is done using the `Minuit` tool of the python-based package `iMinuit` [126, 127]. Consequently, the external interface of the framework (parameter and dataset handling, management of categories ...) is coded in python. When a parallelisation of the work is needed, the required information is passed to the GPU, the computations are done on it, and the results are brought back to the python interface. The operations in the GPU are performed by classes that are coded in CUDA C language. The PDF in Eq. 7.25 is implemented as one of these classes.

For each iteration of the fit, the following computational chain is performed:

1. The parameters of the scalar $K\pi$ mass amplitude are read from `Minuit` and the mass integrals in Eq. 3.22 are computed using the GPU. To do the computation of each integral, the 2-D $K\pi$ mass plane is divided into $500 \times 500$ equal-sized rectangular bins. Each of the bins is assigned to a GPU core, which computes the product of the corresponding mass function, averaged on the four corners of the bin, times the area of the bin (differential

[2]The mass integrals to be computed are those in Eq. 3.22. Since the evolution of the scalar $K\pi$ mass amplitude phase is fixed and only the modulus is varied, there is no need to also recompute the phases in Eq. 3.23

element). The process is done in parallel and, once finished, the integral is computed by summing over the results of all the bins.

2. Using the $c_i^{mass}$ parameters and the previously obtained mass integrals, the normalisation weights are computed using the GPU. In this occasion, the parallelisation is done over the events of the simulated samples. For each normalisation weight in each category, after the parallel process is finished, the weight is computed by summing up the resulting values.

3. After all the $K\pi$ mass related quantities have been obtained, the rest of the fit parameters are read from `Minuit`, and the negative logarithmic likelihood (NLL) is computed. To do so, the contribution from the 4 categories needs to be summed up. The NLL for each category is computed in parallel for all the events in the category. Finally, the contributions from the gaussian constraints are added to the overall NLL.

Using this scheme, the fit takes several hours to converge. If the parameters of the scalar $K\pi$ mass amplitude are fixed, which avoids the need of recomputing the mass integrals and the normalisation weights after the first iteration of the fit, the computing time significantly decreases to around 5 min in total. For this reason, even if the nominal fit and most of the variants in this analysis are done using the full framework, for the computation of some systematics (those that require a large number of fits) some simplified approaches are followed in order to use the reduced version. It should be noted that, without the use of the GPU, even the reduced fit would be very difficult to handle (fitting time from many hours to several days), and the full one would become nearly impossible.

As a final remark, the rotation from the Cartesian amplitude basis into the polar basis is done using the parameter covariance matrix obtained from the fit and the tools for error propagation provided by the `uncertainties` [128] python package.

### 7.7.4 Fit results

The parameters measured in the nominal fit are listed in Table 7.18, and the plots for the one-dimensional projections of the fitted model together with the sWeighted data distributions are shown in Fig. 7.18. The set of amplitudes expressed in polar coordinates (fractions and phases) is written in Table 7.19. Finally, Table 7.20 collects the list of the scalar $K\pi$ mass amplitude parameters and the flavour-tagging and time-resolution calibration parameters.

The values measured for the CP-violating parameters, $\phi_s^{d\bar{d}} = -0.10 \pm 0.13\,\text{rad}$ and $|\lambda| = 1.035 \pm 0.034$, are consistent with no CP violation and with the SM predictions. In the region of phase space considered, the $B_s^0 \to K^{*0}\overline{K}^{*0}$ component has a relatively small fraction, of $f^{VV} = 0.067 \pm 0.004$, mainly due to the large scalar $K\pi$ contributions. Indeed, a relatively large contribution from the scalar-scalar double $\mathrm{S-wave}$ fraction is determined to be $f^{SS} = 0.225 \pm 0.010$. The tensor-tensor double $\mathrm{D-wave}$ fraction is measured to be $f^{TT} = 0.011 \pm 0.003$. The cross-term contributions from the scalar with the vector combination (single $\mathrm{S-wave}$) and the vector with the tensor combination (single $\mathrm{D-wave}$) are also found to be large, $f^{SV} = 0.329 \pm 0.015$, $f^{VS} = 0.133 \pm 0.013$, $f^{VT} = 0.160 \pm 0.016$ and $f^{TV} = 0.036 \pm 0.014$, while a small contribution from the scalar with the tensor combination is found, $f^{TS} = 0.025 \pm 0.007$ and $f^{ST} = 0.014 \pm 0.006$. The appreciable difference between the SV/VS and VT/TV fractions points to an asymmetry between the two $s$ quarks in the final state of the decay, the spectator quark and the one coming from the $b$ transition. The values of the longitudinal polarisation fractions of the vector-vector and tensor-tensor components are found to be small, $f_{\mathrm{L}}^{VV} = 0.208 \pm 0.032$ and $f_{\mathrm{L}}^{TT} = 0.25 \pm 0.14$, while the longitudinal polarisation fractions of the vector with the tensor components are measured to be large, $f_{\mathrm{L}}^{VT} = 0.911 \pm 0.020$ and $f_{\mathrm{L}}^{TV} = 0.62 \pm 0.16$.

In Sect. 7.9, systematic uncertainties are computed for the measured parameters. The final set of results, including all the uncertainties, is written in Table 7.77.

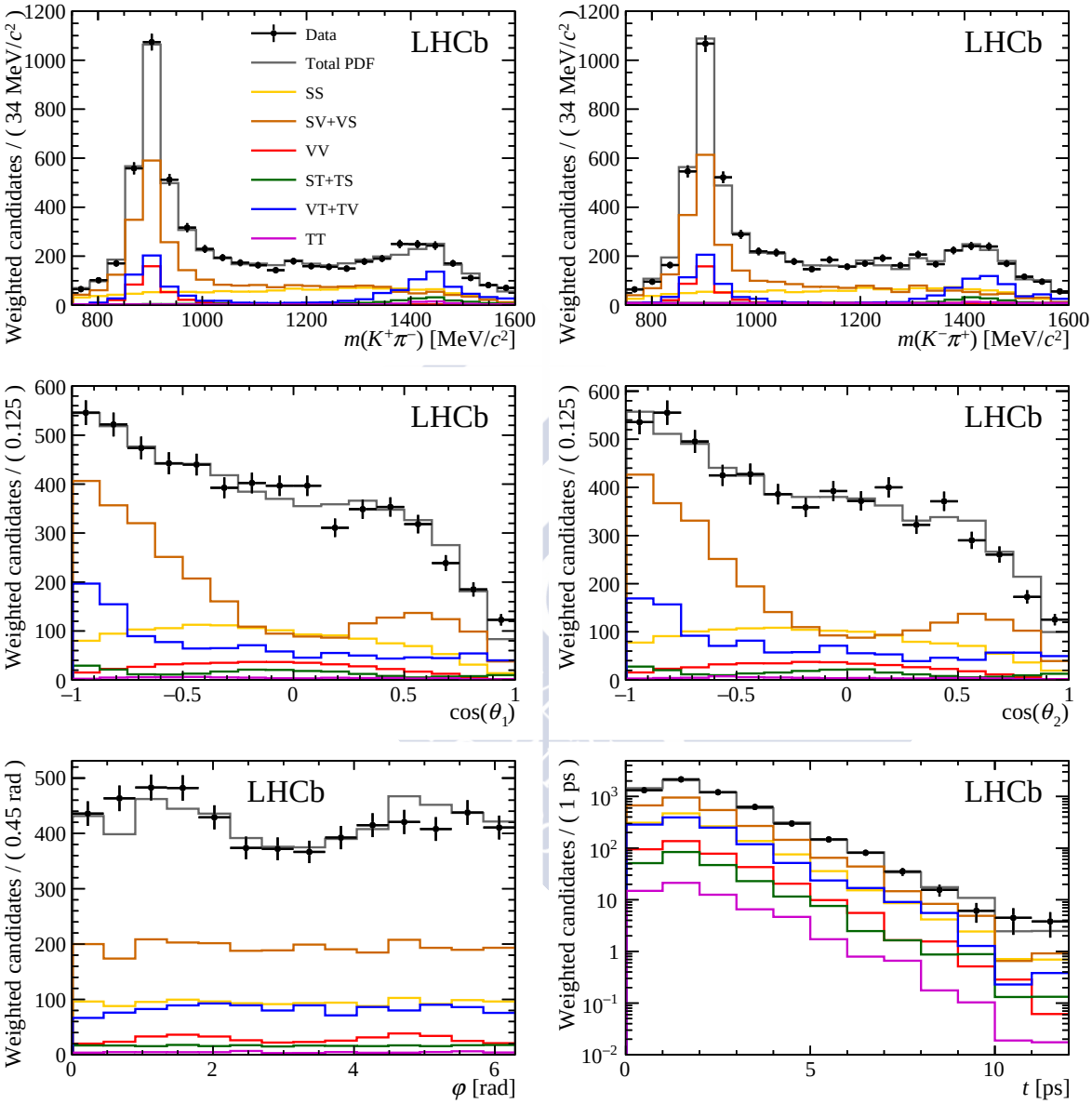



FIGURE 7.18: One-dimensional projections of the decay-time-dependent flavour-tagged fit to (black points) the sWeighted data for (top row) the two $K\pi$ invariant masses, (middle row) the two $\cos\theta$ variables, (bottom left) the $\varphi$ angle and (bottom right) the decay time. The solid gray line represents the total model and the other coloured lines show contributions from specific channels, as indicated in the legend.

| Parameter | Value |
|---|---|
| Common parameters | |
| $\phi_s$ | $-0.10 \pm 0.13$ |
| $\lvert\lambda\rvert$ | $1.035 \pm 0.034$ |
| $\Delta m_{B_s^0}$ | $17.756 \pm 0.021$ |
| $\Gamma_{B_s^0}$ | $0.6618 \pm 0.0018$ |
| $\Delta\Gamma_{B_s^0}$ | $0.089 \pm 0.005$ |
| $B_s^0 \to K^*(892)^0 \bar{K}^*(892)^0$ (VV) | |
| $Re(A_{\parallel}^{VV})$ | $-0.88 \pm 0.11$ |
| $Im(A_{\parallel}^{VV})$ | $0.80 \pm 0.14$ |
| $Re(A_{\perp}^{VV})$ | $-1.34 \pm 0.21$ |
| $Im(A_{\perp}^{VV})$ | $0.8 \pm 0.4$ |
| Single $S-wave$ (SV and VS) | |
| $Re(A^{SV})$ | $1.3 \pm 0.5$ |
| $Im(A^{SV})$ | $-4.7 \pm 0.5$ |
| $Re(A^{VS})$ | $-0.89 \pm 0.34$ |
| $Im(A^{VS})$ | $2.97 \pm 0.33$ |
| Double $S-wave$ (SS) | |
| $Re(A^{SS})$ | $2.0 \pm 0.4$ |
| $Im(A^{SS})$ | $3.53 \pm 0.34$ |
| $Scalar-Tensor$ decays (ST and TS) | |
| $Re(A^{ST})$ | $-0.68 \pm 0.24$ |
| $Im(A^{ST})$ | $-0.73 \pm 0.35$ |
| $Re(A^{TS})$ | $1.35 \pm 0.21$ |
| $Im(A^{TS})$ | $-0.13 \pm 0.35$ |

| Parameter | Value |
|---|---|
| Single $D-wave$ (VT and TV) | |
| $Re(A_L^{VT})$ | $-1.5 \pm 0.5$ |
| $Im(A_L^{VT})$ | $-2.9 \pm 0.5$ |
| $Re(A_{\parallel}^{VT})$ | $-0.09 \pm 0.15$ |
| $Im(A_{\parallel}^{VT})$ | $-0.36 \pm 0.13$ |
| $Re(A_{\perp}^{VT})$ | $-0.94 \pm 0.14$ |
| $Im(A_{\perp}^{VT})$ | $-0.06 \pm 0.27$ |
| $Re(A_L^{TV})$ | $-0.4 \pm 0.4$ |
| $Im(A_L^{TV})$ | $1.21 \pm 0.35$ |
| $Re(A_{\parallel}^{TV})$ | $0.36 \pm 0.16$ |
| $Im(A_{\parallel}^{TV})$ | $0.70 \pm 0.12$ |
| $Re(A_{\perp}^{TV})$ | $0.60 \pm 0.12$ |
| $Im(A_{\perp}^{TV})$ | $0.10 \pm 0.25$ |
| Double $D-wave$ (TT) | |
| $Re(A_L^{TT})$ | $0.11 \pm 0.19$ |
| $Im(A_L^{TT})$ | $0.43 \pm 0.15$ |
| $Re(A_{\parallel_1}^{TT})$ | $-0.36 \pm 0.12$ |
| $Im(A_{\parallel_1}^{TT})$ | $0.05 \pm 0.11$ |
| $Re(A_{\perp_1}^{TT})$ | $-0.40 \pm 0.19$ |
| $Im(A_{\perp_1}^{TT})$ | $0.27 \pm 0.18$ |
| $Re(A_{\parallel_2}^{TT})$ | $-0.08 \pm 0.13$ |
| $Im(A_{\parallel_2}^{TT})$ | $0.08 \pm 0.07$ |
| $Re(A_{\perp_2}^{TT})$ | $0.34 \pm 0.22$ |
| $Im(A_{\perp_2}^{TT})$ | $0.30 \pm 0.21$ |

TABLE 7.18: Results of the nominal fit to data. Amplitudes expressed in the Cartesian basis.

| Parameter | Value |
|---|---|
| Common parameters | |
| $\phi_s$ | $-0.10 \pm 0.13$ |
| $\lvert\lambda\rvert$ | $1.035 \pm 0.034$ |
| $\Delta m_{B_s^0}$ | $17.756 \pm 0.021$ |
| $\Gamma_{B_s^0}$ | $0.6618 \pm 0.0018$ |
| $\Delta\Gamma_{B_s^0}$ | $0.089 \pm 0.005$ |
| $B_s^0 \to K^*(892)^0 \bar{K}^*(892)^0$ (VV) | |
| $f_{VV}$ | $0.067 \pm 0.004$ |
| $f_L^{VV}$ | $0.208 \pm 0.032$ |
| $f_\parallel^{VV}$ | $0.297 \pm 0.029$ |
| $\delta_\parallel^{VV}$ | $2.40 \pm 0.11$ |
| $\delta_\perp^{VV}$ | $2.62 \pm 0.26$ |
| Single $S-wave$ (SV and VS) | |
| $f_{SV}$ | $0.329 \pm 0.014$ |
| $f_{VS}$ | $0.133 \pm 0.013$ |
| $\delta^{SV}$ | $-1.31 \pm 0.10$ |
| $\delta^{VS}$ | $1.86 \pm 0.11$ |
| Double $S-wave$ (SS) | |
| $f_{SS}$ | $0.225 \pm 0.009$ |
| $\delta^{SS}$ | $1.06 \pm 0.10$ |
| $Scalar-Tensor$ decays (ST and TS) | |
| $f_{ST}$ | $0.014 \pm 0.006$ |
| $f_{TS}$ | $0.025 \pm 0.007$ |
| $\delta^{ST}$ | $-2.3 \pm 0.4$ |
| $\delta^{TS}$ | $-0.10 \pm 0.25$ |

| Parameter | Value |
|---|---|
| Single $D-wave$ (VT and TV) | |
| $f_{VT}$ | $0.160 \pm 0.015$ |
| $f_L^{VT}$ | $0.911 \pm 0.020$ |
| $f_\parallel^{VT}$ | $0.012 \pm 0.008$ |
| $f_{TV}$ | $0.036 \pm 0.013$ |
| $f_L^{TV}$ | $0.62 \pm 0.15$ |
| $f_\parallel^{TV}$ | $0.24 \pm 0.10$ |
| $\delta_0^{VT}$ | $-2.06 \pm 0.19$ |
| $\delta_\parallel^{VT}$ | $-1.8 \pm 0.4$ |
| $\delta_\perp^{VT}$ | $-3.08 \pm 0.29$ |
| $\delta_0^{TV}$ | $1.91 \pm 0.29$ |
| $\delta_\parallel^{TV}$ | $1.09 \pm 0.19$ |
| $\delta_\perp^{TV}$ | $0.2 \pm 0.4$ |
| Double $D-wave$ (TT) | |
| $f_{TT}$ | $0.0108 \pm 0.0028$ |
| $f_L^{TT}$ | $0.25 \pm 0.14$ |
| $f_{\parallel 1}^{TT}$ | $0.17 \pm 0.11$ |
| $f_{\perp 1}^{TT}$ | $0.30 \pm 0.18$ |
| $f_{\parallel 2}^{TT}$ | $0.015 \pm 0.032$ |
| $\delta_0^{TT}$ | $1.3 \pm 0.4$ |
| $\delta_{\parallel 1}^{TT}$ | $3.00 \pm 0.29$ |
| $\delta_{\perp 1}^{TT}$ | $2.6 \pm 0.4$ |
| $\delta_{\parallel 2}^{TT}$ | $2.3 \pm 0.8$ |
| $\delta_{\perp 2}^{TT}$ | $0.7 \pm 0.6$ |

TABLE 7.19: Results of the nominal fit to data. Amplitudes expressed in the polar basis.

| Parameter | Value |
|---|---|
| Scalar $K\pi$ mass amplitude | |
| $c_1^{mass}$ | $-0.302 \pm 0.023$ |
| $c_2^{mass}$ | $-0.189 \pm 0.022$ |
| $c_3^{mass}$ | $-0.123 \pm 0.019$ |
| $c_4^{mass}$ | $-0.057 \pm 0.019$ |
| SSK tagger | |
| $p_0^{SSK} - <\eta^{SSK}>$ | $0.007 \pm 0.005$ |
| $1/2\Delta p_0^{SSK}$ | $-0.0081 \pm 0.0014$ |
| $p_1^{SSK}$ | $0.91 \pm 0.08$ |
| $1/2\Delta p_1^{SSK}$ | $-0.014 \pm 0.023$ |
| OS tagger | |
| $p_0^{OS} - <\eta^{OS}>$ | $0.007 \pm 0.004$ |
| $1/2\Delta p_0^{OS}$ | $0.0070 \pm 0.0006$ |
| $p_1^{OS}$ | $0.984 \pm 0.035$ |
| $1/2\Delta p_1^{OS}$ | $0.033 \pm 0.006$ |
| Time resolution | |
| $p_0^{\sigma_t}(2011)$ | $0.03531 \pm 0.00026$ |
| $p_1^{\sigma_t}(2011)$ | $1.17 \pm 0.05$ |
| $p_0^{\sigma_t}(2012)$ | $0.03741 \pm 0.00028$ |
| $p_1^{\sigma_t}(2012)$ | $1.25 \pm 0.06$ |

TABLE 7.20: Calibration parameters obtained in the nominal fit to data.

## 7.8 Checks of the model

In the next sub-sections, a set of checks performed to test different parts of the analysis procedure is presented. As a general note, the values of the $CP$-violating parameters retrieved from the fits where kept blind during the whole analysis procedure and while performing the checks, in order to prevent personal biases in the process. The results were only un-blinded in the end, and the obtained values were shown in the previous section. The use of this method motivates that the results of the fits performed for the checks, covered in the next pages, contain blind values for the $CP$-violating parameters. In a similar way, the Monte Carlo samples used for the checks were not corrected for small mis-modellings in generation. The development of a correction, presented in Sect. 7.9.13, requires an iterative procedure that makes use of the final fitting framework. Consequently, the correction is only applied when obtaining the final results.

### 7.8.1 Comparison between the two simulation samples

As previously explained, the combination of a pure phase space $B_s^0 \to K^+\pi^-K^-\pi^+$ and a vector-vector $B_s^0 \to K^{*0}\bar{K}^{*0}$ simulation samples is used to study the acceptance and resolution effects, in an attempt to properly cover the kinematic phase space of the considered signal decay channels. More specifically, the vector-vector Monte Carlo has almost no statistics in the $K\pi$ mass region of the $K_2^*(1430)^0$, while the pure phase space Monte Carlo covers the whole range but has considerably fewer statistics in the $K\pi$ mass region of the $K^*(892)^0$ than the vector-vector one. In this section, the acceptance and resolution effects on of both simulation samples are compared and checked to be compatible.

As explained in Sect. 7.6.4, the kinematic acceptance is included via complex normalisation weights, $\xi_{ij}$. For this check, we consider the real and imaginary parts of each $\xi_{ij}$ as different normalisation weights, and refer to the resulting real weights as $\hat{\xi}_i$, with the index $i$ running along the $2 \times 190 = 380$ possibilities. For a quantitative comparison between the two simulation samples, we define the following pull variable:

$$Pull(i) = \frac{\hat{\xi}_i^{PhSp} - \hat{\xi}_i^{VV}}{max[\sigma(\hat{\xi}_i^{PhSp}), \sigma(\hat{\xi}_i^{VV})]}, \tag{7.36}$$

where $\hat{\xi}_i^{PhSp}$ ($\hat{\xi}_i^{VV}$) are computed using exclusively the pure phase space (vector-vector) Monte Carlo, and $\sigma$ refers to the statistical uncertainty. The distribution of the $Pull(i)$ variable for the 380 weights is plotted in Fig. 7.19, showing compatibility between the two samples apart from few big deviations of several sigmas. These deviations are checked to correspond to cases where the two $K\pi$-mass-dependent amplitudes associated to either $m_1$ or $m_2$ in Eq. 7.29 have $j = 2$ (shown as a brown filled region in Fig. 7.19). Since in the region of the $K_2^*(1430)^0$ the vector-vector Monte-Carlo has almost no statistics, such deviations are expected.

Concerning the time-dependent acceptance, the one-dimensional time distributions of the two simulation samples divided by the corresponding generation model are plotted together in Fig. 7.20 and shown to be compatible within uncertainties.

Finally, for the time resolution, the scatter plot of $\sigma_t$ (obtained via gaussian fits as explained in Sect. 7.5) versus $\delta_t$ obtained independently with the two simulation samples is shown in Fig. 7.21. No big deviations are found.

### 7.8.2 TD-fitter validation with simulated $B_s^0 \to K^{*0}\bar{K}^{*0}$ data

To validate the time-dependent fitting framework, a sample of $B_s^0 \to K^{*0}\bar{K}^{*0}$ simulated data with large CPV (only used in the analysis for this study) is fitted with a version of the model

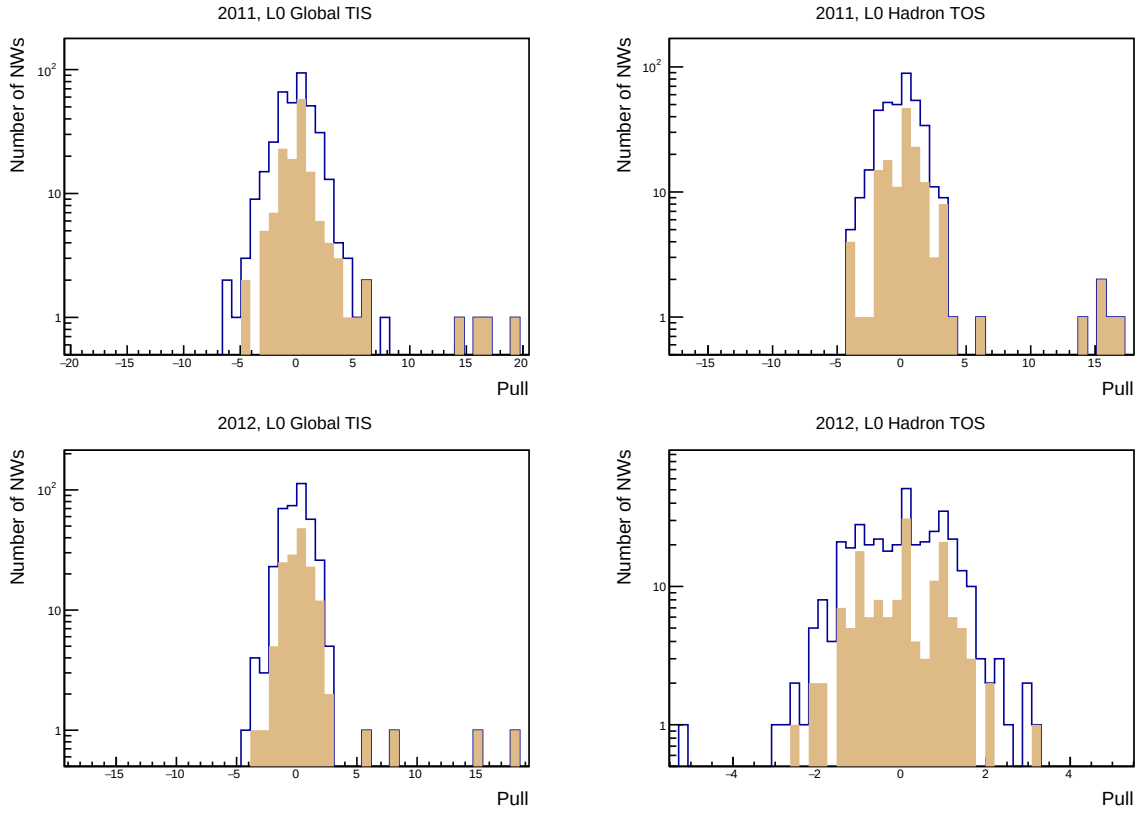



FIGURE 7.19: Distributions of the 380 real normalisation weights on the $Pull(i)$ variable defined in the text, shown in logarithmic scale. The solid blue line corresponds to the whole distribution while the filled brown area represents the cases where the two $K\pi$-mass-dependent amplitudes associated to either $m_1$ or $m_2$ have $j = 2$.

restricted to a $K\pi$ mass window of $\pm 150$ MeV$/c^2$ around the $K^{*0}$ nominal mass[3] and with only the VV decay mode included.

The values resulting from the fit, together with the corresponding generation ones, are shown in Table 7.21, and the model and data projections on the fit variables are shown in Fig. 7.22. A good agreement is found.

| Parameter | Generation value | Fit value |
|---|---|---|
| $\phi_s$ [rad] | -0.8 | -0.767 $\pm$ 0.049 |
| $\Delta^{CP}$ | 0 | 0.068 $\pm$ 0.048 |
| $f_L^{VV}$ | 0.64 | 0.637 $\pm$ 0.003 |
| $f_\parallel^{VV}$ | 0.25 | 0.247 $\pm$ 0.003 |
| $\delta_\parallel^{VV}$ [rad] | 3.14 | 3.07 $\pm$ 0.07 |
| $\delta_\perp^{VV}$ [rad] | 3.14 | 3.06 $\pm$ 3.04 |

TABLE 7.21: Generation and fit values for the sample of $B_s^0 \to K^{*0}\bar{K}^{*0}$ simulated data with large CPV.

[3]The acceptance and time resolution factors (both for fitting and for plotting) are re-obtained using this mass window.

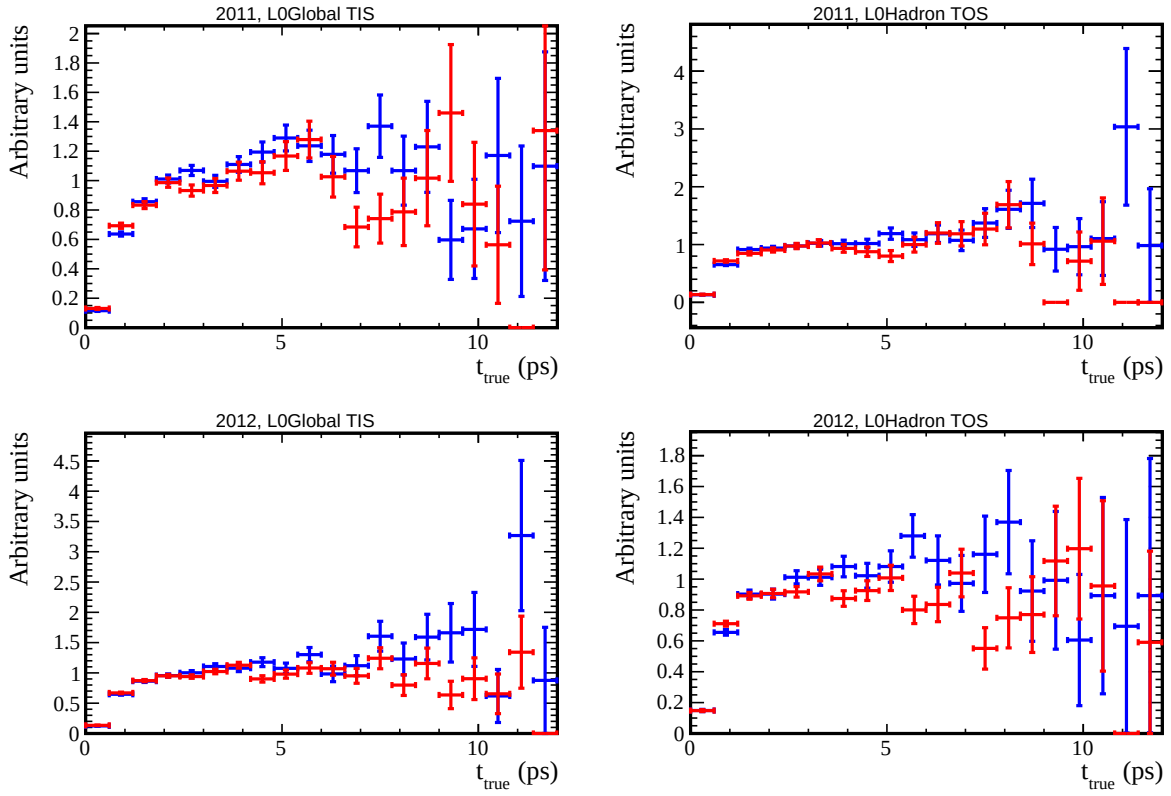



FIGURE 7.20: Comparison between the time acceptance shape obtained using the pure phase space (in blue) and the vector-vector (in red) Monte Carlo.

### 7.8.3 Fit in a narrow $K\pi$ mass window

As another test of the procedure, an alternative fit to data is done using the fit version of the previous check, in the narrow $K^+\pi^-$ mass window, but now including the VV, VS, SV and SS decay modes.

The parameters measured in the fit are listed in Table 7.22, and the plots for the one-dimensional projections of the fitted model with the sWeighted data are shown in Fig. 7.23. The set of amplitudes expressed in polar coordinates (fractions and phases), are written in Table 7.23. Finally, Table 7.24 collects the list of the scalar $K\pi$-mass amplitude parameters and the flavour tagging and time-resolution calibration parameters.

A comparison between CP-averaged parameter values obtained in both this fit and the nominal one with those measured in the previous analysis (resulting from an untagged time-integrated fit to 2011 data) is presented in Table 7.25. For this comparison, the parameters are transformed into the amplitude basis used in the previous analysis. No major differences are observed, even if neither the data sample nor the $K\pi$ mass model are the same, and the selection and acceptance methods differ between the two studies.

### 7.8.4 Higher wave contributions: distributions of Legendre moments

To estimate the size of any potential contribution from higher spin resonances (with $j > 2$), namely from a spin-3 $K_3^*(1780)$ component (which is known to peak outside of our nominal $K\pi$ mass range but has a relatively large width), we use the method of the Legendre moments explained in Sect. 6.4.5. For a system with a maximum momentum $j = 2$, the moments with $l > 4$ should vanish. On the contrary, if a component with $j = 3$ is present, also the moments $\langle P_5 \rangle$ and $\langle P_6 \rangle$ can be different from 0. To study the potential contribution of a $j = 3$ component along the

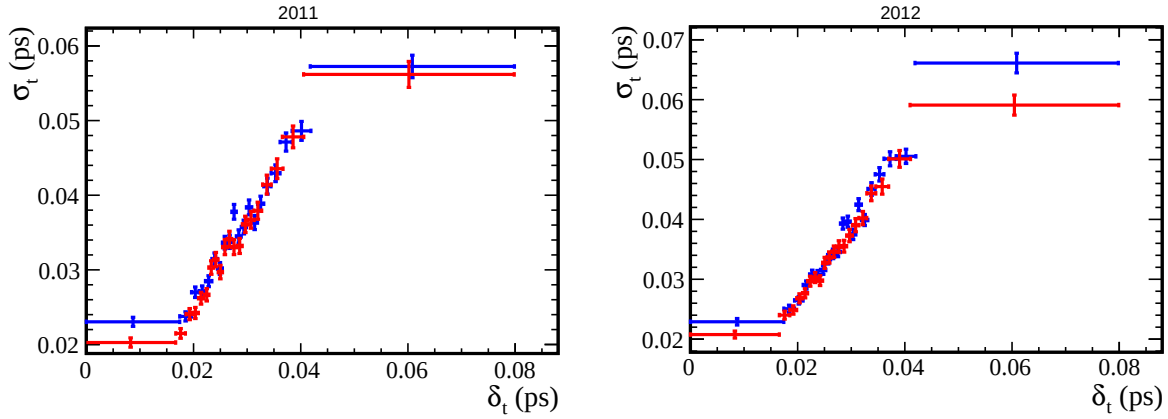



FIGURE 7.21: Comparison of the time resolution scatter plot of $\sigma_t$ versus $\delta_t$ obtained using the pure phase space (in blue) and the vector-vector (in red) Monte Carlo.

$K\pi$ mass, the Legendre moments are obtained in bins of this variable using the expression in Eq. 6.14. For normalisation purposes, the per-event weights in that expression are scaled as:

$$\omega^i \to \omega^i \cdot \left( \frac{N_{signal}}{\sum_k \omega^k} \right), \tag{7.37}$$

where $N_{signal}$ is the measured signal yield. The distributions of the Legendre moments up to $l = 6$ are plotted in Fig. 7.24, excluding $l = 0$, which corresponds to the normal $K\pi$ mass distribution. The $\pm 1\sigma$ error bands are obtained from the uncertainty associated to the per-event weights. As can be seen in the figures, the distributions of $\langle P_5 \rangle$ and $\langle P_6 \rangle$ are essentially flat and equal to 0, apart from some small fluctuations. This is consistent with a negligible $j = 3$ contribution.

To further test the previous conclusion, an acceptance-free toy Monte Carlo sample is generated from our model using the measured physical parameters. The sample contains a number of events equal to the measured signal yield, and a cut of $t > 0.5$ ps is imposed to reproduce the data conditions. The Legrendre moment distributions are obtained for this sample and plotted in Fig. 7.25. The shapes are reasonably similar to the data ones in Fig. 7.24, apart from some small deviations that can be due to systematic uncertainties not taken into account by the error bars shown in the figures. The distributions on $\langle P_5 \rangle$ and $\langle P_6 \rangle$ (which are 0 by construction in the generation model) present some fluctuations in the same regions as the data, which further supports the conclusion that a potential $j = 3$ component in the signal data sample would be very small. Basing on this, no efforts are made to include the extra component in the analysis.

### 7.8.5 Toy MC study of the main fitter

As a check of the default fitting framework and a way to estimate potential biases in the fitted parameters, a toy Monte Carlo study is performed basing on a set of 500 experiments. Each experiment consists of two consecutive steps: the generation of a simulated sample of a number of events equal to the signal yield using our model and the measured physical parameters, and the subsequent fit of such a sample with the same model, comparing the resulting parameters with the generation ones. Below, the process is described in detail.

#### 7.8.5.1 Approximations

As the method of the normalisation weights does not provide any parametric function for the kinematic acceptance, $\epsilon_\Omega(\Omega)$, the approximated expression in Eq. 7.20 is here used both for generation and fit. Combining Eq. 7.18, Eq. 7.29 and Eq. 7.20, the integral terms to be used in

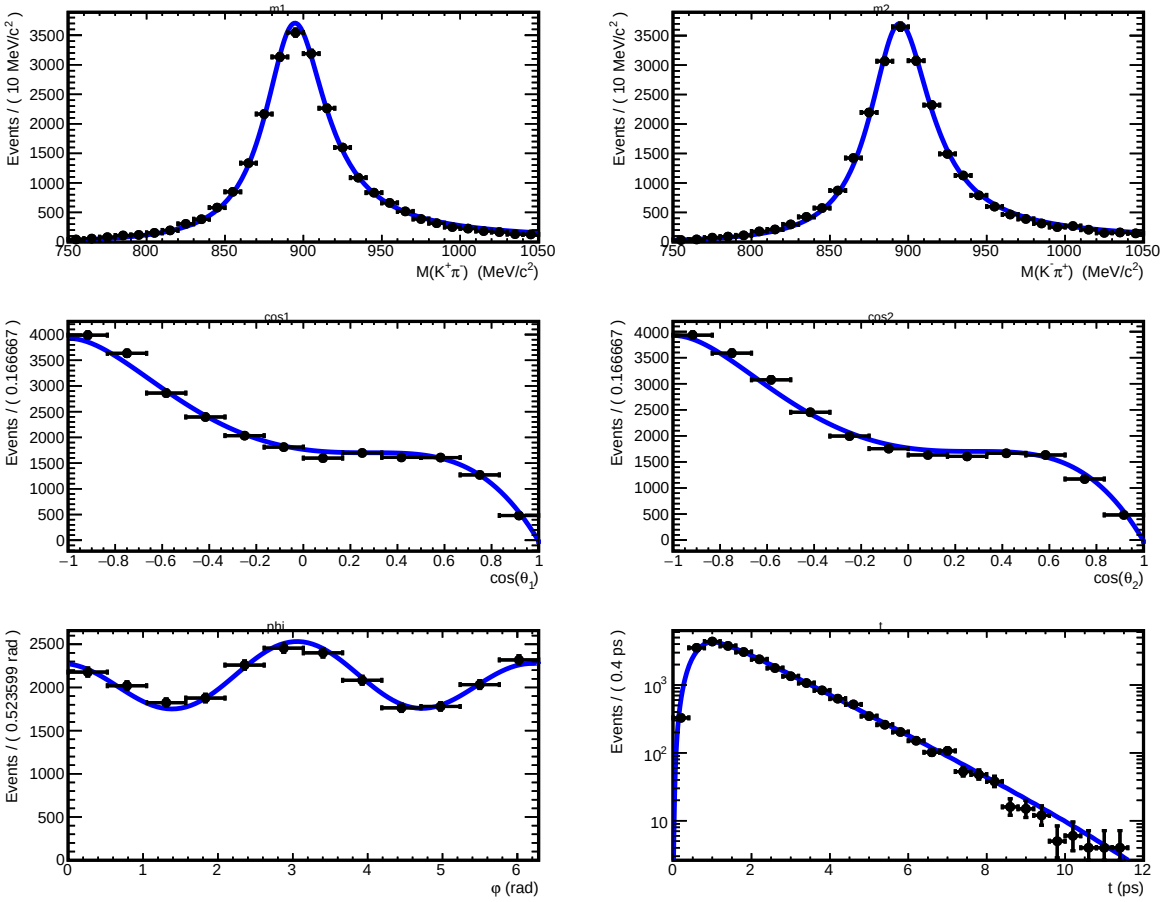



FIGURE 7.22: One-dimensional projections of the fit to the sample of $B_s^0 \to K^{*0}\bar{K}^{*0}$ simulated data with large CPV.

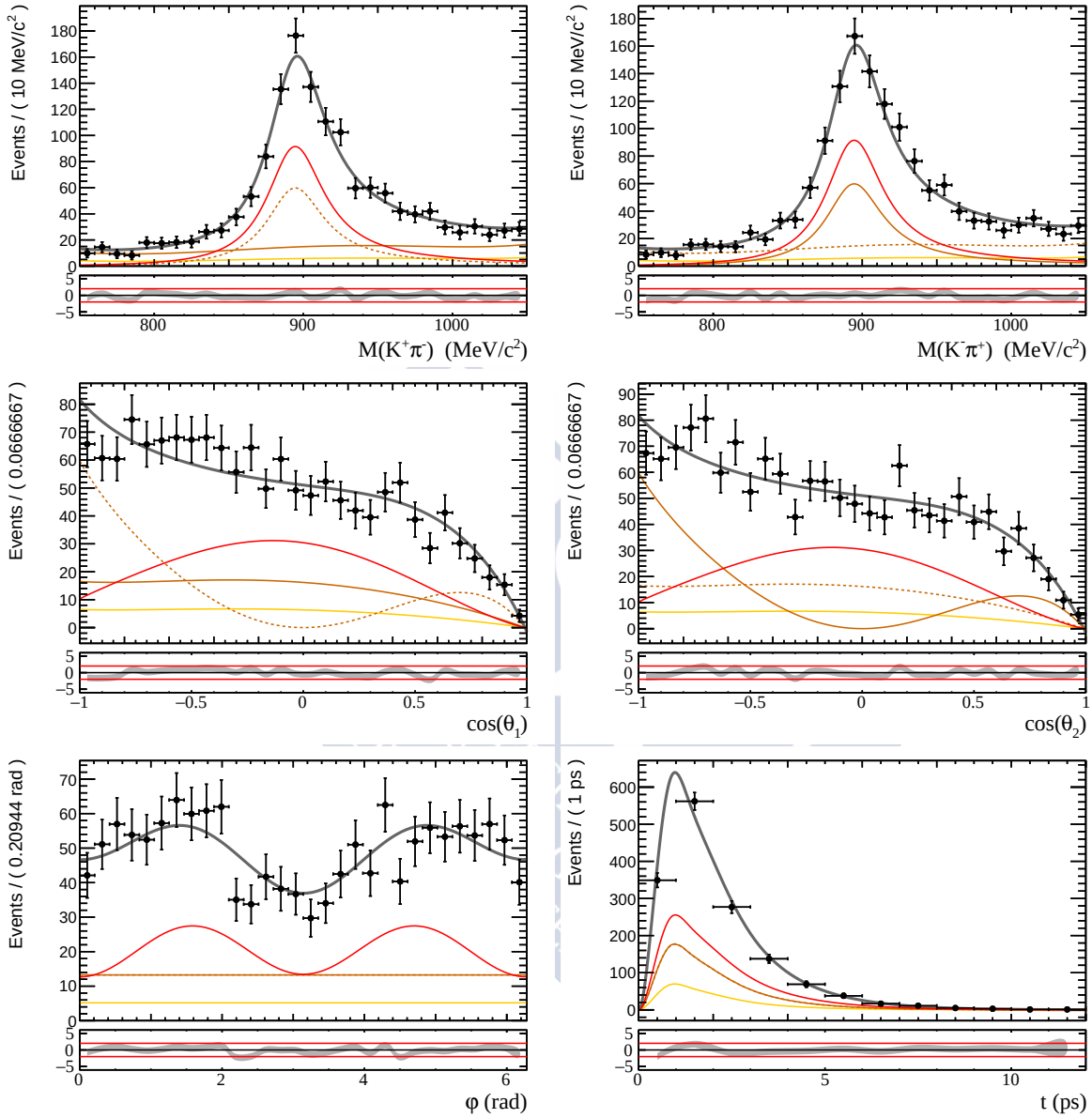



FIGURE 7.23: One dimensional projections of the fit to data using a narrow $K\pi$ mass window. The solid gray line represents the whole model and the black dots correspond to the sWeighted data. The individual contribution of the 4 involved decay channels (summing over the squared modules of the polarisation amplitudes for each channel) is also plotted, representing the VV component by a solid red line, the SV(VS) by a solid(dashed) brown line and the SS by a solid yellow line. The interference terms are not shown.

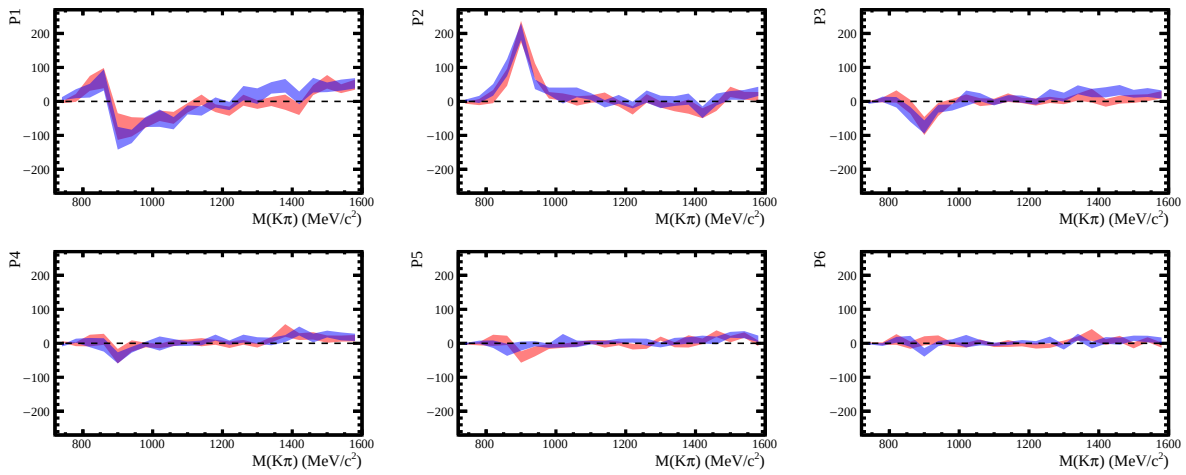



FIGURE 7.24: Legendre moment distributions obtained from the background-subtracted and acceptance-corrected data sample, in bins of the $K\pi$ mass. The distributions corresponding to the $K^+\pi^-$ pair ($\cos\theta_1$, $m_{K^+\pi^-}$) are plotted in red, and those corresponding to the $K^-\pi^+$ pair ($\cos\theta_2$, $m_{K^-\pi^+}$) are plotted in blue.

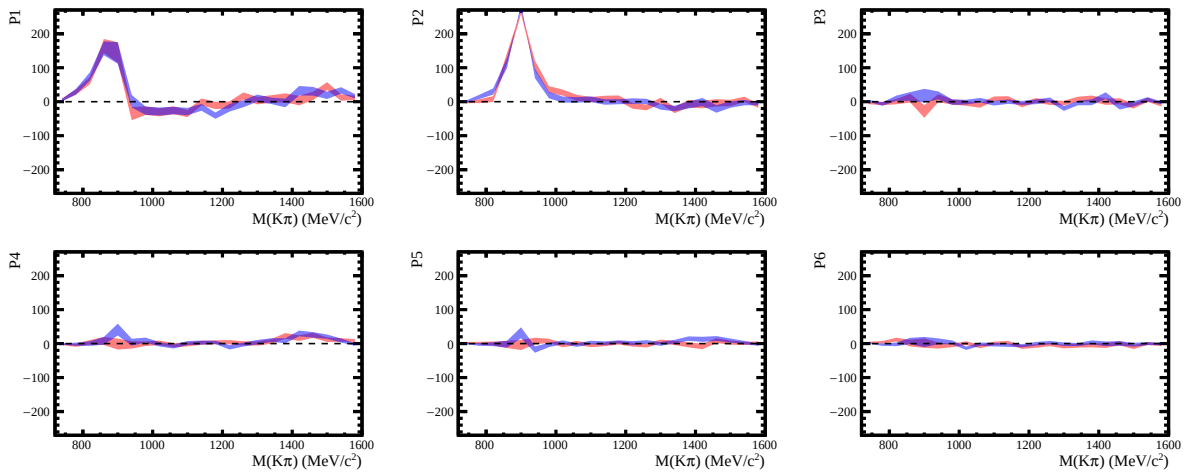



FIGURE 7.25: Legendre moment distributions obtained from the acceptance-free toy Monte Carlo sample generated with the nominal model and the measured physical parameters. The distributions corresponding to the $K^+\pi^-$ pair ($\cos\theta_1$, $m_{K^+\pi^-}$) are plotted in red, and those corresponding to the $K^-\pi^+$ pair ($\cos\theta_2$, $m_{K^-\pi^+}$) are plotted in blue.

| Parameter | Value |
|---|---|
| Common parameters | |
| $\phi_s$ | $xxx \pm 0.20$ |
| $\Delta^{CP}$ | $xxx \pm 0.06$ |
| $\Delta m_{B_s^0}$ | $17.50 \pm 0.09$ |
| $\Gamma_{B_s^0}$ | $0.6626 \pm 0.0018$ |
| $\Delta\Gamma_{B_s^0}$ | $0.091 \pm 0.005$ |
| $B_s^0 \to K^*(892)^0\bar{K}^*(892)^0$ (VV) | |
| $Re(A_\parallel^{VV})$ | $-0.88 \pm 0.17$ |
| $Im(A_\parallel^{VV})$ | $0.77 \pm 0.19$ |
| $Re(A_\perp^{VV})$ | $0.3 \pm 0.5$ |
| $Im(A_\perp^{VV})$ | $1.60 \pm 0.22$ |
| Single $S-wave$ (SV and VS) | |
| $Re(A^{SV})$ | $0.3 \pm 0.4$ |
| $Im(A^{SV})$ | $-2.25 \pm 0.33$ |
| $Re(A^{VS})$ | $-1.1 \pm 0.4$ |
| $Im(A^{VS})$ | $1.79 \pm 0.27$ |
| Double $S-wave$ (SS) | |
| $Re(A^{SS})$ | $0.67 \pm 0.19$ |
| $Im(A^{SS})$ | $1.05 \pm 0.21$ |

TABLE 7.22: Results of the fit to data using a narrow $K\pi$ mass window.

place of the normalisation weights within this framework are the following ones:

$$\xi_{ij}^{toy} = (2-\delta_{ij}) \cdot I_{ij}^{ang} \cdot I_{ij}^{mass}, \tag{7.38}$$

with

$$\begin{aligned} I_{ij}^{ang} &= \int d\,\cos\theta_1 \int d\,\cos\theta_2 \int d\,\varphi\; \Theta_h^{j_1 j_2}(\cos\theta_1, \cos\theta_2, \varphi) \\ &\cdot\; \Theta_{h'}^{j_1' j_2' *}(\cos\theta_1, \cos\theta_2, \varphi) \cdot \epsilon_{\cos\theta}^{fact}(\cos\theta_1) \cdot \epsilon_{\cos\theta}^{fact}(\cos\theta_2) \cdot \epsilon_{\varphi}^{fact}(\varphi), \end{aligned} \tag{7.39}$$

$$\begin{aligned} I_{ij}^{mass} &= \int d\,m_1 \int d\,m_2\; \Phi_4(m_1, m_2) \cdot \mathcal{M}_{j_1}(m_1) \cdot \mathcal{M}_{j_2}(m_2) \cdot \mathcal{M}_{j_1'}^*(m_1) \cdot \mathcal{M}_{j_2'}^*(m_2) \\ &\cdot\; \mathcal{F}_h^{j_1 j_2}(m_1, m_2) \cdot \mathcal{F}_{h'}^{j_1' j_2'}(m_1, m_2) \cdot \mathcal{N}_h^{j_1 j_2} \cdot \mathcal{N}_{h'}^{j_1' j_2' *} \cdot \epsilon_m^{fact}(m_1) \cdot \epsilon_m^{fact}(m_2), \end{aligned} \tag{7.40}$$

where the $i(j)$ index has been associated to the corresponding amplitude quantum numbers, $\{j_1, j_2, h\}(\{j_1', j_2', h'\})$.

For simplicity, only one data category is considered in the study, and the acceptance parameters are obtained as explained in Sect. 7.6.3 and Sect. 7.6.4.2, but using the whole Monte Carlo samples. In the same sense, concerning the time resolution, only the calibration parameters obtained from the 2012 Monte Carlo sample (see Table 7.11) are used for toy generation and fitting.

Finally, the convergence time of the nominal fit is enormously reduced when the parameters of the scalar $K\pi$ mass amplitude are fixed, since the $K\pi$ mass integrals in Eq. 3.22 and the normalisation weights only need to be computed once at the beginning of the fit (instead of at each minimisation step). Here, even if there is no need to compute the normalisation weights, the mass integrals in Eq. 7.40 depend on the $c_i^{mass}$ parameters, so they would also need to be computed per fit iteration, leading to similar computing times as the full nominal fit. For this

| Parameter | Value |
|---|---|
| Common parameters | |
| $\phi_s$ | $xxx \pm 0.20$ |
| $\Delta^{CP}$ | $xxx \pm 0.06$ |
| $\Delta m_{B_s^0}$ | $17.50 \pm 0.09$ |
| $\Gamma_{B_s^0}$ | $0.6626 \pm 0.0018$ |
| $\Delta\Gamma_{B_s^0}$ | $0.091 \pm 0.005$ |
| $B_s^0 \to K^*(892)^0 \bar{K}^*(892)^0$ (VV) | |
| $f_{VV}$ | $0.313 \pm 0.034$ |
| $f_L^{VV}$ | $0.199 \pm 0.035$ |
| $f_\parallel^{VV}$ | $0.273 \pm 0.032$ |
| $\delta_\parallel^{VV}$ | $2.42 \pm 0.18$ |
| $\delta_\perp^{VV}$ | $1.39 \pm 0.33$ |
| Single $S-wave$ (SV and VS) | |
| $f_{SV}$ | $0.32 \pm 0.04$ |
| $f_{VS}$ | $0.27 \pm 0.04$ |
| $\delta^{SV}$ | $-1.46 \pm 0.18$ |
| $\delta^{VS}$ | $2.11 \pm 0.17$ |
| Double $S-wave$ (SS) | |
| $f_{SS}$ | $0.097 \pm 0.013$ |
| $\delta^{SS}$ | $1.00 \pm 0.17$ |

TABLE 7.23: Results of the fit to data using a narrow $K\pi$ mass window, with the amplitudes rotated into the polar basis.

reason, the following method is chosen to only make use of the reduced fit:

- The generation model uses the values of the $c_i^{mass}$ parameters in Table 7.20 for all the experiments.
- For the fit, the values of the $c_i^{mass}$ parameters are fixed, so that the fitting time is reduced to the order of minutes.
- To emulate the extra biases due to the variation of the $c_i^{mass}$ parameters which is done in the nominal fit to data, their values in the toy fit model are randomised for each of the 500 experiments. The randomisation is done according to the $c_i^{mass}$ parameter covariance matrix, obtained from the fit to data, which is shown in Table 7.26. For completeness, the corresponding correlation matrix is shown in Table 7.27.

#### 7.8.5.2 Generation step

For generation purposes, the full PDF introduced in Eq. 7.23 has to be used, instead of the fitting one presented in Eq. 7.25. Specifically, the $\mathcal{P}_{\delta_t}(\delta_t)$, $\mathcal{P}_{\eta^{OS}}(\eta^{OS})$ and $\mathcal{P}_{\eta^{SSK}}(\eta^{SSK})$ marginal PDFs are needed to generate the corresponding values of the conditional variables for each event, which are afterwards inserted in the conditional PDF of Eq. 7.24, to generate the rest of the variables. The marginal PDFs are modelled with one-dimensional parametric functions and obtained by fitting the sWeighted data distributions. The $\eta$ PDFs are parameterised as:

$$\mathcal{P}_{\eta^X}(\eta^X) = G(\eta^X, \mu_1^X, \sigma_1^X) + c^X \cdot G(\eta^X, \mu_2^X, \sigma_2^X), \tag{7.41}$$

| Parameter | Value |
|---|---|
| Scalar $K\pi$ mass amplitude | |
| $c_1^{mass}$ | $1.65 \pm 0.19$ |
| $c_2^{mass}$ | $0.991 \pm 0.019$ |
| $c_3^{mass}$ | $0.39 \pm 0.06$ |
| $c_4^{mass}$ | $0.078 \pm 0.035$ |
| SSK tagger | |
| $p_0^{SSK} - <\eta^{SSK}>$ | $0.006 \pm 0.005$ |
| $1/2\Delta p_0^{SSK}$ | $-0.0081 \pm 0.0014$ |
| $p_1^{SSK}$ | $0.93 \pm 0.08$ |
| $1/2\Delta p_1^{SSK}$ | $-0.018 \pm 0.023$ |
| OS tagger | |
| $p_0^{OS} - <\eta^{OS}>$ | $0.006 \pm 0.004$ |
| $1/2\Delta p_0^{OS}$ | $0.0070 \pm 0.0006$ |
| $p_1^{OS}$ | $0.984 \pm 0.035$ |
| $1/2\Delta p_1^{OS}$ | $0.033 \pm 0.006$ |
| Time resolution | |
| $p_0^{\sigma_t}(2011)$ | $0.0357 \pm 0.0004$ |
| $p_1^{\sigma_t}(2011)$ | $1.22 \pm 0.06$ |
| $p_0^{\sigma_t}(2012)$ | $0.03758 \pm 0.00032$ |
| $p_1^{\sigma_t}(2012)$ | $1.23 \pm 0.06$ |

TABLE 7.24: Calibration parameters obtained in the fit to data using a narrow $K\pi$ mass window.

where $X \in \{OS, SSK\}$ stands for the tagging algorithm, $G(x, \mu, \sigma)$ are gaussian functions of mean $\mu$ and standard deviation $\sigma$, and $c^X$ is a constant. The decay-time-error distribution is represented by:

$$\mathcal{P}_{\delta_t}(\delta_t) = \Gamma(\delta_t, \alpha, \beta), \tag{7.42}$$

where $\Gamma(\delta_t, \alpha, \beta)$ is a Gamma distribution with shape parameter $\alpha$ and rate parameter $\beta$. The sWeighted data distributions for the conditional variables are shown in Fig. 7.26, together with the marginal PDFs resulting from the fits. The measured values for the parameters in the previous expressions are written in Table 7.28.

To properly account for the statistical uncertainties on the parameters which are gaussian constrained during fitting, the corresponding values used in toy generation are randomised for each experiment. With this aim, one-dimensional gaussian PDFs (with the mean and the standard deviation corresponding to the central value and the error of the constrain) are used for the uncorrelated constrained parameters, while multi-dimensional gaussian PDFs (that take into account the correlation coefficients) are used for the correlated ones.

From a technical viewpoint, the event generation is done in the GPU, using accept-reject methods, parallelising on the number of events to be generated. The time needed to generate one experiment is of the order of minutes. Prior to the toy study, the mass integrals in Eq. 3.22 and Eq. 7.40 are computed using the $c_i^{mass}$ parameter values in Table 7.20. All these integrals are computed in the GPU, using the paralellisation scheme explained in the first bullet of Sect. 7.7.3.

#### 7.8.5.3 Fitting step

The fit of the toy samples is done using the approximations explained in Sect. 7.8.5.1. Since, for each experiment, the values of the $c_i^{mass}$ parameters are randomised (and then inserted as

| Parameter | 2011+2012 TD fit, nominal window | 2011+2012 TD fit, narrow window | 2011 TI fit, narrow window |
|---|---|---|---|
| $f_L^{VV}$ | $0.163 \pm 0.032$ | $0.199 \pm 0.035$ | $0.201 \pm 0.057 \pm 0.040$ |
| $f_\parallel^{VV}$ | $0.294 \pm 0.030$ | $0.273 \pm 0.032$ | $0.215 \pm 0.046 \pm 0.015$ |
| $f_{S-}$ | $-$ | $0.563 \pm 0.032$ | $0.485 \pm 0.051 \pm 0.019$ |
| $f_{S+}$ | $-$ | $0.027 \pm 0.011$ | $0.114 \pm 0.037 \pm 0.023$ |
| $f_{SS}$ | $-$ | $0.097 \pm 0.013$ | $0.066 \pm 0.022 \pm 0.007$ |
| $\delta_\parallel^{VV}$ | $2.22 \pm 0.12$ | $2.42 \pm 0.18$ | $2.17 \pm 0.24 \pm 0.14$ |
| $\delta_\perp^{VV} - \delta^{S+}$ | $-2.18 \pm 0.19$ | $-2.28 \pm 0.29$ | $-1.19 \pm 0.21 \pm 0.04$ |
| $\delta^{S-}$ | $1.64 \pm 0.11$ | $1.89 \pm 0.17$ | $1.79 \pm 0.19 \pm 0.19$ |
| $\delta^{SS}$ | $0.82 \pm 0.11$ | $1.00 \pm 0.17$ | $1.06 \pm 0.27 \pm 0.23$ |

TABLE 7.25: Comparison between the full Run 1 time-dependent fits performed in this analysis, both in the nominal and in the narrow $K\pi$ mass window, and the time-integrated fit done in the previous analysis, using 2011 data. The parameterisation of the amplitudes in this case is chosen to be the same as in the previous analysis. The fractions $f_{S-}$, $f_{S+}$ and $f_{SS}$ for the fit in the nominal window are not compared, since they are defined in a different mass range and a different set of polarisation states is used for their normalisation.

| Coefficient | $c_1$ | $c_2$ | $c_3$ | $c_4$ |
|---|---|---|---|---|
| $c_1$ | $3.95e-04$ | $-7.66e-05$ | $1.20e-04$ | $-5.05e-05$ |
| $c_2$ | $-7.66e-05$ | $3.76e-04$ | $-7.34e-05$ | $1.67e-04$ |
| $c_3$ | $1.20e-04$ | $-7.34e-05$ | $2.34e-04$ | $-4.59e-05$ |
| $c_4$ | $-5.05e-05$ | $1.67e-04$ | $-4.59e-05$ | $2.65e-04$ |

TABLE 7.26: Covariance matrix of the scalar $K\pi$ mass amplitude coefficients, as resulting from the nominal fit to data.

constants in the fitting model), the mass integrals in Eq. 3.22 and Eq. 7.40 have to be computed with the new parameter configuration once before each fit. The minimisation process for each experiment is done in the GPU, parallelising on the number of events. After each fit, the resulting values for the parameters, $\lambda_i^{fit}$, are compared with the ones used for generation, $\lambda_i^{gen}$. To normalise the deviations, the estimated uncertainty on the determination of each parameter is used. However, the uncertainties retrieved by the toy fits, $\sigma_i^{fit}$, do not contain the effect of varying the scalar $K\pi$ mass amplitude parameters. Denoting by $\sigma_i^{mass}$ the contribution to the total uncertainty due to this variation, the corrected fit uncertainty, $\sigma_i^{fit,C}$, can be approximated by:

$$\sigma_i^{fit,C} = \sqrt{(\sigma_i^{fit})^2 + (\sigma_i^{mass})^2}. \tag{7.43}$$

To estimate $\sigma_i^{mass}$, an independent set of experiments is done. In this case, only one sample is generated, and then fitted 200 times with the toy fit, using different sets of randomised

| Coefficient | $c_1$ | $c_2$ | $c_3$ | $c_4$ |
|---|---|---|---|---|
| $c_1$ | 1 | $-0.1989$ | 0.3942 | $-0.1562$ |
| $c_2$ | $-0.1989$ | 1 | $-0.2474$ | 0.5310 |
| $c_3$ | 0.3942 | $-0.2474$ | 1 | $-0.1844$ |
| $c_4$ | $-0.1562$ | 0.5310 | $-0.1844$ | 1 |

TABLE 7.27: Correlation matrix of the scalar $K\pi$ mass amplitude coefficients, as resulting from the nominal fit to data.

| Parameter | Value |
|---|---|
| $\mu_1^{OS}$ | $4.26335 \cdot 10^{-1} \pm 6.45592 \cdot 10^{-3}$ |
| $\sigma_1^{OS}$ | $1.05094 \cdot 10^{-1} \pm 7.85419 \cdot 10^{-3}$ |
| $c^{OS}$ | $1.58334 \cdot 10^{-1} \pm 3.05861 \cdot 10^{-2}$ |
| $\mu_2^{OS}$ | $1.88774 \cdot 10^{-1} \pm 1.19822 \cdot 10^{-2}$ |
| $\sigma_2^{OS}$ | $4.68764 \cdot 10^{-2} \pm 6.94291 \cdot 10^{-3}$ |
| $\mu_1^{SSK}$ | $6.54768 \cdot 10^{-1} \pm 4.67320 \cdot 10^{-1}$ |
| $\sigma_1^{SSK}$ | $1.05513 \cdot 10^{-1} \pm 9.97581 \cdot 10^{-2}$ |
| $c^{SSK}$ | $1.37090 \cdot 10^{-2} \pm 5.30951 \cdot 10^{-2}$ |
| $\mu_2^{SSK}$ | $2.97048 \cdot 10^{-1} \pm 5.25451 \cdot 10^{-2}$ |
| $\sigma_2^{SSK}$ | $6.10074 \cdot 10^{-2} \pm 1.84826 \cdot 10^{-2}$ |
| $\alpha$ | $1.50472 \cdot 10 \pm 2.93872 \cdot 10^{-1}$ |
| $\beta$ | $1.84540 \cdot 10^{-3} \pm 3.66684 \cdot 10^{-5}$ |

TABLE 7.28: Measured parameters of the functions used to describe the one-dimensional data distributions on $\eta^{OS}$, $\eta^{SSK}$ and $\delta_t$.

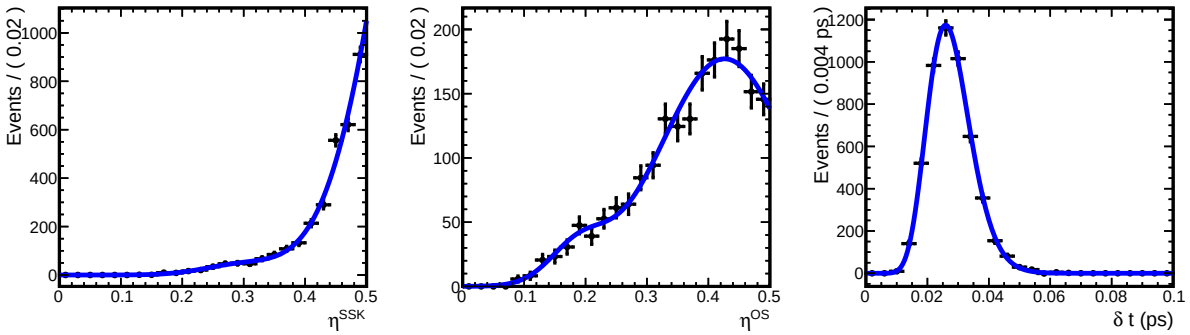



FIGURE 7.26: Signal data distributions on the per-event conditional variables and associated marginal PDFs obtained via one-dimensional fits.

$c_i^{mass}$ parameters. Since the event sample is the same for all the experiments, the biases in the fit parameters are only caused by the variation of $c_i^{mass}$[4]. Using this consideration, we estimate $\sigma_i^{mass}$ by computing the root mean square of the $(\lambda_i^{fit} - \lambda_i^{gen})$ distributions for these 200 experiments. The resulting values are collected in Table 7.29.

With respect to the set of 500 experiments, after computing the correction for the uncertainties, the following pull variable can be constructed for each parameter:

$$pull_i = \frac{\lambda_i^{fit} - \lambda_i^{gen}}{\sigma_i^{fit,C}}. \tag{7.44}$$

If the fitting machinery behaves as expected, the distributions on these pull variables for the set of 500 experiments should be gaussian, with mean 0 and standard deviation 1.

#### 7.8.5.4 Results

The resulting pull distributions are shown in Appendix A. The pull distributions are fitted with gaussian PDFs. The resulting mean and standard deviation values are collected in Table 7.30, Table 7.31 and Table 7.32. No large biases are observed, which validates the fitting machinery.

[4]There is an additional bias with respect to the generation values due to the statistics of the toy sample, but that bias is the same for all the experiments and cancels out for our purposes.

| Parameter | $\sigma^{mass}$ |
|---|---|
| $Re(A^{SS})$ | 0.0984 |
| $Re(A^{SV})$ | 0.0484 |
| $Re(A^{VS})$ | 0.0223 |
| $Re(A^{ST})$ | 0.0734 |
| $Re(A^{TS})$ | 0.0233 |
| $Re(A_{\parallel}^{VV})$ | 0.0093 |
| $Re(A_{\perp}^{VV})$ | 0.0174 |
| $Re(A_{L}^{VT})$ | 0.0732 |
| $Re(A_{\parallel}^{VT})$ | 0.0102 |
| $Re(A_{\perp}^{VT})$ | 0.0402 |
| $Re(A_{L}^{TV})$ | 0.0349 |
| $Re(A_{\parallel}^{TV})$ | 0.0310 |
| $Re(A_{\perp}^{TV})$ | 0.0209 |
| $Re(A_{L}^{TT})$ | 0.0115 |
| $Re(A_{\parallel 1}^{TT})$ | 0.0105 |
| $Re(A_{\perp 1}^{TT})$ | 0.0164 |
| $Re(A_{\parallel 2}^{TT})$ | 0.0062 |
| $Re(A_{\perp 2}^{TT})$ | 0.0131 |
| $\Delta^{CP}$ | 0.0007 |
| $Im(A^{SS})$ | 0.0736 |
| $Im(A^{SV})$ | 0.1070 |
| $Im(A^{VS})$ | 0.0417 |
| $Im(A^{ST})$ | 0.0312 |
| $Im(A^{TS})$ | 0.0991 |
| $Im(A_{\parallel}^{VV})$ | 0.0171 |
| $Im(A_{\perp}^{VV})$ | 0.0203 |
| $Im(A_{L}^{VT})$ | 0.0608 |
| $Im(A_{\parallel}^{VT})$ | 0.0070 |
| $Im(A_{\perp}^{VT})$ | 0.0155 |
| $Im(A_{L}^{TV})$ | 0.0514 |
| $Im(A_{\parallel}^{TV})$ | 0.0119 |

| Parameter | $\sigma^{mass}$ |
|---|---|
| $Im(A_{\perp}^{TV})$ | 0.0187 |
| $Im(A_{L}^{TT})$ | 0.0181 |
| $Im(A_{\parallel 1}^{TT})$ | 0.0270 |
| $Im(A_{\perp 1}^{TT})$ | 0.0499 |
| $Im(A_{\parallel 2}^{TT})$ | 0.0086 |
| $Im(A_{\perp 2}^{TT})$ | 0.0112 |
| $\phi_s$ | 0.0037 |
| $\Delta m_{B_s^0}$ | 0.0022 |
| $\Gamma_{B_s^0}$ | 0.0000 |
| $\Delta\Gamma_{B_s^0}$ | 0.0001 |
| $p_0^{SSK} - <\eta^{SSK}>$ | 0.0000 |
| $p_0^{OS} - <\eta^{OS}>$ | 0.0000 |
| $1/2\Delta p_0^{SSK}$ | 0.0000 |
| $1/2\Delta p_0^{OS}$ | 0.0000 |
| $p_1^{SSK}$ | 0.0007 |
| $p_1^{OS}$ | 0.0002 |
| $1/2\Delta p_1^{SSK}$ | 0.0000 |
| $1/2\Delta p_1^{OS}$ | 0.0000 |
| $p_0^{\sigma_t}(2012)$ | 0.0000 |
| $p_1^{\sigma_t}(2012)$ | 0.0006 |
| $\delta_0^{TT}$ | 0.0856 |
| $f_{VS}$ | 0.0022 |
| $\delta_{\perp 1}^{TT}$ | 0.0236 |
| $\delta_0^{TV}$ | 0.0305 |
| $\delta_{\perp}^{TV}$ | 0.0199 |
| $f_{\parallel 2}^{TT}$ | 0.0061 |
| $f_{SV}$ | 0.0032 |
| $f_{SS}$ | 0.0051 |
| $f_{ST}$ | 0.0006 |
| $f_{VT}$ | 0.0043 |
| $f_L^{VT}$ | 0.0036 |

| Parameter | $\sigma^{mass}$ |
|---|---|
| $f_L^{VV}$ | 0.0029 |
| $f_{VV}$ | 0.0018 |
| $\delta_{\parallel}^{TV}$ | 0.0248 |
| $f_{\perp}^{VT}$ | 0.0025 |
| $f_{\perp}^{VV}$ | 0.0022 |
| $\delta^{ST}$ | 0.0828 |
| $\delta^{TS}$ | 0.0275 |
| $f_{\parallel}^{VT}$ | 0.0013 |
| $\delta_{\perp 2}^{TT}$ | 0.0238 |
| $f_{\parallel}^{VV}$ | 0.0011 |
| $f_{\perp 1}^{TT}$ | 0.0189 |
| $\delta^{VS}$ | 0.0071 |
| $f_{\perp}^{TV}$ | 0.0064 |
| $\delta_{\parallel 2}^{TT}$ | 0.0160 |
| $f_{TT}$ | 0.0009 |
| $f_{TV}$ | 0.0013 |
| $f_{TS}$ | 0.0025 |
| $f_L^{TT}$ | 0.0045 |
| $f_{\parallel 1}^{TT}$ | 0.0142 |
| $f_{\parallel}^{TV}$ | 0.0036 |
| $f_L^{TV}$ | 0.0091 |
| $\delta_{\perp}^{VV}$ | 0.0096 |
| $\delta_{\parallel}^{VT}$ | 0.0154 |
| $f_{\perp 2}^{TT}$ | 0.0033 |
| $\delta^{SS}$ | 0.0098 |
| $\delta_{\perp}^{VT}$ | 0.0195 |
| $\delta^{SV}$ | 0.0083 |
| $\delta_{\parallel 1}^{TT}$ | 0.0326 |
| $\delta_{\parallel}^{VV}$ | 0.0094 |
| $\delta_0^{VT}$ | 0.0091 |

TABLE 7.29: Uncertainties associated to the variation of the scalar $K\pi$ mass amplitude parameters, computed via toy MC studies as explained in the text.

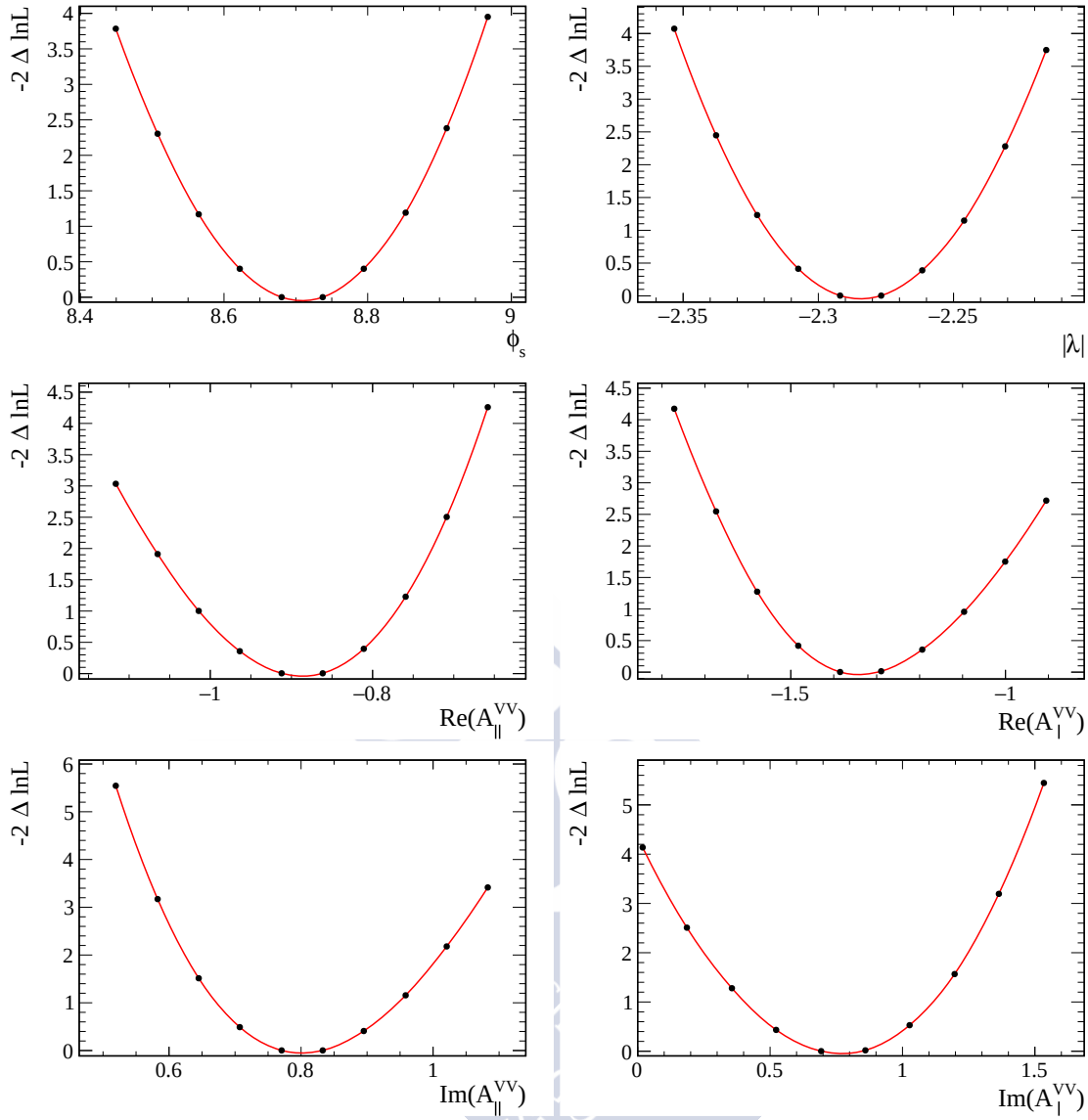



FIGURE 7.27: Distributions of the NLL around the fit best point, for some of the main physical parameters.

The mean values obtained from the gaussian fits are used to estimate systematic uncertainties as explained in Sect. 7.9.4.

### 7.8.6 Likelihood profiles

To check the stability of the fit best point, the one-dimensional profiles of the NLL around the minimum are obtained for some of the main parameters in the fit. The resulting distributions, plotted in Fig. 7.27, show a good behaviour of the fit around the minimum.

### 7.8.7 Exclusive fit to 2012 data

In order to check the compatibility between the 2011 and 2012 data samples, the nominal fit was tried separately for each of the two years. The fit for 2011 did not converge due to the lack of statistics but the one for 2012 succeeded. The measured parameters for this last year are

| Parameter | Mean | Std. Dev. |
|---|---|---|
| $Re(A^{SS})$ | $-0.074 \pm 0.053$ | $0.972 \pm 0.057$ |
| $Re(A^{SV})$ | $0.068 \pm 0.056$ | $1.099 \pm 0.047$ |
| $Re(A^{VS})$ | $0.184 \pm 0.055$ | $1.101 \pm 0.046$ |
| $Re(A^{ST})$ | $0.341 \pm 0.047$ | $0.948 \pm 0.039$ |
| $Re(A^{TS})$ | $-0.394 \pm 0.048$ | $0.982 \pm 0.041$ |
| $Re(A_{\parallel}^{VV})$ | $0.179 \pm 0.052$ | $1.034 \pm 0.044$ |
| $Re(A_{\perp}^{VV})$ | $0.120 \pm 0.060$ | $1.132 \pm 0.055$ |
| $Re(A_{L}^{VT})$ | $0.311 \pm 0.047$ | $0.892 \pm 0.045$ |
| $Re(A_{\parallel}^{VT})$ | $0.067 \pm 0.047$ | $0.968 \pm 0.044$ |
| $Re(A_{\perp}^{VT})$ | $0.321 \pm 0.048$ | $0.973 \pm 0.039$ |
| $Re(A_{L}^{TV})$ | $0.390 \pm 0.046$ | $0.929 \pm 0.042$ |
| $Re(A_{\parallel}^{TV})$ | $-0.031 \pm 0.045$ | $0.882 \pm 0.040$ |
| $Re(A_{\perp}^{TV})$ | $-0.130 \pm 0.051$ | $0.965 \pm 0.041$ |
| $Re(A_{L}^{TT})$ | $-0.177 \pm 0.047$ | $0.972 \pm 0.042$ |
| $Re(A_{\parallel 1}^{TT})$ | $0.063 \pm 0.050$ | $1.003 \pm 0.046$ |
| $Re(A_{\perp 1}^{TT})$ | $0.186 \pm 0.060$ | $1.188 \pm 0.064$ |
| $Re(A_{\parallel 2}^{TT})$ | $0.138 \pm 0.049$ | $0.954 \pm 0.042$ |
| $Re(A_{\perp 2}^{TT})$ | $-0.386 \pm 0.043$ | $0.880 \pm 0.038$ |
| $\Delta^{CP}$ | $0.028 \pm 0.057$ | $1.102 \pm 0.060$ |
| $Im(A^{SS})$ | $-0.215 \pm 0.052$ | $1.015 \pm 0.046$ |
| $Im(A^{SV})$ | $0.285 \pm 0.051$ | $0.932 \pm 0.048$ |
| $Im(A^{VS})$ | $-0.205 \pm 0.044$ | $0.854 \pm 0.036$ |
| $Im(A^{ST})$ | $0.053 \pm 0.061$ | $1.220 \pm 0.059$ |
| $Im(A^{TS})$ | $0.002 \pm 0.054$ | $1.074 \pm 0.047$ |
| $Im(A_{\parallel}^{VV})$ | $-0.119 \pm 0.054$ | $0.923 \pm 0.048$ |
| $Im(A_{\perp}^{VV})$ | $-0.289 \pm 0.041$ | $0.807 \pm 0.033$ |
| $Im(A_{L}^{VT})$ | $0.080 \pm 0.052$ | $1.025 \pm 0.047$ |
| $Im(A_{\parallel}^{VT})$ | $0.168 \pm 0.052$ | $0.969 \pm 0.049$ |
| $Im(A_{\perp}^{VT})$ | $0.048 \pm 0.054$ | $1.059 \pm 0.046$ |
| $Im(A_{L}^{TV})$ | $-0.103 \pm 0.046$ | $0.922 \pm 0.038$ |
| $Im(A_{\parallel}^{TV})$ | $-0.091 \pm 0.047$ | $0.956 \pm 0.039$ |
| $Im(A_{\perp}^{TV})$ | $0.139 \pm 0.051$ | $0.998 \pm 0.049$ |
| $Im(A_{L}^{TT})$ | $0.024 \pm 0.046$ | $0.905 \pm 0.043$ |
| $Im(A_{\parallel 1}^{TT})$ | $-0.227 \pm 0.048$ | $0.954 \pm 0.051$ |
| $Im(A_{\perp 1}^{TT})$ | $-0.339 \pm 0.046$ | $0.909 \pm 0.039$ |
| $Im(A_{\parallel 2}^{TT})$ | $-0.116 \pm 0.048$ | $1.004 \pm 0.041$ |
| $Im(A_{\perp 2}^{TT})$ | $0.006 \pm 0.058$ | $1.109 \pm 0.060$ |
| $\phi_s$ | $-0.001 \pm 0.051$ | $1.013 \pm 0.044$ |
| $\Delta m_{B_s^0}$ | $-0.014 \pm 0.058$ | $1.174 \pm 0.052$ |
| $\Gamma_{B_s^0}$ | $0.005 \pm 0.050$ | $0.987 \pm 0.041$ |

TABLE 7.30: Mean and standard deviation of the pull variable distributions for the fit parameters, as obtained from the 500 toy Monte Carlo experiments. First set of parameters.

| Parameter | Mean | Std. Dev. |
|---|---|---|
| $\Delta\Gamma_{B_s^0}$ | $-0.010 \pm 0.056$ | $1.094 \pm 0.047$ |
| $p_0^{SSK} - <\eta^{SSK}>$ | $-0.086 \pm 0.042$ | $0.876 \pm 0.039$ |
| $p_0^{OS} - <\eta^{OS}>$ | $-0.057 \pm 0.048$ | $0.989 \pm 0.041$ |
| $1/2\Delta p_0^{SSK}$ | $0.340 \pm 0.064$ | $1.274 \pm 0.059$ |
| $1/2\Delta p_0^{OS}$ | $0.070 \pm 0.051$ | $1.004 \pm 0.044$ |
| $p_1^{SSK}$ | $0.041 \pm 0.052$ | $1.044 \pm 0.047$ |
| $p_1^{OS}$ | $-0.077 \pm 0.052$ | $1.046 \pm 0.047$ |
| $1/2\Delta p_1^{SSK}$ | $-0.249 \pm 0.054$ | $1.101 \pm 0.048$ |
| $1/2\Delta p_1^{OS}$ | $-0.049 \pm 0.050$ | $1.010 \pm 0.046$ |
| $p_0^{\sigma_t}(2012)$ | $-0.222 \pm 0.049$ | $0.870 \pm 0.051$ |
| $p_1^{\sigma_t}(2012)$ | $-0.121 \pm 0.051$ | $0.993 \pm 0.059$ |
| $\delta_0^{TT}$ | $0.122 \pm 0.064$ | $1.288 \pm 0.073$ |
| $f_{VS}$ | $0.010 \pm 0.058$ | $1.138 \pm 0.060$ |
| $\delta_{\perp 1}^{TT}$ | $-0.113 \pm 0.051$ | $1.031 \pm 0.052$ |
| $\delta_0^{TV}$ | $-0.310 \pm 0.045$ | $0.923 \pm 0.038$ |
| $\delta_\perp^{TV}$ | $-0.065 \pm 0.054$ | $1.072 \pm 0.048$ |
| $f_{\parallel 2}^{TT}$ | $0.009 \pm 0.047$ | $0.908 \pm 0.043$ |
| $f_{SV}$ | $-0.101 \pm 0.057$ | $1.080 \pm 0.051$ |
| $f_{SS}$ | $-0.107 \pm 0.043$ | $0.882 \pm 0.035$ |
| $f_{ST}$ | $0.086 \pm 0.055$ | $0.981 \pm 0.052$ |
| $f_{VT}$ | $-0.134 \pm 0.054$ | $1.059 \pm 0.054$ |
| $f_L^{VT}$ | $-0.084 \pm 0.047$ | $0.946 \pm 0.046$ |
| $f_L^{VV}$ | $0.168 \pm 0.039$ | $0.776 \pm 0.034$ |
| $f_{VV}$ | $0.115 \pm 0.047$ | $0.940 \pm 0.042$ |
| $\delta_\parallel^{TV}$ | $-0.059 \pm 0.053$ | $1.043 \pm 0.045$ |
| $f_\perp^{VT}$ | $-0.075 \pm 0.049$ | $0.963 \pm 0.042$ |
| $f_\perp^{VV}$ | $-0.152 \pm 0.047$ | $0.938 \pm 0.043$ |
| $\delta^{ST}$ | $0.520 \pm 0.061$ | $0.913 \pm 0.062$ |
| $\delta^{TS}$ | $-0.062 \pm 0.057$ | $1.126 \pm 0.046$ |
| $f_\parallel^{VT}$ | $0.144 \pm 0.043$ | $0.837 \pm 0.036$ |
| $\delta_{\perp 2}^{TT}$ | $-0.073 \pm 0.059$ | $1.104 \pm 0.053$ |
| $f_\parallel^{VV}$ | $-0.057 \pm 0.050$ | $1.008 \pm 0.045$ |
| $f_{\perp 1}^{TT}$ | $-0.081 \pm 0.046$ | $0.952 \pm 0.040$ |
| $\delta^{VS}$ | $-0.204 \pm 0.053$ | $1.037 \pm 0.046$ |
| $f_\perp^{TV}$ | $-0.119 \pm 0.062$ | $1.075 \pm 0.063$ |
| $\delta_{\parallel 2}^{TT}$ | $-0.104 \pm 0.045$ | $0.878 \pm 0.045$ |
| $f_{TT}$ | $0.449 \pm 0.052$ | $1.010 \pm 0.052$ |
| $f_{TV}$ | $0.102 \pm 0.054$ | $1.045 \pm 0.055$ |
| $f_{TS}$ | $-0.187 \pm 0.055$ | $1.119 \pm 0.050$ |
| $f_L^{TT}$ | $0.329 \pm 0.034$ | $0.705 \pm 0.030$ |

TABLE 7.31: Mean and standard deviation of the pull variable distributions for the fit parameters, as obtained from the 500 toy Monte Carlo experiments. Second set of parameters.

| Parameter | Mean | Std. Dev. |
|---|---|---|
| $f_{\parallel 1}^{TT}$ | $-0.156 \pm 0.043$ | $0.889 \pm 0.037$ |
| $f_{\parallel}^{TV}$ | $0.060 \pm 0.053$ | $0.975 \pm 0.051$ |
| $f_{L}^{TV}$ | $0.036 \pm 0.061$ | $1.102 \pm 0.062$ |
| $\delta_{\perp}^{VV}$ | $0.044 \pm 0.059$ | $1.089 \pm 0.052$ |
| $\delta_{\parallel}^{VT}$ | $0.043 \pm 0.051$ | $1.000 \pm 0.048$ |
| $f_{\perp 2}^{TT}$ | $-0.215 \pm 0.047$ | $0.964 \pm 0.042$ |
| $\delta^{SS}$ | $-0.077 \pm 0.058$ | $1.123 \pm 0.056$ |
| $\delta_{\perp}^{VT}$ | $-0.201 \pm 0.054$ | $1.048 \pm 0.043$ |
| $\delta^{SV}$ | $-0.030 \pm 0.056$ | $1.085 \pm 0.048$ |
| $\delta_{\parallel 1}^{TT}$ | $0.147 \pm 0.051$ | $1.032 \pm 0.045$ |
| $\delta_{\parallel}^{VV}$ | $-0.058 \pm 0.055$ | $1.101 \pm 0.048$ |
| $\delta_{0}^{VT}$ | $-0.002 \pm 0.056$ | $1.099 \pm 0.048$ |

TABLE 7.32: Mean and standard deviation of the pull variable distributions for the fit parameters, as obtained from the 500 toy Monte Carlo experiments. Third set of parameters.

written in Table 7.33, together with the pull with respect to the nominal parameters, defined as $(\lambda^{2012} - \lambda^{nom})/\sigma_{stat}(\lambda^{2012})$. They are found to be overall consistent.

### 7.8.8 Exclusive fit to the high $K\pi$ mass region

To check the consistency of the model in different regions of the $K\pi$ mass plane, the fit to data is repeated after removing a square region in this plane corresponding to $750 < M(K^+\pi^-) < 1050\,\mathrm{MeV}/c^2$ and $750 < M(K^-\pi^+) < 1050\,\mathrm{MeV}/c^2$ (the region of the $K^*(892)^0$). The form factor of the scalar $K\pi$ mass term is fixed in this fit (using the nominal values of the $c_i^{mass}$ parameters), given the lack of information from the low $K\pi$ mass region. Additionally, since the VV component is highly suppressed, the normalisation of the fit is done through the $\Re e(A^{00})$ and $\Im m(A^{00})$ terms (instead of $\Re e(A_0^{11})$ and $\Im m(A_0^{11})$), which are fixed to the values obtained in the nominal fit.

The one-dimensional projections of this alternative fit are shown in Fig. 7.28 and the measured parameters are written in Table 7.34. The pulls with respect to the nominal values, defined as $(\lambda^{alt} - \lambda^{nom})/\sigma_{stat}(\lambda^{alt})$, are also written. The deviations with respect to the nominal fit results are reasonably small, taking into account the significant loss of statistics in the region of the VV component.

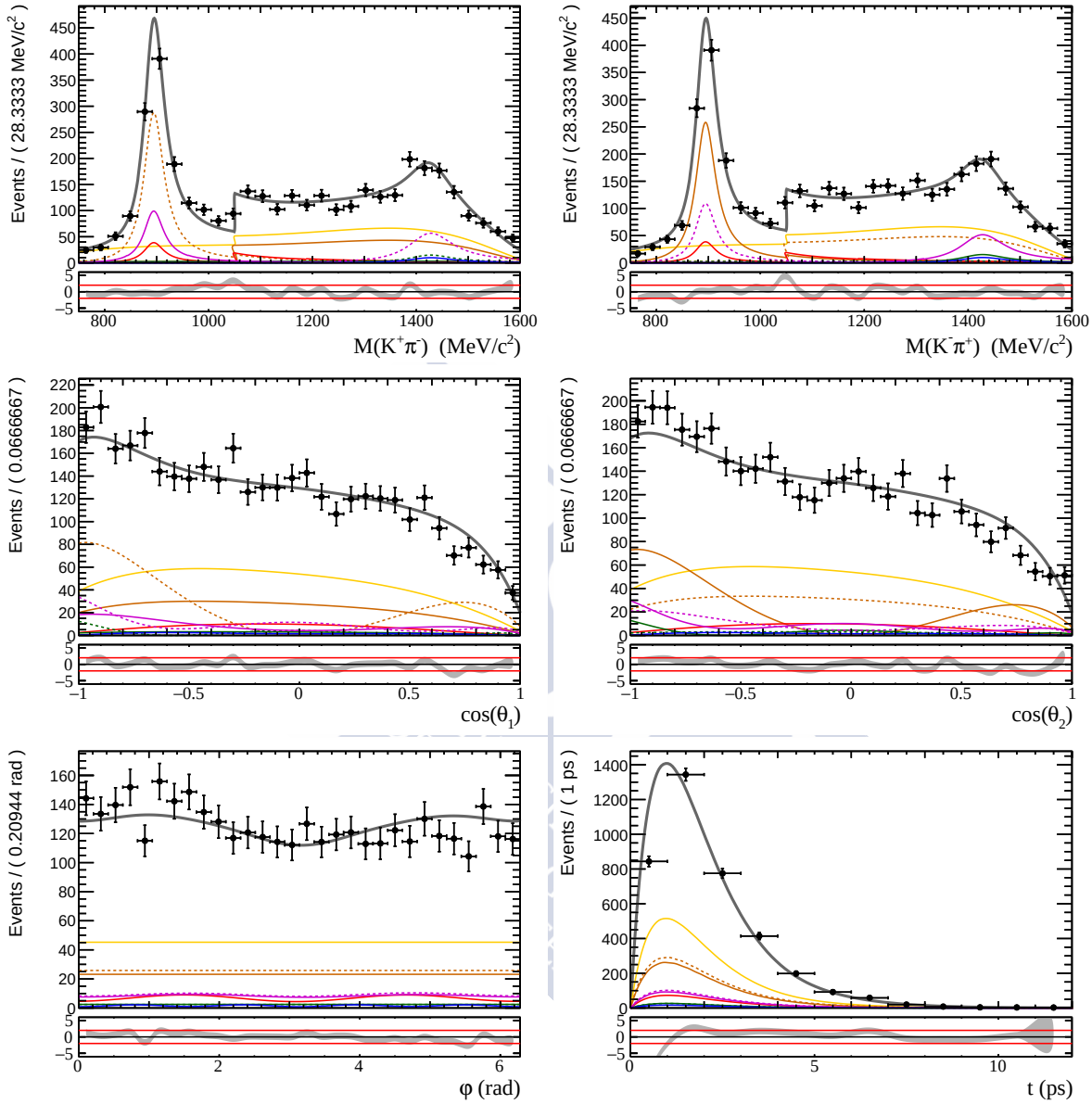



FIGURE 7.28: Result of the fit to data after excluding a square region in the 2D $K\pi$ mass plane corresponding to $750 < M(K^+\pi^-) < 1050\,\mathrm{MeV}/c^2$ and $750 < M(K^-\pi^+) < 1050\,\mathrm{MeV}/c^2$. The solid gray line represents the whole model and the black dots correspond to the sWeighted data. The individual contribution of the 9 decay channels (summing over the squared modules of the polarisation amplitudes for each channel) is also plotted, representing the VV component by a solid red line, the SV(VS) by a solid(dashed) brown line, the SS by a solid yellow line, the VT(TV) by a solid(dashed) magenta line, the ST(TS) by a solid(dashed) green line and the TT by a solid blue line. The interference terms are not shown.

| Parameter | Value | Pull | Parameter | Value | Pull |
|---|---|---|---|---|---|
| $\phi_s$ | $xxx \pm 0.1805$ | 0.9826 | $f_{\parallel}^{VT}$ | $0.0252 \pm 0.0218$ | 0.0093 |
| $\Delta^{CP}$ | $xxx \pm 0.0401$ | $-0.4228$ | $f_{TV}$ | $0.0457 \pm 0.0115$ | 0.5116 |
| $\Delta m_{B_s^0}$ | $17.6477 \pm 0.1284$ | 0.2306 | $f_L^{TV}$ | $0.6756 \pm 0.1254$ | 0.2219 |
| $f_{VV}$ | $0.0673 \pm 0.0048$ | $-1.8603$ | $f_{\parallel}^{TV}$ | $0.2090 \pm 0.0880$ | 0.6338 |
| $f_L^{VV}$ | $0.1595 \pm 0.0349$ | 0.3192 | $\delta_0^{VT}$ | $-2.5036 \pm 0.2689$ | 0.4551 |
| $f_{\parallel}^{VV}$ | $0.3673 \pm 0.0385$ | 1.5668 | $\delta_{\parallel}^{VT}$ | $-2.0426 \pm 0.4554$ | 0.7417 |
| $\delta_{\parallel}^{VV}$ | $1.9653 \pm 0.1580$ | $-0.7764$ | $\delta_{\perp}^{VT}$ | $2.3770 \pm 0.4700$ | $-0.3357$ |
| $\delta_{\perp}^{VV}$ | $1.8759 \pm 0.4460$ | $-0.1422$ | $\delta_0^{TV}$ | $0.9439 \pm 0.3686$ | $-1.7307$ |
| $f_{SV}$ | $0.3212 \pm 0.0254$ | $-0.5456$ | $\delta_{\parallel}^{TV}$ | $0.4348 \pm 0.2583$ | $-0.7018$ |
| $f_{VS}$ | $0.0934 \pm 0.0245$ | $-1.5087$ | $\delta_{\perp}^{TV}$ | $-0.6806 \pm 0.8778$ | 0.0861 |
| $\delta^{SV}$ | $-1.9895 \pm 0.1814$ | $-0.9028$ | $f_{TT}$ | $0.0089 \pm 0.0035$ | $-0.0736$ |
| $\delta^{VS}$ | $1.4464 \pm 0.2218$ | $-1.2046$ | $f_L^{TT}$ | $0.1243 \pm 0.1595$ | 0.5529 |
| $f_{SS}$ | $0.3099 \pm 0.0150$ | 1.8150 | $f_{\parallel 1}^{TT}$ | $0.2497 \pm 0.1815$ | $-0.2193$ |
| $\delta^{SS}$ | $0.4495 \pm 0.1530$ | $-1.1870$ | $f_{\perp 1}^{TT}$ | $0.2209 \pm 0.2387$ | $-0.3231$ |
| $f_{ST}$ | $0.0145 \pm 0.0126$ | 0.6699 | $f_{\parallel 2}^{TT}$ | $0.2757 \pm 0.2229$ | 1.1004 |
| $f_{TS}$ | $0.0241 \pm 0.0117$ | $-0.7703$ | $\delta_0^{TT}$ | $0.8563 \pm 0.7988$ | $-0.1235$ |
| $\delta^{ST}$ | $-2.8015 \pm 0.7357$ | 0.0794 | $\delta_{\parallel 1}^{TT}$ | $2.3633 \pm 0.3161$ | 0.0077 |
| $\delta^{TS}$ | $-0.5195 \pm 0.5969$ | 0.6538 | $\delta_{\perp 1}^{TT}$ | $2.1231 \pm 0.9542$ | 0.4216 |
| $f_{VT}$ | $0.1149 \pm 0.0131$ | 2.0863 | $\delta_{\parallel 2}^{TT}$ | $2.2019 \pm 0.2716$ | $-0.5373$ |
| $f_L^{VT}$ | $0.8052 \pm 0.0479$ | $-0.0807$ | $\delta_{\perp 2}^{TT}$ | $0.1788 \pm 1.2784$ | 0.3815 |

TABLE 7.33: Parameters obtained in the fit to the 2012 data alone and pulls with respect to the values obtained in the nominal fit.

| Parameter | Value | Pull | Parameter | Value | Pull |
|---|---|---|---|---|---|
| $\phi_s$ | $xxx \pm 0.1463$ | 0.3964 | $f_{\parallel}^{VT}$ | $0.0230 \pm 0.0154$ | $-0.1293$ |
| $\Delta^{CP}$ | $xxx \pm 0.0346$ | 1.7063 | $f_{TV}$ | $0.0189 \pm 0.0050$ | $-4.1567$ |
| $\Delta m_{B_s^0}$ | $17.7828 \pm 0.1173$ | 1.4036 | $f_L^{TV}$ | $0.3884 \pm 0.1809$ | $-1.4341$ |
| $f_{VV}$ | $0.1599 \pm 0.0187$ | 4.4823 | $f_{\parallel}^{TV}$ | $0.3346 \pm 0.1084$ | 1.6735 |
| $f_L^{VV}$ | $0.2097 \pm 0.0716$ | 0.8559 | $\delta_0^{VT}$ | $-2.2546 \pm 0.1843$ | 2.0152 |
| $f_{\parallel}^{VV}$ | $0.2773 \pm 0.0575$ | $-0.5173$ | $\delta_{\parallel}^{VT}$ | $-2.5211 \pm 0.3359$ | $-0.4192$ |
| $\delta_{\parallel}^{VV}$ | $2.0702 \pm 0.1017$ | $-0.1745$ | $\delta_{\perp}^{VT}$ | $-2.9893 \pm 0.3545$ | $-15.5813$ |
| $\delta_{\perp}^{VV}$ | $2.8713 \pm 0.3658$ | 2.5481 | $\delta_0^{TV}$ | $1.3405 \pm 0.5427$ | $-0.4447$ |
| $f_{SV}$ | $0.3354 \pm 0.0173$ | 0.0202 | $\delta_{\parallel}^{TV}$ | $0.7569 \pm 0.1908$ | 0.7376 |
| $f_{VS}$ | $0.0711 \pm 0.0161$ | $-3.6826$ | $\delta_{\perp}^{TV}$ | $0.4075 \pm 0.5219$ | 2.2296 |
| $\delta^{SV}$ | $-1.7201 \pm 0.0967$ | 1.0921 | $f_{TT}$ | $0.0091 \pm 0.0024$ | $-0.0331$ |
| $\delta^{VS}$ | $1.3648 \pm 0.1987$ | $-1.7550$ | $f_L^{TT}$ | $0.0572 \pm 0.0846$ | 0.2494 |
| $f_{SS}$ | $0.2757 \pm 0.0122$ | $-0.5602$ | $f_{\parallel 1}^{TT}$ | $0.2998 \pm 0.1411$ | 0.0733 |
| $\delta^{SS}$ | 0.6312 | 0 | $f_{\perp 1}^{TT}$ | $0.3027 \pm 0.1696$ | 0.0276 |
| $f_{ST}$ | $0.0156 \pm 0.0075$ | 1.2620 | $f_{\parallel 2}^{TT}$ | $0.0223 \pm 0.0726$ | $-0.1123$ |
| $f_{TS}$ | $0.0155 \pm 0.0078$ | $-2.2577$ | $\delta_0^{TT}$ | $1.1259 \pm 0.8570$ | 0.1995 |
| $\delta^{ST}$ | $-2.3184 \pm 0.3625$ | 1.4937 | $\delta_{\parallel 1}^{TT}$ | $2.3873 \pm 0.2170$ | 0.1220 |
| $\delta^{TS}$ | $-0.3523 \pm 0.3357$ | 1.6603 | $\delta_{\perp 1}^{TT}$ | $2.7216 \pm 0.6358$ | 1.5740 |
| $f_{VT}$ | $0.0986 \pm 0.0086$ | 1.2795 | $\delta_{\parallel 2}^{TT}$ | $2.3207 \pm 0.6122$ | $-0.0444$ |
| $f_L^{VT}$ | $0.8637 \pm 0.0314$ | 1.7379 | $\delta_{\perp 2}^{TT}$ | $0.7865 \pm 0.6099$ | 1.7960 |

TABLE 7.34: Parameters obtained in the fit to data after excluding a square region in the 2D $K\pi$ mass plane corresponding to $750 < M(K^+\pi^-) < 1050\,\mathrm{MeV}/c^2$ and $750 < M(K^-\pi^+) < 1050\,\mathrm{MeV}/c^2$. The pulls with respect to the values obtained in the nominal fit are also shown.

## 7.9 Systematic uncertainties

This section details the studies of various sources of systematic uncertainty, how they are treated and how they are propagated to the observables.

### 7.9.1 Yield of the 4-body-mass-model components

Two sets of new sWeights are computed by shifting all of the yields found in Sec. 7.2.4 up and down by $1\sigma$. For each set of weights, the time-dependent fit is re-performed and the deviations in the parameters with respect to the nominal fit are computed. The overall uncertainty is taken to be the quadrature sum of the deviations. The size of the systematic uncertainty for each parameter is shown in Table 7.35.

| Parameter | $\Delta$ (-1$\sigma_N$) | $\Delta$ (+1$\sigma_N$) | $\sigma$ | Parameter | $\Delta$ (-1$\sigma_N$) | $\Delta$ (+1$\sigma_N$) | $\sigma$ |
|---|---|---|---|---|---|---|---|
| $\phi_s$ | $-0.0071$ | $0.0027$ | $0.0076$ | $f_{\parallel}^{VT}$ | $0.0002$ | $-0.0002$ | $0.0003$ |
| $\Delta^{CP}$ | $-0.0008$ | $0.0000$ | $0.0008$ | $f_{TV}$ | $0.0002$ | $0.0001$ | $0.0002$ |
| $\Delta m_{B_s^0}$ | $-0.0020$ | $0.0016$ | $0.0026$ | $f_L^{TV}$ | $0.0220$ | $-0.0109$ | $0.0246$ |
| $f_{VV}$ | $-0.0007$ | $0.0008$ | $0.0011$ | $f_{\parallel}^{TV}$ | $-0.0134$ | $0.0048$ | $0.0142$ |
| $f_L^{VV}$ | $-0.0027$ | $0.0029$ | $0.0040$ | $\delta_0^{VT}$ | $-0.0140$ | $0.0096$ | $0.0170$ |
| $f_{\parallel}^{VV}$ | $0.0028$ | $-0.0017$ | $0.0033$ | $\delta_{\parallel}^{VT}$ | $-0.0779$ | $0.0352$ | $0.0854$ |
| $\delta_{\parallel}^{VV}$ | $-0.0010$ | $0.0079$ | $0.0079$ | $\delta_{\perp}^{VT}$ | $-0.0260$ | $0.0136$ | $0.0294$ |
| $\delta_{\perp}^{VV}$ | $-0.0116$ | $0.0126$ | $0.0172$ | $\delta_0^{TV}$ | $0.0172$ | $0.0115$ | $0.0207$ |
| $f_{SV}$ | $-0.0002$ | $-0.0007$ | $0.0008$ | $\delta_{\parallel}^{TV}$ | $0.0101$ | $0.0053$ | $0.0114$ |
| $f_{VS}$ | $-0.0012$ | $0.0018$ | $0.0022$ | $\delta_{\perp}^{TV}$ | $-0.0292$ | $0.0122$ | $0.0317$ |
| $\delta^{SV}$ | $-0.0135$ | $0.0169$ | $0.0217$ | $f_{TT}$ | $-0.0001$ | $-0.0003$ | $0.0003$ |
| $\delta^{VS}$ | $0.0075$ | $-0.0001$ | $0.0075$ | $f_L^{TT}$ | $0.0266$ | $-0.0200$ | $0.0333$ |
| $f_{SS}$ | $0.0016$ | $-0.0015$ | $0.0021$ | $f_{\parallel 1}^{TT}$ | $0.0024$ | $0.0121$ | $0.0123$ |
| $\delta^{SS}$ | $-0.0062$ | $0.0100$ | $0.0117$ | $f_{\perp 1}^{TT}$ | $-0.0221$ | $-0.0173$ | $0.0281$ |
| $f_{ST}$ | $-0.0008$ | $0.0007$ | $0.0010$ | $f_{\parallel 2}^{TT}$ | $-0.0008$ | $0.0009$ | $0.0012$ |
| $f_{TS}$ | $0.0018$ | $-0.0012$ | $0.0022$ | $\delta_0^{TT}$ | $0.0046$ | $-0.0278$ | $0.0281$ |
| $\delta^{ST}$ | $-0.0600$ | $0.0381$ | $0.0711$ | $\delta_{\parallel 1}^{TT}$ | $-0.0138$ | $0.0194$ | $0.0238$ |
| $\delta^{TS}$ | $-0.0131$ | $0.0088$ | $0.0157$ | $\delta_{\perp 1}^{TT}$ | $-0.0031$ | $0.0082$ | $0.0088$ |
| $f_{VT}$ | $-0.0006$ | $0.0004$ | $0.0007$ | $\delta_{\parallel 2}^{TT}$ | $-0.0417$ | $0.0288$ | $0.0507$ |
| $f_L^{VT}$ | $-0.0015$ | $0.0009$ | $0.0017$ | $\delta_{\perp 2}^{TT}$ | $-0.0615$ | $0.0156$ | $0.0635$ |

TABLE 7.35: Impact on the physical parameters retrieved by time-dependent fit when the 4-body-mass PDF used to obtain the sWeights has each yield parameter shifted up or down by one standard deviation, and quadrature sum of the found deviations, taken as systematic uncertainty.

### 7.9.2 Shape of the 4-body-mass-model components

The sWeights are re-produced using double Crystal Ball functions instead of the default *Ipatia* functions for the signal. Another set of sWeights is produced when swapping the combinatorial background model for a single order polynomial instead of an exponential. In both cases, the time-dependent fit is re-performed with the new set of sWeights. The quadrature sum of the absolute differences between the nominal fit and the alternate fits is taken to be the size of the systematic uncertainty for each observable. The quantities are shown in Table 7.36.

| Parameter | $\Delta$ (signal) | $\Delta$ (bkg.) | $\sigma$ | Parameter | $\Delta$ (signal) | $\Delta$ (bkg.) | $\sigma$ |
|---|---|---|---|---|---|---|---|
| $\phi_s$ | $-0.0016$ | $-0.0094$ | 0.0095 | $f_{\parallel}^{VT}$ | 0.0001 | 0.0005 | 0.0005 |
| $\Delta^{CP}$ | 0.0005 | 0.0004 | 0.0006 | $f_{TV}$ | 0.0001 | 0.0006 | 0.0006 |
| $\Delta m_{B_s^0}$ | 0.0002 | $-0.0028$ | 0.0028 | $f_L^{TV}$ | 0.0001 | 0.0353 | 0.0353 |
| $f_{VV}$ | 0.0001 | $-0.0007$ | 0.0007 | $f_{\parallel}^{TV}$ | $-0.0007$ | $-0.0202$ | 0.0202 |
| $f_L^{VV}$ | 0.0002 | $-0.0007$ | 0.0008 | $\delta_0^{VT}$ | $-0.0007$ | $-0.0158$ | 0.0158 |
| $f_{\parallel}^{VV}$ | $-0.0002$ | 0.0024 | 0.0024 | $\delta_{\parallel}^{VT}$ | $-0.0095$ | $-0.0692$ | 0.0699 |
| $\delta_{\parallel}^{VV}$ | 0.0011 | 0.0075 | 0.0076 | $\delta_{\perp}^{VT}$ | $-0.0029$ | $-0.0459$ | 0.0460 |
| $\delta_{\perp}^{VV}$ | $-0.0000$ | $-0.0103$ | 0.0103 | $\delta_0^{TV}$ | 0.0092 | 0.0479 | 0.0487 |
| $f_{SV}$ | 0.0000 | $-0.0021$ | 0.0021 | $\delta_{\parallel}^{TV}$ | 0.0031 | 0.0135 | 0.0139 |
| $f_{VS}$ | 0.0004 | $-0.0017$ | 0.0017 | $\delta_{\perp}^{TV}$ | $-0.0052$ | $-0.0571$ | 0.0573 |
| $\delta^{SV}$ | 0.0006 | $-0.0064$ | 0.0065 | $f_{TT}$ | $-0.0002$ | $-0.0001$ | 0.0003 |
| $\delta^{VS}$ | $-0.0010$ | 0.0219 | 0.0219 | $f_L^{TT}$ | 0.0002 | 0.0297 | 0.0297 |
| $f_{SS}$ | $-0.0006$ | 0.0037 | 0.0037 | $f_{\parallel 1}^{TT}$ | 0.0103 | $-0.0099$ | 0.0143 |
| $\delta^{SS}$ | 0.0010 | $-0.0020$ | 0.0022 | $f_{\perp 1}^{TT}$ | $-0.0213$ | $-0.0107$ | 0.0239 |
| $f_{ST}$ | 0.0002 | $-0.0015$ | 0.0015 | $f_{\parallel 2}^{TT}$ | $-0.0000$ | $-0.0011$ | 0.0011 |
| $f_{TS}$ | $-0.0001$ | 0.0030 | 0.0030 | $\delta_0^{TT}$ | $-0.0212$ | 0.0153 | 0.0262 |
| $\delta^{ST}$ | 0.0016 | $-0.0856$ | 0.0856 | $\delta_{\parallel 1}^{TT}$ | 0.0045 | $-0.0127$ | 0.0135 |
| $\delta^{TS}$ | 0.0007 | $-0.0165$ | 0.0165 | $\delta_{\perp 1}^{TT}$ | 0.0028 | $-0.0001$ | 0.0028 |
| $f_{VT}$ | 0.0002 | $-0.0011$ | 0.0011 | $\delta_{\parallel 2}^{TT}$ | 0.0193 | 0.0573 | 0.0604 |
| $f_L^{VT}$ | $-0.0001$ | $-0.0022$ | 0.0022 | $\delta_{\perp 2}^{TT}$ | $-0.0106$ | $-0.0935$ | 0.0941 |

TABLE 7.36: Impact on the physical parameters retrieved by the time-dependent fit when the 4-body-mass PDF used to obtain the sWeights has either the signal component replaced with a double Crystal Ball function instead of an Ipatia function or the combinatorial background component replaced with a single order polynomial instead of an exponential function. Also shown are the associated systematic uncertainties.

### 7.9.3 Correlations in the sWeights

The method of the sWeights assumes no correlation between the 4-body mass and the analysis variables. To asses the effect of residual correlations with the $\cos(\theta)$ variables, the 4-body mass fit is re-performed using data in different bins of the $\cos(\theta)$ for the reconstructed $K^{*0}$ and $\overline{K}^{*0}$. Four sub-categories are defined for events where i) both the $K^{*0}$ and $\overline{K}^{*0}$ candidates have $\cos(\theta) < 0$, ii) the $K^{*0}$ candidate has $\cos(\theta) > 0$ and the $\overline{K}^{*0}$ candidate has $\cos(\theta) < 0$, iii) the $K^{*0}$ candidate has $\cos(\theta) < 0$ and the $\overline{K}^{*0}$ candidate has $\cos(\theta) > 0$ and iv) both the $K^{*0}$ and $\overline{K}^{*0}$ candidates have $\cos(\theta) > 0$. The results of the mass fit in each sub-category are used to obtain sWeights for the whole data sample and the time-dependent fit is re-performed using those weights. The largest difference with respect to the nominal fit results is taken as the systematic uncertainty. The values found are shown in Table 7.37.

| Parameter | $\Delta$ (bin 1) | $\Delta$ (bin 2) | $\Delta$ (bin 3) | $\Delta$ (bin 4) | $\sigma$ |
|---|---|---|---|---|---|
| $\phi_s$ | 0.0115 | −0.0112 | −0.0030 | −0.0083 | 0.0115 |
| $\Delta^{CP}$ | −0.0003 | 0.0019 | 0.0003 | −0.0068 | 0.0068 |
| $\Delta m_{B_s^0}$ | 0.0051 | −0.0012 | −0.0020 | −0.0145 | 0.0145 |
| $f_{VV}$ | 0.0015 | −0.0012 | 0.0004 | −0.0014 | 0.0015 |
| $f_L^{VV}$ | 0.0057 | −0.0037 | 0.0042 | −0.0052 | 0.0057 |
| $f_\parallel^{VV}$ | −0.0053 | 0.0053 | −0.0013 | 0.0047 | 0.0053 |
| $\delta_\parallel^{VV}$ | −0.0007 | 0.0076 | 0.0182 | −0.0240 | 0.0240 |
| $\delta_\perp^{VV}$ | 0.0180 | −0.0059 | 0.0035 | −0.1123 | 0.1123 |
| $f_{SV}$ | −0.0007 | −0.0010 | −0.0040 | −0.0034 | 0.0040 |
| $f_{VS}$ | 0.0046 | −0.0031 | 0.0006 | −0.0016 | 0.0046 |
| $\delta^{SV}$ | 0.0184 | −0.0122 | 0.0192 | −0.0489 | 0.0489 |
| $\delta^{VS}$ | −0.0144 | 0.0195 | 0.0218 | 0.0096 | 0.0218 |
| $f_{SS}$ | −0.0044 | 0.0041 | 0.0029 | 0.0046 | 0.0046 |
| $\delta^{SS}$ | 0.0088 | −0.0051 | 0.0140 | −0.0468 | 0.0468 |
| $f_{ST}$ | 0.0016 | −0.0018 | −0.0011 | −0.0036 | 0.0036 |
| $f_{TS}$ | −0.0039 | 0.0041 | 0.0018 | 0.0063 | 0.0063 |
| $\delta^{ST}$ | 0.0931 | −0.1513 | −0.0509 | −0.1471 | 0.1513 |
| $\delta^{TS}$ | −0.0039 | −0.0252 | −0.0035 | −0.1047 | 0.1047 |
| $f_{VT}$ | 0.0011 | −0.0015 | −0.0007 | −0.0019 | 0.0019 |
| $f_L^{VT}$ | 0.0008 | −0.0028 | 0.0020 | −0.0012 | 0.0028 |
| $f_\parallel^{VT}$ | −0.0005 | 0.0007 | 0.0005 | −0.0013 | 0.0013 |
| $f_{TV}$ | 0.0005 | 0.0004 | 0.0004 | 0.0010 | 0.0010 |
| $f_L^{TV}$ | −0.0195 | 0.0432 | 0.0167 | 0.0420 | 0.0432 |
| $f_\parallel^{TV}$ | 0.0075 | −0.0248 | −0.0102 | −0.0285 | 0.0285 |
| $\delta_0^{VT}$ | 0.0010 | −0.0250 | −0.0031 | −0.0159 | 0.0250 |
| $\delta_\parallel^{VT}$ | 0.0454 | −0.1257 | −0.0139 | 0.0125 | 0.1257 |
| $\delta_\perp^{VT}$ | 0.0352 | −0.0481 | −0.0188 | −0.1308 | 0.1308 |
| $\delta_0^{TV}$ | −0.0079 | 0.0597 | 0.0799 | −0.0622 | 0.0799 |
| $\delta_\parallel^{TV}$ | 0.0127 | 0.0162 | 0.0173 | −0.0730 | 0.0730 |
| $\delta_\perp^{TV}$ | 0.0316 | −0.0512 | −0.0279 | −0.1495 | 0.1495 |
| $f_{TT}$ | −0.0003 | 0.0000 | −0.0003 | −0.0000 | 0.0003 |
| $f_L^{TT}$ | −0.0573 | 0.0663 | 0.0123 | 0.0365 | 0.0663 |
| $f_{\parallel 1}^{TT}$ | 0.0252 | −0.0091 | −0.0150 | −0.0198 | 0.0252 |
| $f_{\perp 1}^{TT}$ | −0.0238 | −0.0197 | −0.0058 | −0.0153 | 0.0238 |
| $f_{\parallel 2}^{TT}$ | 0.0022 | −0.0023 | −0.0009 | 0.0004 | 0.0023 |
| $\delta_0^{TT}$ | −0.1471 | 0.0859 | −0.0225 | −0.0734 | 0.1471 |
| $\delta_{\parallel 1}^{TT}$ | 0.0331 | −0.0271 | 0.0045 | −0.0462 | 0.0462 |
| $\delta_{\perp 1}^{TT}$ | −0.0100 | −0.0039 | −0.0055 | −0.1118 | 0.1118 |
| $\delta_{\parallel 2}^{TT}$ | 0.0907 | −0.0517 | 0.1227 | −0.0647 | 0.1227 |
| $\delta_{\perp 2}^{TT}$ | 0.0448 | −0.1176 | −0.0714 | −0.2149 | 0.2149 |

TABLE 7.37: Impact on the physical parameters when re-computing the sWeights using 4-body-mass fits to data sub-samples that correspond to different $\cos(\theta)$ regions, and associated systematic uncertainties.

| Parameter | Bias | $\sigma$ | Parameter | Bias | $\sigma$ |
|---|---|---|---|---|---|
| $\phi_s$ | $-0.0001$ | 0.0058 | $f_\parallel^{VT}$ | 0.0024 | 0.0024 |
| $\Delta^{CP}$ | 0.0009 | 0.0019 | $f_{TV}$ | 0.0015 | 0.0015 |
| $\Delta m_{B_s^0}$ | $-0.0011$ | 0.0047 | $f_L^{TV}$ | 0.0049 | 0.0084 |
| $f_{VV}$ | 0.0005 | 0.0005 | $f_\parallel^{TV}$ | 0.0046 | 0.0046 |
| $f_L^{VV}$ | 0.0055 | 0.0055 | $\delta_0^{VT}$ | $-0.0005$ | 0.0119 |
| $f_\parallel^{VV}$ | $-0.0018$ | 0.0018 | $\delta_\parallel^{VT}$ | 0.0208 | 0.0247 |
| $\delta_\parallel^{VV}$ | $-0.0071$ | 0.0071 | $\delta_\perp^{VT}$ | $-0.0693$ | 0.0693 |
| $\delta_\perp^{VV}$ | 0.0125 | 0.0168 | $\delta_0^{TV}$ | $-0.0617$ | 0.0617 |
| $f_{SV}$ | $-0.0027$ | 0.0027 | $\delta_\parallel^{TV}$ | $-0.0174$ | 0.0174 |
| $f_{VS}$ | 0.0003 | 0.0015 | $\delta_\perp^{TV}$ | $-0.0296$ | 0.0296 |
| $\delta^{SV}$ | $-0.0037$ | 0.0070 | $f_{TT}$ | 0.0012 | 0.0012 |
| $\delta^{VS}$ | $-0.0273$ | 0.0273 | $f_L^{TT}$ | 0.0217 | 0.0217 |
| $f_{SS}$ | $-0.0013$ | 0.0013 | $f_{\parallel 1}^{TT}$ | $-0.0220$ | 0.0220 |
| $\delta^{SS}$ | $-0.0087$ | 0.0087 | $f_{\perp 1}^{TT}$ | $-0.0142$ | 0.0142 |
| $f_{ST}$ | 0.0005 | 0.0005 | $f_{\parallel 2}^{TT}$ | 0.0008 | 0.0042 |
| $f_{TS}$ | $-0.0016$ | 0.0016 | $\delta_0^{TT}$ | 0.1266 | 0.1266 |
| $\delta^{ST}$ | 0.2480 | 0.2480 | $\delta_{\parallel 1}^{TT}$ | 0.0364 | 0.0364 |
| $\delta^{TS}$ | $-0.0166$ | 0.0166 | $\delta_{\perp 1}^{TT}$ | $-0.0682$ | 0.0682 |
| $f_{VT}$ | $-0.0022$ | 0.0022 | $\delta_{\parallel 2}^{TT}$ | $-0.0578$ | 0.0578 |
| $f_L^{VT}$ | $-0.0037$ | 0.0037 | $\delta_{\perp 2}^{TT}$ | $-0.0395$ | 0.0395 |

TABLE 7.38: Biases on the fit parameters induced by the fitting machinery, as computed from toy Monte Carlo experiments, and associated systematic uncertainties.

### 7.9.4 Bias of the time-dependent amplitude fit

The studies with toy Monte Carlo experiments performed in Sect. 7.8.5 are used to estimate the biases on the fit parameters induced by the fitting machinery. These biases are obtained by multiplying the mean of the pull distributions (written in Table 7.30, Table 7.31 and Table 7.32) by the statistical uncertainty of each parameter, retrieved from the nominal fit. A symmetric systematic uncertainty is estimated as the maximum between the bias and its uncertainty (obtained from the one of the mean). The biases and the related systematic uncertainties are written in Table 7.38.

### 7.9.5 Meson-radius parameter in Blatt-Weisskopf functions

The effective meson-radius parameter, $d$, introduced in Table 3.3, is fixed in the nominal fit to the value $d = 1.6$ GeV $^{-1}$. The effect of fixing this parameter is studied by repeating the fit with alternative choices for the value. If the parameter is left free in the full fit, it is pushed to values close to 0, but yielding a fit with poor quality. We use $d = 0$ as a minimum possible value to estimate the systematics. In the opposite direction, we try a value of $d = 3$ GeV $^{-1}$, used in several analyses (for instance, in BaBar's fits to $M(K^+\pi^-)$ in $B^0 \to J/\psi K^+\pi^-$ decays). The variation in the fitted parameters when the alternative values for $d$ are used can be seen in Table 7.39. We assign a symmetric systematic uncertainty for each parameter by taking the maximum deviation between the two cases. These uncertainties are also shown in Table 7.39.

| Parameter | $\Delta$ $(d=0)$ | $\Delta$ $(d=3)$ | $\sigma$ | Parameter | $\Delta$ $(d=0)$ | $\Delta$ $(d=3)$ | $\sigma$ |
|---|---|---|---|---|---|---|---|
| $\phi_s$ | $-0.0281$ | $-0.0185$ | $0.0281$ | $f_{\parallel}^{VT}$ | $-0.0018$ | $0.0004$ | $0.0018$ |
| $\Delta^{CP}$ | $0.0024$ | $-0.0029$ | $0.0029$ | $f_{TV}$ | $0.0033$ | $0.0039$ | $0.0039$ |
| $\Delta m_{B_s^0}$ | $-0.0106$ | $-0.0064$ | $0.0106$ | $f_L^{TV}$ | $0.0018$ | $0.0226$ | $0.0226$ |
| $f_{VV}$ | $0.0033$ | $-0.0035$ | $0.0035$ | $f_{\parallel}^{TV}$ | $0.0004$ | $-0.0167$ | $0.0167$ |
| $f_L^{VV}$ | $-0.0063$ | $0.0078$ | $0.0078$ | $\delta_0^{VT}$ | $-0.0220$ | $-0.0448$ | $0.0448$ |
| $f_{\parallel}^{VV}$ | $0.0018$ | $-0.0018$ | $0.0018$ | $\delta_{\parallel}^{VT}$ | $-0.0092$ | $-0.0914$ | $0.0914$ |
| $\delta_{\parallel}^{VV}$ | $0.0592$ | $-0.0370$ | $0.0592$ | $\delta_{\perp}^{VT}$ | $-0.0331$ | $-0.1078$ | $0.1078$ |
| $\delta_{\perp}^{VV}$ | $0.0463$ | $-0.0947$ | $0.0947$ | $\delta_0^{TV}$ | $-0.0112$ | $-0.0346$ | $0.0346$ |
| $f_{SV}$ | $0.0064$ | $-0.0117$ | $0.0117$ | $\delta_{\parallel}^{TV}$ | $-0.0026$ | $0.0128$ | $0.0128$ |
| $f_{VS}$ | $0.0013$ | $-0.0002$ | $0.0013$ | $\delta_{\perp}^{TV}$ | $-0.0514$ | $-0.1324$ | $0.1324$ |
| $\delta^{SV}$ | $0.0004$ | $-0.0164$ | $0.0164$ | $f_{TT}$ | $0.0001$ | $-0.0000$ | $0.0001$ |
| $\delta^{VS}$ | $0.0000$ | $0.0217$ | $0.0217$ | $f_L^{TT}$ | $-0.0249$ | $0.0045$ | $0.0249$ |
| $f_{SS}$ | $-0.0100$ | $0.0142$ | $0.0142$ | $f_{\parallel 1}^{TT}$ | $0.0147$ | $0.0042$ | $0.0147$ |
| $\delta^{SS}$ | $-0.0095$ | $0.0058$ | $0.0095$ | $f_{\perp 1}^{TT}$ | $-0.0562$ | $-0.0161$ | $0.0562$ |
| $f_{ST}$ | $0.0007$ | $-0.0027$ | $0.0027$ | $f_{\parallel 2}^{TT}$ | $-0.0111$ | $0.0046$ | $0.0111$ |
| $f_{TS}$ | $-0.0043$ | $0.0025$ | $0.0043$ | $\delta_0^{TT}$ | $-0.7074$ | $-0.0873$ | $0.7074$ |
| $\delta^{ST}$ | $0.1197$ | $-0.1715$ | $0.1715$ | $\delta_{\parallel 1}^{TT}$ | $-0.0487$ | $0.0108$ | $0.0487$ |
| $\delta^{TS}$ | $0.0031$ | $-0.0867$ | $0.0867$ | $\delta_{\perp 1}^{TT}$ | $-0.2625$ | $-0.1643$ | $0.2625$ |
| $f_{VT}$ | $-0.0009$ | $-0.0025$ | $0.0025$ | $\delta_{\parallel 2}^{TT}$ | $-0.0615$ | $0.0452$ | $0.0615$ |
| $f_L^{VT}$ | $-0.0003$ | $-0.0090$ | $0.0090$ | $\delta_{\perp 2}^{TT}$ | $0.0347$ | $-0.1853$ | $0.1853$ |

TABLE 7.39: Systematic uncertainties obtained when varying the meson radius parameter, $d$, in the fitting model.

### 7.9.6 Central mass and width of the $K\pi$-mass-dependent amplitudes

The central masses and widths of the Breit-Wigner functions used for the $K^*(892)^0$ and $K_2^*(1430)^0$ resonances are fixed in the nominal fit to the values written in Table 3.5. This approach is chosen to reduce the already large number of parameters under determination. To estimate a corresponding systematic uncertainty, the full fit is repeated with these parameters floated, and the results are compared with the nominal ones. For completeness, the mass and width parameters resulting from the fit are shown in Table 7.40.

| Parameter | $K^*(892)$ | $K_2^*(1430)$ |
|---|---|---|
| $M$ [ MeV/$c^2$ ] | $897.40 \pm 0.61$ | $1435.0 \pm 4.0$ |
| $\Gamma$ [ MeV ] | $51.7 \pm 1.5$ | $101.9 \pm 8.1$ |

TABLE 7.40: Breit-Wigner parameters of the $K^*(892)^0$ and $K_2^*(1430)^0$ resonances as determined from a full fit to data.

The deviations in the fit parameters with respect to the nominal values, that are shown in Table 7.41, are taken as systematic uncertainties.

| Parameter | $\Delta$ | Parameter | $\Delta$ |
|---|---|---|---|
| $\phi_s$ | 0.0070 | $f_\parallel^{VT}$ | $-0.0002$ |
| $\Delta^{CP}$ | 0.0011 | $f_{TV}$ | $-0.0009$ |
| $\Delta m_{B_s^0}$ | 0.0010 | $f_L^{TV}$ | $-0.0172$ |
| $f_{VV}$ | 0.0050 | $f_\parallel^{TV}$ | 0.0082 |
| $f_L^{VV}$ | 0.0017 | $\delta_0^{VT}$ | 0.0070 |
| $f_\parallel^{VV}$ | $-0.0017$ | $\delta_\parallel^{VT}$ | 0.0077 |
| $\delta_\parallel^{VV}$ | 0.0023 | $\delta_\perp^{VT}$ | 0.0630 |
| $\delta_\perp^{VV}$ | $-0.0050$ | $\delta_0^{TV}$ | 0.0001 |
| $f_{SV}$ | 0.0113 | $\delta_\parallel^{TV}$ | $-0.0018$ |
| $f_{VS}$ | 0.0003 | $\delta_\perp^{TV}$ | 0.0607 |
| $\delta^{SV}$ | $-0.0170$ | $f_{TT}$ | $-0.0003$ |
| $\delta^{VS}$ | $-0.0394$ | $f_L^{TT}$ | $-0.0007$ |
| $f_{SS}$ | $-0.0176$ | $f_{\parallel 1}^{TT}$ | $-0.0153$ |
| $\delta^{SS}$ | $-0.0320$ | $f_{\perp 1}^{TT}$ | 0.0128 |
| $f_{ST}$ | 0.0011 | $f_{\parallel 2}^{TT}$ | $-0.0064$ |
| $f_{TS}$ | $-0.0004$ | $\delta_0^{TT}$ | 0.0652 |
| $\delta^{ST}$ | 0.0933 | $\delta_{\parallel 1}^{TT}$ | $-0.0076$ |
| $\delta^{TS}$ | 0.0036 | $\delta_{\perp 1}^{TT}$ | 0.1574 |
| $f_{VT}$ | 0.0016 | $\delta_{\parallel 2}^{TT}$ | $-0.0663$ |
| $f_L^{VT}$ | 0.0022 | $\delta_{\perp 2}^{TT}$ | 0.0566 |

TABLE 7.41: Variation of the fit parameters when floating the $K^*(892)^0$ and $K_2^*(1430)^0$ central mass and width in the fit.

| Parameter | Value |
|---|---|
| $\alpha_1$ | $-0.854 \pm 0.038$ |
| $\alpha_2$ | $-0.381 \pm 0.040$ |
| $\alpha_3$ | $-0.105 \pm 0.032$ |
| $\alpha_4$ | $0.046 \pm 0.027$ |
| $\beta_0$ | $0.278 \pm 0.038$ |
| $\beta_1$ | $0.817 \pm 0.079$ |
| $\beta_2$ | $-0.206 \pm 0.082$ |
| $\beta_3$ | $-0.367 \pm 0.053$ |
| $\beta_4$ | $-0.115 \pm 0.040$ |

TABLE 7.42: Parameters of the model independent parameterisation of the scalar $K\pi$-mass amplitude, as determined from the fit to data.

### 7.9.7 Scalar $K\pi$-mass dependent amplitude

The difficulty of parameterising the scalar $K\pi$-mass amplitude motivates a specific study to assign a proper systematic uncertainty. In order to do so, we compare the results using the nominal mass function with those obtained with two alternative models.

First, a model independent approach is used, where the real and imaginary parts of the complex $K\pi$-mass amplitude are parameterised independently using 4th-degree polynomials:

$$\mathcal{M}_0^{MI}(m) = \left[1 + \sum_{i=1}^{4} \alpha_i \cdot T_i(X(m))\right] + i \cdot \left[\sum_{j=0}^{4} \beta_j \cdot T_j(X(m))\right], \tag{7.45}$$

where $T_i$ are Chebyshev polynomials (see Sect. 3.2.2.1 for their definition) and the $K\pi$-mass variable is mapped as:

$$m \to X(m) = \frac{m - 1175\,\mathrm{MeV}/c^2}{425\,\mathrm{MeV}/c^2}, \quad X(m) \in [-1, 1]. \tag{7.46}$$

As can be seen in Eq. 7.45, we impose normalisation by fixing to 1 the first term in the expansion of the real part of the amplitude. The rest of the coefficients, $\alpha_i$ and $\beta_i$, are floated in the alternative time-dependent fit. Their resulting values are written in Table 7.42. A comparison of the scalar mass amplitude shape for the model independent approach and the nominal parameterisation is shown in Fig. 7.29. The two amplitudes are found to be qualitatively similar.

As a second alternative model, we try the usual LASS parameterisation [66], where the mass amplitude is given by:

$$\mathcal{M}_0(m) = \frac{1}{\cot\delta_B(m) - i} + e^{2i\delta_B(m)} \frac{1}{\cot\delta_R(m) - i}. \tag{7.47}$$

The first term in the expression above corresponds to a non-resonant contribution, with the following parametrization:

$$\cot\delta_B(m) = \frac{1}{aq} + \frac{1}{2} rq, \tag{7.48}$$

where we have abbreviated $q \equiv q(m)$. The second term represents the amplitude of the $K_0^*(1430)$ resonance, with the identification:

$$\cot\delta_R(m) = \frac{M_{K_0^*(1430)}^2 - m^2}{M_{K_0^*(1430)}\Gamma_0(m)}. \tag{7.49}$$

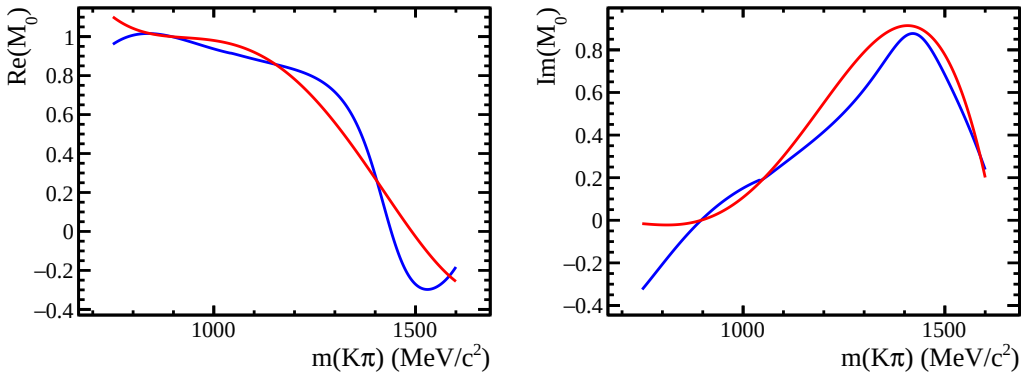



FIGURE 7.29: Line shape of the real and imaginary parts of the scalar mass amplitude. The nominal parameterisation is shown in blue and the model independent one is shown in red. For this comparision, the amplitudes are normalised by setting their module to 1 and their phase to 0 at the $K^*(892)^0$ nominal mass.

| Parameter | Value |
|---|---|
| $a$ [ MeV $^{-1}c$] | $0.06 \pm 0.15$ |
| $r$ [ MeV $^{-1}c$] | $0.0065 \pm 0.0013$ |
| $M_{K_0^*(1430)}$ [ MeV/$c^2$ ] | $1400 \pm 23$ |
| $\Gamma_{K_0^*(1430)}$ [ MeV ] | $459 \pm 33$ |

TABLE 7.43: Parameters of the LASS parameterisation resulting from the fit to data.

Above, $\Gamma_0(m)$ is the running width of a spin-0 resonance, given by:

$$\Gamma_0(m) = \Gamma_{K_0^*(1430)} \frac{q(m)}{q_0} \frac{M_{K_0^*(1430)}}{m}, \tag{7.50}$$

with $q_0 = q(M_{K_0^*(1430)})$.

We let all the LASS parameters vary in the fit, and their resulting values can be found in Table 7.43. In this case, the fit presents a bad quality, indicating that this parameterisation is not very suitable to fit the data within the considered framework.

We summarise the deviations obtained for the fit parameters when using each of the two alternative models, with respect to the nominal values, in Table 7.44. Given the poor quality of the fit with the LASS paramaterisation, it is omitted in the computation of systematic uncertainties, which are here estimated by symmeterising the deviations found then using the model-independent mass amplitude.

| Param. | $\Delta$ (Mod. Ind.) | $\Delta$ (LASS) | $\sigma$ | Param. | $\Delta$ (Mod. Ind.) | $\Delta$ (LASS) | $\sigma$ |
|---|---|---|---|---|---|---|---|
| $\phi_s$ | $-0.0052$ | $0.0222$ | $0.0052$ | $f_{\parallel}^{VT}$ | $0.0074$ | $0.0020$ | $0.0074$ |
| $\Delta^{CP}$ | $0.0019$ | $0.0144$ | $0.0019$ | $f_{TV}$ | $0.0034$ | $-0.0039$ | $0.0034$ |
| $\Delta m_{B_s^0}$ | $-0.0011$ | $0.0293$ | $0.0011$ | $f_L^{TV}$ | $0.0192$ | $-0.0811$ | $0.0192$ |
| $f_{VV}$ | $0.0014$ | $0.0079$ | $0.0014$ | $f_{\parallel}^{TV}$ | $-0.0301$ | $-0.0006$ | $0.0301$ |
| $f_L^{VV}$ | $-0.0019$ | $0.0114$ | $0.0019$ | $\delta_0^{VT}$ | $-0.1493$ | $-0.3485$ | $0.1493$ |
| $f_{\parallel}^{VV}$ | $0.0009$ | $0.0023$ | $0.0009$ | $\delta_{\parallel}^{VT}$ | $-0.0641$ | $-0.5766$ | $0.0641$ |
| $\delta_{\parallel}^{VV}$ | $0.0166$ | $-0.0732$ | $0.0166$ | $\delta_{\perp}^{VT}$ | $-0.1049$ | $-0.1947$ | $0.1049$ |
| $\delta_{\perp}^{VV}$ | $-0.0095$ | $-0.0406$ | $0.0095$ | $\delta_0^{TV}$ | $0.0471$ | $-0.2595$ | $0.0471$ |
| $f_{SV}$ | $-0.0042$ | $-0.0015$ | $0.0042$ | $\delta_{\parallel}^{TV}$ | $-0.0215$ | $-0.3251$ | $0.0215$ |
| $f_{VS}$ | $0.0096$ | $0.0037$ | $0.0096$ | $\delta_{\perp}^{TV}$ | $-0.0992$ | $-0.1581$ | $0.0992$ |
| $\delta^{SV}$ | $0.0240$ | $0.0898$ | $0.0240$ | $f_{TT}$ | $-0.0014$ | $0.0020$ | $0.0014$ |
| $\delta^{VS}$ | $-0.0167$ | $-0.0098$ | $0.0167$ | $f_L^{TT}$ | $-0.0014$ | $0.0630$ | $0.0014$ |
| $f_{SS}$ | $0.0003$ | $-0.0253$ | $0.0003$ | $f_{\parallel 1}^{TT}$ | $0.0106$ | $-0.0571$ | $0.0106$ |
| $\delta^{SS}$ | $0.0056$ | $0.2144$ | $0.0056$ | $f_{\perp 1}^{TT}$ | $0.0466$ | $0.0944$ | $0.0466$ |
| $f_{ST}$ | $-0.0007$ | $0.0062$ | $0.0007$ | $f_{\parallel 2}^{TT}$ | $-0.0198$ | $-0.0285$ | $0.0198$ |
| $f_{TS}$ | $-0.0005$ | $-0.0043$ | $0.0005$ | $\delta_0^{TT}$ | $-0.1857$ | $-0.7202$ | $0.1857$ |
| $\delta^{ST}$ | $-0.1098$ | $5.9958$ | $0.1098$ | $\delta_{\parallel 1}^{TT}$ | $-0.0242$ | $-0.7925$ | $0.0242$ |
| $\delta^{TS}$ | $-0.1633$ | $-0.2523$ | $0.1633$ | $\delta_{\perp 1}^{TT}$ | $-0.2140$ | $-0.2186$ | $0.2140$ |
| $f_{VT}$ | $-0.0078$ | $0.0153$ | $0.0078$ | $\delta_{\parallel 2}^{TT}$ | $-0.4776$ | $-2.1872$ | $0.4776$ |
| $f_L^{VT}$ | $-0.0062$ | $0.0197$ | $0.0062$ | $\delta_{\perp 2}^{TT}$ | $-0.0986$ | $-0.2115$ | $0.0986$ |

TABLE 7.44: Variation in the fit parameters when using alternative models for the scalar $K\pi$-mass amplitude.

### 7.9.8 Angular-momentum barrier factors

In the nominal fit, the orbital angular momentum of the $K\pi$ pairs in the $B_s^0$ rest frame, $L$, is fixed to the lowest allowed value for each channel, $L = |j_1 - j_2|$ (see Sect. 3.2.2 for details). This parameter only appears in one of the three form factors of Eq. 3.21, thus having a small impact on the fit results. However, to estimate the effect of using this simplification, we repeat the fit increasing the orbital angular momentum by one unit in all the possible cases. This implies to change: $0 \to 1$ in VV and TT, and $1 \to 2$ in VT and TV. The deviations between the fit parameters obtained with this configuration with respect to their nominal values, shown in Table 7.45, are taken as systematic uncertainties.

| Parameter | $\Delta$ | Parameter | $\Delta$ |
|---|---|---|---|
| $\phi_s$ | $-0.0001$ | $f_{\parallel}^{VT}$ | $0.0000$ |
| $\Delta^{CP}$ | $0.0000$ | $f_{TV}$ | $-0.0001$ |
| $\Delta m_{B_s^0}$ | $0.0002$ | $f_L^{TV}$ | $-0.0004$ |
| $f_{VV}$ | $-0.0000$ | $f_{\parallel}^{TV}$ | $0.0000$ |
| $f_L^{VV}$ | $0.0001$ | $\delta_0^{VT}$ | $0.0003$ |
| $f_{\parallel}^{VV}$ | $-0.0001$ | $\delta_{\parallel}^{VT}$ | $-0.0037$ |
| $\delta_{\parallel}^{VV}$ | $-0.0004$ | $\delta_{\perp}^{VT}$ | $-0.0005$ |
| $\delta_{\perp}^{VV}$ | $0.0002$ | $\delta_0^{TV}$ | $0.0014$ |
| $f_{SV}$ | $0.0000$ | $\delta_{\parallel}^{TV}$ | $0.0014$ |
| $f_{VS}$ | $-0.0000$ | $\delta_{\perp}^{TV}$ | $-0.0001$ |
| $\delta^{SV}$ | $0.0002$ | $f_{TT}$ | $0.0000$ |
| $\delta^{VS}$ | $-0.0005$ | $f_L^{TT}$ | $0.0004$ |
| $f_{SS}$ | $0.0001$ | $f_{\parallel 1}^{TT}$ | $0.0010$ |
| $\delta^{SS}$ | $-0.0001$ | $f_{\perp 1}^{TT}$ | $0.0011$ |
| $f_{ST}$ | $0.0000$ | $f_{\parallel 2}^{TT}$ | $-0.0006$ |
| $f_{TS}$ | $0.0000$ | $\delta_0^{TT}$ | $-0.0030$ |
| $\delta^{ST}$ | $-0.0000$ | $\delta_{\parallel 1}^{TT}$ | $-0.0012$ |
| $\delta^{TS}$ | $0.0006$ | $\delta_{\perp 1}^{TT}$ | $0.0005$ |
| $f_{VT}$ | $-0.0000$ | $\delta_{\parallel 2}^{TT}$ | $0.0021$ |
| $f_L^{VT}$ | $0.0000$ | $\delta_{\perp 2}^{TT}$ | $-0.0004$ |

TABLE 7.45: Variation of the fit parameters when increasing the orbitar angular momentum $L$ in one unity, whenever possible.

| Parameter | $K_1^*(1410)^0$ | $K_1^*(1680)^0$ |
|---|---|---|
| $M$ [ MeV/$c^2$ ] | 1414 | 1717 |
| $\Gamma$ [ MeV ] | 232 | 322 |

TABLE 7.46: Nominal mass and width [69] of the extra vector resonances considered for systematic studies.

| Parameter | Value |
|---|---|
| $\Re e(\delta)$ | $-0.0020 \pm 0.0066$ |
| $\Im m(\delta)$ | $0.0217 \pm 0.0068$ |
| $\Re e(\gamma)$ | $-0.0531 \pm 0.0077$ |
| $\Im m(\gamma)$ | $0.004 \pm 0.011$ |

TABLE 7.47: Values of the complex coupling coefficients of the $K_1^*(1410)^0$ and $K_1^*(1680)^0$ resonances, obtained from the fit to data.

### 7.9.9 High $K\pi$-mass vector resonances

In the nominal fit, any vector resonance apart from the $K^*(892)^0$ is neglected since, given the small data sample available, this expectedly small contributions represented by a large amount of unknown physical parameters would be very difficult to determine. We study the systematic effects of neglecting these components by performing a set of 100 toy Monte Carlo experiments. In each experiment, an event sample is generated from an extension of the nominal fit model which contains contributions from the $K_1^*(1410)^0$ and $K_1^*(1680)^0$ resonances. After that, the sample is fitted twice consecutively, once including these resonances in the fitting model and once excluding them. The results of the two fits are compared for each experiment and systematic uncertainties are obtained by analysing the whole set of toys. Below, the procedure is described in detail.

Prior to the toy Monte Carlo study, the extended model with the extra vector resonances is fitted to the nominal data sample, in order to get some realistic description of the new components. To reduce the number of free parameters in the fit, we make the assumption that the physical polarisation amplitudes are common to all the vector resonances. Within this approximation, the original model can be extended by substituting the vector $K\pi$-mass amplitude by a linear combination of three Breit-Wigner functions, following the isobar model:

$$\begin{aligned} \mathcal{M}_1^{alt}(m) &= BW(m, M_{K^*(892)^0}, \Gamma_{K^*(892)^0}) \\ &+ \delta \cdot BW(m, M_{K_1^*(1410)^0}, \Gamma_{K_1^*(1410)^0}) \\ &+ \gamma \cdot BW(m, M_{K_1^*(1680)^0}, \Gamma_{K_1^*(1680)^0}). \end{aligned} \tag{7.51}$$

Above, $\delta$ and $\gamma$ are complex factors that represent the coupling to the two extra resonances. The Breit-Wigner parameters (masses and widths) for the $K_1^*(1410)^0$ and the $K_1^*(1680)^0$ are fixed to the values in Table 7.46, while the $\delta$ and $\gamma$ coefficients are floated in the fit.

The projection of the fit to data on the $K^+\pi^-$ mass distribution is shown in Fig. 7.30. Overall, no big deviations are observed with respect to the nominal fit (see Fig. 7.18), and the contribution from the extra resonances is found to be very small. The measured values for the $\delta$ and $\gamma$ parameters are written in Table 7.47, their covariance matrix is shown in Table 7.48 and their correlation matrix is shown in Table 7.49.

The set of 100 experiments is generated using the toy model explained in Sect. 7.8.5, with the modification of substituting the vector $K\pi$-mass-dependent amplitude by the expression in Eq. 7.51. To account for the uncertainty on our determination of the $\delta$ and $\gamma$ coupling parameters, they are randomised for each experiment using the central values in Table 7.47 and the covariance matrix in Table 7.48. As previously stated, each sample is first fitted with a model which contains

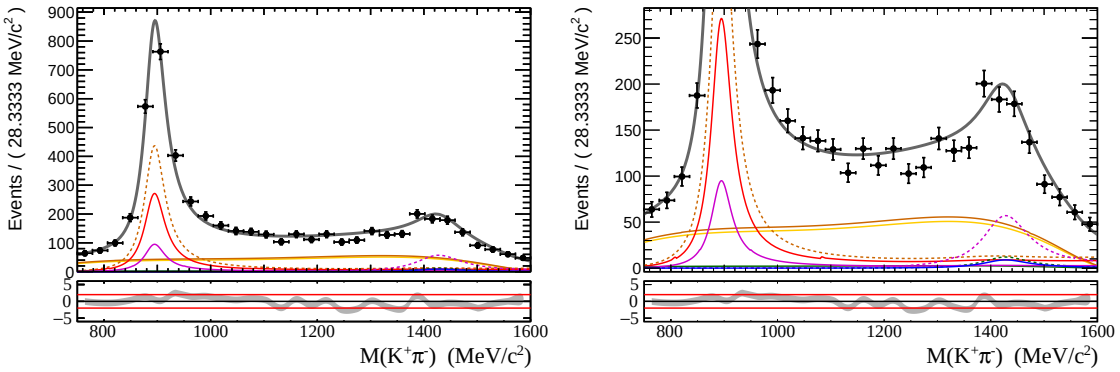



FIGURE 7.30: Projection on the $K^+\pi^-$ mass of the fit to data using the extended fitting model, which includes the $K_1^*(1410)^0$ and $K_1^*(1680)^0$ resonances in a simplified way. The same plot is shown with the usual scales on the left and with a zoom in the vertical axis on the right. The solid gray line represents the whole model and the black dots correspond to the sWeighted data. The individual contribution of the 9 decay channels (summing over the squared modules of the polarisation amplitudes for each channel) is also plotted, representing the VV component (with the two extra resonances included) by a solid red line, the SV(VS) by a solid(dashed) brown line, the SS by a solid yellow line, the VT(TV) by a solid(dashed) magenta line, the ST(TS) by a solid(dashed) green line and the TT by a solid blue line. The interference terms are not shown.

| Parameter | $\Re e(\delta)$ | $\Im m(\delta)$ | $\Re e(\gamma)$ | $\Im m(\gamma)$ |
|---|---|---|---|---|
| $\Re e(\delta)$ | $4.31e-05$ | $1.15e-06$ | $-1.45e-05$ | $-4.66e-05$ |
| $\Im m(\delta)$ | $1.15e-06$ | $4.64e-05$ | $3.12e-05$ | $-1.90e-05$ |
| $\Re e(\gamma)$ | $-1.45e-05$ | $3.12e-05$ | $5.97e-05$ | $1.86e-05$ |
| $\Im m(\gamma)$ | $-4.66e-05$ | $-1.90e-05$ | $1.86e-05$ | $1.26e-04$ |

TABLE 7.48: Covariance matrix of the complex coupling coefficients of the $K_1^*(1410)^0$ and $K_1^*(1680)^0$ resonances, obtained from the fit to data.

| Parameter | $\Re e(\delta)$ | $\Im m(\delta)$ | $\Re e(\gamma)$ | $\Im m(\gamma)$ |
|---|---|---|---|---|
| $\Re e(\delta)$ | 1 | 0.0258 | $-0.2856$ | $-0.6339$ |
| $\Im m(\delta)$ | 0.0258 | 1 | 0.5933 | $-0.2490$ |
| $\Re e(\gamma)$ | $-0.2856$ | 0.5933 | 1 | 0.2149 |
| $\Im m(\gamma)$ | $-0.6339$ | $-0.2490$ | 0.2149 | 1 |

TABLE 7.49: Correlation matrix of the complex coupling coefficients of the $K_1^*(1410)^0$ and $K_1^*(1680)^0$ resonances, obtained from the fit to data.

| Param. | $\mu$ | RMS | $\sigma$ | Param. | $\mu$ | RMS | $\sigma$ |
|---|---|---|---|---|---|---|---|
| $\phi_s$ | 0.0045 | 0.0390 | 0.0393 | $f_{\parallel}^{VT}$ | 0.0082 | 0.0152 | 0.0173 |
| $\Delta^{CP}$ | 0.0006 | 0.0124 | 0.0124 | $f_{TV}$ | 0.0020 | 0.0059 | 0.0062 |
| $\Delta m_{B_s^0}$ | 0.0038 | 0.0761 | 0.0762 | $f_L^{TV}$ | −0.0444 | 0.0573 | 0.0725 |
| $f_{VV}$ | −0.0194 | 0.0047 | 0.0200 | $f_{\parallel}^{TV}$ | 0.0025 | 0.0316 | 0.0317 |
| $f_L^{VV}$ | −0.0190 | 0.0132 | 0.0231 | $\delta_0^{VT}$ | −0.2092 | 0.1172 | 0.2398 |
| $f_{\parallel}^{VV}$ | 0.0230 | 0.0118 | 0.0258 | $\delta_{\parallel}^{VT}$ | −0.1287 | 0.1968 | 0.2352 |
| $\delta_{\parallel}^{VV}$ | −0.1581 | 0.0790 | 0.1767 | $\delta_{\perp}^{VT}$ | −0.1833 | 0.1854 | 0.2607 |
| $\delta_{\perp}^{VV}$ | 0.0032 | 0.1781 | 0.1781 | $\delta_0^{TV}$ | −0.2105 | 0.1404 | 0.2530 |
| $f_{SV}$ | −0.0355 | 0.0156 | 0.0387 | $\delta_{\parallel}^{TV}$ | −0.1804 | 0.1365 | 0.2263 |
| $f_{VS}$ | −0.0243 | 0.0134 | 0.0278 | $\delta_{\perp}^{TV}$ | −0.2838 | 0.2293 | 0.3649 |
| $\delta^{SV}$ | −0.1285 | 0.0864 | 0.1549 | $f_{TT}$ | 0.0048 | 0.0021 | 0.0052 |
| $\delta^{VS}$ | −0.2064 | 0.1003 | 0.2295 | $f_L^{TT}$ | 0.0112 | 0.0428 | 0.0442 |
| $f_{SS}$ | 0.0576 | 0.0149 | 0.0595 | $f_{\parallel 1}^{TT}$ | −0.0340 | 0.0581 | 0.0673 |
| $\delta^{SS}$ | −0.2020 | 0.0967 | 0.2240 | $f_{\perp 1}^{TT}$ | 0.0443 | 0.0728 | 0.0852 |
| $f_{ST}$ | 0.0040 | 0.0038 | 0.0056 | $f_{\parallel 2}^{TT}$ | −0.0070 | 0.0287 | 0.0296 |
| $f_{TS}$ | 0.0156 | 0.0051 | 0.0164 | $\delta_0^{TT}$ | −0.3083 | 0.9149 | 0.9655 |
| $\delta^{ST}$ | −0.4842 | 0.5070 | 0.7011 | $\delta_{\parallel 1}^{TT}$ | −0.1058 | 0.1595 | 0.1914 |
| $\delta^{TS}$ | 0.0141 | 0.1624 | 0.1630 | $\delta_{\perp 1}^{TT}$ | −0.3097 | 0.4833 | 0.5740 |
| $f_{VT}$ | −0.0049 | 0.0062 | 0.0079 | $\delta_{\parallel 2}^{TT}$ | −0.0279 | 0.6601 | 0.6607 |
| $f_L^{VT}$ | −0.0427 | 0.0286 | 0.0514 | $\delta_{\perp 2}^{TT}$ | −0.2672 | 0.3287 | 0.4236 |

TABLE 7.50: Mean and RMS of the distributions on $\lambda_i^{mod} - \lambda_i^{diff}$ for each parameter, obtained from the set of 100 toy MC experiments. Also written is the systematic uncertainty associated to neglect the $K_1^*(1410)^0$ and $K_1^*(1680)^0$ resonances in the nominal fit, computed by adding in quadrature the mean and the RMS.

the extra contributions fixed to their generation values, to obtain a set of reference parameters, $\lambda_i^{ref}$. Afterwards, the sample is refitted using the nominal model (equivalent to set $\delta = \gamma = 0$) to obtain a set of modified parameters, $\lambda_i^{mod}$. For these studies, the reduced (fast) version of the fit is used, and the $c_i^{mass}$ parameters of the fitting model are randomised for each experiment (as explained in Sect. 7.8.5). The two fits of each experiment share the same set of $c_i^{mass}$ parameters.

For the computation of systematic uncertainties, the distributions on the $\lambda_i^{mod} - \lambda_i^{ref}$ differences corresponding to the sample of 100 experiments are studied. The mean and the root mean square (RMS) of the distribution for each parameter is computed, and the values obtained are collected in Table 7.50. The systematic uncertainties written in the table are computed by adding in quadrature the mean and the RMS for each parameter.

### 7.9.10 Normalisation weights

When computing the normalisation weights, the limited size of the Monte Carlo samples induces an uncertainty which propagates into the fit parameters. To study this effect, a set of 100 experiments is performed, where the data sample is fitted using normalisation weights that have been randomised. The variation of the weights is done according to this scheme:

1. The real and imaginary parts of the normalisation weights are treated as separate elements, leading to $2 \times 190 = 380$ real quantities.

2. A set of 336 non-zero, independent normalisation weights is extracted from the previous ones, by removing multiplicities and normalisation weights that are null by construction.

3. Let's denote the previous independent weights as $\tilde{\xi}_i$. The covariance matrix of these elements, $C$, is computed using the Monte Carlo events as follows:

$$\begin{aligned} C_{ij} &= cov(\tilde{\xi}_i, \tilde{\xi}_j) = \sum_{ev=1}^{N_{events}} \mathcal{F}_i(\Omega_{ev}) \cdot \mathcal{F}_j(\Omega_{ev}) \\ &- \frac{1}{N_{events}} \cdot \left( \sum_{ev'=1}^{N_{events}} \mathcal{F}_i(\Omega_{ev'}) \right) \cdot \left( \sum_{ev''=1}^{N_{events}} \mathcal{F}_j(\Omega_{ev''}) \right), \end{aligned} \tag{7.52}$$

   where $\mathcal{F}$ correspond to the real or imaginary parts of the functions that appear in the summation of Eq. 7.19[5].

4. The previous covariance matrix is diagonalised, gaussian deviations are generated in the diagonal basis according to the covariance eigenvalues, the deviations are rotated into the original basis and finally added to the $\tilde{\xi}_i$ weights.

5. The remaining $380 - 336 = 44$ weights either remain 0, if they had this value by construction, or are assigned the value of their partner in the list of randomised $\tilde{\xi}_i$ weights.

As an extra consideration, the fit where the scalar $K\pi$-mass-amplitude parameters are free to vary is quite slow, so its reduced version is used here. To correct for the effect of fixing the $c_i^{mass}$ parameters in the fit, their values are randomised for each experiment (as explained in Sect. 7.8.5).

In summary, the fit is done by performing the following actions, in turn, per minimisation step:

1. The values of the $c_i^{mass}$ parameters are randomised.

2. The normalisation mass integrals in Eq. 3.22 are computed in the GPU using those parameters, as explained in the first bullet of Sect. 7.7.3.

3. The normalisation weights are computed using the $c_i^{mass}$ parameters and the mass integrals, as explained in the second bullet of Sect. 7.7.3.

4. The normalisation weights are randomised as explained above in this section. For an efficient computation of the covariance matrix, the values of the 336 kernel functions evaluated at each event, $\mathcal{F}_i(\Omega_{ev})$, are computed once per experiment and stored in a buffer. Then, these values are passed to the GPU and the $336 \times 336$ $C_{ij}$ elements are computed in parallel.

5. Finally, using all the previously obtained terms, the NLL is computed as explained in the third bullet of Sect. 7.7.3.

[5] Note the different use of the $ij$ indices between the two expressions. The two indices of the elements in Eq. 7.19, associated to a pair of amplitudes, collapse here into a single index, associated to a $\tilde{\xi}$ weight.

| Parameter | $\sigma$ | Parameter | $\sigma$ |
|---|---|---|---|
| $\phi_s$ | 0.1059 | $f_{\parallel}^{VT}$ | 0.0536 |
| $\Delta^{CP}$ | 0.0778 | $f_{TV}$ | 0.0271 |
| $\Delta m_{B_s^0}$ | 0.1628 | $f_L^{TV}$ | 0.1989 |
| $f_{VV}$ | 0.0042 | $f_{\parallel}^{TV}$ | 0.1018 |
| $f_L^{VV}$ | 0.0312 | $\delta_0^{VT}$ | 1.1169 |
| $f_{\parallel}^{VV}$ | 0.0291 | $\delta_{\parallel}^{VT}$ | 0.8884 |
| $\delta_{\parallel}^{VV}$ | 0.2360 | $\delta_{\perp}^{VT}$ | 1.0800 |
| $\delta_{\perp}^{VV}$ | 0.5637 | $\delta_0^{TV}$ | 0.7124 |
| $f_{SV}$ | 0.0367 | $\delta_{\parallel}^{TV}$ | 0.4165 |
| $f_{VS}$ | 0.0392 | $\delta_{\perp}^{TV}$ | 0.9466 |
| $\delta^{SV}$ | 0.2495 | $f_{TT}$ | 0.0032 |
| $\delta^{VS}$ | 0.2897 | $f_L^{TT}$ | 0.1352 |
| $f_{SS}$ | 0.0154 | $f_{\parallel 1}^{TT}$ | 0.1103 |
| $\delta^{SS}$ | 0.2561 | $f_{\perp 1}^{TT}$ | 0.1272 |
| $f_{ST}$ | 0.0137 | $f_{\parallel 2}^{TT}$ | 0.0774 |
| $f_{TS}$ | 0.0149 | $\delta_0^{TT}$ | 1.3280 |
| $\delta^{ST}$ | 1.4630 | $\delta_{\parallel 1}^{TT}$ | 0.4540 |
| $\delta^{TS}$ | 0.7192 | $\delta_{\perp 1}^{TT}$ | 1.3478 |
| $f_{VT}$ | 0.0257 | $\delta_{\parallel 2}^{TT}$ | 1.4426 |
| $f_L^{VT}$ | 0.1451 | $\delta_{\perp 2}^{TT}$ | 1.1612 |

TABLE 7.51: Systematic uncertainties associated to the size of the MC samples used to compute the normalisation weights.

The parameter values resulting from each of these experiments, $\lambda_i^{exp}$, are compared with the nominal ones, $\lambda_i^{nom}$. The distributions of the $\lambda_i^{exp} - \lambda_i^{nom}$ differences for the set of 100 experiments are shown in Appendix B. For each parameter, the root mean square of the associated distribution is taken as a systematic uncertainty. The resulting values are written in Table 7.51.

| Coef. | $c_4$ | $c_5$ | $c_6$ | $c_7$ | $c_8$ |
|---|---|---|---|---|---|
| $c_4$ | 1.0000 | 0.7005 | 0.8049 | 0.3878 | 0.7783 |
| $c_5$ | 0.7005 | 1.0000 | 0.5308 | 0.6322 | 0.6710 |
| $c_6$ | 0.8049 | 0.5308 | 1.0000 | 0.0314 | 0.8453 |
| $c_7$ | 0.3878 | 0.6322 | 0.0314 | 1.0000 | 0.0930 |
| $c_8$ | 0.7783 | 0.6710 | 0.8453 | 0.0930 | 1.0000 |

TABLE 7.52: Correlation matrix for the spline coefficients of the time acceptance, category 1.

| Coef. | $c_4$ | $c_5$ | $c_6$ | $c_7$ | $c_8$ |
|---|---|---|---|---|---|
| $c_4$ | 1.0000 | 0.7134 | 0.4923 | 0.8217 | $-0.0010$ |
| $c_5$ | 0.7134 | 1.0000 | 0.1091 | 0.9024 | 0.0028 |
| $c_6$ | 0.4923 | 0.1091 | 1.0000 | 0.2410 | $-0.0113$ |
| $c_7$ | 0.8217 | 0.9024 | 0.2410 | 1.0000 | 0.0070 |
| $c_8$ | $-0.0010$ | 0.0028 | $-0.0113$ | 0.0070 | 1.0000 |

TABLE 7.53: Correlation matrix for the spline coefficients of the time acceptance, category 2.

### 7.9.11 Decay-time acceptance: Monte Carlo statistics

The systematic uncertainties related to the size of the Monte Carlo samples used to compute the spline coefficients are obtained by performing a set of 100 experiments, where the fit to data is done using randomised spline coefficients. For each category, the spline coefficients are varied using their central values (in Table 7.16) and their covariance matrix, obtained from the fit to Monte Carlo data. We show the correlation matrix of the coefficients for each of the fit categories (defined in Table 7.12) in Table 7.52, Table 7.53, Table 7.54 and Table 7.55.

The reduced version of the fit is used in this study, and the $c_i^{mass}$ parameters are randomised for each experiment. The fit is done in a similar way as in Sect. 7.9.10 and the collection of resulting parameter values, $\lambda_i^{exp}$, are compared with those from the nominal fit, $\lambda_i^{nom}$. We construct the distributions of the $\lambda_i^{exp} - \lambda_i^{nom}$ differences for the set of 100 experiments, obtain their root mean square and use these quantities as systematic uncertainties. The resulting values for these uncertainties are written in Table 7.56.

### 7.9.12 Decay-time acceptance: configuration of knots

The position of the knots in the nominal configuration is chosen to correspond to the quantiles of the decay time distribution. An alternative configuration is tried here by placing the knots at equally-spaced positions in the decay time range, corresponding to 0, 2.4, 4.8, 7.2, 9.6 and 12 ps. The new splines obtained from Monte Carlo are shown in Fig. 7.31. The fit is redone with this

| Coef. | $c_4$ | $c_5$ | $c_6$ | $c_7$ | $c_8$ |
|---|---|---|---|---|---|
| $c_4$ | 1.0000 | 0.7104 | 0.7936 | 0.5096 | 0.7915 |
| $c_5$ | 0.7104 | 1.0000 | 0.5060 | 0.7229 | 0.6868 |
| $c_6$ | 0.7936 | 0.5060 | 1.0000 | 0.1442 | 0.8357 |
| $c_7$ | 0.5096 | 0.7229 | 0.1442 | 1.0000 | 0.2559 |
| $c_8$ | 0.7915 | 0.6868 | 0.8357 | 0.2559 | 1.0000 |

TABLE 7.54: Correlation matrix for the spline coefficients of the time acceptance, category 3.

| Coef. | $c_4$ | $c_5$ | $c_6$ | $c_7$ | $c_8$ |
|---|---|---|---|---|---|
| $c_4$ | 1.0000 | 0.6843 | 0.6388 | 0.6611 | 0.5337 |
| $c_5$ | 0.6843 | 1.0000 | 0.2643 | 0.8327 | 0.4063 |
| $c_6$ | 0.6388 | 0.2643 | 1.0000 | 0.1369 | 0.6322 |
| $c_7$ | 0.6611 | 0.8327 | 0.1369 | 1.0000 | 0.1331 |
| $c_8$ | 0.5337 | 0.4063 | 0.6322 | 0.1331 | 1.0000 |

TABLE 7.55: Correlation matrix for the spline coefficients of the time acceptance, category 4.

| Parameter | $\sigma$ | Parameter | $\sigma$ |
|---|---|---|---|
| $\phi_s$ | 0.0222 | $f_{\parallel}^{VT}$ | 0.0011 |
| $\Delta^{CP}$ | 0.0027 | $f_{TV}$ | 0.0038 |
| $\Delta m_{B_s^0}$ | 0.0047 | $f_L^{TV}$ | 0.0245 |
| $f_{VV}$ | 0.0014 | $f_{\parallel}^{TV}$ | 0.0108 |
| $f_L^{VV}$ | 0.0029 | $\delta_0^{VT}$ | 0.0167 |
| $f_{\parallel}^{VV}$ | 0.0022 | $\delta_{\parallel}^{VT}$ | 0.0383 |
| $\delta_{\parallel}^{VV}$ | 0.0179 | $\delta_{\perp}^{VT}$ | 0.0260 |
| $\delta_{\perp}^{VV}$ | 0.0168 | $\delta_0^{TV}$ | 0.0344 |
| $f_{SV}$ | 0.0044 | $\delta_{\parallel}^{TV}$ | 0.0448 |
| $f_{VS}$ | 0.0022 | $\delta_{\perp}^{TV}$ | 0.0435 |
| $\delta^{SV}$ | 0.0126 | $f_{TT}$ | 0.0011 |
| $\delta^{VS}$ | 0.0223 | $f_L^{TT}$ | 0.0098 |
| $f_{SS}$ | 0.0049 | $f_{\parallel 1}^{TT}$ | 0.0246 |
| $\delta^{SS}$ | 0.0149 | $f_{\perp 1}^{TT}$ | 0.0223 |
| $f_{ST}$ | 0.0013 | $f_{\parallel 2}^{TT}$ | 0.0081 |
| $f_{TS}$ | 0.0031 | $\delta_0^{TT}$ | 0.0807 |
| $\delta^{ST}$ | 0.1215 | $\delta_{\parallel 1}^{TT}$ | 0.0395 |
| $\delta^{TS}$ | 0.0452 | $\delta_{\perp 1}^{TT}$ | 0.0621 |
| $f_{VT}$ | 0.0043 | $\delta_{\parallel 2}^{TT}$ | 0.0598 |
| $f_L^{VT}$ | 0.0040 | $\delta_{\perp 2}^{TT}$ | 0.0693 |

TABLE 7.56: Systematic uncertainties associated to the size of the MC samples used to compute the spline coefficients of the time acceptance.

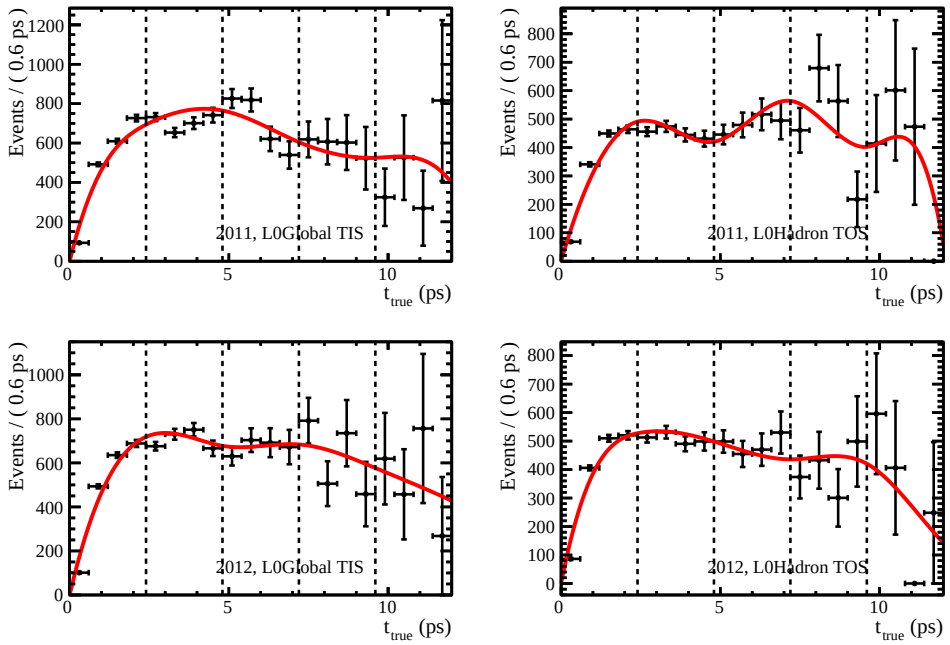



FIGURE 7.31: Spline-based parameterisation of the time acceptance, obtained from Monte Carlo, using 6 equally spaced knots.

alternative scheme and the deviations of the fit parameters with respect to the nominal ones are written in Table 7.57. The symmeterised deviations are taken as systematic uncertainties.

| Parameter | $\Delta$ | $\sigma$ | Parameter | $\Delta$ | $\sigma$ |
|---|---|---|---|---|---|
| $\phi_s$ | $-0.0582$ | $0.0582$ | $f_{\parallel}^{VT}$ | $-0.0001$ | $0.0001$ |
| $\Delta^{CP}$ | $0.0001$ | $0.0001$ | $f_{TV}$ | $0.0027$ | $0.0027$ |
| $\Delta m_{B_s^0}$ | $-0.0055$ | $0.0055$ | $f_L^{TV}$ | $0.0173$ | $0.0173$ |
| $f_{VV}$ | $0.0005$ | $0.0005$ | $f_{\parallel}^{TV}$ | $-0.0085$ | $0.0085$ |
| $f_L^{VV}$ | $-0.0018$ | $0.0018$ | $\delta_0^{VT}$ | $-0.0370$ | $0.0370$ |
| $f_{\parallel}^{VV}$ | $-0.0032$ | $0.0032$ | $\delta_{\parallel}^{VT}$ | $-0.0155$ | $0.0155$ |
| $\delta_{\parallel}^{VV}$ | $-0.0090$ | $0.0090$ | $\delta_{\perp}^{VT}$ | $-0.0409$ | $0.0409$ |
| $\delta_{\perp}^{VV}$ | $-0.0272$ | $0.0272$ | $\delta_0^{TV}$ | $-0.0022$ | $0.0022$ |
| $f_{SV}$ | $-0.0007$ | $0.0007$ | $\delta_{\parallel}^{TV}$ | $-0.0081$ | $0.0081$ |
| $f_{VS}$ | $-0.0010$ | $0.0010$ | $\delta_{\perp}^{TV}$ | $-0.0591$ | $0.0591$ |
| $\delta^{SV}$ | $-0.0178$ | $0.0178$ | $f_{TT}$ | $0.0002$ | $0.0002$ |
| $\delta^{VS}$ | $0.0039$ | $0.0039$ | $f_L^{TT}$ | $0.0016$ | $0.0016$ |
| $f_{SS}$ | $-0.0010$ | $0.0010$ | $f_{\parallel 1}^{TT}$ | $-0.0079$ | $0.0079$ |
| $\delta^{SS}$ | $-0.0116$ | $0.0116$ | $f_{\perp 1}^{TT}$ | $0.0053$ | $0.0053$ |
| $f_{ST}$ | $-0.0004$ | $0.0004$ | $f_{\parallel 2}^{TT}$ | $-0.0014$ | $0.0014$ |
| $f_{TS}$ | $0.0013$ | $0.0013$ | $\delta_0^{TT}$ | $-0.0122$ | $0.0122$ |
| $\delta^{ST}$ | $-0.1099$ | $0.1099$ | $\delta_{\parallel 1}^{TT}$ | $-0.0096$ | $0.0096$ |
| $\delta^{TS}$ | $-0.0444$ | $0.0444$ | $\delta_{\perp 1}^{TT}$ | $-0.0637$ | $0.0637$ |
| $f_{VT}$ | $-0.0014$ | $0.0014$ | $\delta_{\parallel 2}^{TT}$ | $-0.0176$ | $0.0176$ |
| $f_L^{VT}$ | $-0.0069$ | $0.0069$ | $\delta_{\perp 2}^{TT}$ | $-0.0738$ | $0.0738$ |

TABLE 7.57: Systematic uncertainties related to the chosen position of the knots used to compute the splines for the time acceptance.

### 7.9.13 Data/Monte Carlo acceptance correction

The simulated samples used to describe the acceptance and resolution are known to present some small mismodelling effects, that can propagate into the measured parameters. Particularly, in the previous time-integrated analysis of $B_s^0 \to K^{*0}\bar{K}^{*0}$ [129] it was pointed out that imperfections in the the $B_s^0$, $K$ and $\pi$ momentum distributions can impact the acceptance in $\cos(\theta_{1,2})$. To address this effect and related ones, we study in this section the biases induced by the computation of normalisation weights from simulation.

The mismodelling effects in Monte Carlo can be compensated by applying a data-driven correction. The corrected normalisation weights are used to obtain the nominal results presented in Sect. 7.7.4 and to compute systematic uncertainties, by comparing the new measured values with the uncorrected ones. In this analysis, the correction to simulation is implemented via a multi-dimensional reweighting on a set of relevant variables. Apart from the decay kinematics, the PID variable distributions are also known to be not well reproduced in simulation. These variables depend on the $K/\pi$ momentum and pseudorapidity and on the number of tracks in the event. To account for all the previous effects, the following set of variables is considered in the reweight:

- The momentum of the kaons and pions.
- The pseudorapidity of the kaons and pions.
- The transverse momentum of the $B_s^0$.
- The number of tracks.

Apart from the performance mismodelling, some deviations between the simulation and data distributions are expected due to the difference between the Monte Carlo generation model and the real $B_s^0 \to (K^+\pi^-)(K^-\pi^+)$ physical distribution. Such deviations are legitimate and should be excluded from the correction. Consequently, the reweight of the Monte Carlo which is used to correct the normalisation weights and redo the fit needs itself knowledge of the real physical parameters. This inter-dependence problem is solved by using an iterative method, which proceeds as follows:

1. Perform the fit to data without correcting the normalisation weights. Use the obtained physical parameters to construct a flavour-untagged, time-integrated and acceptance- and resolution-free version of the PDF used for fitting, which constitutes and approximation to the real, time-integrated, physical model of the decay.
2. Correct the Monte Carlo for physics, by weighting the simulated events with the previously obtained PDF divided by the generation model.
3. Use the `GBReweighter` [105] tool to obtain a set of data/MC correction weights, by comparing the physics-correct simulation samples with the sWeighted signal datasets. These weights are computed separately for the 4 fitting categories.
4. Use the per-event weights obtained in the previous step to correct the Monte Carlo samples and compute a set of corrected normalisation weights.
5. Redo the fit with the new normalisation weights. Use the resulting parameter values to update the physical model of the decay.
6. Repeat steps 2-5 until convergence is achieved.

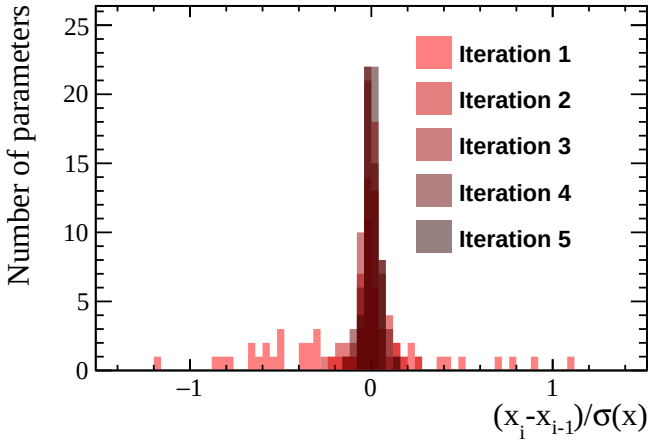



FIGURE 7.32: Evolution with the iteration step ($i$) of the distribution of the fit parameters ($x$) on the pull-like variables $(x_i - x_{i-1})/\sigma(x)$.

| Iteration ($i$) | 1 | 2 | 3 | 4 | 5 |
|---|---|---|---|---|---|
| RMS$[(x_i - x_{i-1})/\sigma(x)]$ | 0.4304 | 0.0879 | 0.0437 | 0.0484 | 0.0368 |

TABLE 7.58: Root mean square values of the distributions shown in Fig. 7.32.

The convergence of the procedure is evaluated by studying the overall behaviour of the fit parameters. With this aim, a pull-like variable is constructed for each parameter, by computing the difference between its value at a given iteration step and the one of the previous iteration, and dividing this difference by the statistical uncertainty. The distribution of the fit parameters on these variables presents a gaussian-like shape, whose width depends on the number of iterations. The evolution of this distribution for the first 5 iterations is shown in Fig. 7.32. It can be seen that the biggest deviations correspond to the first iteration, and then the distribution becomes narrower until it stabilises from the third iteration. This behaviour can be better seen by looking at the values of the RMS of each distribution, which are written in Table 7.58.

Even if no significant improvement is found after the third iteration, we apply a 5-iteration correction to follow a conservative approach. The reweight of the Monte Carlo samples at the final stage is illustrated in Fig. 7.33. The effect of the physics reweight (using the parameters measured in the fourth iteration) and the effect of the whole reweight, obtained from `GBReweighter`, are shown separately. The differences between the new measured parameters and the ones obtained from the uncorrected fit are written in Table 7.59. These deviations serve to estimate the associated systematic uncertainties.

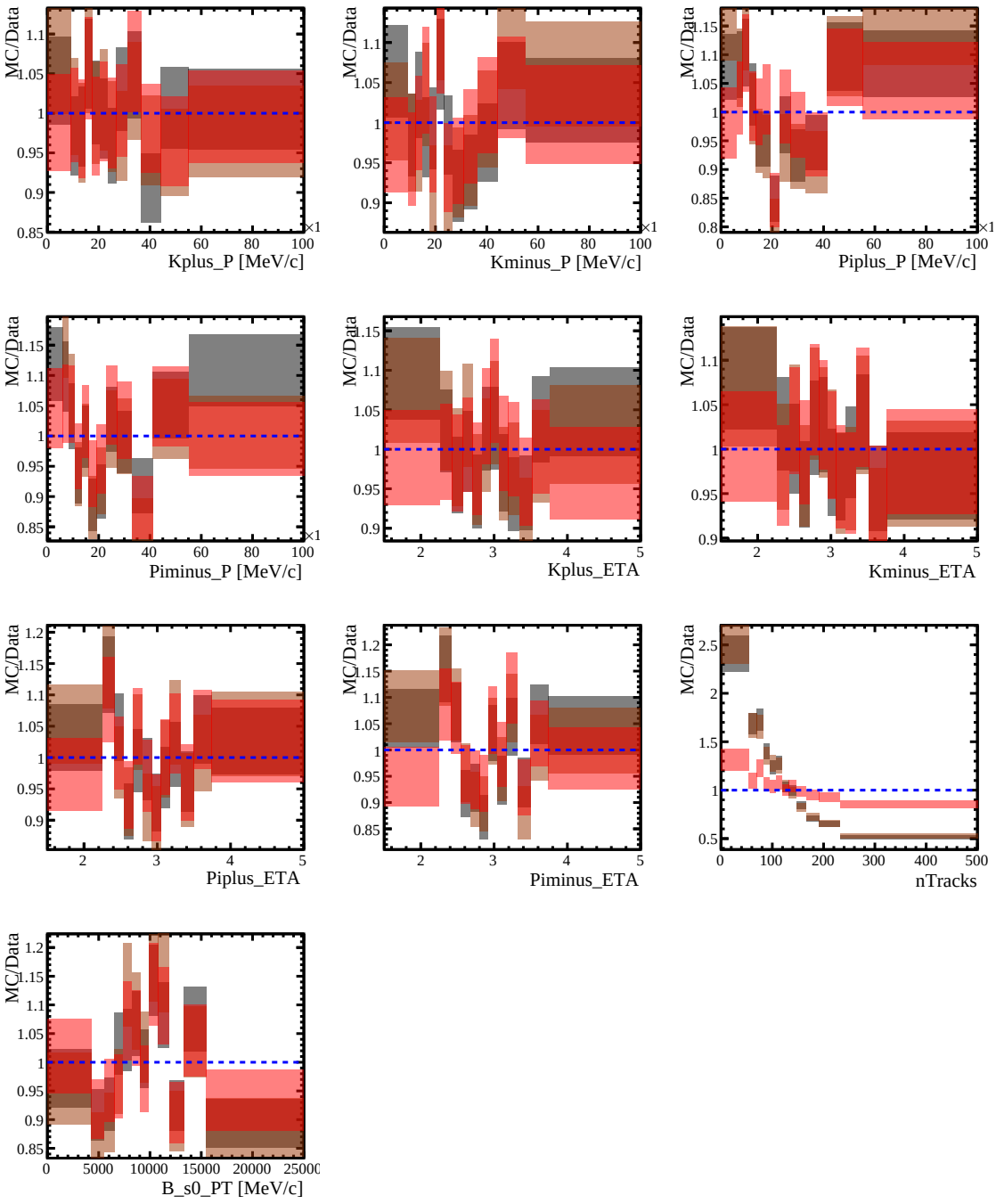



FIGURE 7.33: Reweights of the simulation samples corresponding to the last iteration. The one-dimensional projections on each of the reweight variables show the ratio between the Monte Carlo and the sWeighted data distributions. The ideal behaviour is represented by a horizontal blue line and the different steps of the reweight are represented by color bands (corresponding to the statistical uncertainties) in equal-size bins of each variable. The uncorrected Monte Carlo distribution is shown in black, the one corrected for physics is shown in brown, and the fully corrected one (physics + simulation mismodelling) is shown in red.

| Parameter | $\sigma$ | Parameter | $\sigma$ |
|---|---|---|---|
| $\phi_s$ | $-0.0025$ | $f_{\parallel}^{VT}$ | $0.0028$ |
| $\Delta^{CP}$ | $0.0072$ | $f_{TV}$ | $0.0018$ |
| $\Delta m_{B_s^0}$ | $0.0082$ | $f_L^{TV}$ | $0.0318$ |
| $f_{VV}$ | $-0.0045$ | $f_{\parallel}^{TV}$ | $-0.0061$ |
| $f_L^{VV}$ | $0.0175$ | $\delta_0^{VT}$ | $0.1547$ |
| $f_{\parallel}^{VV}$ | $0.0022$ | $\delta_{\parallel}^{VT}$ | $0.1805$ |
| $\delta_{\parallel}^{VV}$ | $0.1336$ | $\delta_{\perp}^{VT}$ | $0.1542$ |
| $\delta_{\perp}^{VV}$ | $0.1393$ | $\delta_0^{TV}$ | $0.2248$ |
| $f_{SV}$ | $0.0036$ | $\delta_{\parallel}^{TV}$ | $0.2386$ |
| $f_{VS}$ | $0.0026$ | $\delta_{\perp}^{TV}$ | $0.1449$ |
| $\delta^{SV}$ | $0.1642$ | $f_{TT}$ | $-0.0011$ |
| $\delta^{VS}$ | $0.1213$ | $f_L^{TT}$ | $0.0284$ |
| $f_{SS}$ | $-0.0166$ | $f_{\parallel 1}^{TT}$ | $0.0062$ |
| $\delta^{SS}$ | $0.1920$ | $f_{\perp 1}^{TT}$ | $-0.0502$ |
| $f_{ST}$ | $-0.0012$ | $f_{\parallel 2}^{TT}$ | $0.0217$ |
| $f_{TS}$ | $0.0008$ | $\delta_0^{TT}$ | $0.1906$ |
| $\delta^{ST}$ | $0.0491$ | $\delta_{\parallel 1}^{TT}$ | $0.2717$ |
| $\delta^{TS}$ | $0.2136$ | $\delta_{\perp 1}^{TT}$ | $0.1165$ |
| $f_{VT}$ | $0.0147$ | $\delta_{\parallel 2}^{TT}$ | $0.3257$ |
| $f_L^{VT}$ | $0.0220$ | $\delta_{\perp 2}^{TT}$ | $0.1979$ |

TABLE 7.59: Systematic uncertainties related to the mismodelling of the simulated samples used to compute the normalisation weights.

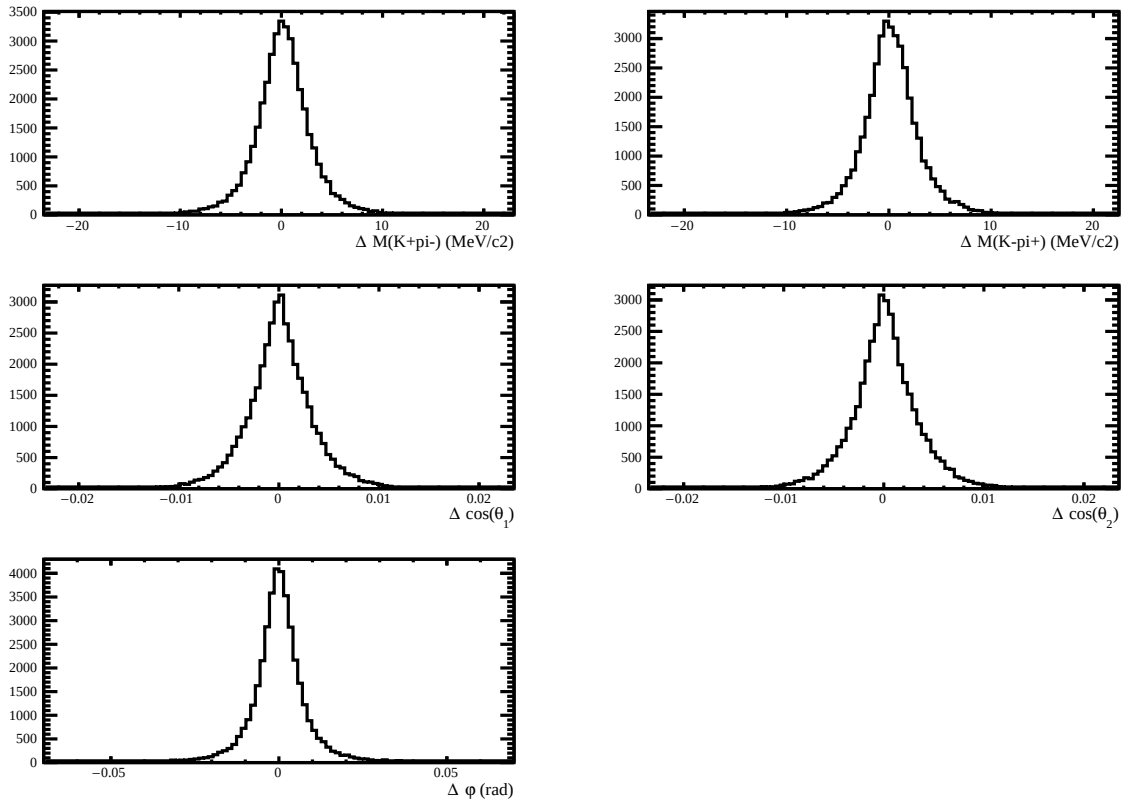



FIGURE 7.34: One-dimensional projections of the Monte Carlo distribution used to study the resolution on $K\pi$ masses and angular variables.

### 7.9.14 Angular and $K\pi$-mass resolution

The resolution on the $K\pi$ invariant masses and the angular variables is neglected in the nominal fit. Their effect is analysed in this section and toy Monte Carlo studies are performed to compute the associated systematic uncertainties.

The resolution is obtained from the combined signal Monte Carlo sample (vector-vector + phase space) with truth-matching applied, by studying the distribution of the $\Delta_i = x_i^{reco} - x_i^{true}$ differences for each variable, $x_i$. To account for the correlation among the variables, the 5-dimensional distribution is analysed as a whole. The individual projections on each variable are shown in Fig. 7.34. The observed behaviour can be approximately described by a multi-dimensional gaussian function (accounting for central displacements and variable correlations). The central values, computed from the sample mean in each dimension, $\langle\Delta_i\rangle$, are written in Table 7.60. The widths and correlation parameters of the gaussians are determined from the sample covariance matrix, $C$, whose elements are computed as follows:

$$C_{ij} = cov(\Delta_i, \Delta_j) = \frac{1}{N_{events} - 1} \sum_{ev=1}^{N_{events}} (\Delta_i^{ev} - \langle\Delta_i\rangle) \cdot (\Delta_j^{ev} - \langle\Delta_j\rangle). \tag{7.53}$$

The covariance matrix is shown in Table 7.61. For completeness, the corresponding correlation matrix can be seen in Table 7.62.

Using the previously obtained information, a resolution smearing can be applied to a given data sample by adding random variable displacements generated from the gaussian resolution model.

A set of 100 toy Monte Carlo experiments is performed, each consisting on the generation of

| Variable | $\langle \Delta_i \rangle$ |
|---|---|
| $m_{K^+\pi^-}$ [ MeV/$c^2$ ] | $1.58e-01$ |
| $m_{K^-\pi^+}$ [ MeV/$c^2$ ] | $1.47e-01$ |
| $\cos(\theta_1)$ | $9.86e-05$ |
| $\cos(\theta_2)$ | $1.17e-04$ |
| $\varphi$ [rad] | $4.78e-05$ |

TABLE 7.60: Central displacements for the $\Delta_i$ distributions used to study the resolution on $K\pi$ masses and angular variables.

| Variable | $m_{K^+\pi^-}$ [ MeV/$c^2$ ] | $m_{K^-\pi^+}$ [ MeV/$c^2$ ] | $\cos(\theta_1)$ | $\cos(\theta_2)$ | $\varphi$ [rad] |
|---|---|---|---|---|---|
| $m_{K^+\pi^-}$ [MeV/$c^2$] | $9.06e+00$ | $5.38e-01$ | $8.62e-04$ | $2.06e-04$ | $1.92e-04$ |
| $m_{K^-\pi^+}$ [MeV/$c^2$] | $5.38e-01$ | $9.07e+00$ | $1.73e-04$ | $9.62e-04$ | $-1.29e-05$ |
| $\cos(\theta_1)$ | $8.62e-04$ | $1.73e-04$ | $1.23e-05$ | $2.10e-07$ | $-6.45e-08$ |
| $\cos(\theta_2)$ | $2.06e-04$ | $9.62e-04$ | $2.10e-07$ | $1.25e-05$ | $-1.60e-07$ |
| $\varphi$ [rad] | $1.92e-04$ | $-1.29e-05$ | $-6.45e-08$ | $-1.60e-07$ | $8.86e-05$ |

TABLE 7.61: Covariance matrix of the Monte Carlo distribution used to study the resolution on $K\pi$ masses and angular variables.

| Variable | $m_{K^+\pi^-}$ [ MeV/$c^2$ ] | $m_{K^-\pi^+}$ [ MeV/$c^2$ ] | $\cos(\theta_1)$ | $\cos(\theta_2)$ | $\varphi$ [rad] |
|---|---|---|---|---|---|
| $m_{K^+\pi^-}$ [ MeV/$c^2$ ] | 1 | 0.0594 | 0.0817 | 0.0194 | 0.0068 |
| $m_{K^-\pi^+}$ [ MeV/$c^2$ ] | 0.0594 | 1 | 0.0164 | 0.0903 | −0.0005 |
| $\cos(\theta_1)$ | 0.0817 | 0.0164 | 1 | 0.0169 | −0.0020 |
| $\cos(\theta_2)$ | 0.0194 | 0.0903 | 0.0169 | 1 | −0.0048 |
| $\varphi$ [rad] | 0.0068 | −0.0005 | −0.0020 | −0.0048 | 1 |

TABLE 7.62: Correlation matrix of the Monte Carlo distribution used to study the resolution on $K\pi$ masses and angular variables.

| Param. | $\mu$ | RMS | $\sigma$ | Param. | $\mu$ | RMS | $\sigma$ |
|---|---|---|---|---|---|---|---|
| $\phi_s$ | 0.0003 | 0.0047 | 0.0047 | $f_{\parallel}^{VT}$ | $-0.0003$ | 0.0031 | 0.0031 |
| $\Delta^{CP}$ | 0.0000 | 0.0017 | 0.0017 | $f_{TV}$ | 0.0000 | 0.0014 | 0.0014 |
| $\Delta m_{B_s^0}$ | 0.0002 | 0.0088 | 0.0088 | $f_L^{TV}$ | 0.0014 | 0.0115 | 0.0116 |
| $f_{VV}$ | $-0.0001$ | 0.0003 | 0.0004 | $f_{\parallel}^{TV}$ | $-0.0007$ | 0.0070 | 0.0070 |
| $f_L^{VV}$ | $-0.0002$ | 0.0029 | 0.0029 | $\delta_0^{VT}$ | 0.0003 | 0.0323 | 0.0323 |
| $f_{\parallel}^{VV}$ | $-0.0001$ | 0.0022 | 0.0022 | $\delta_{\parallel}^{VT}$ | 0.0016 | 0.0392 | 0.0392 |
| $\delta_{\parallel}^{VV}$ | $-0.0007$ | 0.0185 | 0.0186 | $\delta_{\perp}^{VT}$ | 0.0014 | 0.0441 | 0.0441 |
| $\delta_{\perp}^{VV}$ | 0.0029 | 0.0387 | 0.0388 | $\delta_0^{TV}$ | $-0.0001$ | 0.0266 | 0.0266 |
| $f_{SV}$ | 0.0000 | 0.0026 | 0.0026 | $\delta_{\parallel}^{TV}$ | 0.0013 | 0.0320 | 0.0320 |
| $f_{VS}$ | $-0.0003$ | 0.0025 | 0.0025 | $\delta_{\perp}^{TV}$ | 0.0015 | 0.0511 | 0.0511 |
| $\delta^{SV}$ | 0.0011 | 0.0214 | 0.0214 | $f_{TT}$ | 0.0000 | 0.0001 | 0.0001 |
| $\delta^{VS}$ | 0.0031 | 0.0140 | 0.0143 | $f_L^{TT}$ | 0.0009 | 0.0057 | 0.0058 |
| $f_{SS}$ | 0.0004 | 0.0006 | 0.0007 | $f_{\parallel 1}^{TT}$ | 0.0008 | 0.0085 | 0.0086 |
| $\delta^{SS}$ | 0.0027 | 0.0182 | 0.0184 | $f_{\perp 1}^{TT}$ | $-0.0003$ | 0.0084 | 0.0084 |
| $f_{ST}$ | 0.0000 | 0.0004 | 0.0004 | $f_{\parallel 2}^{TT}$ | $-0.0001$ | 0.0039 | 0.0039 |
| $f_{TS}$ | $-0.0000$ | 0.0005 | 0.0005 | $\delta_0^{TT}$ | $-0.0046$ | 0.0889 | 0.0890 |
| $\delta^{ST}$ | $-0.0025$ | 0.0639 | 0.0639 | $\delta_{\parallel 1}^{TT}$ | 0.0003 | 0.0204 | 0.0204 |
| $\delta^{TS}$ | 0.0014 | 0.0394 | 0.0394 | $\delta_{\perp 1}^{TT}$ | 0.0030 | 0.0524 | 0.0524 |
| $f_{VT}$ | $-0.0000$ | 0.0013 | 0.0013 | $\delta_{\parallel 2}^{TT}$ | 0.0021 | 0.0867 | 0.0867 |
| $f_L^{VT}$ | 0.0003 | 0.0039 | 0.0039 | $\delta_{\perp 2}^{TT}$ | 0.0143 | 0.2017 | 0.2022 |

TABLE 7.63: Mean and root mean square of the distributions on the $\lambda_i^{smear} - \lambda_i^{ref}$ variables, obtained from the set of 100 toy Monte Carlo experiments, and systematic uncertainties obtained from them.

a resolution-free signal sample, and two additional fits to the sample, one before and one after applying the resolution smearing. For this study, the reduced (fast) version of the fit is used, and the $c_i^{mass}$ parameters of the fitting model are randomised for each experiment (as explained in Sect. 7.8.5). The two fits of each experiment share the same set of $c_i^{mass}$ parameters. The smearing is different for each experiment, given its random nature.

Let's denote the parameter values resulting from the fits where no smearing has been applied as $\lambda_i^{ref}$, and the corresponding ones with smearing as $\lambda_i^{smear}$. We obtain the distributions on the $\lambda_i^{smear} - \lambda_i^{ref}$ differences for the set of 100 experiments. These distributions have a gaussian-like shape, and their mean and root mean square values for the relevant physical parameters are written in Table 7.63. Systematic uncertainties are computed by adding in quadrature the mean and the RMS for each parameter. The resulting values are also shown in Table 7.63.

| Parameter | 2011 sample | 2012 sample |
|---|---|---|
| $p_0^{\sigma_t,alt}$ | $1.2368 \pm 0.0089$ | $1.2957 \pm 0.0096$ |
| $p_1^{\sigma_t,alt}$ [ps$^{-1}$] | $-3.3899 \pm 1.8568$ | $-0.5321 \pm 2.0529$ |

TABLE 7.64: Parameters of the quadratic function used for time-resolution calibration, obtained from the combined Monte Carlo sample.

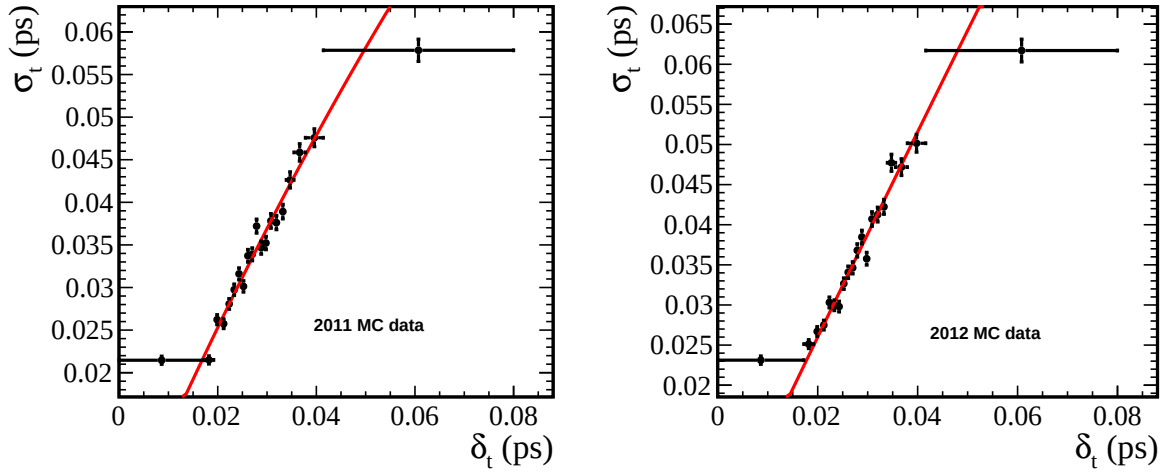



FIGURE 7.35: Plots of the fit to the $\sigma_t$ vs $\delta_t$ scatter plot using a quadratic calibration function.

### 7.9.15 Time-resolution calibration model

An alternative parameterisation of the time resolution calibration function is tried in this section, by changing the linear expresion in Eq. 7.12 by the following quadratic form (inspired by the parameterisation in [130]):

$$\sigma_t^{alt}(\delta_t) = \left(p_0^{\sigma_t,alt} + p_1^{\sigma_t,alt} \cdot (\delta_t - \langle\delta_t\rangle)\right) \cdot \delta_t. \tag{7.54}$$

The parameters $p_0^{\sigma_t,alt}$ and $p_1^{\sigma_t,alt}$ are determined using the combined signal Monte Carlo sample (vector-vector + pure phase space), following the procedure described in Sect. 7.5. The resulting values are written in Table 7.64 and the corresponding calibration plots are shown in Fig. 7.35. The correlation between $p_0^{\sigma_t,alt}$ and $p_1^{\sigma_t,alt}$ is found to be $\rho = 0.0075$ for 2011 and $\rho = 0.0740$ for 2012 data.

The nominal fit to data is repeated using this new calibration function, instead of the original one. The values of the calibration parameters are gaussian constrained to the previously obtained quantities. In Table 7.65, we show the deviations between the values of the relevant physical parameters resulting from the new fit with respect to the original ones. The symmeterised deviations are taken as systematic uncertainties associated to the choice of the nominal calibration function. These uncertainties are also written in Table 7.65.

| Parameter | $\Delta$ | $\sigma$ | Parameter | $\Delta$ | $\sigma$ |
|---|---|---|---|---|---|
| $\phi_s$ | $-0.0002$ | $0.0002$ | $f_{\parallel}^{VT}$ | $-0.0000$ | $0.0000$ |
| $\Delta^{CP}$ | $-0.0001$ | $0.0001$ | $f_{TV}$ | $-0.0001$ | $0.0001$ |
| $\Delta m_{B_s^0}$ | $-0.0001$ | $0.0001$ | $f_L^{TV}$ | $-0.0008$ | $0.0008$ |
| $f_{VV}$ | $0.0000$ | $0.0000$ | $f_{\parallel}^{TV}$ | $0.0006$ | $0.0006$ |
| $f_L^{VV}$ | $-0.0000$ | $0.0000$ | $\delta_0^{VT}$ | $0.0007$ | $0.0007$ |
| $f_{\parallel}^{VV}$ | $-0.0000$ | $0.0000$ | $\delta_{\parallel}^{VT}$ | $-0.0009$ | $0.0009$ |
| $\delta_{\parallel}^{VV}$ | $-0.0002$ | $0.0002$ | $\delta_{\perp}^{VT}$ | $0.0029$ | $0.0029$ |
| $\delta_{\perp}^{VV}$ | $-0.0002$ | $0.0002$ | $\delta_0^{TV}$ | $-0.0001$ | $0.0001$ |
| $f_{SV}$ | $0.0001$ | $0.0001$ | $\delta_{\parallel}^{TV}$ | $0.0001$ | $0.0001$ |
| $f_{VS}$ | $-0.0000$ | $0.0000$ | $\delta_{\perp}^{TV}$ | $0.0037$ | $0.0037$ |
| $\delta^{SV}$ | $-0.0000$ | $0.0000$ | $f_{TT}$ | $0.0000$ | $0.0000$ |
| $\delta^{VS}$ | $-0.0004$ | $0.0004$ | $f_L^{TT}$ | $-0.0005$ | $0.0005$ |
| $f_{SS}$ | $-0.0000$ | $0.0000$ | $f_{\parallel 1}^{TT}$ | $0.0005$ | $0.0005$ |
| $\delta^{SS}$ | $-0.0003$ | $0.0003$ | $f_{\perp 1}^{TT}$ | $-0.0003$ | $0.0003$ |
| $f_{ST}$ | $0.0000$ | $0.0000$ | $f_{\parallel 2}^{TT}$ | $-0.0002$ | $0.0002$ |
| $f_{TS}$ | $-0.0001$ | $0.0001$ | $\delta_0^{TT}$ | $-0.0000$ | $0.0000$ |
| $\delta^{ST}$ | $0.0066$ | $0.0066$ | $\delta_{\parallel 1}^{TT}$ | $-0.0017$ | $0.0017$ |
| $\delta^{TS}$ | $0.0020$ | $0.0020$ | $\delta_{\perp 1}^{TT}$ | $0.0031$ | $0.0031$ |
| $f_{VT}$ | $0.0001$ | $0.0001$ | $\delta_{\parallel 2}^{TT}$ | $0.0010$ | $0.0010$ |
| $f_L^{VT}$ | $0.0001$ | $0.0001$ | $\delta_{\perp 2}^{TT}$ | $0.0046$ | $0.0046$ |

TABLE 7.65: Deviations in the physical parameters obtained from the fit to data which uses a quadratic calibration function for the time resolution with respect to those obtained from the nominal fit, which uses a linear calibration function. The associated systematic uncertainties are also shown.

| $s$ | MC | Data |
|---|---|---|
| Prompt | 1.231 | 1.45 |
| Signal | 1.162 | – |

TABLE 7.66: Values of the scale factors obtained from the different $B_s^0 \to J/\psi\phi$ samples [131].

### 7.9.16 Data/Monte Carlo time-resolution correction

In this section we account for the mismodelling of the time resolution in simulation, by applying a correction to our calibration function. Given the topological similarity between our decay and the $B_s^0 \to J/\psi\phi$ mode (quasi-two-body structure with four charged tracks in the final state), we make use of the study performed in [131] for this channel. The resolution is studied in that analysis using three different sources: prompt $J/\psi$ data candidates, prompt $J/\psi$ simulated candidates and signal simulated candidates. The used calibration model consists on a single gaussian, as in our analysis, but with a width which is given by:

$$\sigma_t^{J/\psi\phi} = s \cdot \delta_t, \tag{7.55}$$

where $s$ is a constant scale factor. The values obtained for the $B_s^0 \to J/\psi\phi$ samples are collected in Table 7.66.

The data-driven calibration of the time resolution for signal events is obtained from the scale factor measured in prompt $J/\psi$ data, corrected by the ratio of scale factors in simulated signal and simulated prompt $J/\psi$ events:

$$\sigma_t^{J/\psi\phi,Data} = s_{Prompt}^{Data} \cdot \left( \frac{s_{Signal}^{MC}}{s_{Prompt}^{MC}} \right) \cdot \delta_t. \tag{7.56}$$

If only simulation was used (as in our case), the equivalent expression would be:

$$\sigma_t^{J/\psi\phi,MC} = s_{Signal}^{MC} \cdot \delta_t. \tag{7.57}$$

Coming back to $B_s^0 \to (K^+\pi^-)(K^-\pi^+)$, we can correct our calibration function using the ratio of resolutions in $B_s^0 \to J/\psi\phi$, as follows:

$$\begin{aligned} \sigma_t^{alt}(\delta_t) &= \left( \frac{\sigma_t^{J/\psi\phi,Data}}{\sigma_t^{J/\psi\phi,MC}} \right) \cdot \sigma_t(\delta_t) = \left( \frac{s_{Prompt}^{Data}}{s_{Prompt}^{MC}} \right) \cdot \sigma_t(\delta_t) \\ &= r_{MC}^{Data} \cdot (p_0^{\sigma_t} + p_1^{\sigma_t} \cdot (\delta_t - \langle \delta_t \rangle)) \,, \end{aligned} \tag{7.58}$$

where $r_{MC}^{Data} = s_{Prompt}^{Data}/s_{Prompt}^{MC} = 1.178$ and $p_0^{\sigma_t}$ and $p_1^{\sigma_t}$ are the nominal calibration parameters.

We repeat the nominal fit to data using the corrected calibration function, and compute the deviations in the resulting parameters with respect to the nominal ones. These deviations, written in Table 7.67 are symmeterised and taken as systematic uncertainties.

| Parameter | $\Delta$ | Parameter | $\Delta$ |
|---|---|---|---|
| $\phi_s$ | 0.0065 | $f_{\parallel}^{VT}$ | 0.0004 |
| $\Delta^{CP}$ | $-0.0002$ | $f_{TV}$ | 0.0003 |
| $\Delta m_{B_s^0}$ | 0.0024 | $f_L^{TV}$ | 0.0038 |
| $f_{VV}$ | $-0.0000$ | $f_{\parallel}^{TV}$ | $-0.0033$ |
| $f_L^{VV}$ | 0.0000 | $\delta_0^{VT}$ | $-0.0091$ |
| $f_{\parallel}^{VV}$ | $-0.0002$ | $\delta_{\parallel}^{VT}$ | $-0.0254$ |
| $\delta_{\parallel}^{VV}$ | $-0.0017$ | $\delta_{\perp}^{VT}$ | $-0.0162$ |
| $\delta_{\perp}^{VV}$ | 0.0128 | $\delta_0^{TV}$ | 0.0028 |
| $f_{SV}$ | 0.0001 | $\delta_{\parallel}^{TV}$ | 0.0191 |
| $f_{VS}$ | $-0.0006$ | $\delta_{\perp}^{TV}$ | $-0.0189$ |
| $\delta^{SV}$ | 0.0017 | $f_{TT}$ | 0.0001 |
| $\delta^{VS}$ | $-0.0030$ | $f_L^{TT}$ | 0.0023 |
| $f_{SS}$ | $-0.0000$ | $f_{\parallel 1}^{TT}$ | $-0.0038$ |
| $\delta^{SS}$ | $-0.0008$ | $f_{\perp 1}^{TT}$ | 0.0066 |
| $f_{ST}$ | 0.0002 | $f_{\parallel 2}^{TT}$ | $-0.0038$ |
| $f_{TS}$ | 0.0000 | $\delta_0^{TT}$ | 0.0029 |
| $\delta^{ST}$ | $-0.0182$ | $\delta_{\parallel 1}^{TT}$ | $-0.0026$ |
| $\delta^{TS}$ | 0.0029 | $\delta_{\perp 1}^{TT}$ | 0.0091 |
| $f_{VT}$ | $-0.0000$ | $\delta_{\parallel 2}^{TT}$ | $-0.0151$ |
| $f_L^{VT}$ | $-0.0000$ | $\delta_{\perp 2}^{TT}$ | 0.0090 |

TABLE 7.67: Deviations between the parameters obtained from the fit with the data/MC corrected time-resolution calibration function and the nominal ones.

### 7.9.17 Production asymmetry

The $B_s^0$ production asymmetry, $\Delta_{prod}$, is fixed in the nominal fit to the value obtained in Sect. 7.4. To estimate the effect of its variation, we repeat the time-dependent fit twice, one with the value of $\Delta_{prod}$ decreased by one standard deviation and one with its value increased by one standard deviation. We use $\sigma(\Delta_{prod}) = 0.019$, resulting from the quadratic sum of the statistical and systematic uncertainties in Eq. 7.7. The result of this study is shown in Table 7.68. We assign symmetric systematic uncertainties using the maximum difference found in the value of each parameter.

| Parameter | $\Delta$ $(\Delta_{prod} - 1\sigma)$ | $\Delta$ $(\Delta_{prod} + 1\sigma)$ | $\sigma$ |
|---|---|---|---|
| $\phi_s$ | $-0.0019$ | $0.0021$ | $0.0021$ |
| $\Delta^{CP}$ | $0.0004$ | $-0.0015$ | $0.0015$ |
| $\Delta m_{B_s^0}$ | $-0.0029$ | $-0.0003$ | $0.0029$ |
| $f_{VV}$ | $-0.0000$ | $0.0001$ | $0.0001$ |
| $f_L^{VV}$ | $0.0000$ | $-0.0001$ | $0.0001$ |
| $f_\parallel^{VV}$ | $-0.0002$ | $0.0002$ | $0.0002$ |
| $\delta_\parallel^{VV}$ | $-0.0001$ | $0.0010$ | $0.0010$ |
| $\delta_\perp^{VV}$ | $-0.0016$ | $-0.0167$ | $0.0167$ |
| $f_{SV}$ | $-0.0000$ | $-0.0019$ | $0.0019$ |
| $f_{VS}$ | $0.0001$ | $0.0018$ | $0.0018$ |
| $\delta^{SV}$ | $-0.0006$ | $-0.0018$ | $0.0018$ |
| $\delta^{VS}$ | $-0.0020$ | $0.0077$ | $0.0077$ |
| $f_{SS}$ | $-0.0001$ | $0.0001$ | $0.0001$ |
| $\delta^{SS}$ | $-0.0007$ | $0.0021$ | $0.0021$ |
| $f_{ST}$ | $0.0002$ | $-0.0007$ | $0.0007$ |
| $f_{TS}$ | $-0.0001$ | $0.0005$ | $0.0005$ |
| $\delta^{ST}$ | $0.0097$ | $-0.0365$ | $0.0365$ |
| $\delta^{TS}$ | $0.0083$ | $-0.0262$ | $0.0262$ |
| $f_{VT}$ | $0.0002$ | $-0.0014$ | $0.0014$ |
| $f_L^{VT}$ | $0.0007$ | $-0.0027$ | $0.0027$ |
| $f_\parallel^{VT}$ | $-0.0001$ | $0.0007$ | $0.0007$ |
| $f_{TV}$ | $-0.0003$ | $0.0015$ | $0.0015$ |
| $f_L^{TV}$ | $-0.0021$ | $0.0115$ | $0.0115$ |
| $f_\parallel^{TV}$ | $0.0008$ | $-0.0061$ | $0.0061$ |
| $\delta_0^{VT}$ | $0.0027$ | $-0.0149$ | $0.0149$ |
| $\delta_\parallel^{VT}$ | $-0.0181$ | $0.0102$ | $0.0181$ |
| $\delta_\perp^{VT}$ | $0.0035$ | $-0.0296$ | $0.0296$ |
| $\delta_0^{TV}$ | $0.0030$ | $-0.0022$ | $0.0030$ |
| $\delta_\parallel^{TV}$ | $0.0068$ | $0.0023$ | $0.0068$ |
| $\delta_\perp^{TV}$ | $0.0059$ | $-0.0410$ | $0.0410$ |
| $f_{TT}$ | $-0.0000$ | $0.0000$ | $0.0000$ |
| $f_L^{TT}$ | $0.0015$ | $-0.0023$ | $0.0023$ |
| $f_{\parallel 1}^{TT}$ | $-0.0007$ | $0.0003$ | $0.0007$ |
| $f_{\perp 1}^{TT}$ | $0.0063$ | $-0.0076$ | $0.0076$ |
| $f_{\parallel 2}^{TT}$ | $-0.0030$ | $0.0034$ | $0.0034$ |
| $\delta_0^{TT}$ | $0.0045$ | $0.0001$ | $0.0045$ |
| $\delta_{\parallel 1}^{TT}$ | $-0.0024$ | $0.0018$ | $0.0024$ |
| $\delta_{\perp 1}^{TT}$ | $0.0227$ | $-0.0617$ | $0.0617$ |
| $\delta_{\parallel 2}^{TT}$ | $-0.0103$ | $0.0150$ | $0.0150$ |
| $\delta_{\perp 2}^{TT}$ | $0.0109$ | $-0.0433$ | $0.0433$ |

TABLE 7.68: Systematic uncertainties associated to the $B_s^0$ production asymmetry.

### 7.9.18 Summary of the systematic uncertainties

In this sub-section, the systematic uncertainties computed for the fit parameters are summarised and combined in a total systematic uncertainty.

| Parameter | $\phi_s$ | $\Delta^{CP}$ | $\Delta m_{B_s^0}$ | $f_L^{VV}$ | $\delta_\parallel^{VV}$ |
|---|---|---|---|---|---|
| 4-body mass fit yields | 0.0076 | 0.0008 | 0.0026 | 0.0040 | 0.0079 |
| 4-body mass fit model | 0.0095 | 0.0006 | 0.0028 | 0.0008 | 0.0076 |
| 4-body mass correlations | 0.0115 | 0.0068 | 0.0145 | 0.0057 | 0.0240 |
| TD fit bias | 0.0058 | 0.0019 | 0.0047 | 0.0055 | 0.0071 |
| Meson radius, $d$ | 0.0281 | 0.0029 | 0.0106 | 0.0078 | 0.0592 |
| Resonance mass and width | +0.0070 | +0.0011 | +0.0010 | +0.0017 | +0.0023 |
| S-wave mass model | 0.0052 | 0.0019 | 0.0011 | 0.0019 | 0.0166 |
| Extra vector resonances | 0.0393 | 0.0124 | 0.0762 | 0.0231 | 0.1767 |
| Orbital angular momentum, $L$ | −0.0001 | +0.0000 | +0.0002 | +0.0001 | −0.0004 |
| Normalisation weights | 0.1059 | 0.0778 | 0.1628 | 0.0312 | 0.2360 |
| Splines (MC stat.) | 0.0222 | 0.0027 | 0.0047 | 0.0029 | 0.0179 |
| Splines (knot position) | 0.0582 | 0.0001 | 0.0055 | 0.0018 | 0.0090 |
| Data/MC acceptance corr. | −0.0025 | +0.0072 | +0.0082 | +0.0175 | +0.1336 |
| Angular and mass resolution | 0.0047 | 0.0017 | 0.0088 | 0.0029 | 0.0186 |
| Time reso. calibration model | 0.0002 | 0.0001 | 0.0001 | 0.0000 | 0.0002 |
| Data/MC resolution corr. | +0.0065 | −0.0002 | +0.0024 | +0.0000 | −0.0017 |
| Production asymmetry | 0.0021 | 0.0015 | 0.0029 | 0.0001 | 0.0010 |
| Total | +0.1337<br>−0.1334 | +0.0796<br>−0.0793 | +0.1813<br>−0.1811 | +0.0445<br>−0.0409 | +0.3318<br>−0.3037 |

TABLE 7.69: Summary of the systematic uncertainties of the fit parameters.

USC UNIVERSIDADE DE SANTIAGO DE COMPOSTELA

| Parameter | $f_L^{TV}$ | $f_{VV}$ | $f_\parallel^{TV}$ | $f_\parallel^{VT}$ | $\delta_0^{VT}$ |
|---|---|---|---|---|---|
| 4-body mass fit yields | 0.0246 | 0.0011 | 0.0142 | 0.0003 | 0.0170 |
| 4-body mass fit model | 0.0353 | 0.0007 | 0.0202 | 0.0005 | 0.0158 |
| 4-body mass correlations | 0.0432 | 0.0015 | 0.0285 | 0.0013 | 0.0250 |
| TD fit bias | 0.0084 | 0.0005 | 0.0046 | 0.0024 | 0.0119 |
| Meson radius, $d$ | 0.0226 | 0.0035 | 0.0167 | 0.0018 | 0.0448 |
| Resonance mass and width | $-0.0172$ | $+0.0050$ | $+0.0082$ | $-0.0002$ | $+0.0070$ |
| S-wave mass model | 0.0192 | 0.0014 | 0.0301 | 0.0074 | 0.1493 |
| Extra vector resonances | 0.0725 | 0.0200 | 0.0317 | 0.0173 | 0.2398 |
| Orbital angular momentum, $L$ | $-0.0004$ | $-0.0000$ | $+0.0000$ | $+0.0000$ | $+0.0003$ |
| Normalisation weights | 0.1989 | 0.0042 | 0.1018 | 0.0536 | 1.1169 |
| Splines (MC stat.) | 0.0245 | 0.0014 | 0.0108 | 0.0011 | 0.0167 |
| Splines (knot position) | 0.0173 | 0.0005 | 0.0085 | 0.0001 | 0.0370 |
| Data/MC acceptance corr. | $+0.0318$ | $-0.0045$ | $-0.0061$ | $+0.0028$ | $+0.1547$ |
| Angular and mass resolution | 0.0116 | 0.0004 | 0.0070 | 0.0031 | 0.0323 |
| Time reso. calibration model | 0.0008 | 0.0000 | 0.0006 | 0.0000 | 0.0007 |
| Data/MC resolution corr. | $+0.0038$ | $-0.0000$ | $-0.0033$ | $+0.0004$ | $-0.0091$ |
| Production asymmetry | 0.0115 | 0.0001 | 0.0061 | 0.0007 | 0.0149 |
| Total | $+0.2274$<br>$-0.2257$ | $+0.0215$<br>$-0.0214$ | $+0.1197$<br>$-0.1197$ | $+0.0570$<br>$-0.0570$ | $+1.1651$<br>$-1.1548$ |

TABLE 7.70: Summary of the systematic uncertainties of the fit parameters.

| Parameter | $f_\parallel^{VV}$ | $\delta_\parallel^{VT}$ | $f_{TV}$ | $\delta_\perp^{VT}$ | $\delta_\perp^{VV}$ |
|---|---|---|---|---|---|
| 4-body mass fit yields | 0.0033 | 0.0854 | 0.0002 | 0.0294 | 0.0172 |
| 4-body mass fit model | 0.0024 | 0.0699 | 0.0006 | 0.0460 | 0.0103 |
| 4-body mass correlations | 0.0053 | 0.1257 | 0.0010 | 0.1308 | 0.1123 |
| TD fit bias | 0.0018 | 0.0247 | 0.0015 | 0.0693 | 0.0168 |
| Meson radius, $d$ | 0.0018 | 0.0914 | 0.0039 | 0.1078 | 0.0947 |
| Resonance mass and width | $-0.0017$ | $+0.0077$ | $-0.0009$ | $+0.0630$ | $-0.0050$ |
| S-wave mass model | 0.0009 | 0.0641 | 0.0034 | 0.1049 | 0.0095 |
| Extra vector resonances | 0.0258 | 0.2352 | 0.0062 | 0.2607 | 0.1781 |
| Orbital angular momentum, $L$ | $-0.0001$ | $-0.0037$ | $-0.0001$ | $-0.0005$ | $+0.0002$ |
| Normalisation weights | 0.0291 | 0.8884 | 0.0271 | 1.0800 | 0.5637 |
| Splines (MC stat.) | 0.0022 | 0.0383 | 0.0038 | 0.0260 | 0.0168 |
| Splines (knot position) | 0.0032 | 0.0155 | 0.0027 | 0.0409 | 0.0272 |
| Data/MC acceptance corr. | $+0.0022$ | $+0.1805$ | $+0.0018$ | $+0.1542$ | $+0.1393$ |
| Angular and mass resolution | 0.0022 | 0.0392 | 0.0014 | 0.0441 | 0.0388 |
| Time reso. calibration model | 0.0000 | 0.0009 | 0.0001 | 0.0029 | 0.0002 |
| Data/MC resolution corr. | $-0.0002$ | $-0.0254$ | $+0.0003$ | $-0.0162$ | $+0.0128$ |
| Production asymmetry | 0.0002 | 0.0181 | 0.0015 | 0.0296 | 0.0167 |
| Total | $+0.0399$<br>$-0.0399$ | $+0.9602$<br>$-0.9434$ | $+0.0289$<br>$-0.0288$ | $+1.1467$<br>$-1.1346$ | $+0.6279$<br>$-0.6121$ |

TABLE 7.71: Summary of the systematic uncertainties of the fit parameters.

| Parameter | $\delta_0^{TV}$ | $f_{SV}$ | $\delta_\parallel^{TV}$ | $f_{VS}$ | $\delta_\perp^{TV}$ |
|---|---|---|---|---|---|
| 4-body mass fit yields | 0.0207 | 0.0008 | 0.0114 | 0.0022 | 0.0317 |
| 4-body mass fit model | 0.0487 | 0.0021 | 0.0139 | 0.0017 | 0.0573 |
| 4-body mass correlations | 0.0799 | 0.0040 | 0.0730 | 0.0046 | 0.1495 |
| TD fit bias | 0.0617 | 0.0027 | 0.0174 | 0.0015 | 0.0296 |
| Meson radius, $d$ | 0.0346 | 0.0117 | 0.0128 | 0.0013 | 0.1324 |
| Resonance mass and width | $+0.0001$ | $+0.0113$ | $-0.0018$ | $+0.0003$ | $+0.0607$ |
| S-wave mass model | 0.0471 | 0.0042 | 0.0215 | 0.0096 | 0.0992 |
| Extra vector resonances | 0.2530 | 0.0387 | 0.2263 | 0.0278 | 0.3649 |
| Orbital angular momentum, $L$ | $+0.0014$ | $+0.0000$ | $+0.0014$ | $-0.0000$ | $-0.0001$ |
| Normalisation weights | 0.7124 | 0.0367 | 0.4165 | 0.0392 | 0.9466 |
| Splines (MC stat.) | 0.0344 | 0.0044 | 0.0448 | 0.0022 | 0.0435 |
| Splines (knot position) | 0.0022 | 0.0007 | 0.0081 | 0.0010 | 0.0591 |
| Data/MC acceptance corr. | $+0.2248$ | $+0.0036$ | $+0.2386$ | $+0.0026$ | $+0.1449$ |
| Angular and mass resolution | 0.0266 | 0.0026 | 0.0320 | 0.0025 | 0.0511 |
| Time reso. calibration model | 0.0001 | 0.0001 | 0.0001 | 0.0000 | 0.0037 |
| Data/MC resolution corr. | $+0.0028$ | $+0.0001$ | $+0.0191$ | $-0.0006$ | $-0.0189$ |
| Production asymmetry | 0.0030 | 0.0019 | 0.0068 | 0.0018 | 0.0410 |
| Total | $^{+0.8003}_{-0.7680}$ | $^{+0.0566}_{-0.0553}$ | $^{+0.5401}_{-0.4841}$ | $^{+0.0495}_{-0.0495}$ | $^{+1.0575}_{-1.0460}$ |

TABLE 7.72: Summary of the systematic uncertainties of the fit parameters.

| Parameter | $\delta^{SV}$ | $f_{TT}$ | $\delta^{VS}$ | $f_L^{TT}$ | $f_{SS}$ |
|---|---|---|---|---|---|
| 4-body mass fit yields | 0.0217 | 0.0003 | 0.0075 | 0.0333 | 0.0021 |
| 4-body mass fit model | 0.0065 | 0.0003 | 0.0219 | 0.0297 | 0.0037 |
| 4-body mass correlations | 0.0489 | 0.0003 | 0.0218 | 0.0663 | 0.0046 |
| TD fit bias | 0.0070 | 0.0012 | 0.0273 | 0.0217 | 0.0013 |
| Meson radius, $d$ | 0.0164 | 0.0001 | 0.0217 | 0.0249 | 0.0142 |
| Resonance mass and width | $-0.0170$ | $-0.0003$ | $-0.0394$ | $-0.0007$ | $-0.0176$ |
| S-wave mass model | 0.0240 | 0.0014 | 0.0167 | 0.0014 | 0.0003 |
| Extra vector resonances | 0.1549 | 0.0052 | 0.2295 | 0.0442 | 0.0595 |
| Orbital angular momentum, $L$ | $+0.0002$ | $+0.0000$ | $-0.0005$ | $+0.0004$ | $+0.0001$ |
| Normalisation weights | 0.2495 | 0.0032 | 0.2897 | 0.1352 | 0.0154 |
| Splines (MC stat.) | 0.0126 | 0.0011 | 0.0223 | 0.0098 | 0.0049 |
| Splines (knot position) | 0.0178 | 0.0002 | 0.0039 | 0.0016 | 0.0010 |
| Data/MC acceptance corr. | $+0.1642$ | $-0.0011$ | $+0.1213$ | $+0.0284$ | $-0.0166$ |
| Angular and mass resolution | 0.0214 | 0.0001 | 0.0143 | 0.0058 | 0.0007 |
| Time reso. calibration model | 0.0000 | 0.0000 | 0.0004 | 0.0005 | 0.0000 |
| Data/MC resolution corr. | $+0.0017$ | $+0.0001$ | $-0.0030$ | $+0.0023$ | $-0.0000$ |
| Production asymmetry | 0.0018 | 0.0000 | 0.0077 | 0.0023 | 0.0001 |
| Total | $^{+0.3434}_{-0.3021}$ | $^{+0.0065}_{-0.0066}$ | $^{+0.3932}_{-0.3761}$ | $^{+0.1693}_{-0.1668}$ | $^{+0.0636}_{-0.0681}$ |

TABLE 7.73: Summary of the systematic uncertainties of the fit parameters.

| Parameter | $f_{\parallel 1}^{TT}$ | $\delta^{SS}$ | $f_{\perp 1}^{TT}$ | $f_{ST}$ | $f_{\parallel 2}^{TT}$ |
|---|---|---|---|---|---|
| 4-body mass fit yields | 0.0123 | 0.0117 | 0.0281 | 0.0010 | 0.0012 |
| 4-body mass fit model | 0.0143 | 0.0022 | 0.0239 | 0.0015 | 0.0011 |
| 4-body mass correlations | 0.0252 | 0.0468 | 0.0238 | 0.0036 | 0.0023 |
| TD fit bias | 0.0220 | 0.0087 | 0.0142 | 0.0005 | 0.0042 |
| Meson radius, $d$ | 0.0147 | 0.0095 | 0.0562 | 0.0027 | 0.0111 |
| Resonance mass and width | $-0.0153$ | $-0.0320$ | $+0.0128$ | $+0.0011$ | $-0.0064$ |
| S-wave mass model | 0.0106 | 0.0056 | 0.0466 | 0.0007 | 0.0198 |
| Extra vector resonances | 0.0673 | 0.2240 | 0.0852 | 0.0056 | 0.0296 |
| Orbital angular momentum, $L$ | $+0.0010$ | $-0.0001$ | $+0.0011$ | $+0.0000$ | $-0.0006$ |
| Normalisation weights | 0.1103 | 0.2561 | 0.1272 | 0.0137 | 0.0774 |
| Splines (MC stat.) | 0.0246 | 0.0149 | 0.0223 | 0.0013 | 0.0081 |
| Splines (knot position) | 0.0079 | 0.0116 | 0.0053 | 0.0004 | 0.0014 |
| Data/MC acceptance corr. | $+0.0062$ | $+0.1920$ | $-0.0502$ | $-0.0012$ | $+0.0217$ |
| Angular and mass resolution | 0.0086 | 0.0184 | 0.0084 | 0.0004 | 0.0039 |
| Time reso. calibration model | 0.0005 | 0.0003 | 0.0003 | 0.0000 | 0.0002 |
| Data/MC resolution corr. | $-0.0038$ | $-0.0008$ | $+0.0066$ | $+0.0002$ | $-0.0038$ |
| Production asymmetry | 0.0007 | 0.0021 | 0.0076 | 0.0007 | 0.0034 |
| Total | $^{+0.1388}_{-0.1396}$ | $^{+0.3948}_{-0.3464}$ | $^{+0.1782}_{-0.1845}$ | $^{+0.0157}_{-0.0157}$ | $^{+0.0893}_{-0.0869}$ |

TABLE 7.74: Summary of the systematic uncertainties of the fit parameters.

| Parameter | $f_{TS}$ | $\delta_0^{TT}$ | $\delta^{ST}$ | $\delta_{\parallel 1}^{TT}$ | $\delta^{TS}$ |
|---|---|---|---|---|---|
| 4-body mass fit yields | 0.0022 | 0.0281 | 0.0711 | 0.0238 | 0.0157 |
| 4-body mass fit model | 0.0030 | 0.0262 | 0.0856 | 0.0135 | 0.0165 |
| 4-body mass correlations | 0.0063 | 0.1471 | 0.1513 | 0.0462 | 0.1047 |
| TD fit bias | 0.0016 | 0.1266 | 0.2480 | 0.0364 | 0.0166 |
| Meson radius, $d$ | 0.0043 | 0.7074 | 0.1715 | 0.0487 | 0.0867 |
| Resonance mass and width | $-0.0004$ | $+0.0652$ | $+0.0933$ | $-0.0076$ | $+0.0036$ |
| S-wave mass model | 0.0005 | 0.1857 | 0.1098 | 0.0242 | 0.1633 |
| Extra vector resonances | 0.0164 | 0.9655 | 0.7011 | 0.1914 | 0.1630 |
| Orbital angular momentum, $L$ | $+0.0000$ | $-0.0030$ | $-0.0000$ | $-0.0012$ | $+0.0006$ |
| Normalisation weights | 0.0149 | 1.3280 | 1.4630 | 0.4540 | 0.7192 |
| Splines (MC stat.) | 0.0031 | 0.0807 | 0.1215 | 0.0395 | 0.0452 |
| Splines (knot position) | 0.0013 | 0.0122 | 0.1099 | 0.0096 | 0.0444 |
| Data/MC acceptance corr. | $+0.0008$ | $+0.1906$ | $+0.0491$ | $+0.2717$ | $+0.2136$ |
| Angular and mass resolution | 0.0005 | 0.0890 | 0.0639 | 0.0204 | 0.0394 |
| Time reso. calibration model | 0.0001 | 0.0000 | 0.0066 | 0.0017 | 0.0020 |
| Data/MC resolution corr. | $+0.0000$ | $+0.0029$ | $-0.0182$ | $-0.0026$ | $+0.0029$ |
| Production asymmetry | 0.0005 | 0.0045 | 0.0365 | 0.0024 | 0.0262 |
| Total | $^{+0.0241}_{-0.0240}$ | $^{+1.8234}_{-1.8123}$ | $^{+1.6774}_{-1.6742}$ | $^{+0.5708}_{-0.5021}$ | $^{+0.8010}_{-0.7720}$ |

TABLE 7.75: Summary of the systematic uncertainties of the fit parameters.

| Parameter | $\delta_{\perp 1}^{TT}$ | $f_{VT}$ | $\delta_{\parallel 2}^{TT}$ | $f_L^{VT}$ | $\delta_{\perp 2}^{TT}$ |
|---|---|---|---|---|---|
| 4-body mass fit yields | 0.0088 | 0.0007 | 0.0507 | 0.0017 | 0.0635 |
| 4-body mass fit model | 0.0028 | 0.0011 | 0.0604 | 0.0022 | 0.0941 |
| 4-body mass correlations | 0.1118 | 0.0019 | 0.1227 | 0.0028 | 0.2149 |
| TD fit bias | 0.0682 | 0.0022 | 0.0578 | 0.0037 | 0.0395 |
| Meson radius, $d$ | 0.2625 | 0.0025 | 0.0615 | 0.0090 | 0.1853 |
| Resonance mass and width | $+0.1574$ | $+0.0016$ | $-0.0663$ | $+0.0022$ | $+0.0566$ |
| S-wave mass model | 0.2140 | 0.0078 | 0.4776 | 0.0062 | 0.0986 |
| Extra vector resonances | 0.5740 | 0.0079 | 0.6607 | 0.0514 | 0.4236 |
| Orbital angular momentum, $L$ | $+0.0005$ | $-0.0000$ | $+0.0021$ | $+0.0000$ | $-0.0004$ |
| Normalisation weights | 1.3478 | 0.0257 | 1.4426 | 0.1451 | 1.1612 |
| Splines (MC stat.) | 0.0621 | 0.0043 | 0.0598 | 0.0040 | 0.0693 |
| Splines (knot position) | 0.0637 | 0.0014 | 0.0176 | 0.0069 | 0.0738 |
| Data/MC acceptance corr. | $+0.1165$ | $+0.0147$ | $+0.3257$ | $+0.0220$ | $+0.1979$ |
| Angular and mass resolution | 0.0524 | 0.0013 | 0.0867 | 0.0039 | 0.2022 |
| Time reso. calibration model | 0.0031 | 0.0001 | 0.0010 | 0.0001 | 0.0046 |
| Data/MC resolution corr. | $+0.0091$ | $-0.0000$ | $-0.0151$ | $-0.0000$ | $+0.0090$ |
| Production asymmetry | 0.0617 | 0.0014 | 0.0150 | 0.0027 | 0.0433 |
| Total | $+1.5267$<br>$-1.5141$ | $+0.0323$<br>$-0.0287$ | $+1.7006$<br>$-1.6705$ | $+0.1563$<br>$-0.1547$ | $+1.3145$<br>$-1.2982$ |

TABLE 7.76: Summary of the systematic uncertainties of the fit parameters.

TABLE 7.77: Results of the decay-time-dependent amplitude fit to data. The first uncertainty is statistical and the second uncertainty is systematic.

| Parameter | Value |
|---|---|
| **Common parameters** | |
| $\phi_s^{d\bar{d}}$ [rad] | $-0.10 \pm 0.13 \pm 0.14$ |
| $\lvert\lambda\rvert$ | $1.035 \pm 0.034 \pm 0.089$ |
| **Vector/Vector (VV)** | |
| $f^{VV}$ | $0.067 \pm 0.004 \pm 0.024$ |
| $f_{\rm L}^{VV}$ | $0.208 \pm 0.032 \pm 0.046$ |
| $f_{\parallel}^{VV}$ | $0.297 \pm 0.029 \pm 0.042$ |
| $\delta_{\parallel}^{VV}$ [rad] | $2.40 \pm 0.11 \pm 0.33$ |
| $\delta_{\perp}^{VV}$ [rad] | $2.62 \pm 0.26 \pm 0.64$ |
| **Scalar/Vector (SV and VS)** | |
| $f^{SV}$ | $0.329 \pm 0.015 \pm 0.071$ |
| $f^{VS}$ | $0.133 \pm 0.013 \pm 0.065$ |
| $\delta^{SV}$ [rad] | $-1.31 \pm 0.10 \pm 0.35$ |
| $\delta^{VS}$ [rad] | $1.86 \pm 0.11 \pm 0.41$ |
| **Scalar/Scalar (SS)** | |
| $f^{SS}$ | $0.225 \pm 0.010 \pm 0.069$ |
| $\delta^{SS}$ [rad] | $1.07 \pm 0.10 \pm 0.40$ |
| **Scalar/Tensor (ST and TS)** | |
| $f^{ST}$ | $0.014 \pm 0.006 \pm 0.031$ |
| $f^{TS}$ | $0.025 \pm 0.007 \pm 0.033$ |
| $\delta^{ST}$ [rad] | $-2.3 \pm 0.4 \pm 1.7$ |
| $\delta^{TS}$ [rad] | $-0.10 \pm 0.26 \pm 0.82$ |

| Parameter | Value |
|---|---|
| **Vector/Tensor (VT and TV)** | |
| $f^{VT}$ | $0.160 \pm 0.016 \pm 0.049$ |
| $f_{\rm L}^{VT}$ | $0.911 \pm 0.020 \pm 0.165$ |
| $f_{\parallel}^{VT}$ | $0.012 \pm 0.008 \pm 0.053$ |
| $f^{TV}$ | $0.036 \pm 0.014 \pm 0.048$ |
| $f_{\rm L}^{TV}$ | $0.62 \pm 0.16 \pm 0.25$ |
| $f_{\parallel}^{TV}$ | $0.24 \pm 0.10 \pm 0.14$ |
| $\delta_0^{VT}$ [rad] | $-2.06 \pm 0.19 \pm 1.17$ |
| $\delta_{\parallel}^{VT}$ [rad] | $-1.8 \pm 0.4 \pm 1.0$ |
| $\delta_{\perp}^{VT}$ [rad] | $-3.2 \pm 0.3 \pm 1.2$ |
| $\delta_0^{TV}$ [rad] | $1.91 \pm 0.30 \pm 0.80$ |
| $\delta_{\parallel}^{TV}$ [rad] | $1.09 \pm 0.19 \pm 0.55$ |
| $\delta_{\perp}^{TV}$ [rad] | $0.2 \pm 0.4 \pm 1.1$ |
| **Tensor/Tensor (TT)** | |
| $f^{TT}$ | $0.011 \pm 0.003 \pm 0.007$ |
| $f_{\rm L}^{TT}$ | $0.25 \pm 0.14 \pm 0.18$ |
| $f_{\parallel_1}^{TT}$ | $0.17 \pm 0.11 \pm 0.14$ |
| $f_{\perp_1}^{TT}$ | $0.30 \pm 0.18 \pm 0.21$ |
| $f_{\parallel_2}^{TT}$ | $0.015 \pm 0.033 \pm 0.107$ |
| $\delta_0^{TT}$ [rad] | $1.3 \pm 0.5 \pm 1.8$ |
| $\delta_{\parallel_1}^{TT}$ [rad] | $3.00 \pm 0.29 \pm 0.57$ |
| $\delta_{\perp_1}^{TT}$ [rad] | $2.6 \pm 0.4 \pm 1.5$ |
| $\delta_{\parallel_2}^{TT}$ [rad] | $2.3 \pm 0.8 \pm 1.7$ |
| $\delta_{\perp_2}^{TT}$ [rad] | $0.7 \pm 0.6 \pm 1.3$ |

## 7.10 Summary

A flavour-tagged decay-time-dependent amplitude analysis of the $B_s^0 \to (K^+\pi^-)(K^-\pi^+)$ decay, for $(K^\pm\pi^\mp)$ invariant masses in the range from 750 to 1600 $\mathrm{MeV}/c^2$, is performed on a data set corresponding to an integrated luminosity of $3.0\,\mathrm{fb}^{-1}$ obtained by the LHCb experiment with $pp$ collisions at $\sqrt{s} = 7\,\mathrm{TeV}$ and $\sqrt{s} = 8\,\mathrm{TeV}$. Several quasi-two-body decay components are considered, corresponding to $(K^\pm\pi^\mp)$ combinations with spins of 0, 1 and 2.

As shown in Table 7.77, the longitudinal polarisation fraction for the $B_s^0 \to K^{*0}\overline{K}^{*0}$ vector-vector decay is determined to be $f_{\rm L}^{VV} = 0.208 \pm 0.032 \pm 0.046$, where the first uncertainty is statistical and the second one systematic. This confirms, with improved precision, the relatively low value reported previously by LHCb [19].

The first determination of the $CP$ asymmetry of the $(K^+\pi^-)(K^-\pi^+)$ final state and the best, sometimes the first, measurements of 19 $CP$-averaged amplitude parameters corresponding to scalar, vector and tensor final states, are also reported.

This analysis determines for the first time the mixing-induced $CP$-violating phase $\phi_s$ using a

$b \to d\bar{d}s$ transition. The value of this phase is measured to be $\phi_s^{d\bar{d}} = -0.10 \pm 0.13 \pm 0.14\,\text{rad}$, which is consistent with both the SM expectation [17] and the corresponding LHCb result of $\phi^{ss\bar{s}} = -0.17 \pm 0.15 \pm 0.03\,\text{rad}$ measured using $B_s^0 \to \phi\phi$ decays [10]. The statistical uncertainty of the two measurements is at a similar level although the systematic uncertainty of this measurement is larger, which is mainly due to the treatment of the multi-dimensional acceptance. It is expected that this can be reduced by increasing the size of the simulation sample used to determine the acceptance effects. Most other sources of systematic uncertainty are expected to scale with larger data samples.

USC UNIVERSIDADE DE SANTIAGO DE COMPOSTELA

USC
UNIVERSIDADE
DE SANTIAGO
DE COMPOSTELA

# Chapter 8

# Measurement of the $R(D^{(*)+})$ ratios using $\overline{B}^0 \to D^+ l \bar{\nu}_l$ decays

This chapter presents the second data analysis performed in this thesis. The basis of the study is already finished and some preliminary, partial results are available. The used data samples are presented in Sect. 8.1 and the event selection is described in Sect. 8.2. In section Sect. 8.3, the procedure to obtain the templates needed for the final fit is explained. The fit implementation and some checks and sensitivity studies are presented in Sect. 8.4. Finally, a summary of the achieved goals and the future plans for the analysis are written in Sect. 8.5.

## 8.1 Data samples

The studies of semileptonic decays presented in this thesis are based on $328$ pb$^{-1}$ of data from proton-proton collisions at $\sqrt{s} = 13$ TeV recorded by LHCb during 2015. In the near future, the developed strategy will be also applied to a data sample corresponding to $1665$ pb$^{-1}$ taken at $\sqrt{s} = 13$ TeV, collected in the year 2016. The final $R(D^+)$ measurement will be performed using the combined 2015+2016 data sample.

The trigger lines used for the analysis are listed in Table 8.1. The `Hlt2XcMuXForTauB2XcMu` line was specifically designed for this analysis and is aimed at minimising the biases on the muon distributions, that may affect the distinction between the tauonic and the muonic decays. This line was not available for 2011 and 2012, which motivates that only Run 2 data are used in the analysis. The employed stripping line is `Strippingb2DpMuXB2DMuForTauMuLine`.

| **L0 Any of:** |
|---|
| L0Global TIS |
| L0Hadron TOS |
| **Hlt1 Any of:** |
| Hlt1TrackMVA TOS |
| Hlt1TwoTrackMVA TOS |
| **Hlt2:** |
| Hlt2XcMuXForTauB2XcMu TOS |

TABLE 8.1: Trigger lines used in this analysis.

The simulated samples used in the analysis are listed in Table 8.2. Additionally, two control data samples are used to study specific backgrounds.

- A wrong-sign (WS) sample, composed of events with the visible final state $D^+\mu^+$. This dataset is used to study combinatorial background resulting from a random combination of a true $D^+$ with an uncorrelated muon.

| Sample | Type | Generated events |
|---|---|---|
| $\bar{B}^0 \to D^+ \tau (\to \mu \bar{\nu}_\mu \nu_\tau) \bar{\nu}_\tau$ | Signal | 100K |
| $\bar{B}^0 \to D^{*+} (\to D^+ \pi^0) \tau (\to \mu \bar{\nu}_\mu \nu_\tau) \bar{\nu}_\tau$ | Signal | 100K |
| $\bar{B}^0 \to D^+ \mu \bar{\nu}_\mu$ | Normalisation | 500K |
| $\bar{B}^0 \to D^{*+} (\to D^+ \pi^0) \mu \bar{\nu}_\mu$ | Normalisation | 500K |
| $\bar{B}^0 \to D^{**+} (\to D^+ X) \mu \bar{\nu}_\mu$ | Background | 100K |
| $\bar{B}^0 \to D^{**+} (\to D^+ X) \mu \bar{\nu}_\mu$, higher mass resonances | Background | 50K |
| $B^- \to D^{**0} (\to D^+ X) \mu \bar{\nu}_\mu$ | Background | 100K |
| $\bar{B}^0 \to D^+ H_c (\to \mu \bar{\nu}_\mu X') X$ | Background | 300K |
| $B^- \to D^+ H_c (\to \mu \bar{\nu}_\mu X') X$ | Background | 150K |

TABLE 8.2: List of Monte Carlo samples used.

- A muon mis-id sample, composed of events with the visible final state $D^+ h^\pm$ where $h^\pm$ is a charged hadron. This sample, which uses the line `Hlt2XcMuXForTauB2XcFakeMu` (identical to the nominal one but requiring no associated hits in the muon chambers for the muon candidates), is used to study the background originating from a hadron been misidentified as a muon.

## 8.2 Event selection

The selection of candidates is performed in a sequence of steps. The procedure focuses on finding well reconstructed and isolated $D^+$ candidates, avoiding as much as possible imposing requirements on the muons, since they can affect the distributions on the fit variables. An initial pre-selection is followed by a set of PID requirements on the kaons and pions. Then, a BDT is trained against non-$D^+$ background, and charged and neutral isolation techniques are applied to reduce the contribution from partially reconstructed backgrounds.

### 8.2.1 Pre-selection requirements

The list of pre-selection requirements is written in Table 8.3. On top of the trigger and stripping cuts, a requirement on the $\mu$ $PID\mu$ variable is applied, following Ref. [24].

### 8.2.2 Particle identification

In order to suppress the contribution from hadron mis-id backgrounds, apart from the PID requirements based on DLL variables that are applied in the stripping, a tighter filtering is done basing on the ProbNN variables. Specifically, the combination $ProbNNpik \equiv ProbNNpi * (1 - ProbNNk)$ is used for the pions and the combination $ProbNNkpi \equiv ProbNNk * (1 - ProbNNpi)$ is used for the kaons.

Since the Monte Carlo is known not to properly reproduce the PID variable distributions, the requirements are optimised using the real data sample. For this purpose, the fraction of signal and non-$D^+$ background for a given PID requirement is determined trough a fit to the $K\pi\pi$ invariant mass distribution. The $D^+$ line shape is modelled with an Ipatia function (see Eq. 7.2), where the parameters $\zeta$ and $\beta$ are fixed to zero, the central mass and the width are floated and the rest of the parameters are fixed to those obtained from a fit to the $\overline{B}^0 \to D^+ \mu^- \overline{\nu}_\mu$ Monte Carlo sample with only the pre-selection requirements applied. The plot of the fit to simulated data is shown in Fig. 8.1 and the resulting parameter values are written in Table 8.4. In order to model the background contribution, a linear polynomial with a free coefficient is used. The result of a fit

| Particle | Variable | Hlt2 cuts | Stripping cuts | Extra pre-selection cuts |
|---|---|---|---|---|
| $K, \pi$ | $K\ PIDK$ | $> 2$ | $> 4$ | – |
| | $\pi\ PIDK$ | $< 4$ | $< 2$ | – |
| | Track $IP_{\chi^2}$ | $> 9$ | – | – |
| | Track $p_T$ [MeV/$c$] | $> 200$ | $> 300$ | – |
| | Track $p$ [MeV/$c$] | $> 5000$ | – | – |
| | $\geq 1$ track $p_T$ [MeV/$c$] | $> 800$ | – | – |
| | $\sum$ track $p_T$ [MeV/$c$] | $> 2500$ | – | – |
| | Track GhostProb | – | $< 0.5$ | – |
| $D$ | $D$ mass interval [MeV/$c^2$] | $1830 - 1910$ | – | – |
| | $D$ $p_T$ [MeV/$c$] | $> 2000$ | – | – |
| | $D$ child pair DOCA [mm] | $< 0.10$ | – | – |
| | $D$ $\chi^2_{vertex}/ndf$ | $< 10$ | $< 4$ | – |
| | $D$ DIRA | $> 0.999$ | – | – |
| | $D\ FD_{\chi^2}$ | $> 25$ | – | – |
| $\mu$ | $\mu\ IP_{\chi^2}$ | $> 16$ | – | – |
| | $\mu\ PID\mu$ | – | $> -200$ | $> 2$ |
| | $\mu$ GhostProb | – | $< 0.5$ | – |
| | $\mu$ $p$ [MeV/$c$] | – | $> 3000$ | – |
| $D\mu$ | $D\mu$ $\chi^2_{vertex}/ndf$ | $< 15$ | $< 6$ | – |
| | $D\mu$ DIRA | $> 0.999$ | – | – |
| | $D\mu$ DOCA [mm] | $< 0.50$ | – | – |
| | $D\mu\ FD_{\chi^2}$ | $> 50$ | – | – |
| | $D\mu$ mass interval [MeV/$c^2$] | – | $0 - 10000$ | – |

TABLE 8.3: Summary of pre-selection requirements.

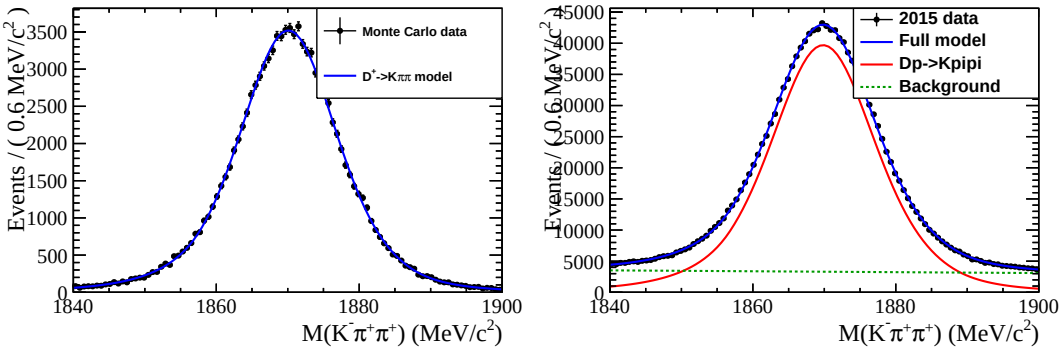



FIGURE 8.1: Fits to the $M(K\pi\pi)$ distribution for (left) $\overline{B}^0 \to D^+\mu^-\overline{\nu}_\mu$ Monte Carlo events and for (right) the nominal data sample, before the tight hadron PID requirements are applied.

| Parameter | Value |
|---|---|
| $\mu$ | $1870.09 \pm 0.03\,\mathrm{MeV}/c^2$ |
| $\sigma$ | $8.7 \pm 0.3\,\mathrm{MeV}/c^2$ |
| $a1$ | $1.39 \pm 0.04$ |
| $a2$ | $2.0 \pm 0.2$ |
| $\lambda$ | $-2.90 \pm 0.4$ |
| $n1$ | $5.8 \pm 0.7$ |
| $n2$ | $5 \pm 2$ |

TABLE 8.4: Parameters measured in the fit to the $M(K\pi\pi)$ distribution of $\overline{B}^0 \to D^+\mu^-\overline{\nu}_\mu$ Monte Carlo events, before the tight hadron PID requirements are applied.

to data without any extra PID cut applied is displayed on Fig. 8.1, and the measured parameters are written in Table 8.5.

The pion and kaon PID variables are assumed not to be correlated with each other, and are thus optimised independently. Each variable is sampled along its range, applying the corresponding PID cut to data at each step and computing the associated signal significance, $S/\sqrt{S+B}$, where the signal $S$ and the background $B$ are determined from the three-body-mass fits. The optimisation curves are shown in Fig. 8.2. The maximum significance is achieved for $ProbNNpik > 0.14$ and $ProbNNkpi > 0.12$.

### 8.2.3 Decay kinematics and topology

In order to suppress the non $D^+$ background, a BDT is trained using $\overline{B}^0 \to D^+\tau^-\overline{\nu}_\tau$ simulated events as signal and data mass sidebands, $1830 < M(K\pi\pi) \leq 1840\ \mathrm{MeV}/c^2$ and $1900 < M(K\pi\pi) \leq 1910\ \mathrm{MeV}/c^2$, as background. The PID cuts developed in the previous section are

| Parameter | Value |
|---|---|
| $\mu_{D^+}$ | $1869.830 \pm 0.009\,\mathrm{MeV}/c^2$ |
| $\sigma_{D^+}$ | $9.39 \pm 0.01\,\mathrm{MeV}/c^2$ |
| $N_{D^+}$ | $1317291 \pm 1871$ |
| $c_{bkg}$ | $-0.0004297 \pm 0.000005$ |
| $N_{bkg}$ | $330628 \pm 1587$ |

TABLE 8.5: Parameters measured in the fit to the $M(K\pi\pi)$ distribution of data, before the tight hadron PID requirements are applied.

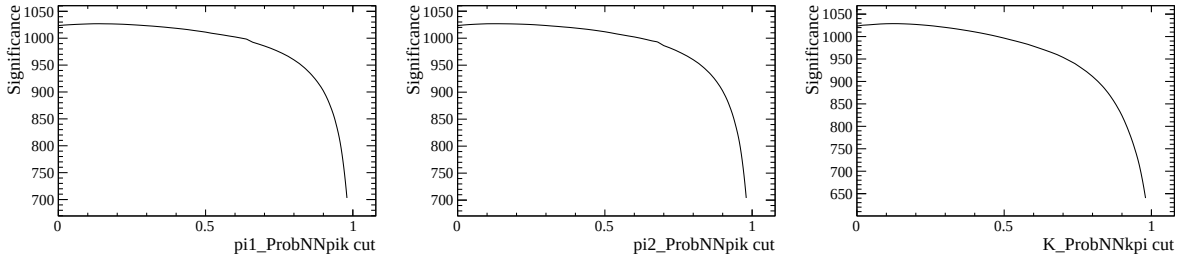



FIGURE 8.2: Signal significance as a function of the hadron PID cuts.

applied to the real data sample but not to the simulated one, to avoid biases due to the incorrect description of the PID variables in simulation. Half of the signal and background samples is used for training and the other half is used for testing.

The BDT is input with the following kinematic and topological variables:

- $log_pi1_PT$, $log_p2_PT$ and $log_K_PT$: natural logarithm of the pion and kaon transverse momenta.
- $log_pi1_IPCHI2_OWNPV$, $log_pi2_IPCHI2_OWNPV$ and $log_K_IPCHI2_OWNPV$: natural logarithm of the pion and kaon $\chi^2$ on the impact parameter with respect to the primary vertex.
- $log_pi1_TRACK_GhostProb$, $log_pi2_TRACK_GhostProb$ and $log_K_TRACK_GhostProb$: natural logarithm of the probability for pion and kaon tracks of being ghosts (pseudo-random combinations of hits).
- $Dplus_ENDVERTEX_CHI2NDOF$: reduced $\chi^2$ of the $D^+$ decay vertex.
- $log_B0_dXY$: natural logarithm of the $B^0$ transverse flight distance.

The signal and background distributions on these variables are shown in Fig. 8.3 and the corresponding linear correlation coefficients are shown in Fig. 8.4. The BDT output distributions for the training and testing samples are plotted on Fig. 8.5. No visible overtraining is found.

In order to find the optimal BDT cut, the signal significance, $S/\sqrt{S+B}$, is used as figure of merit. The signal and background yields at each point are obtained from the fraction of simulated signal events and data sideband events that pass the corresponding BDT cut, together with the initial (pre-cut) yields for signal and background that are obtained through a three-body mass fit, as described in the previous section. The significance is maximal when the BDT output values are required to be larger than $-0.23$.

### 8.2.4 Isolation from charged particles

Extra charged tracks accompanying the $D^+\mu^-$ candidates, coming from partially reconstructed decays, are suppressed by using the MVA method introduced in Sect. 6.4.6. The output variable takes higher values for tracks that are likely to be originated from the signal $B$ candidate and lower values for those likely to come from the rest of the event. Signal candidates are isolated by requiring the MVA output variable to be below a given threshold for any of the extra tracks in the event. The threshold value is optimised for this analysis by comparing the MVA output distribution of a simulated background sample of $B^0 \to DD$ events, with a $DD$ cocktail where one of the $D$ mesons decays semileptonically, with the distribution of a simulated signal sample of $\overline{B}^0 \to D^+\mu^-\overline{\nu}_\mu$ events. Both distributions are shown in Fig. 8.6(a). For a quantitative comparison, the associated ROC curve is constructed by sampling the range of possible thresholds. This curve

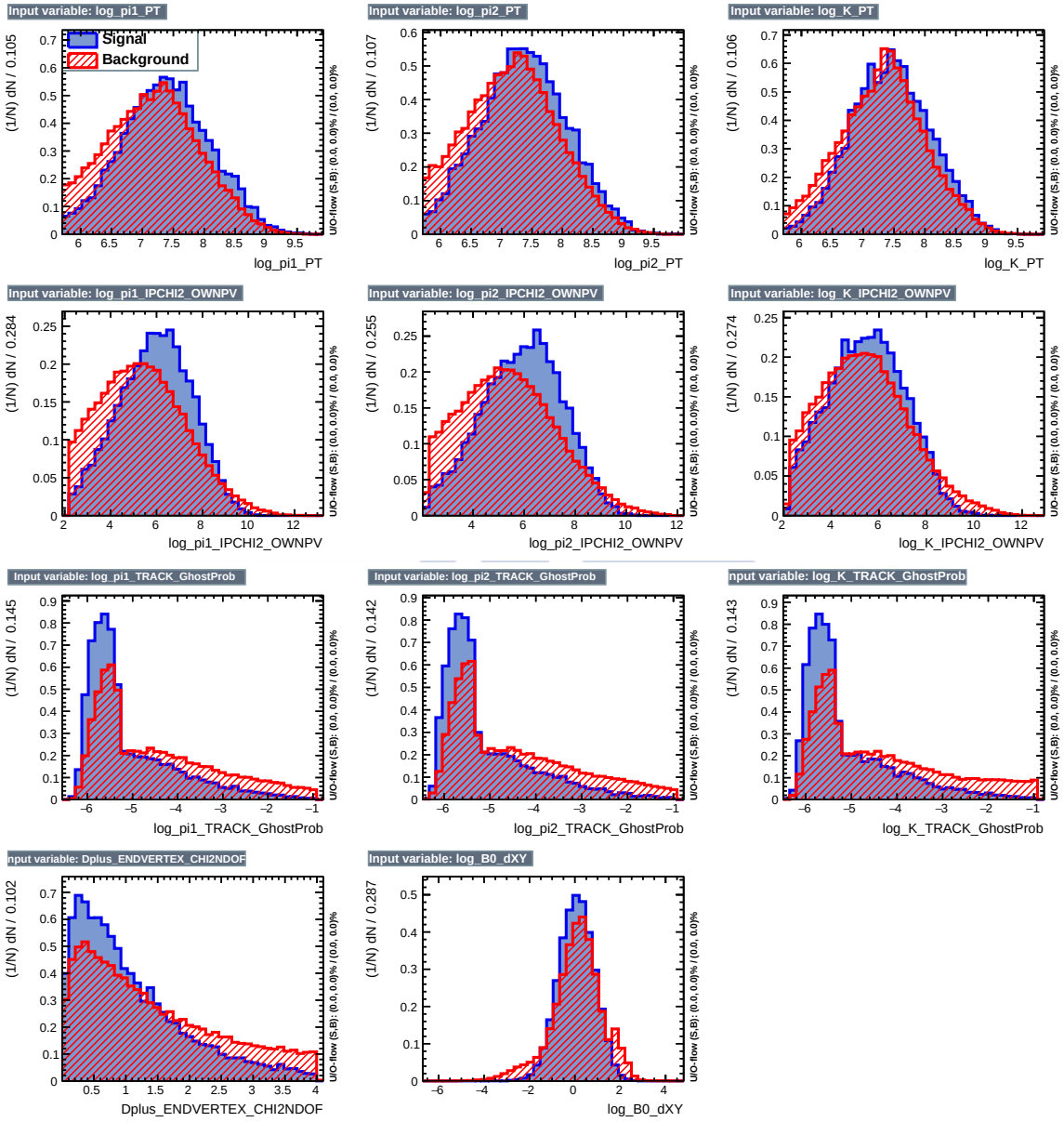



FIGURE 8.3: Input variable distributions for signal and background used in the BDT aimed at suppressing the non $D^+$ background.

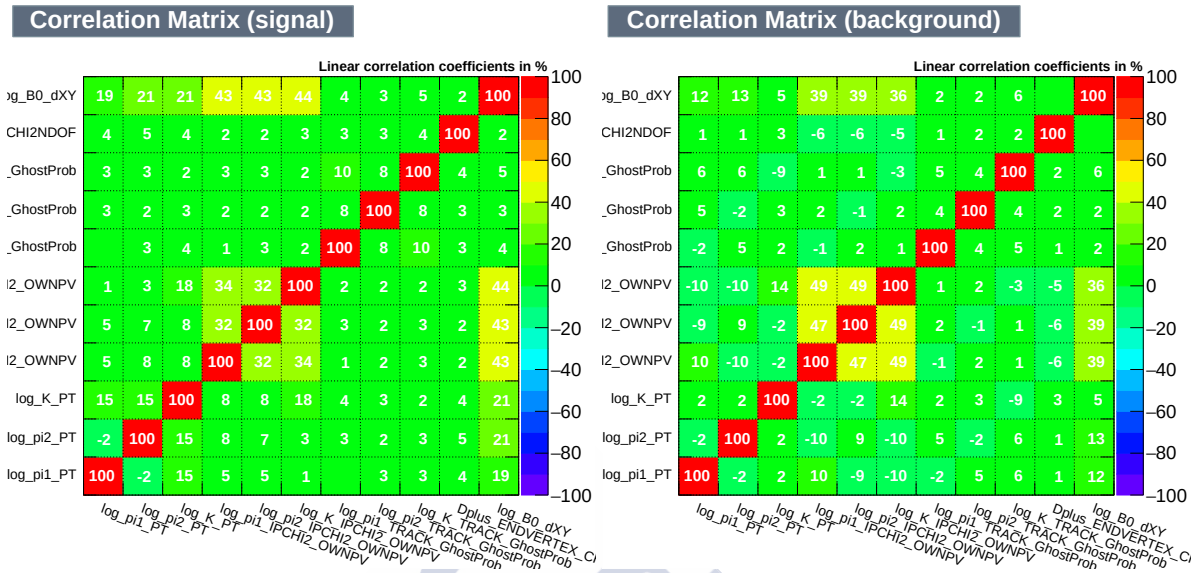



FIGURE 8.4: Signal and background matrix of linear correlation coefficients among the input variables of the BDT used to suppress the non $D^+$ background.

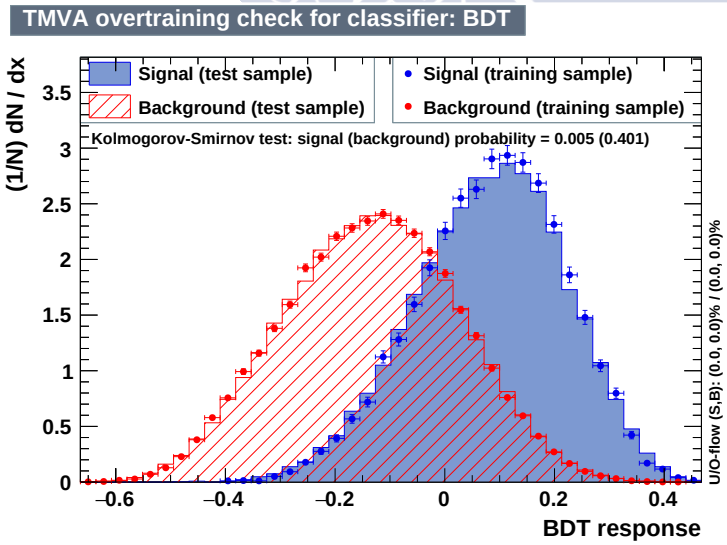



FIGURE 8.5: Output distributions and test of overtraining for the BDT used to suppress the non $D^+$ background.

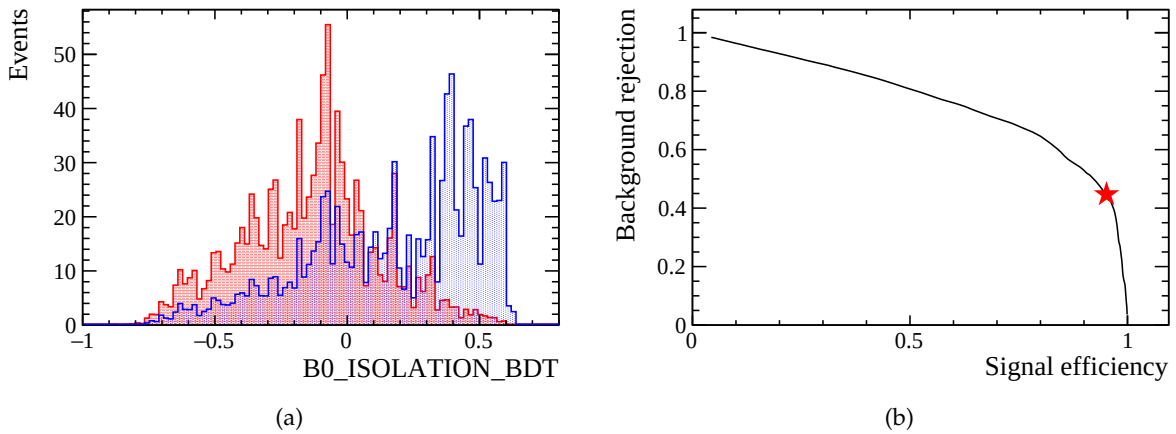



FIGURE 8.6: Optimisation of the threshold value for the MVA used for charged isolation. Figure (a) shows the MVA output distributions for (red) signal and (blue) background simulated samples. Figure (b) shows the corresponding ROC curve. The chosen working point is indicated with a red star.

is shown in Fig. 8.6(b) and the working point is placed where the signal efficiency starts to drop, corresponding to a threshold value of 0.32.

### 8.2.5 Isolation from neutral particles

Contributions from events with extra neutral particles are suppressed using the method introduced in Sect. 6.4.7. The information from resolved neutral pions and from neutral cones around the $D^+$ flight direction is processed independently and afterwards combined to create a per-event isolation BDT. Simulated $\overline{B}^0 \to D^+ \mu^- \overline{\nu}_\mu$ events are used as a signal (isolated) sample and simulated $\overline{B}^0 \to D^{*+}(\to D^+ \pi^0) \mu^- \overline{\nu}_\mu$ events as a background (non-isolated) sample[1].

#### 8.2.5.1 Resolved neutral pions

The reconstruction process associates a variable number of neutral pion candidates to each event. All of them are false positives for the $\overline{B}^0 \to D^+ \mu^- \overline{\nu}_\mu$ sample, while the $\overline{B}^0 \to D^{*+}(\to D^+ \pi^0) \mu^- \overline{\nu}_\mu$ sample contains a fraction of true neutral pions. To separate between signal-like (false) pions from background-like (truth) ones, a per-$\pi^0$-candidate BDT is trained, using all the resolved pions from $\overline{B}^0 \to D^+ \mu^- \overline{\nu}_\mu$ against those from $\overline{B}^0 \to D^{*+}(\to D^+ \pi^0) \mu^- \overline{\nu}_\mu$ that are selected by a truth-matching tool that I developed. This tool looks for correctly identified neutral pions that decay into two photons which are also correctly identified. The per-event truth-matching efficiency is found to be $\sim 10\%$. The simulated events providing the pions for the BDT training are requested to pass the previous selection steps, excepting the PID requirements. Half of the signal and background samples are used for training and the other halves are used for testing.

The following variables are used to train the BDT:

- $Dplus_Pi0_M$: invariant mass of the resolved $\pi^0$.
- $Dplus_Pi0_DeltaM$: difference in invariant mass between the $D^+$ and the $D^+\pi^0$ combination.

[1] Even if the $\overline{B}^0 \to D^{*+}(\to D^+ \pi^0) l^- \overline{\nu}_l$ events serve in this analysis to measure the $R(D^{*+})$ ratio, the main goal is to maximise the sensitivity on $R(D^+)$. This justifies that, in this step of the selection, the $\overline{B}^0 \to D^{*+}(\to D^+ \pi^0) \mu^- \overline{\nu}_\mu$ events are treated as background in order to increase the purity of the $\overline{B}^0 \to D^+ l^- \overline{\nu}_l$ decays in the data sample.

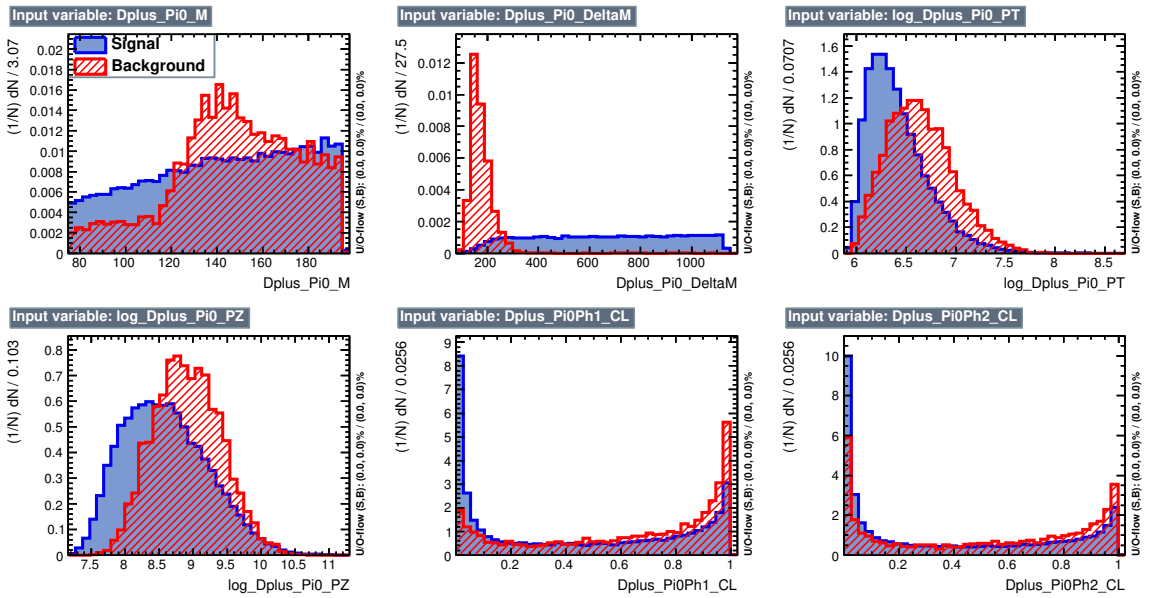



FIGURE 8.7: Input variable distributions for the resolved $\pi^0$ BDT.

- $log_Dplus_Pi0_PT$: natural logarithm of the $\pi^0$ transverse momentum.
- $log_Dplus_Pi0_PZ$: natural logarithm of the $\pi^0$ longitudinal momentum.
- $Dplus_Pi0Ph1_CL$ and $Dplus_Pi0Ph2_CL$: confidence level of each of the two photons that result from the decay of the $\pi^0$.

The signal and background distributions in the BDT training variables are shown in Fig. 8.7, and the corresponding linear correlation coefficients can be seen in Fig. 8.8. The resulting BDT output distributions, both for training and testing samples, are plotted in Fig. 8.9. No overtraining is observed.

In a second step of the procedure, the information from the per-$\pi^0$ BDT has to be translated into a per-event quantity. The discriminant variable chosen in this case is the number of resolved neutral pions per-event that have a BDT value less than 0, which correspond to the most true-like $\pi^0$ candidates.

#### 8.2.5.2 Analysis of neutral cones

Neutral cones around the $D^+$ flight direction with different radii, $\rho \in \{0.1, 0.2, 0.3, 0.4, 0.5, 0.6\}$, are investigated[2]. For each radius choice, a per-event BDT is trained on simulated $\overline{B}^0 \to D^+\mu^-\overline{\nu}_\mu$ (signal) and $\overline{B}^0 \to D^{*+}(\to D^+\pi^0)\mu^-\overline{\nu}_\mu$ (background) events. In the background case, a truth-matching algorithm is applied to select events with cones in which there is at least one correctly identified photon, coming from a correctly identified $\pi^0$ which has the same mother particle as the $D^+$. The simulated events are requested to pass the previous selection steps, excepting the PID requirements. Half of the signal and background samples are used for training and the other halves are used for testing. The best cone radius is chosen after training the BDTs and comparing the integral values for the ROC curves. The optimal working point is found to be $\rho = 0.2$, where the truth matching efficiency is $\sim 30\%$. The rest of this subsection, devoted to describe the construction of the BDT, particularises for the use of cones with this radius.

The following variables are used as input for the BDT:

[2]For a definition of the cone topology see Ref. [112].

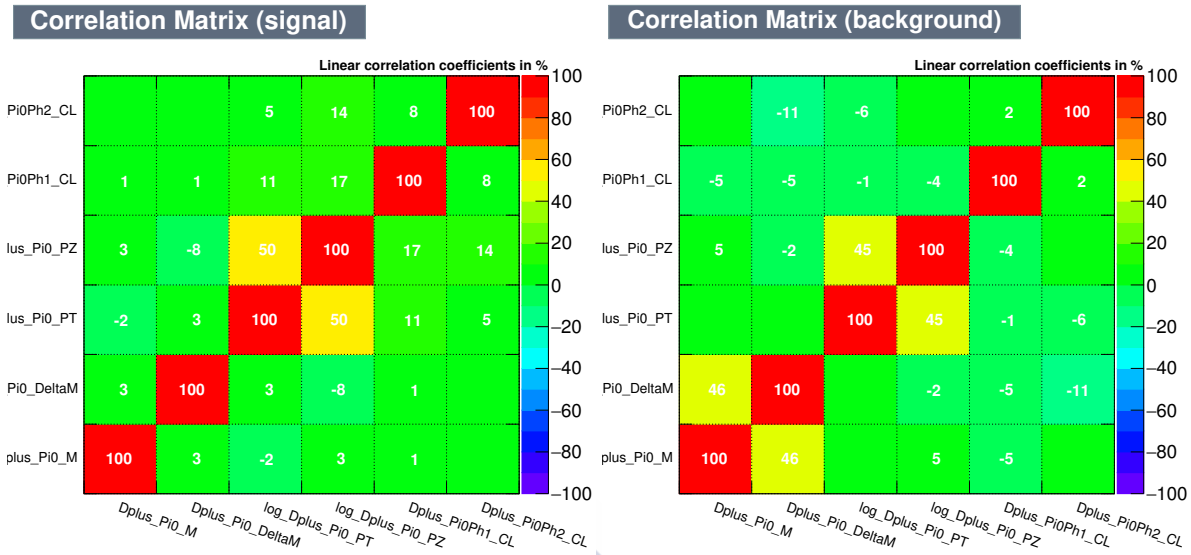



FIGURE 8.8: Signal and background matrix of linear correlation coefficients among the input variables for the resolved $\pi^0$ BDT.

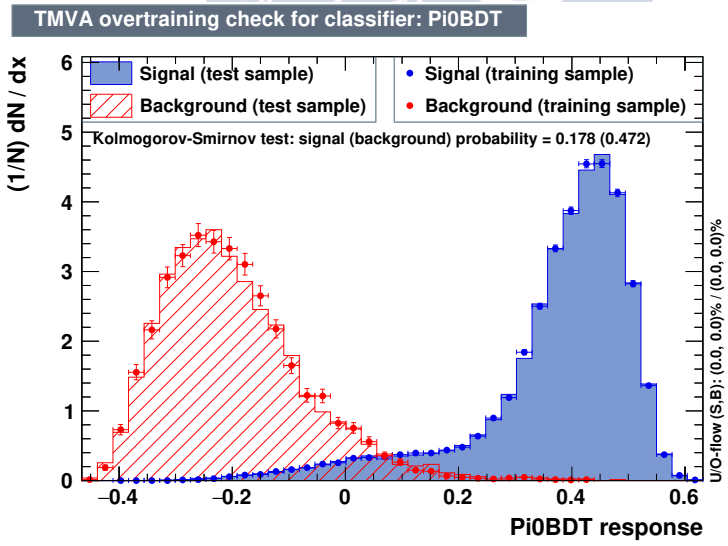



FIGURE 8.9: Output distributions and test of overtraining for the resolved $\pi^0$ BDT.

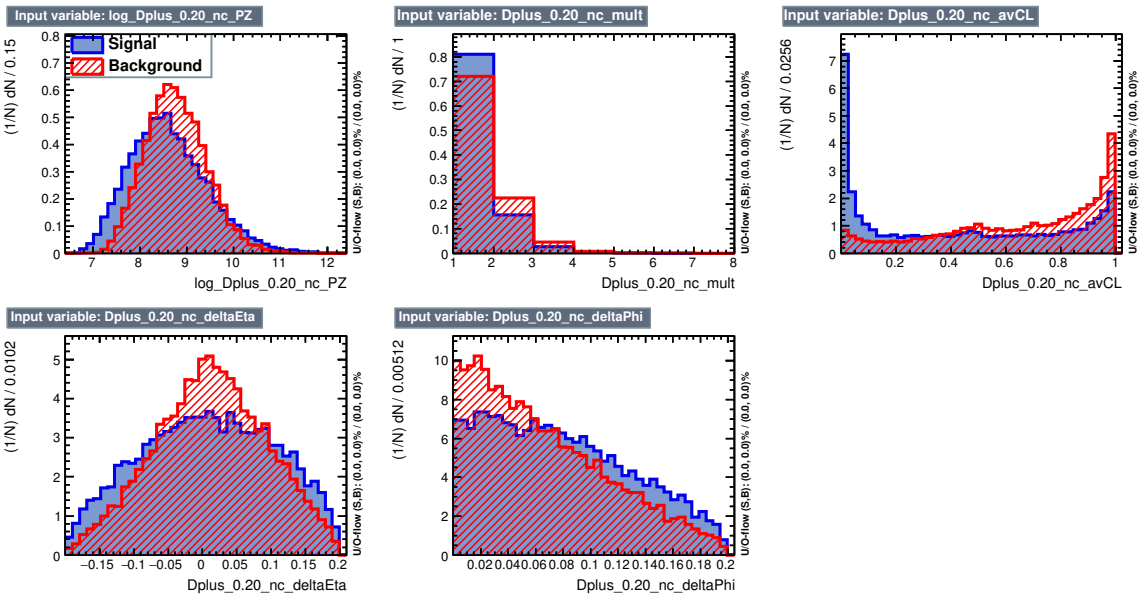



FIGURE 8.10: Input variable distributions for the neutral cone BDT.

- $log_Dplus_0.2_nc_PZ$: natural logarithm of the cone's longitudinal momentum[3].
- $Dplus_0.20_nc_mult$: photon multiplicity of the cone.
- $Dplus_0.20_nc_avCL$: average photon confidence level in the cone.
- $Dplus_0.20_nc_deltaEta$: difference in pseudorapidity between the 3-momentum of the $D^+$ and that of the neutral cone.
- $Dplus_0.20_nc_deltaPhi$: difference in azimuthal angle between the 3-momentum of the $D^+$ and that of the neutral cone.

The signal and background distributions for these variables are shown in Fig. 8.10 and the corresponding linear correlation coefficients can be seen in Fig. 8.11. The BDT output distributions, both for training and testing samples, are shown in Fig. 8.12. No overtraining is observed.

#### 8.2.5.3 Combined neutral isolation

The information from the number of selected, resolved, neutral pions per-event is combined with the information from the neutral cone BDT to create a single BDT for neutral isolation. For training and testing purposes, the same $\overline{B}^0 \to D^+\mu^-\overline{\nu}_\mu$ and $\overline{B}^0 \to D^{*+}(\to D^+\pi^0)\mu^-\overline{\nu}_\mu$ simulation samples are used, but without any truth-matching requirement applied. This situation represents more accurately the one found in real data and the overall performances get worse due to the low LHCb efficiency in the reconstruction of true photons and neutral pions. The linear correlation between the two input variables in simulation is found to be $-40\%$ for signal and $-36\%$ for background.

The BDT output distributions for the training and testing samples are shown in Fig. 8.13(a). No overtraining is observed. The corresponding ROC curve is shown in Fig. 8.13(b). The working point is set at a signal efficiency level of $90\%$, which corresponds to a BDT output requirement of $> -0.16$ and a background rejection power of $30\%$.

[3]The kinematic properties of the cone correspond to those of the combination of photons within it.

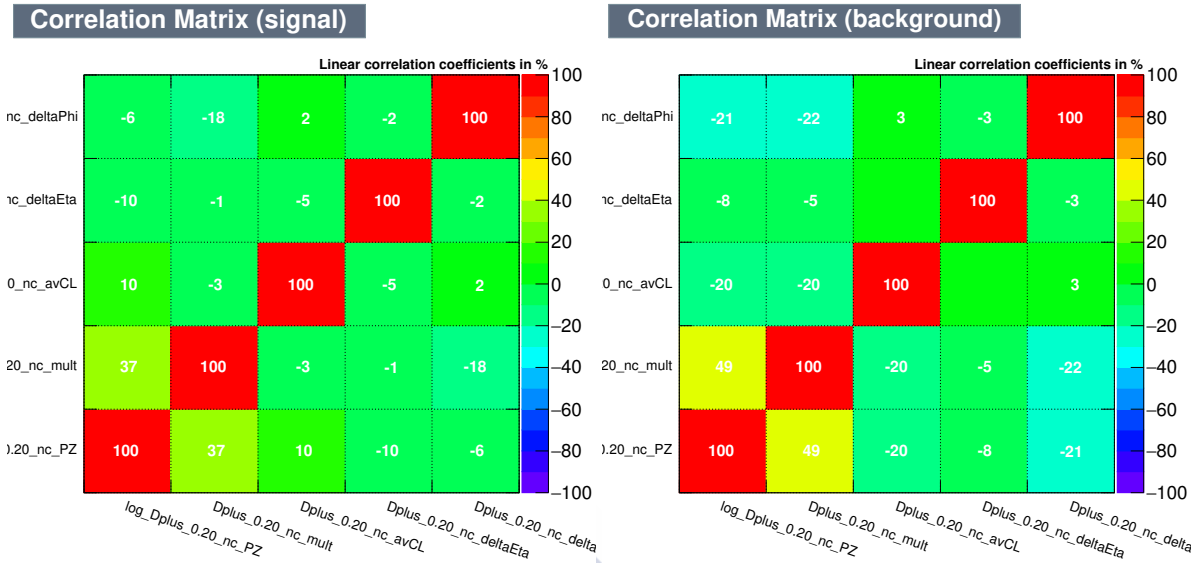



FIGURE 8.11: Signal and background matrix of linear correlation coefficients among the input variables for the neutral cone BDT.

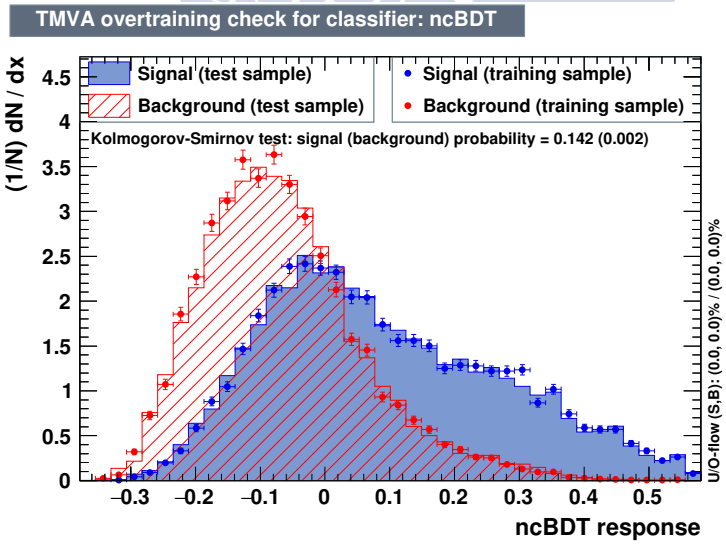
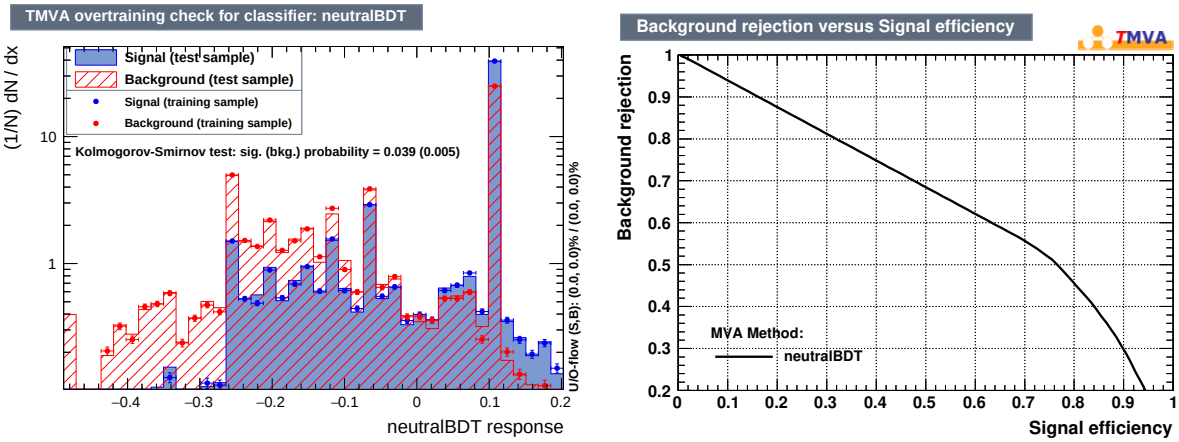



FIGURE 8.12: Output distributions and test of overtraining for the neutral cone BDT.




(a) (b)

FIGURE 8.13: Performance of the final BDT used for neutral isolation. Figure (a) shows the output distributions, in logarithmic scale, and the test of overtraining. Figure (b) shows the associated ROC curve.

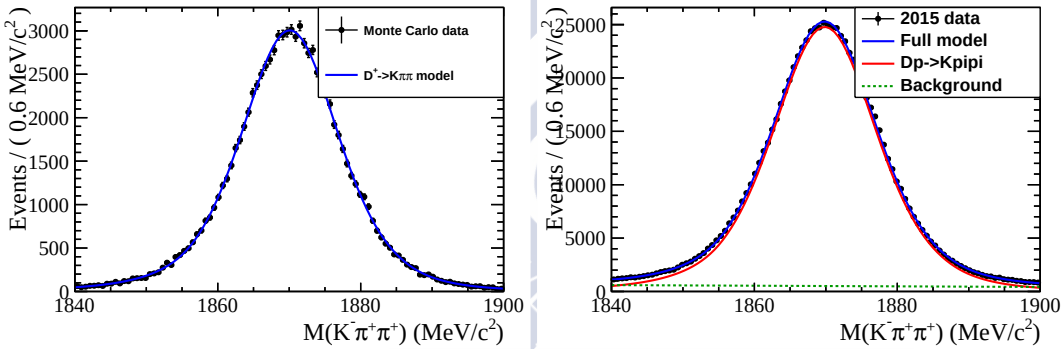



FIGURE 8.14: Fits to the $M(K\pi\pi)$ distribution for (left) $\overline{B}^0 \to D^+\mu^-\overline{\nu}_\mu$ Monte Carlo events and for (right) the nominal data sample, after the full selection is applied.

### 8.2.6 Fit to the filtered $M(K\pi\pi)$ distribution

To evaluate the overall performance of the event selection in terms of $D^+$ versus non-$D^+$ candidates, a fit to the three-body-mass distribution of the filtered data sample is done. Following Sect. 8.2.2, the $D^+$ component is modelled with an Ipatia function and the background is modelled with a linear polynomial. A prior fit to simulated $\overline{B}^0 \to D^+\mu^-\overline{\nu}_\mu$ events is done to determine several parameters that will be fixed in the model when fitting the data. The result of the fit to Monte Carlo events is shown in Fig. 8.14 and the obtained parameter values are written in Table 8.6. The final fit to data is presented in Fig. 8.14 and the measured parameters are collected in Table 8.7. A $D^+$ yield of $(8.124 \pm 0.012) \cdot 10^5$ events is found and the amount of non-$D^+$ background is determined to be a fraction of $\sim 6\%$ of the whole data sample.

For the final measurement, to be performed after the PhD thesis, the data collected by LHCb during 2016 will be combined with the 2015 data sample that has been used for these studies. Considering that the proton collision energy was $\sqrt{s} = 13\,\text{TeV}$ in both data taking periods, assuming similar efficiencies and taking into account that the integrated luminosity was $328\,\text{pb}^{-1}$ in 2015 and $1665\,\text{pb}^{-1}$ in 2016, a total sample of $\sim 5 \cdot 10^6$ $D^+$ candidates is expected.

| Parameter | Value |
|---|---|
| $\mu$ | $1870.07 \pm 0.03\,\mathrm{MeV}/c^2$ |
| $\sigma$ | $8.8 \pm 0.1\,\mathrm{MeV}/c^2$ |
| $a1$ | $1.56 \pm 0.05$ |
| $a2$ | $1.99 \pm 0.05$ |
| $\lambda$ | $-2.80 \pm 0.2$ |
| $n1$ | $4.7 \pm 0.7$ |
| $n2$ | $6 \pm 2$ |

TABLE 8.6: Parameters measured in the fit to the $M(K\pi\pi)$ distribution of $\overline{B}^0 \to D^+\mu^-\overline{\nu}_\mu$ Monte Carlo events, after the selection is applied.

USC UNIVERSIDADE DE SANTIAGO DE COMPOSTELA

| Parameter | Value |
|---|---|
| $\mu_{D^+}$ | $1869.84 \pm 0.01\,\mathrm{MeV}/c^2$ |
| $\sigma_{D^+}$ | $9.38 \pm 0.02\,\mathrm{MeV}/c^2$ |
| $N_{D^+}$ | $812413 \pm 1227$ |
| $c_{bkg}$ | $-0.0004885 \pm 0.000003(\,\mathrm{MeV}/c^2)^1$ |
| $N_{bkg}$ | $51046 \pm 862$ |

TABLE 8.7: Parameters measured in the fit to the $M(K\pi\pi)$ distribution of data, after the full selection is applied.

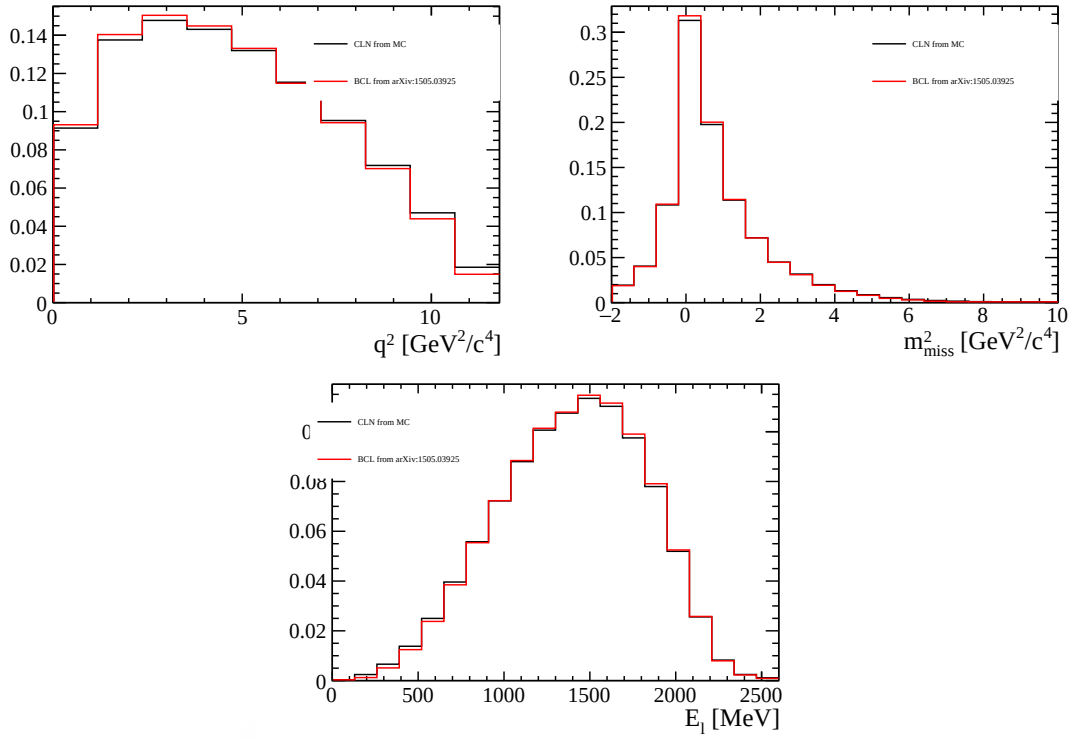



FIGURE 8.15: Re-weighting of the MC template of $\overline{B}^0 \to D^+\mu\overline{\nu}_\mu$, to correct the modelling of the form factors used in generation.

## 8.3 Multi-dimensional templates

The different components of the final fit are modelled with templates, which correspond to three-dimensional histograms on the discriminant variables presented in Sect. 4.2. For signal, normalisation, and backgrounds coming from feed-down and double-charm, these templates are obtained from Monte Carlo samples. The muon mis-id and combinatorial background templates are obtained from control data samples (see Sect. 8.1). All the datasets are filtered by the event selection presented in the previous section.

### 8.3.1 Monte Carlo templates

As explained in Sect. 4.3, the parameterisation of the form factors used in event generation relies on the CLN formalism. In order to use the BCL approach instead, the Monte Carlo samples are re-weighted on a per-event way using several kinematic variables, following the method presented in the first LHCb measurement of $R(D^*)$ [24]. For illustration, the effect of the re-weighting on a Monte Carlo sample of $\overline{B}^0 \to D^+\mu\overline{\nu}_\mu$ events is shown in Fig. 8.15. The resulting templates obtained from the simulated samples are shown in Fig. 8.16.

### 8.3.2 Data templates

Both the muon mis-id and combinatorial backgrounds contain a true $D^+$ resonance. Consequently, the control samples are sWeighted using fits to the $K\pi\pi$ invariant mass (as the one in Sect. 8.2.6), in order to remove non-$D^+$ contributions. The resulting templates are shown in Fig. 8.17.

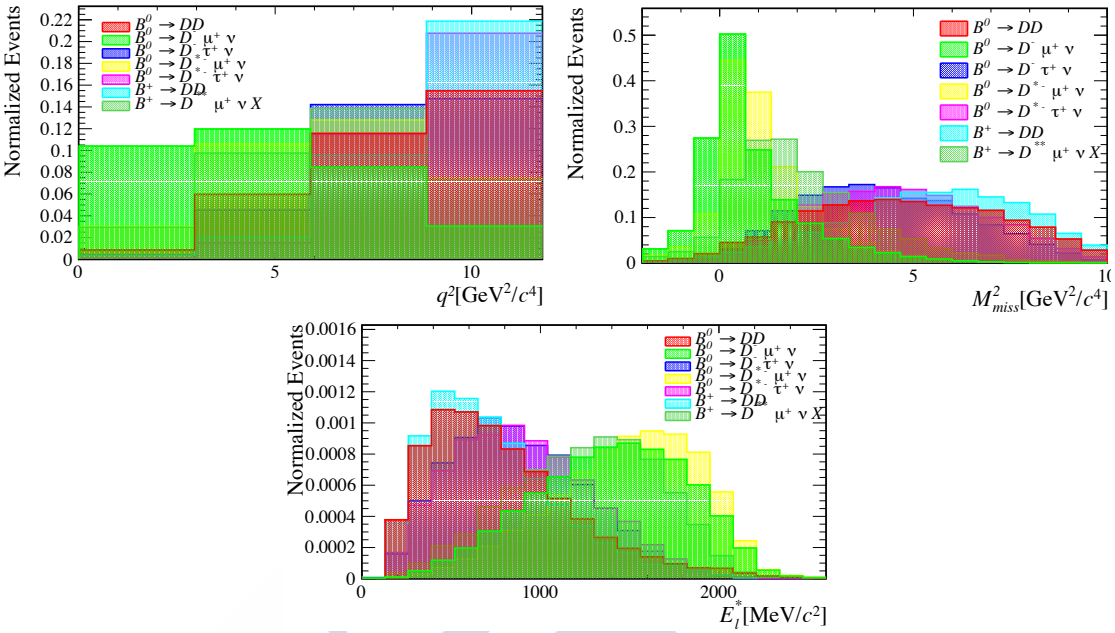



FIGURE 8.16: Templates obtained from Monte Carlo samples.

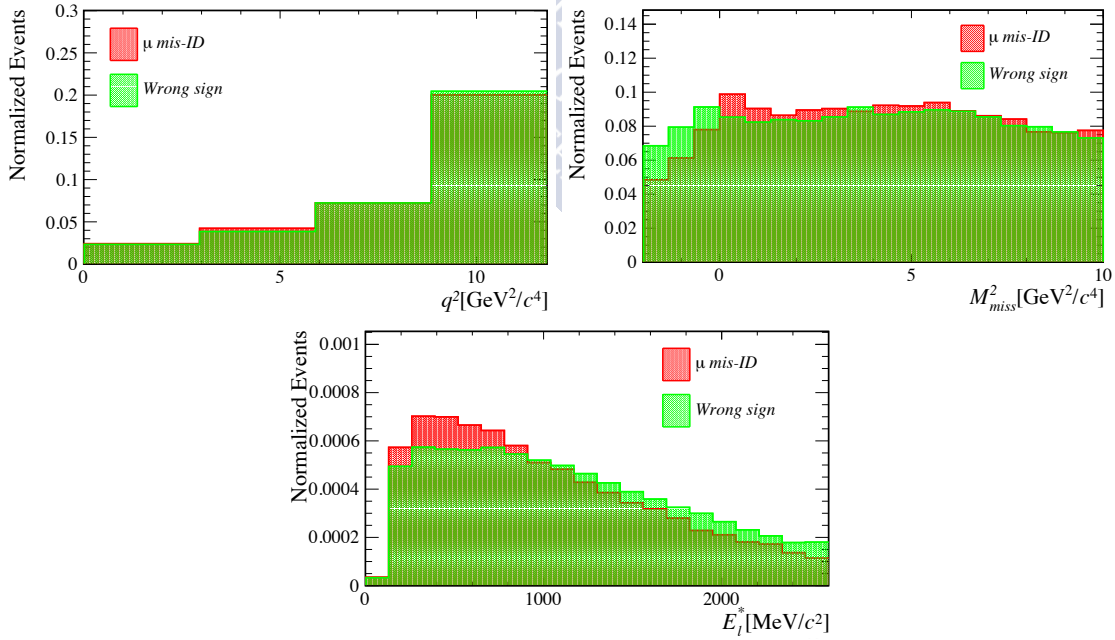



FIGURE 8.17: Templates obtained from control data samples.

| Sample | Visible $\mathcal{B}$ [%] | Efficiency [%] |
|---|---|---|
| DpMuNu | 2.2 | 18 |
| DpTauNu | 0.15 | 15 |
| DstMuNu | 1.6 | 12.7 |
| DstTauNu | 0.08 | 11.2 |
| BDststMuNu | 2.3 | 6.5 |
| B2DD | 1.2 | 5.9 |

TABLE 8.8: Expected visible branching fraction and efficiency for different full Monte Carlo samples that correspond to components included in the model.

## 8.4 Fit and sensitivity studies

In this section, the implementation of the baseline fitting framework and some checks and sensitivity studies are presented.

### 8.4.1 Setup of the fit

The measurement of the $R(D^{(*)+})$ ratios bases on a three-dimensional template-based fit to the filtered data. The fit variables are described in Sect. 4.2. The construction of the templates used in the fit is explained in Sect. 8.3. The yields of the normalisation and background channels, listed in Sect. 4.1, are floated in the fit. The yields of the tauonic signal components, $\overline{B}^0 \to D^+\tau\overline{\nu_\tau}$ and $\overline{B}^0 \to D^{*+}\tau\overline{\nu_\tau}$, are parameterised in terms of the yields of the corresponding muonic normalisation channels multiplied by the raw $R$ ratios, $R_{raw}(D^+)$ and $R_{raw}(D^{*+})$. The raw ratios need to be later transformed in order to obtain $R(D^+)$ and $R(D^{*+})$, using the expressions in Sect. 4.1. The systematic effect on the uncertainty due the finite size of the samples used to construct the templates is directly accounted for during fitting, using the so called Barlow-Beeston method [132]. This effect caused the dominant systematic uncertainty in the previous LHCb measurements of $R(D^*)$ [25, 44].

This thesis features a series of toy Monte Carlo studies performed with the developed fitting framework. They are aimed at optimising and checking the procedure, as well as estimating the sensitivity on the measured parameters. The fit to real data is not included in the document, since it will be done in the period after the thesis.

When generating toy Monte Carlo samples, the yields of the components that have a full Monte Carlo sample associated are obtained by multiplying the expected visible branching fraction for that component by the efficiency found in simulation. The values of these fractions are given in Table 8.8. The size of the contributions from the combinatorial and muon mis-ID backgrounds are estimated using the control data samples. Approximated overall fractions of $\sim 0.1\%$ and $\sim 0.08\%$ are found for the combinatorial and muon mis-ID backgrounds, respectively. For illustration, the result from a fit to a toy Monte Carlo sample which was generated using the expected total yield for the 2015+2016 combined data sample is shown in Fig. 8.18.

### 8.4.2 Optimisation of the binning

The size of the three-dimensional bins used in the fit affects the sensitivity on the measured parameters. A finer binning can reduce the uncertainties but it can also lead to the existence of bins with zero or a negative number of events (in the case of sWeighted templates), which would prevent the fit from working properly. To optimise the binning scheme, a set of toy experiments (generation and fit) with different number of bins for the $M^2_{miss}$ and $E^*_\mu$ variables is constructed. The resulting correlated uncertainties for the $R(D^+)$ and $R(D^{*+})$ parameters, as retrieved from the toys, are shown in Fig. 8.19. The optimal working point is found to correspond to 18 bins in

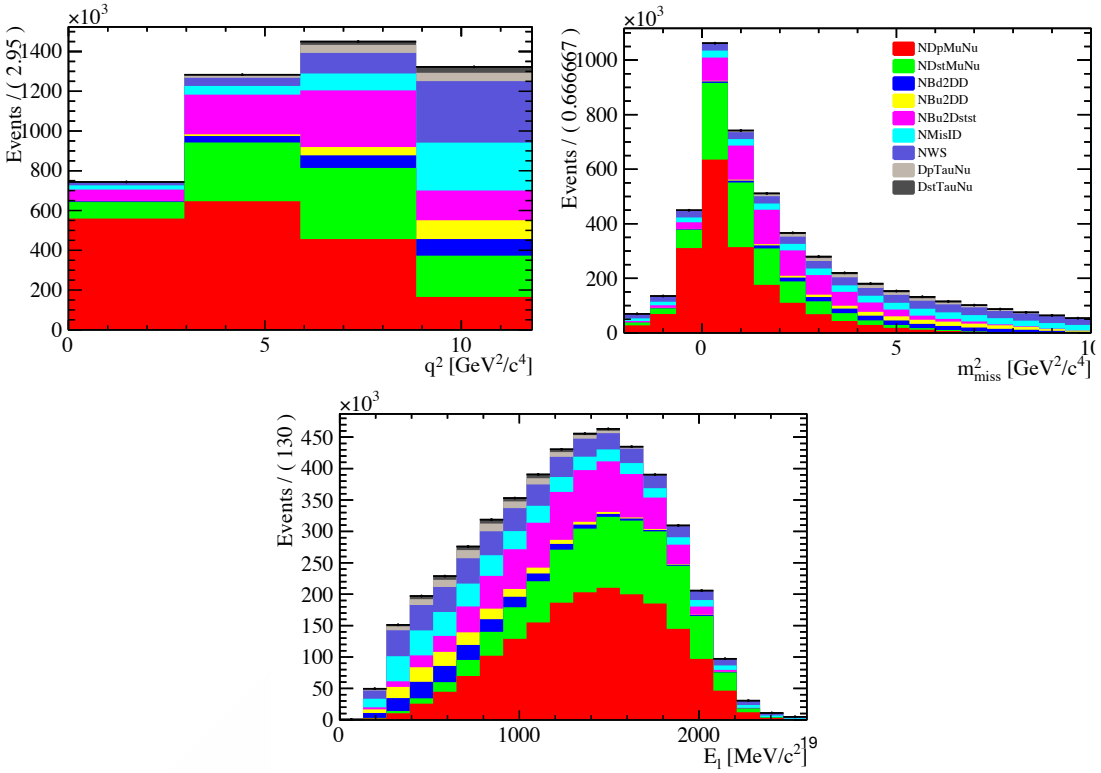



FIGURE 8.18: Fit to a toy Monte Carlo sample that was generated using the expected total yield for the 2015+2016 combined data sample.

$M^2_{miss}$ and 20 bins in $E^*_\mu$. Finally, the number of bins in the $q^2$ variable is set to be 4, the same as in the first LHCb measurement of $R(D^*)$ [44].

### 8.4.3 Toy Monte Carlo studies and sensitivity estimation

A set of 250 toy Monte Carlo experiments are performed to check the fitting framework. The Barlow-Beeston method is not used for this check since it significantly increases the fitting time. The experiments are generated using the estimated total yield for the 2015+2016 data sample. The resulting pull distributions for the raw $R$ parameters are shown in Fig. 8.20. A good behaviour of the distributions is observed.

To estimate the sensitivity on the raw $R$ ratios, another set of 159 experiments is performed. In this occasion, the Barlow-Beeston method is used. The distributions of the uncertainties obtained in the fits are shown in Fig. 8.21. These uncertainties account both for the statistical uncertainty inherent to the fitting procedure and for the effect of the finite size of the samples used to obtain the templates. No other systematic effect is included. These uncertainties can be improved in the future, by using an alternative, optimised set of fit variables.

### 8.4.4 Effect of the Monte Carlo sample size on the sensitivity

Since the effect of the limited size of the Monte Carlo samples used to obtain the templates showed to be the dominant contribution to the systematic uncertainties in the previous LHCb analyses [25, 44], the uncertainty obtained from the toy studies in different scenarios for the sample sizes is evaluated. The results are shown in Fig. 8.22. The uncertainty for the case of infinite Monte Carlo statistics is evaluated by turning off the Barlow-Beeston method. The study shows that the simulation sample size plays indeed a mayor role in the sensitivity. Consequently,

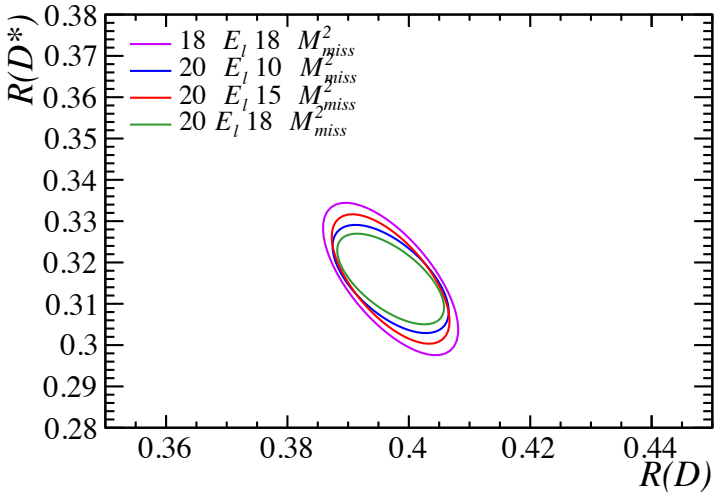



FIGURE 8.19: Correlated uncertainty on the $R(D^+)$ and $R(D^{*+})$ measurements, as a function of the number of bins in the $E^*_\mu$ and $M^2_{miss}$ variables.

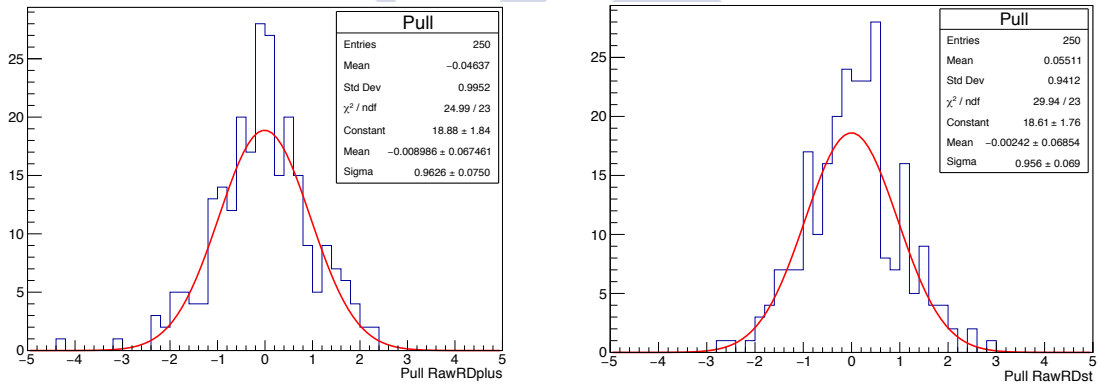



FIGURE 8.20: Pull distributions for the $R_{raw}(D^+)$ and $R_{raw}(D^{*+})$ parameters for an ensemble of toy experiments.

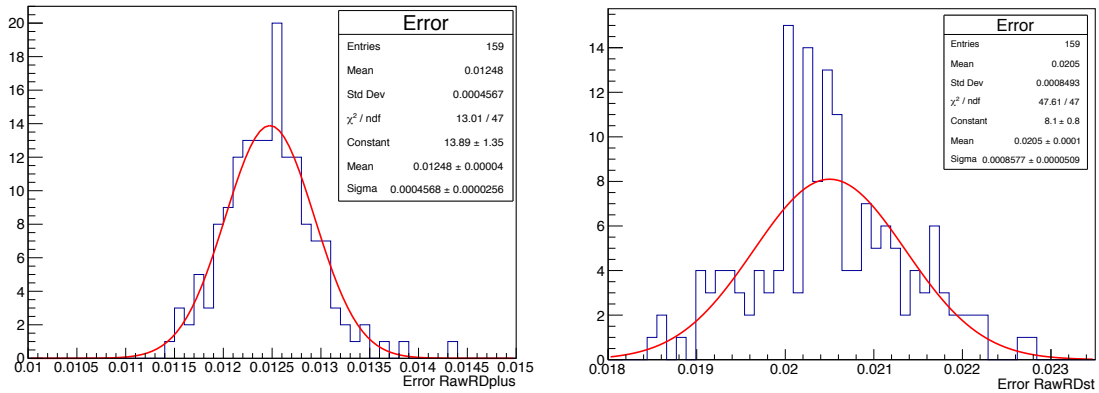



FIGURE 8.21: Distributions of the uncertainties on the $R_{raw}(D^+)$ and $R_{raw}(D^{*+})$ parameters for an ensemble of toy experiments.

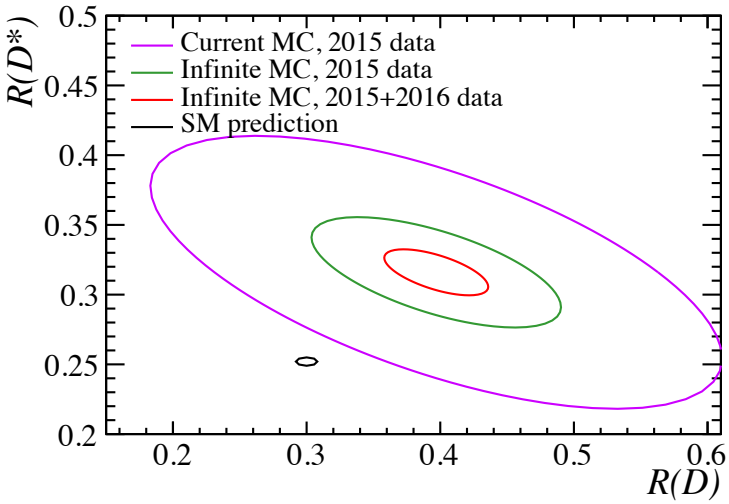



FIGURE 8.22: Sensitivity on the $R(D^+)$ and $R(D^{*+})$ measurements under different assumptions for the data and Monte Carlo sample sizes.

a very large simulation sample is going to be produced in the future, to be used in the final measurement of this analysis.

## 8.5 Summary and future of the analysis

As explained in this chapter, several main aspects of this analysis are finished. In particular, the event selection strategy is done, including the development of a new tool aimed at isolating signal from events with extra neutral particles.

The templates to be used in the nominal fit have been constructed and the basic fitting framework has been implemented. Some checks on the measurement of the $R(D^{(*)+})$ ratios using toy Monte Carlo experiments have been performed, as well as several sensitivity studies which included the systematic effect due to the limited statistics of the samples used to obtain the templates.

As reported in Sect. 8.2.6, a yield of $(8.124 \pm 0.012) \cdot 10^5$ $D^+$ candidates is found in the 2015 data sample. An extrapolation for the 2015+2016 combined data sample gives a value of $\sim 5 \cdot 10^6$ $D^+$ candidates. Using this expected yield, some studies on the sensitivity to the measurement of the $R(D^{(*)+})$ ratios are presented in Sect. 8.4.3. The obtained uncertainties can be improved with larger simulation samples and some planned upgrades for the fitting strategy (as discussed below). The final measurement is expected to have an important impact on the World's averaged combination of $R(D)$ and $R(D^*)$.

As future plans for the analysis, to be carried out in the period after the PhD, several steps have to be performed. First, the 2016 data sample needs to be processed, using the already developed selection strategy. Large-statistics Monte Carlo samples need to be produced and used in the analysis, in order to reduce the related systematic uncertainties. A fit to data has to be performed and potential mis-matches between model and data have to be looked for across the phase-space. Further corrections to the simulation and control samples can be considered. The nominal set of fit variables is planned to be substituted by an alternative one, in order to improve the sensitivity. The signal and normalisation efficiencies need to be properly determined in order to transform the raw $R$ ratios into the final ones. To conclude, the remaining systematic uncertainties on the determination of $R(D^{(*)+})$ have to be determined.

USC UNIVERSIDADE DE SANTIAGO DE COMPOSTELA

USC
UNIVERSIDADE
DE SANTIAGO
DE COMPOSTELA

# Chapter 9

# Conclusions

This PhD thesis is focused on the analysis of different particle decays coming from proton - proton collisions that occurred in the LHC and were registered by the LHCb experiment, with the goal of accurately measuring several observables sensitive to the existence of New Physics beyond the Standard Model.

Two analyses are reported, the first being the main one and corresponding to an approximate 70% of the thesis, and the second one, whose basis is settled but will be finished in the future, corresponding to a 30%. Even if both analyses are aimed at testing the flavour structure of the standard model, their relationship is mostly complementary, both in the sense of the research lines and in the methods employed. The first analysis follows a historical line in LHCb, as is CP violation, while the second one follows on a quite recent new one in the experiment, the test of Lepton Universality in semi-leptonic decays. I led the strategy of the first analysis and implemented almost all its aspects, excepting the event selection. This last topic is indeed the main one of which I was in charge in the second analysis, which I did in collaboration with people from other universities. During the work on the thesis I developed several tools that can be exported to other analyses in the future. As explained in the introduction, I also did a small instrumentation project on silicon detectors and took a small part in another data analysis [27], even if those activities are not covered in this document.

The results of the first analysis have been accepted by the high impact journal JHEP and are already available in arXiv [133]. It corresponds to a flavour tagged, time, angular and invariant mass dependent amplitude analysis of $B_s^0 \to (K^+\pi^-)(K^-\pi^+)$ decays. The main goal is to measure for the first time the CP-violating phase $\phi_s^{d\bar{d}}$, which is found to be

$$\phi_s^{d\bar{d}} = -0.10 \pm 0.13 \pm 0.14\,\text{rad}. \tag{9.1}$$

This value is compatible with the Standard Model expectation, but with relatively large uncertainties. In addition, many amplitude parameters for the system are measured, most of them for the first time. In particular, the longitudinal polarisation fraction for the $B^0 \to K^{*0}\overline{K}^{*0}$ decay is measured to be

$$f_{\rm L} = 0.208 \pm 0.032 \pm 0.046, \tag{9.2}$$

which confirms previous measurements and seems to deviate from QCD estimations. Some work from the theory community is expected in the near future for an interpretation of these results. This can be particularly interesting when constraining the New Physics models that are considered as potential alternatives to explain the $b \to sll$ anomalies, since many of them also predict effects in $b \to sqq$ transitions. The uncertainties on the parameters measured in this thesis are expected to scale with more real and simulated data, which enhances the motivation for an updated study in the future.

The second analysis of this thesis aims at measuring for the first time in LHCb the $R(D^+)$ ratio and doing a complementary measurement of the existing ones for $R(D^{*+})$, through the analysis of $\overline{B}^0 \to D^{(*)+}l\bar{\nu}_l$ decays. The large data sample accumulated in LHCb for this case

motivates the expectation of a large impact of the results from this analysis on the World's averaged combination of $R(D)$ and $R(D^*)$. This will shed light on the nature of the current observed deviation from the SM prediction of 4.1 $\sigma$. The 2015 data sample has already being filtered, and a total of $(8.124 \pm 0.012) \times 10^5$ $D^+$ candidates are found. The expectation for the combined 2015+2016 sample that will be used in the final measurement is of $\sim 5 \times 10^6$ $D^+$ candidates. The baseline fitting framework has already being developed and some checks and sensitivity studies have been performed. The plans for finalising this measurement in the near future have already being settled.

To summarize, the different works performed during my PhD thesis provided me with a very wide basis on the different techniques used in current experimental Particle Physics, as well as with an overall and structural vision of the data analysis system. It has also allowed me to develop my creativity by designing new tools and procedures. The first analysis has been widely recognized as one of the most challenging studies performed in the experiment nowadays and the many new measurements performed within it will allow the phenomenologists to constrain possible New Physics scenarios. Finally, the large observed deviations from Lepton Universality will be one of the hottest topics in Particle Physics for the next years, and the results from the second analysis will have something important to say about them.

USC UNIVERSIDADE DE SANTIAGO DE COMPOSTELA

# Chapter 10

# Resumo da tese en galego

## 10.1 Introdución

Esta tese versa sobre dúas análises de datos relativas a dous procesos de desintegración de partículas que recolleu o experimento LHCb, situado no CERN, nos últimos anos. A primeira análise, que constitúe un 70% da tese , está rematada, dispoñible en arXiv [133] e foi enviada á revista de alto impacto JHEP para a súa publicación. A segunda análise constitúe un 30% da tese e foi realizada no último período do doutoramento en colaboración con investigadores doutras universidades. A base deste estudo está rematada é recollida neste documento, así como certos estudos de sensibilidade nas medidas. A análise será rematada nun futuro próximo, despois do depósito da tese. A relación entre ambas análises é esencialmente complementaria, tanto a nivel de liñas de investigación como de métodos empregados, o que me permitiu adquirir unha formación moi ampla no campo de estudo. Ademáis das análisis de datos, fixen un pequeno proxecto de instrumentacion sobre detectores de silicio para física de partículas, que non se recolle neste documento. Finalmente, fixen tamén unha colaboración nunha terceira análise de datos que tampouco se recolle aquí. A publicación asociada a dito estudo pode atoparse en Ref. [27].

Neste capítulo recóllese unha versión abreviada do corpo da tese, escrita en ingles. Para detalles en cada apartado, o lector queda referido ás seccións correspondentes do corpo principal. Non se recolle neste capítulo una sección análoga á Sect. 6, destinada a explicar diferentes técnicas e ferramentas específicas empregadas nas dúas análises, por considerarse demasiado detallada. En dito capítulo, inclúese a primeira descripción formal dunha serie de métodos orixinais que desenvolvín durante o transcurso da tese e que poden ser usados en futuras análises.

Na sección Sect. 10.2, explícase a motivación física xeral para as dúas analisis presentadas nesta tese, e particularízase para a súa fenomenoloxía concreta. Na sección Sect. 10.3, resúmense as características do detector LHCb. Na sección Sect. 10.4, descríbese o procedemento da primeira análise e recóllense os resultados obtidos. O equivalente para a segunda análise recóllese na sección Sect. 10.5. Finalmente, as conclusións globais e as perspectivas de futuro preséntanse na sección Sect. 10.6.

## 10.2 Motivación teórica

O Modelo Estándar constitúe unha teoría exitosa que describe con gran precisión o mundo microscópico das partículas, pero aínda así é incapaz de ofrecer unha explicación para certos fenómenos observados na estructura do universo e carece dunha explicacion fundamental para certas características que forman parte do propio modelo. Unha destas características é a chamada estrutura de sabor, que consiste na existencia de tres familias de fermións (quarks e leptóns) que semellan idénticas entre si agás na interacción co bosón de Higgs. Esta interacción confírelles masas diferentes, permite a mistura entre quarks de diferentes familias e ofrece a única fonte de violación CP no Modelo Estándar. Esta tese destínase a poñer a proba dous aspectos diferentes da estrutura de sabor do Modelo Estándar, que poderían cambiar no caso de que elementos de

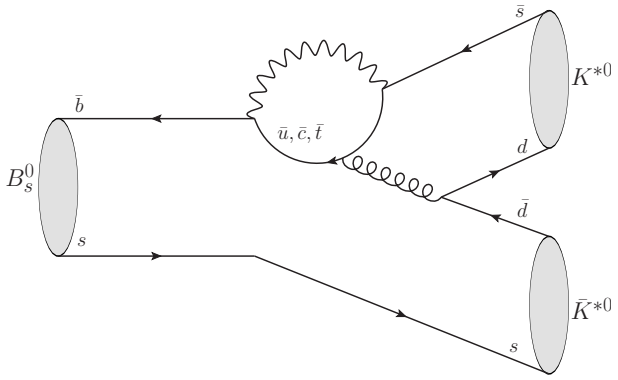



FIGURE 10.1: Contribución dominante ó decaemento $B_s^0 \to K^{*0}\overline{K}^{*0}$ no Modelo Estándar.

Nova Física contribuísen nos procesos. A primeira análise adícase á busca de novas fontes de violación CP que permitan explicar a gran diferencia de abundancia entre materia e antimateria que observamos hoxe en día no universo. A segunda análise está destinada a poñer a proba a chamada Universalidade Leptónica, que consiste na igualdade das tres familias de leptóns ante a interacción electro-feble, salvo no que atinxe a interacción co boson de Higgs. Esta segunda análise está motivada pola recente observación de anomalías neste campo por parte de diferentes experimentos.

### 10.2.1 Fenomenoloxía da desintegración $B_s^0 \to (K^+\pi^-)(K^-\pi^+)$

O primeiro estudo céntrase en medir a fase de violación CP $\phi_s^{d\bar{d}}$ que aparece na desintegración $B_s^0 \to K^{*0}\overline{K}^{*0}$, froito de interferencia entre a oscilacion $B_s^0 - \overline{B}_s^0$ e o decaemento destas partículas ó estado final considerado. O Modelo Estándar predí un valor cercano a cero para esta cantidade. A desintegración $B_s^0 \to K^{*0}\overline{K}^{*0}$ leva moito tempo sendo considerada como un candidato excepcional para a procura de nova física involucrada na violación CP. Un dos motivos para elo é a súa alta sensibilidade a novas compoñentes debido á supresión deste decaemento no Modelo Estándar, que soamente permite a transición mediante diagramas de tipo lazo, segundo se amosa na Figura 10.1. Outro dos motivos radica na posibilidade de controlar a contribución teórica de termos de máis alta orde no Modelo Estándar a $\phi_s^{d\bar{d}}$ mediante un estudo do decaemento relacionado $B^0 \to K^{*0}\overline{K}^{*0}$. Dito estudo permitiría reducir a incerteza teórica na fase.

O decaemento $B_s^0 \to K^{*0}\overline{K}^{*0}$ foi observado por primeira vez por LHCb en 2012 e un segundo estudo foi feito en 2015. Non obstante, en ningún dos dous casos se mediu dita fase por falta dunha cantidade de datos suficiente. O decaemento observouse no caso particular $K^{*0} \to K^+\pi^-$ e $\overline{K}^{*0} \to K^-\pi^+$. En ambos estudos se atopou unha compoñente $K\pi$ escalar en combinación coa resonancia $K^{*0}$, relativamente grande e imposible de illar. Tanto os decaementos con esta compoñente como con outra tensorial nunha rexión próxima do espazo-fase pode considerarse que teñen a mesma fase de violación CP, dentro dos límites actuais de precisión experimental. Coa motivación de ter un estudo mellor das diferentes compoñentes e aumentar a precisión da medida, a análise presentada nesta tese non só estuda o decaemento $B_s^0 \to K^{*0}\overline{K}^{*0}$, senón diferentes decaementos da forma $B_s^0 \to (K^+\pi^-)(K^-\pi^+)$ que contribúen nunha ventá de masa invariante $K\pi$ de entre 750 e 1600 $\mathrm{MeV}/c^2$. Considéranse compoñentes $K\pi$ escalares (S), que aglutinan unha contribución da resonancia $K^*(800)^0$, outra da resonancia $K_0^*(1430)^0$ e outra non-resoante; compoñentes $K\pi$ vectoriais (V), dominadas polo $K^{*0}$, e compoñentes $K\pi$ tensoriais (T), dominadas polo $K_2^*(1430)^0$. Isto correspóndese cun sistema de 19 amplitudes de decaemento,

TABLE 10.1: Modos de desintegración e amplitudes de polarización correspondentes que contribúen ó estado final $B_s^0 \to (K^+\pi^-)(K^-\pi^+)$ nunha ventá de masa $K\pi$ de 750 a 1600 $\mathrm{MeV}/c^2$. As diferentes contribucións identifícanse polo espín $j_1$ ($j_2$) do par $K^+\pi^-$ ($K^-\pi^+$) e pola helicidade $h$. Nos modos nos que contribúen varias amplitudes, as polarizacións defínense como lonxitudinal, paralela ou perpendicular, e denótanse por $0$, $\parallel$ e $\perp$, respectivamente. Os subíndices 1 e 2 nas helicidades paralela e perpendicular da compoñente tensor-tensor denotan configuracións angulares diferentes que levan a unha polarización paralela ou a unha perpendicular.

| Decaemento | Modo | $j_1$ | $j_2$ | Valores permitidos de $h$ |
|---|---|---|---|---|
| $B_s^0 \to (K^+\pi^-)_0^*(K^-\pi^+)_0^*$ | escalar-escalar | 0 | 0 | 0 |
| $B_s^0 \to (K^+\pi^-)_0^*\overline{K}^*(892)^0$ | escalar-vector | 0 | 1 | 0 |
| $B_s^0 \to K^*(892)^0(K^-\pi^+)_0^*$ | vector-escalar | 1 | 0 | 0 |
| $B_s^0 \to (K^+\pi^-)_0^*\overline{K}_2^*(1430)^0$ | escalar-tensor | 0 | 2 | 0 |
| $B_s^0 \to K_2^*(1430)^0(K^-\pi^+)_0^*$ | tensor-escalar | 2 | 0 | 0 |
| $B_s^0 \to K^*(892)^0\overline{K}^*(892)^0$ | vector-vector | 1 | 1 | 0, $\parallel$, $\perp$ |
| $B_s^0 \to K^*(892)^0\overline{K}_2^*(1430)^0$ | vector-tensor | 1 | 2 | 0, $\parallel$, $\perp$ |
| $B_s^0 \to K_2^*(1430)^0\overline{K}^*(892)^0$ | tensor-vector | 2 | 1 | 0, $\parallel$, $\perp$ |
| $B_s^0 \to K_2^*(1430)^0\overline{K}_2^*(1430)^0$ | tensor-tensor | 2 | 2 | 0, $\parallel$ 1, $\perp$ 1, $\parallel$ 2, $\perp$ 2 |

que aparecen definidas na Táboa 10.1. Para medir a fase $\phi_s^{d\bar{d}}$ é preciso facer un estudo multidimensional dos decaementos considerados, que inclúe diferentes variables angulares, as masas invariantes dos pares $K\pi$ e o tempo de decaemento do $B_s^0$. Mentres que a distribución en termos de variables angulares e tempo de decaemento é relativamente estándar, a parte dependente das masas invariantes precisa un estudo pormenorizado.

### 10.2.2 Fenomenoloxía das desintegracións $\overline{B}^0 \to D^{(*)+}l\bar{\nu}_l$

A segunda análise pretende facer a primeira medida en LHCb do cociente $R(D^+)$ e unha medida do cociente $R(D^{*+})$ complementaria ás xa existentes no experimento. Os cocientes $R(D^{(*)})$, que serven para poñer a proba a Universalidade Leptónica, caracterízanse por unha grande precisión tanto na medida experimental como na predicción teórica. Estas cantidades defínense como:

$$R(D^{(*)}) = \frac{\mathcal{B}(B \to D^{(*)}\tau\overline{\nu}_\tau)}{\mathcal{B}(B \to D^{(*)}l\overline{\nu}_l)}, \tag{10.1}$$

onde $D$ pode ser $D^0$ ou $D^+$, $D^*$ pode ser $D^*(2007)^0$ ou $D^*(2010)^+$, e $l$ denota un leptón lixeiro, que pode ser $\mu$ ou $e$. A combinación das diferentes medidas existentes destas cantidades amósase na Figura 10.2. A desviación total observada respecto da predicción do Modelo Estándar é de 4.1 $\sigma$. Esta anomalía pode ser explicada en termos de novas contribucións que se acoplan preferentemente á terceira familia de leptóns.

A análise presentada nesta tese estuda en particular os decaementos $\overline{B}^0 \to D^{(*)+}l\bar{\nu}_l$, onde $D^{*+} \to D^+\pi^0$, $D^+ \to K^-\pi^+\pi^+$, $l \in \{\tau, \mu\}$ e $\tau \to \mu\overline{\nu}_\mu\nu_\tau$, sendo o estado final visible no experimento $K^-\pi^+\pi^+\mu^-$. A contribución das compoñentes muónica e tauónica determínase mediante un axuste multidimensional ós datos, que usa diferentes variables cinematicas do estado final visible, sensibles á diferenza no número de neutrinos do estado final e á diferente masa dos leptóns cargados. Ademais dos decaementos de interese, deben incluírse no modelo de axuste

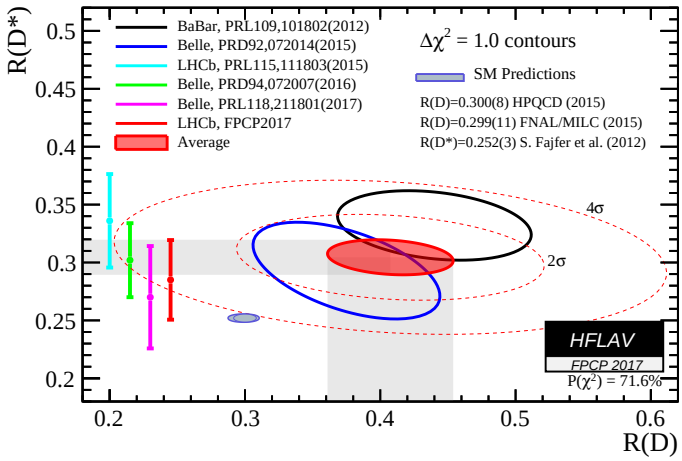



FIGURE 10.2: Combinación das diferentes medidas realizadas ata a data sobre os cocientes $R(D)$ e $R(D^*)$.

diferentes desintegracións incorrectamente reconstruídas que se confunden cos decaemento de sinal.

## 10.3 Condicións experimentais

Os resultados presentados nesta tese baséanse na análise de desintegracións orixinadas en colisións proton-proton que tiveron lugar no LHC durante os anos 2011 e 2012 (para a primeira análise) e 2015 (para a segunda análise). As colisións foron rexistradas polo experimento LHCb, un dos catro principais do LHC. Este experimento adícase principalmente a estudar a física de sabor examinando decaementos de partículas que conteñen o quark $b$. A xeometría do detector está orientada na dirección cara adiante dado que ditas partículas se crean en pares $b\bar{b}$ que voan nun estreito cono entorno ó eixo de colisión. Un esquema do detector pode verse na Figura 10.3.

As partículas orixinadas no decaemento dun hadrón con quark $b$ son caracterizadas no experimento combinando a información de diferentes subdetectores. Primeiramente, o detector VELO identifica o vértice de colisión e o vértice de decaemento do hadrón. Seguidamente, un sistema de trazado, que conta cun campo magnético que desvía as partículas cargadas na dirección horizontal, permite medir o camiño destas partículas, o seu momento lineal e o signo da súa carga. Un sistema de detectores baseados na radiación Cherenkov permite distinguir entre pions, kaóns e protons. Un sistema de calorímetros serve tanto para medir a enerxía das partículas que sinten a interacción electromagnética e os hadróns, como para distinguir entre ditas partículas. Finalmente, os muóns detéctanse ó final do experimento mediante unhas cámaras de muóns. Os requerimentos do proceso de lectura de datos de LHCb, en termos de tempo de computación e capacidade de almacenamento, motivan o uso dun sistema de disparo automático que emprega información parcial acumulada polos diferentes subdetectores, en combinación cuns algoritmos de software que fan unha reconstrucción en diferentes niveis dos eventos.

A gran precisión dos detectores de vértice é de traza son esenciais para ter boa resolución nas variables cinemáticas empregadas nas dúas análises desta tese. A boa identificación de partículas que ofrece o detector é crucial para reducir contribucións non desexadas provintes doutras desintegracións de fondo. O detector VELO é particularmente importante para a primeira análise, dado que permite medir con precisión o tempo de decaemento da particula $B_s^0$, imprescindible para a medida da fase $\phi_s^{d\bar{d}}$. A información proporcionada polo calorímetro electromagnético sobre os fotóns e os pións neutros usouse na segunda análise desta tese para desenvolver unha

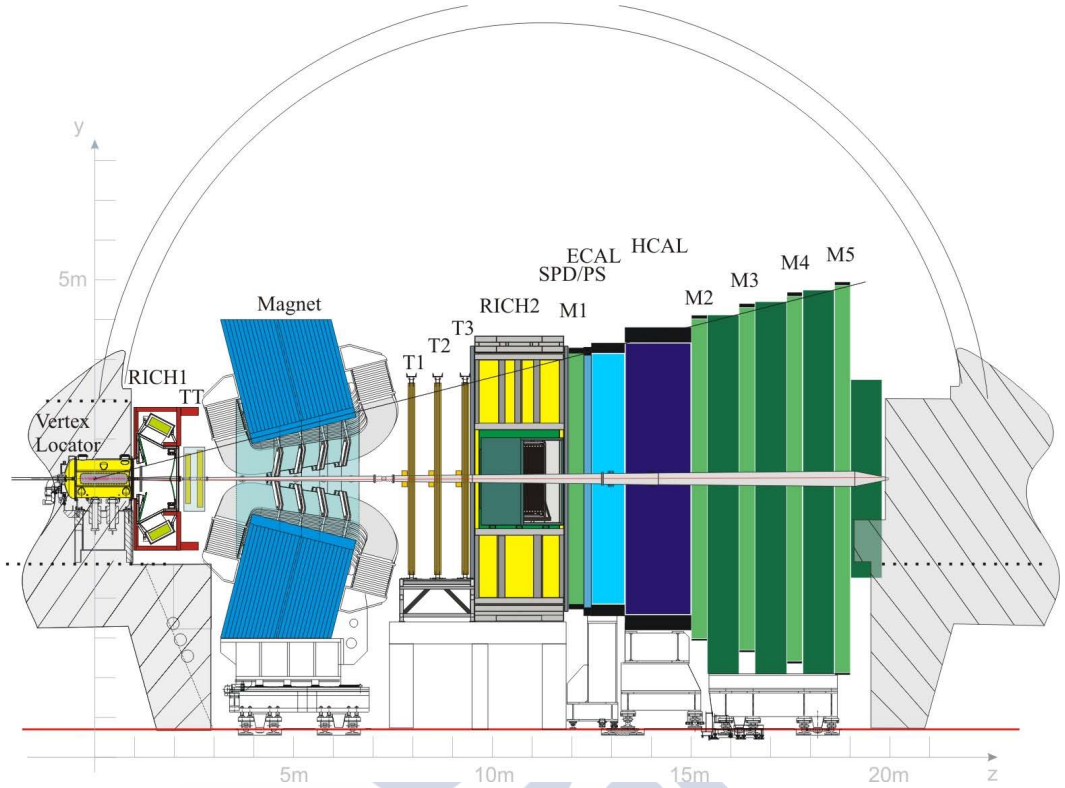



FIGURE 10.3: Esquema do detector de LHCb, desde unha perspectiva lateral.

ferramenta nova, que axudara a eliminar o fondo procedente de desintegracións parcialmente reconstruídas que contiñan estas partículas neutras no estado final. Para rematar, a grande cantidade de datos orixinada pola gran sección eficaz de produción de pares $b\bar{b}$ nun colisionador hadrónico permite reducir as incertezas de tipo estadístico nas medidas, en comparación coas análises de decaementos de partículas orixinadas en colisionadores leptónicos, como no caso das factorías de $B$.

## 10.4 Análise da desintegración $B_s^0 \to (K^+\pi^-)(K^-\pi^+)$

A análise experimental do decaemento $B_s^0 \to (K^+\pi^-)(K^-\pi^+)$ comeza por unha selección de candidatos. Para isto, considéranse primeiramente requerimentos na calidade de reconstrución e en diferentes variables cinemáticas do evento, para o cal se fai uso de técnicas de análise multivariante. Aplícanse despois requerimientos destinados a reducir a contribución de fondos procedentes de desintegracións con particulas mal identificadas, e vetos para eliminar a contribución de decaementos correspondentes a agrupacións alternativas das particulas $K^+\pi^-K^-\pi^+$, como $(K^+K^-\pi^+)\pi^-$ e $(K^+K^-)(\pi^+\pi^-)$. Finalmente, os fondos restantes cancélanse de xeito estadístico mediante o uso de eventos con pesos negativos.

Despois da selección, desenvólvese un sistema que permita coñecer o sabor inicial da partícula $B_s^0$ que decae, o cal é preciso para medir a fase $\phi_s^{d\bar{d}}$. Os algoritmos empregados permiten identificar correctamente un $5.15 \pm 0.14\%$ dos eventos, o que constitúe unha fracción típica nas análises similares de LHCb. Con similar obxectivo, debe estimarse a asimetría de produción $B_s^0/\overline{B}_s^0$.

Para facer un axuste ós datos é preciso construir un modelo que describa adecuadamente a distribución multidimensional de todas as compoñentes. Unha complexidade particular de dito modelo radica na descripción da dependencia na masa invariante $K\pi$ dos pares escalares (de espín cero). Isto débese á inexistencia actualmente dun modelo fenomenolóxico que describa

este decaemento no caso particular considerado. A alternativa escollida foi empregar unha parametrización recentemente publicada sobre a amplitude de dispersión $K\pi$, e combinala cun factor de forma polinómico, dependente da masa $K\pi$, que se deixou libre no axuste ós datos. Comprobouse además que o resultado obtido era semellante ó que se obtén usando unha parametrización independente de modelo, que se deixa axustar libremente ós datos.

Aparte da distribución teórica, o modelo de axuste debe dar conta da aceptancia e a resolución inducidas por una imperfecta reconstrución do evento, a xeometría do detector e o proceso de selección. Nesta análise considerouse unha aceptancia multidimensional, factorizada na parte dependente do tempo de decaemento e as demais variables (ángulos e masas). A parte temporal tratouse de xeito analítico e a outra de xeito numérico. Para o modelo nominal só se considerou a resolución na parte dependente do tempo, por ser a que máis inflúe na medida da fase $\phi_s^{d\bar{d}}$. Dita resolución inclueuse mediante unha convolucion e de forma analítica. O modelado dos efectos de aceptancia e resolución extraeuse de mostras de eventos simulados.

Unha vez se preparou o modelo combinando todos os ingredientes, debe facerse un axuste multidimensional á mostra de datos filtrada, para medir tanto os parámetros de violación CP como os parámetros que caracterizan ás 19 amplitudes involucradas no proceso. A complexidade de dito axuste motivou o uso dun novo sistema de computación en paralelo baseado no uso de tarxetas gráficas. En particular, contribuín ó desenvolvemento dun novo paquete de software que serve para ese tipo de procedementos [28].

Finalmente, debe facerse unha serie de comprobacións de diferentes partes do proceso de medida e unha avaliación das incertezas de tipo sistemático. Entre as diferentes comprobacións que se fixeron inclúese unha comparación entre a descripción dos efectos de aceptancia e resolución obtidos usando diferentes mostras simuladas, a validación do método de axuste con eventos simulados, axustes a submostras de datos (seleccionando zonas diferentes do espazo fase dispoñible ou separando en canto ó ano de recolección de datos), e un estudo de posibles contribucións ós pares $K\pi$ cun momento angular maior que dous. Entre as incertezas sistemáticas que se estudaron, atópanse una serie delas referidas ó proceso de selección, outras referidas ós pequenos sesgos inherentes ó propio proceso de medida, estudos do efecto de usar parametrizacións alternativas para diferentes compoñentes do modelo, o efecto de despreciar certas contribucións pequenas provintes doutras resonancias no modelo nominal, o tratamento específico da aceptancia e a resolución na análise e unha posible variación da asimetría de producción.

O resultado do axuste ós datos amósase na Figura 10.4 e o conxunto de parámetros medidos recóllese na táboa 10.2. A medida da fase de violación CP resulta ser $\phi_s^{d\bar{d}} = -0.10 \pm 0.13 \pm 0.14\,\mathrm{rad}$, que é compatible coa predicción do Modelo Estándar e coa medida da fase equivalente no decaemento $B_s^0 \to \phi\phi$. Entre os diferentes parámetros de amplitude medidos, atópase unha fraccion de polarización lonxitudinal para o decaemento $B_s^0 \to K^{*0}\overline{K}^{*0}$ de $f_\mathrm{L} = 0.208 \pm 0.032 \pm 0.046$. Este valor confirma as medidas previas e presenta certa tensión con estimacións de QCD no marco do Modelo Estándar.

## 10.5 Análise das desintegracións $\overline{B}^0 \to D^{(*)+} l \bar{\nu}_l$

Como no caso anterior, o proceso de análise comeza por unha selección de candidatos. O primeiro paso da mesma consistiu no deseño dunha serie de requerimentos para reducir a contribución de decaementos con partículas mal identificadas. A continuación, usáronse varias técnicas de análise multivariante para reducir certas contribuciones específicas. En primeiro lugar, deseñouse un método para reducir a contribución de eventos con combinacións aleatorias de partículas $K^-\pi^+\pi^+$, usando variables topolóxicas e cinemáticas. Despois, empregouse unha ferramenta deseñada anteriormente en LHCb para reducir os fondos provintes de desintegracións parcialmente reconstruidas que conteñen partículas cargadas adicionais. Para rematar a selección, desenvolveuse unha ferramenta semellante á anterior, para identificar partículas neutras adicionais e

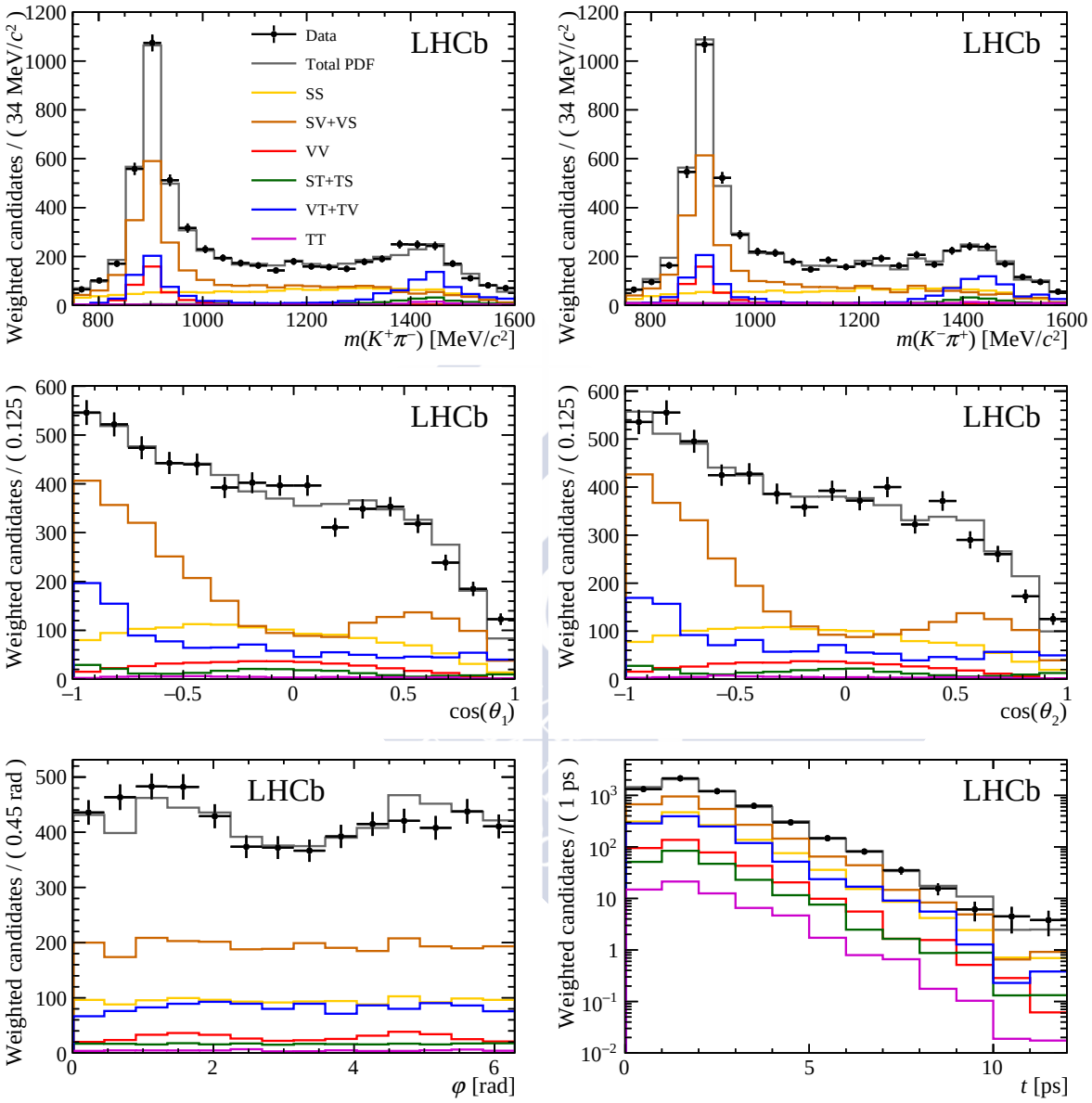



FIGURE 10.4: Proxeccións unidimensionais do axuste final (puntos negros) ós datos filtrados para (fila superior) as dúas masas invariantes $K\pi$, (fila central) dúas variables angulares relativas a cada un dos pares, (fila inferior, esquerda) unha terceira variable angular referida ó decaemento total e (fila inferior, dereita) o tempo de decaemento do $B_s^0$. A liña gris representa o modelo total e as demáis liñas coloreadas amosan contribucións específicas por separado, como indica a lenda.

TABLE 10.2: Parámetros medidos na primeira análise desta tese. Para cada un deles, a primeira incerteza citada é estadística e a segunda é sistemática.

| Parámetro | Valor |
|---|---|
| **Parámetros comúns** | |
| $\phi_s^{d\bar{d}}$ [rad] | $-0.10 \pm 0.13 \pm 0.14$ |
| $\lvert\lambda\rvert$ | $1.035 \pm 0.034 \pm 0.089$ |
| **Vector/Vector (VV)** | |
| $f^{VV}$ | $0.067 \pm 0.004 \pm 0.024$ |
| $f_{\mathrm{L}}^{VV}$ | $0.208 \pm 0.032 \pm 0.046$ |
| $f_{\parallel}^{VV}$ | $0.297 \pm 0.029 \pm 0.042$ |
| $\delta_{\parallel}^{VV}$ [rad] | $2.40 \pm 0.11 \pm 0.33$ |
| $\delta_{\perp}^{VV}$ [rad] | $2.62 \pm 0.26 \pm 0.64$ |
| **Escalar/Vector (SV and VS)** | |
| $f^{SV}$ | $0.329 \pm 0.015 \pm 0.071$ |
| $f^{VS}$ | $0.133 \pm 0.013 \pm 0.065$ |
| $\delta^{SV}$ [rad] | $-1.31 \pm 0.10 \pm 0.35$ |
| $\delta^{VS}$ [rad] | $1.86 \pm 0.11 \pm 0.41$ |
| **Escalar/Escalar (SS)** | |
| $f^{SS}$ | $0.225 \pm 0.010 \pm 0.069$ |
| $\delta^{SS}$ [rad] | $1.07 \pm 0.10 \pm 0.40$ |
| **Escalar/Tensor (ST and TS)** | |
| $f^{ST}$ | $0.014 \pm 0.006 \pm 0.031$ |
| $f^{TS}$ | $0.025 \pm 0.007 \pm 0.033$ |
| $\delta^{ST}$ [rad] | $-2.3 \pm 0.4 \pm 1.7$ |
| $\delta^{TS}$ [rad] | $-0.10 \pm 0.26 \pm 0.82$ |

| Parámetro | Valor |
|---|---|
| **Vector/Tensor (VT and TV)** | |
| $f^{VT}$ | $0.160 \pm 0.016 \pm 0.049$ |
| $f_{\mathrm{L}}^{VT}$ | $0.911 \pm 0.020 \pm 0.165$ |
| $f_{\parallel}^{VT}$ | $0.012 \pm 0.008 \pm 0.053$ |
| $f^{TV}$ | $0.036 \pm 0.014 \pm 0.048$ |
| $f_{\mathrm{L}}^{TV}$ | $0.62 \pm 0.16 \pm 0.25$ |
| $f_{\parallel}^{TV}$ | $0.24 \pm 0.10 \pm 0.14$ |
| $\delta_0^{VT}$ [rad] | $-2.06 \pm 0.19 \pm 1.17$ |
| $\delta_{\parallel}^{VT}$ [rad] | $-1.8 \pm 0.4 \pm 1.0$ |
| $\delta_{\perp}^{VT}$ [rad] | $-3.2 \pm 0.3 \pm 1.2$ |
| $\delta_0^{TV}$ [rad] | $1.91 \pm 0.30 \pm 0.80$ |
| $\delta_{\parallel}^{TV}$ [rad] | $1.09 \pm 0.19 \pm 0.55$ |
| $\delta_{\perp}^{TV}$ [rad] | $0.2 \pm 0.4 \pm 1.1$ |
| **Tensor/Tensor (TT)** | |
| $f^{TT}$ | $0.011 \pm 0.003 \pm 0.007$ |
| $f_{\mathrm{L}}^{TT}$ | $0.25 \pm 0.14 \pm 0.18$ |
| $f_{\parallel_1}^{TT}$ | $0.17 \pm 0.11 \pm 0.14$ |
| $f_{\perp_1}^{TT}$ | $0.30 \pm 0.18 \pm 0.21$ |
| $f_{\parallel_2}^{TT}$ | $0.015 \pm 0.033 \pm 0.107$ |
| $\delta_0^{TT}$ [rad] | $1.3 \pm 0.5 \pm 1.8$ |
| $\delta_{\parallel_1}^{TT}$ [rad] | $3.00 \pm 0.29 \pm 0.57$ |
| $\delta_{\perp_1}^{TT}$ [rad] | $2.6 \pm 0.4 \pm 1.5$ |
| $\delta_{\parallel_2}^{TT}$ [rad] | $2.3 \pm 0.8 \pm 1.7$ |
| $\delta_{\perp_2}^{TT}$ [rad] | $0.7 \pm 0.6 \pm 1.3$ |

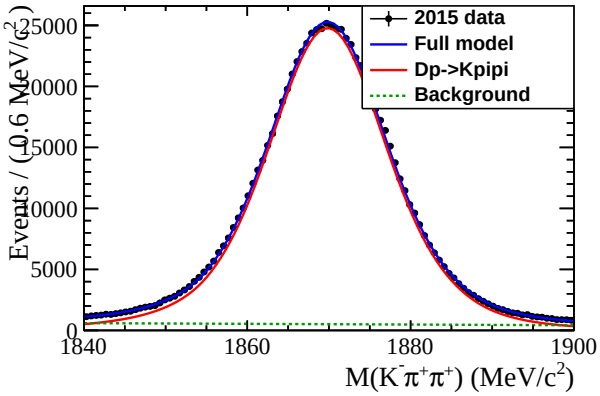



FIGURE 10.5: Axuste á masa invariante $M(K\pi\pi)$ para os eventos filtrados, que se emprega para coñecer o número total de candidatos a $D^+$.

reducir os fondos asociados. Mediante un axuste ó espectro de masa invariante $K^-\pi^+\pi^+$ determinouse que un total de $(8.124 \pm 0.012) \times 10^5$ candidatos a $D^+$ pasaba a selección. O resultado de dito axuste amósase na Figura 10.5.

Para esta segunda análise, o axuste final para medir $R(D^{(*)+})$ faise mediante histogramas tridimensionais, que empregan plantillas predefinidas para as diferentes compoñentes. As plantillas deben obterse a priori, ben empregando mostras de eventos simulados, ben usando mostras de control de eventos reais, enriquecidas en certo tipo de compoñentes. No caso de eventos simulados, as distribucións deben correxirse lixeiramente para dar conta das mellores parametrizacións existentes actualmente para as distribucións das diferentes compoñentes, respecto das usadas no momento de xeneración das mostras. A continuación, debe implementarse unha infraestructura de software para facer o axuste e realizar certas comprobacións da mesma. A modo de exemplo, na Figura 10.6 amósase o resultado do axuste a unha mostra de datos simulados.

O traballo realizado ata a data e incluído nesta memoria abrangue ata o punto anterior da análise. No futuro próximo, despois do depósito da tese, deberá facerse o axuste ós datos usando a infraestrutura creada e optimizar certos puntos da análise. Entre eles, á mostra de datos actualmente empregada, que corresponde ó ano 2015, engadirase outra correspondente a datos tomados no ano 2016. Contémplase, asimesmo, a produción e o uso na análise de mostras de eventos simulados de gran tamaño, que permitan reducir as incertezas sistemáticas asociadas. Neste sentido, fixéronse una serie de estudos de sensibilidade para a medida final baixo diferentes condicións, que se recolle no corpo principal desta tese. O número de candidatos a $D^+$ na mostra combinada de 2015+2016 espérase que sexa de $\sim 5 \times 10^6$.

## 10.6 Conclusións

A primeira análise desta tese conduciu á primeira medida no mundo da fase de violación CP $\phi_s^{d\bar{d}}$, usando o decaemento $B_s^0 \to (K^+\pi^-)(K^-\pi^+)$. O resultado é compatible coa predición do Modelo Estándar aínda que as incertezas son relativamente grandes. Ademáis desta fase, medíronse outros parámetros que caracterizan 19 amplitudes contribuíntes no proceso, moitos deles por primeira vez e, no caso dos que non, mellorouse a precisión das medidas anteriores. A fracción de polarizacion lonxitudinal medida para o decaemento $B_s^0 \to K^{*0}\overline{K}^{*0}$ presenta certa tensión con estimacións de QCD no marco do Modelo Estándar. Cabe destacar que esta análise está sendo amplamente recoñecida como unha das máis complexas realizadas no experimento LHCb e os seus resultados se están presentando en diferentes conferencias internacionais de gran prestixio. Ditos resultados poden ser empregados no futuro próximo pola comunidade teórica, para estudar a súa consistencia con diferentes modelos de Nova Física usados para explicar certas anomalías

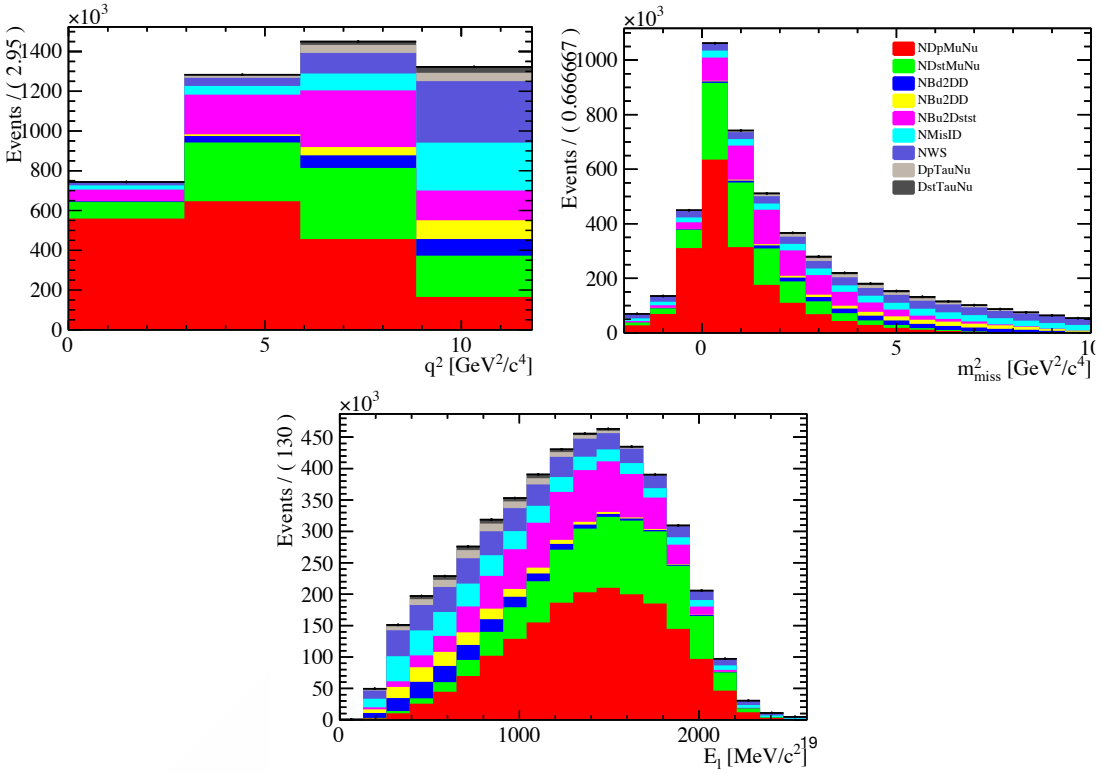



FIGURE 10.6: Resultado do axuste multidimensional a unha mostra simulada de datos, xerada co propio modelo de axuste asumindo unhas condicións similares ás que se esperan para a mostra combinada de datos 2015+2016.

observadas en transicións $b \to sll$, dado que moitos deles tamén predín efectos en transicións $b \to sqq$. As incertezas na medida experimental de $\phi_s^{d\bar{d}}$ poden reducirse con mostras máis grandes de datos reais e simulados. Isto motiva unha actualización da medida no futuro.

O segundo traballo da tese consistiu no establecemento da base necesaria para a primeira medida de $R(D^+)$ en LHCb e unha nova medida de $R(D^{*+})$, complementaria ás anteriores. Tras aplicar a selección obsérvase un gran número de eventos, que se traduce nunha alta sensibilidade a estes cocientes. A medida final axudará a dilucidar a verdadeira natureza detrás da desviación actual respecto do Modelo Estándar de 4.1 $\sigma$, correspondente á combinación mundial das medidas dos cocientes feitas ata a data.

A realización destas dúas análises conferiume una ampla formación en métodos e liñas de investigación da física de partículas experimental de hoxe en día. Permitiume asimesmo desenvolver a miña creatividade, deseñando estratexias para as análises e novos métodos e ferramentas que poden ser utilizados en futuros estudos. Para finalizar, permitiume posicionarme moi adecuadamente para o futuro próximo, dado que as análises abordan dous dos temas de investigación máis candentes do campo actualmente, e se prevé que esta condición continue nos próximos anos.

No caso de confirmarse finalmente as desviacións respecto da Universalidade Leptónica observadas nos cocientes $R(D^{(*)})$, será preciso sustituir o Modelo Estándar por unha teoría máis completa, que dea conta delas. Restaría saber se dita teoría ofrece tamén unha explicación das anomalías observadas recentemente en transicións $b \to sll$ e se estas teñen conexión con posible efectos en transicións $b \to sqq$, podendo quizáis explicar a anormalmente baixa fraccion de polarizacion lonxitudinal medida no decaemento $B_s^0 \to K^{*0}\overline{K}^{*0}$.

# Appendix A

# Measurement of $\phi_s$: pull distributions of the physical parameters

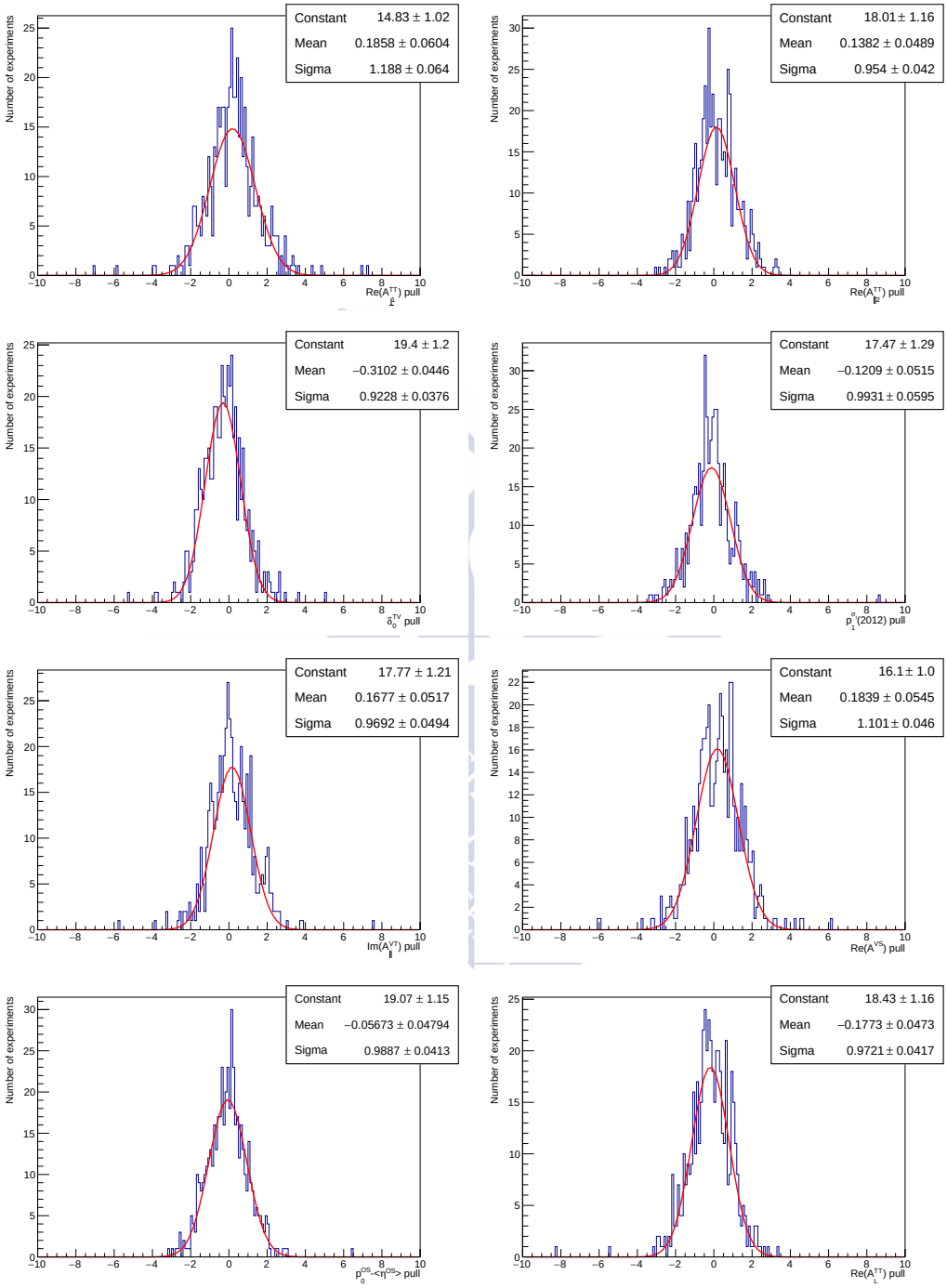



FIGURE A.1: Pull distributions of the fitted parameters.

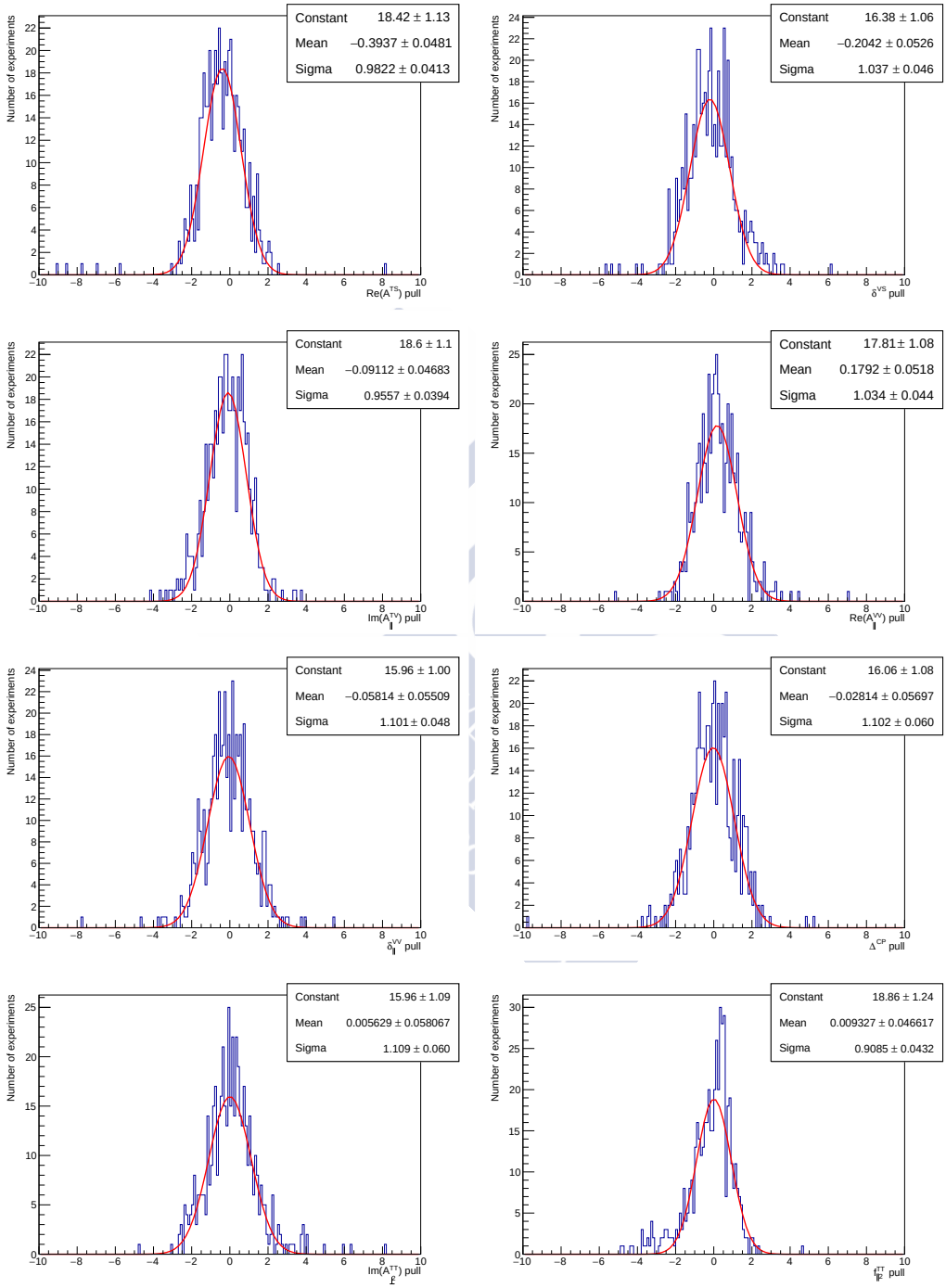



FIGURE A.2: Pull distributions of the fitted parameters.

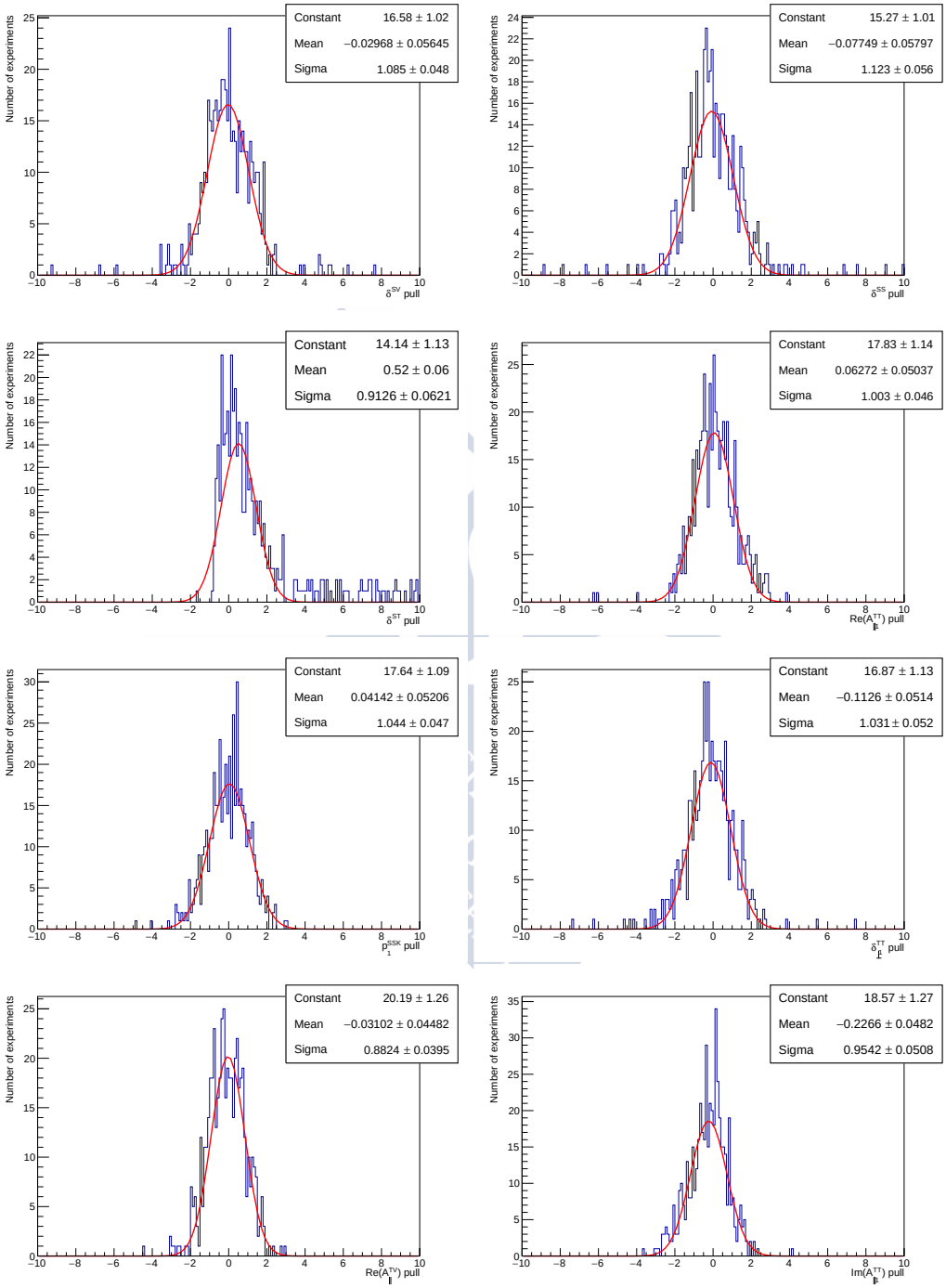



FIGURE A.3: Pull distributions of the fitted parameters.

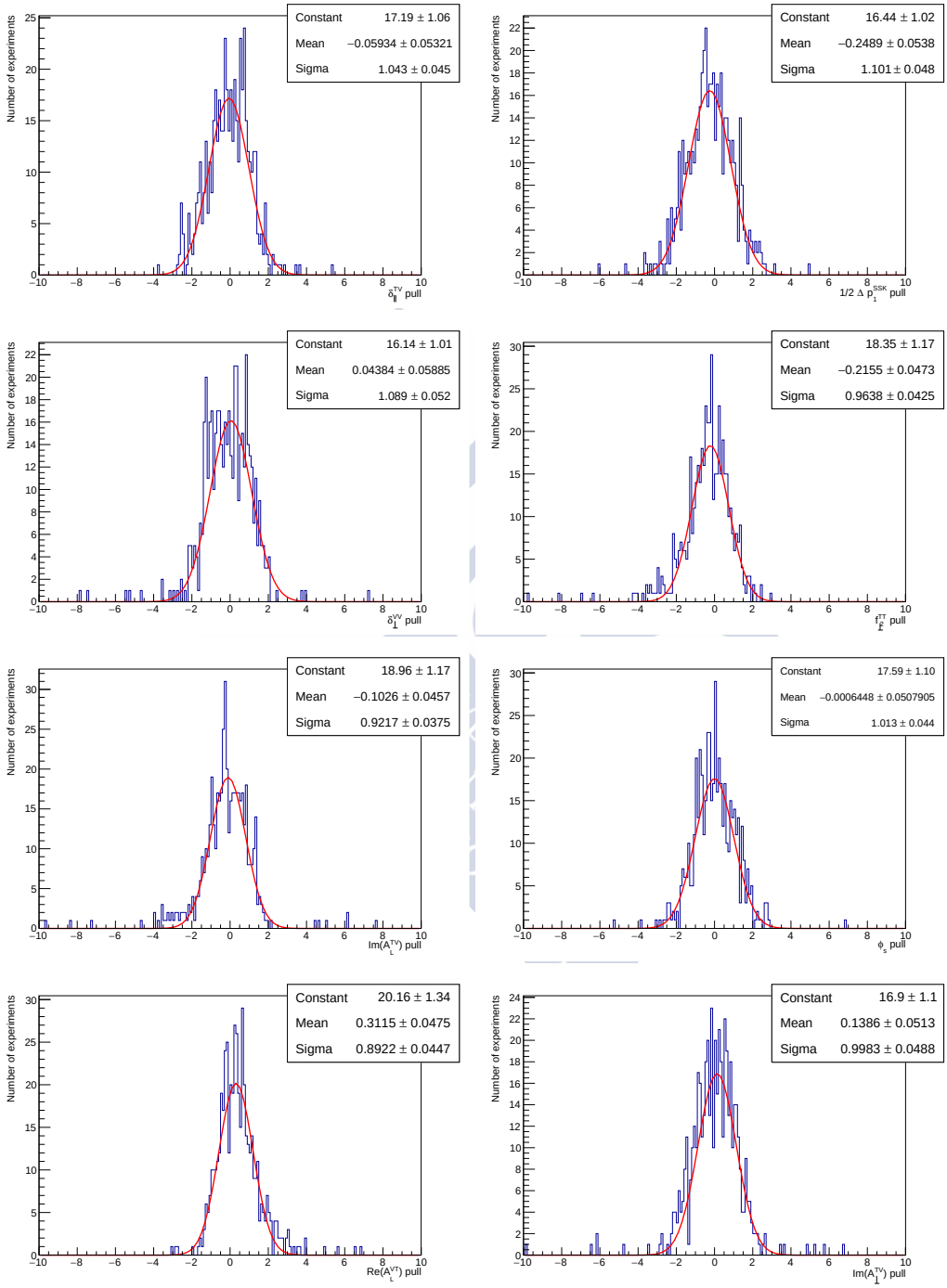



FIGURE A.4: Pull distributions of the fitted parameters.

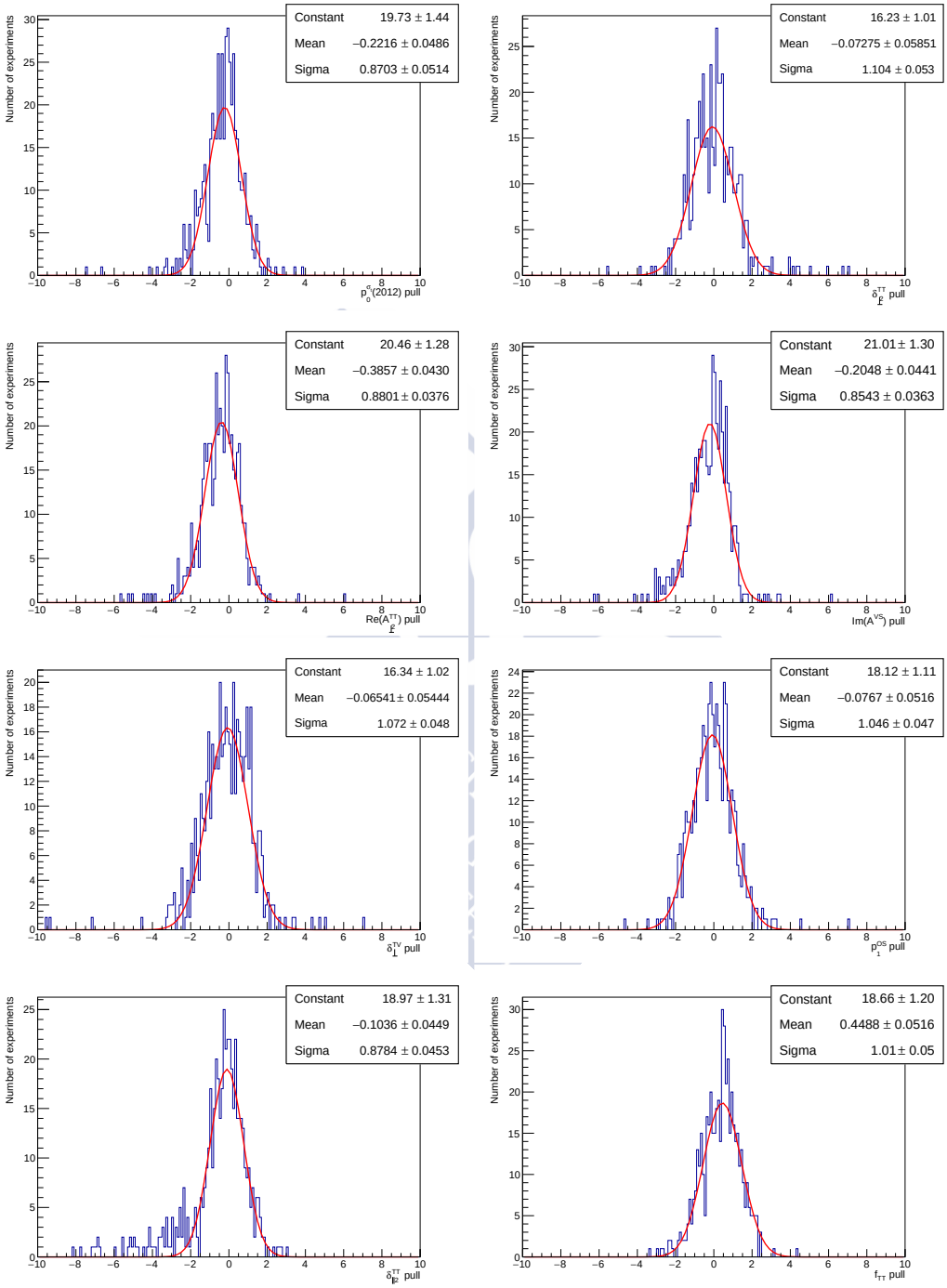



FIGURE A.5: Pull distributions of the fitted parameters.

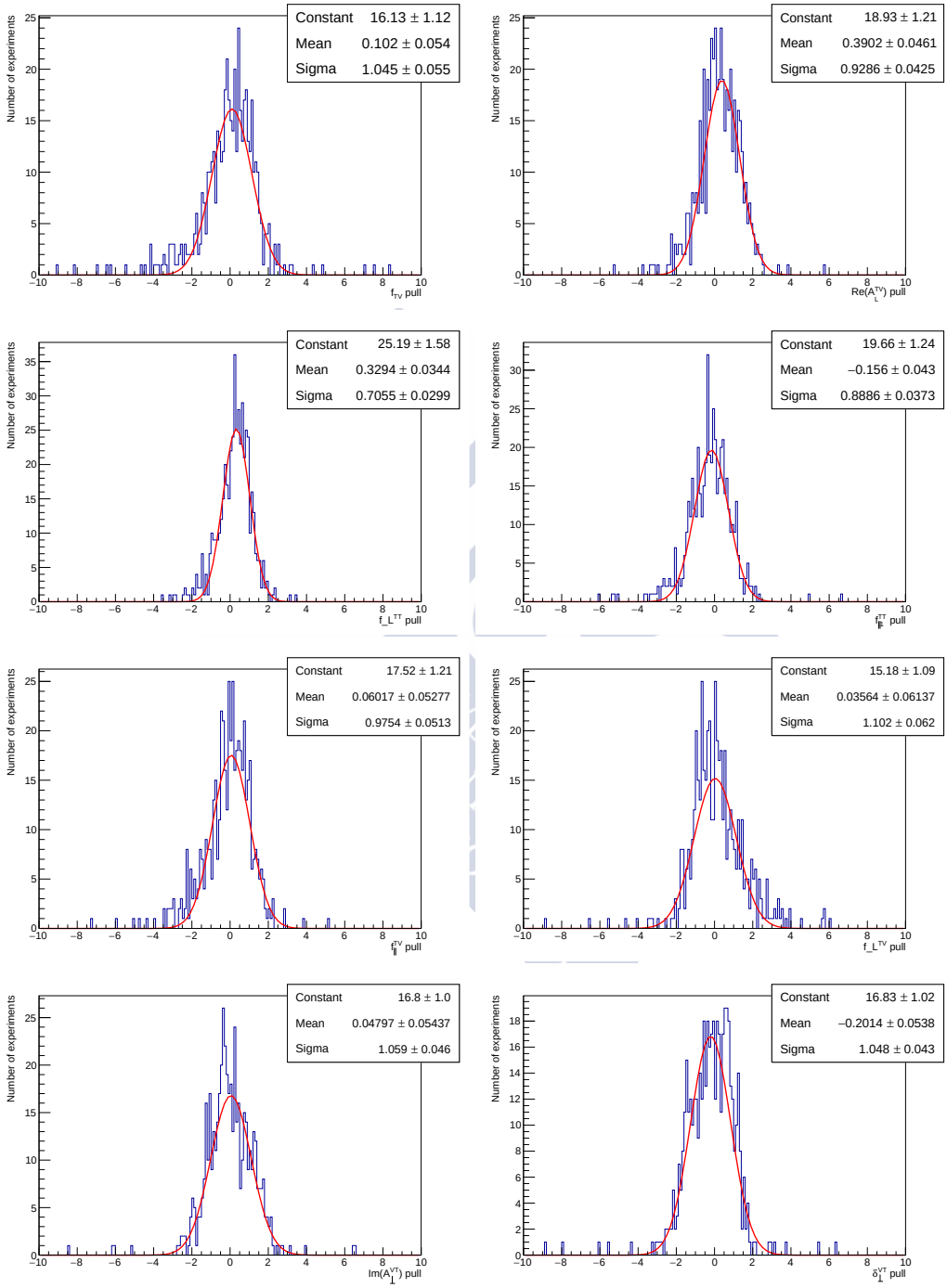



FIGURE A.6: Pull distributions of the fitted parameters.

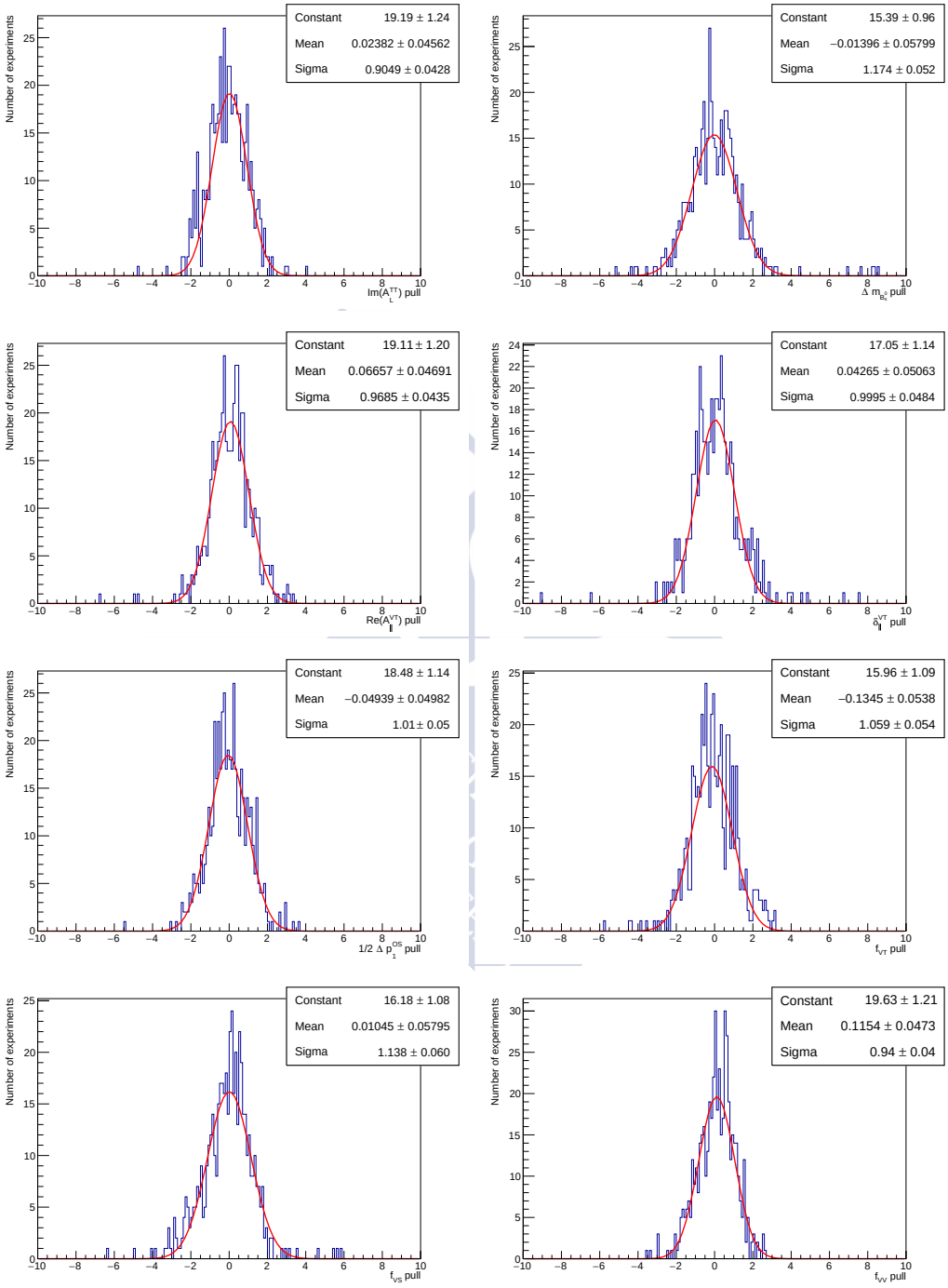



FIGURE A.7: Pull distributions of the fitted parameters.

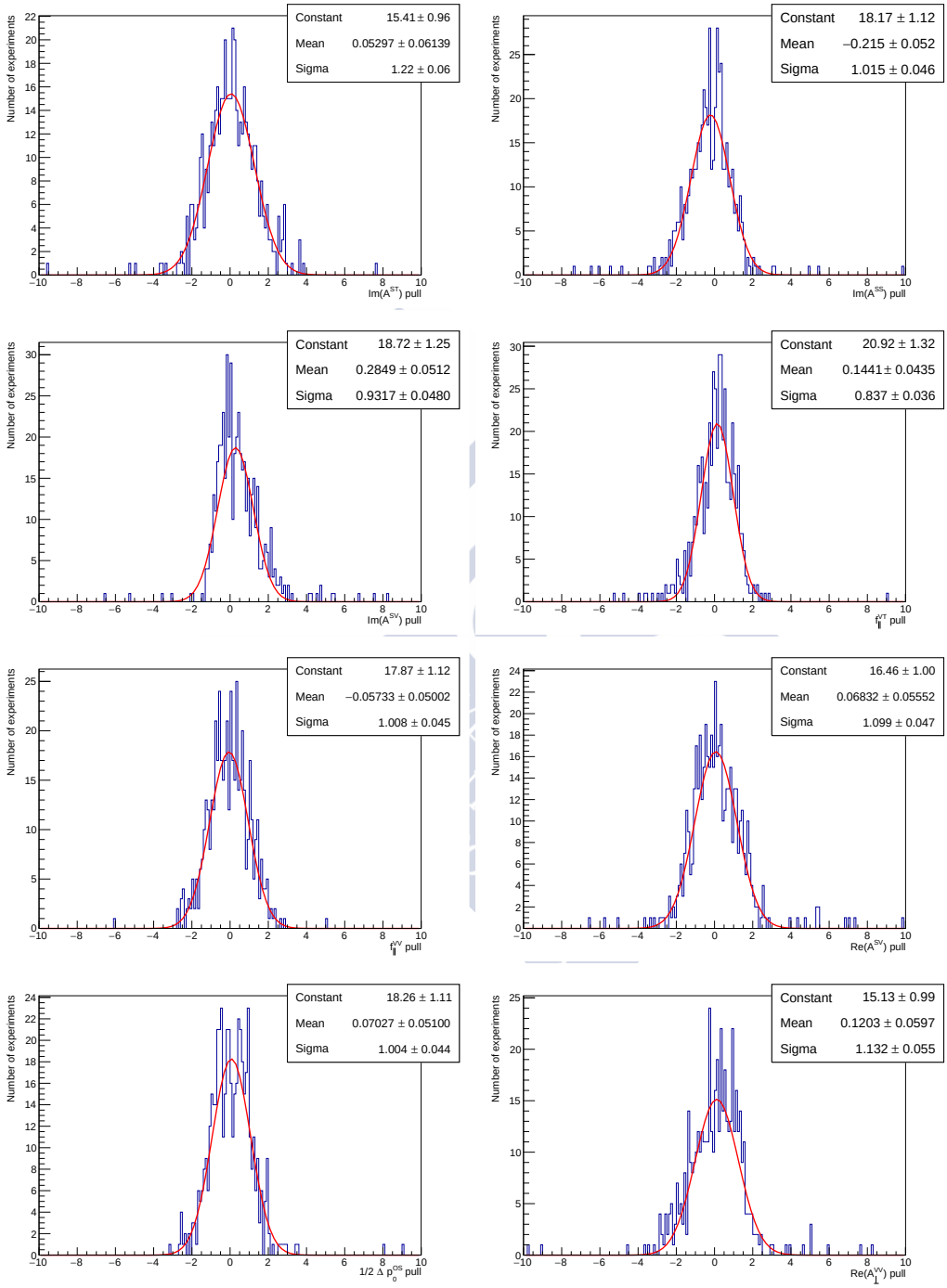



FIGURE A.8: Pull distributions of the fitted parameters.

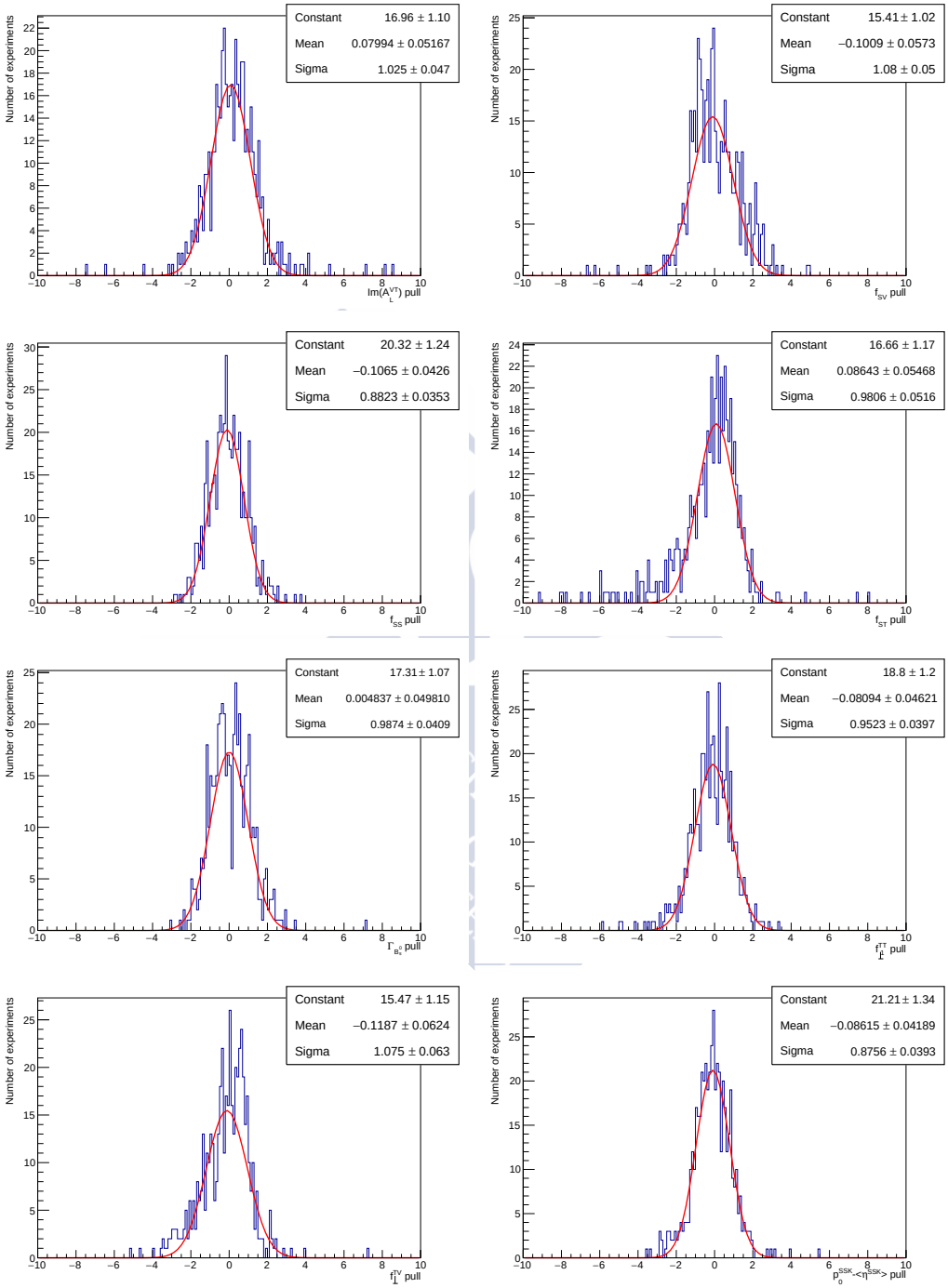



FIGURE A.9: Pull distributions of the fitted parameters.

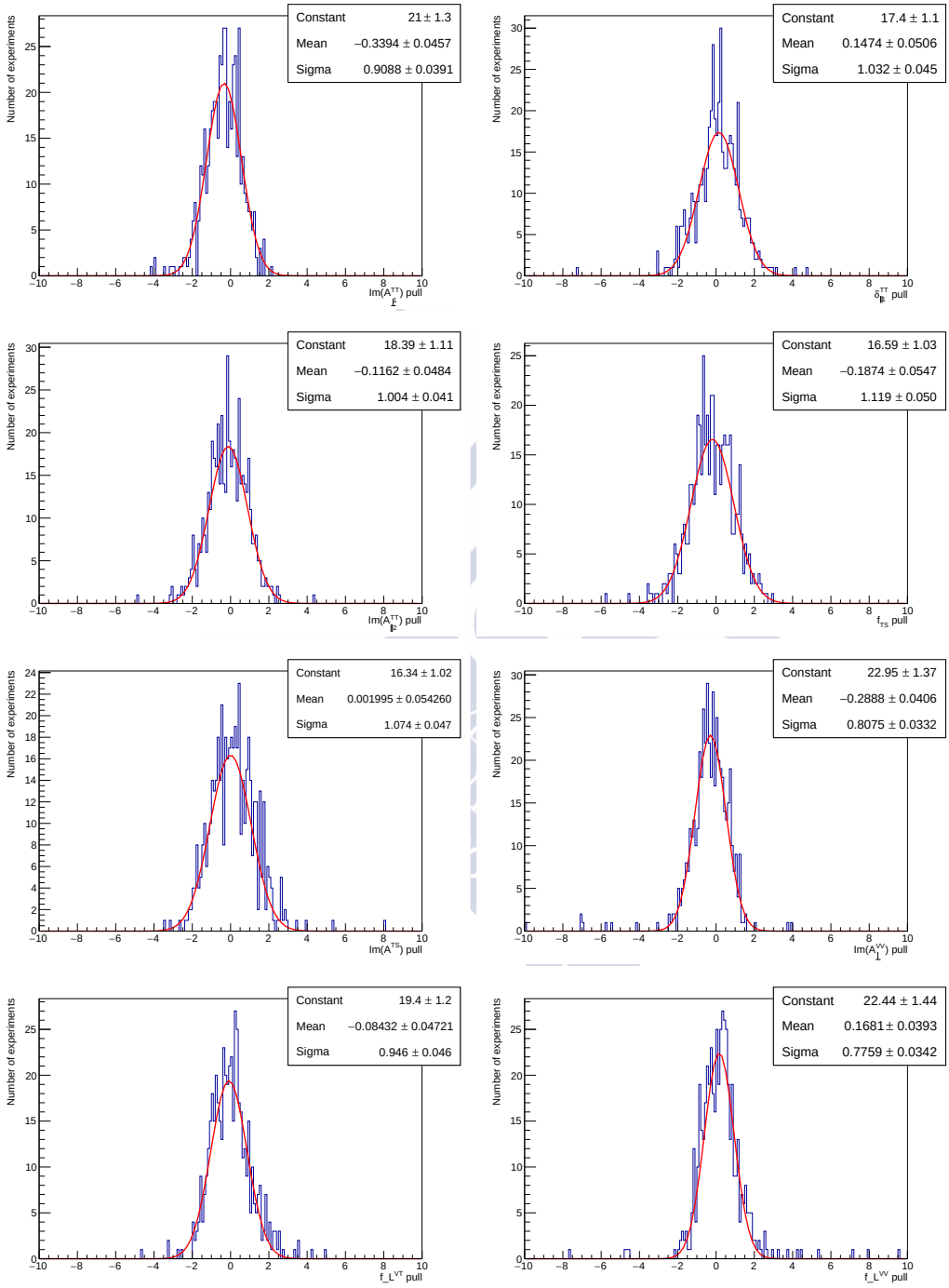



FIGURE A.10: Pull distributions of the fitted parameters.

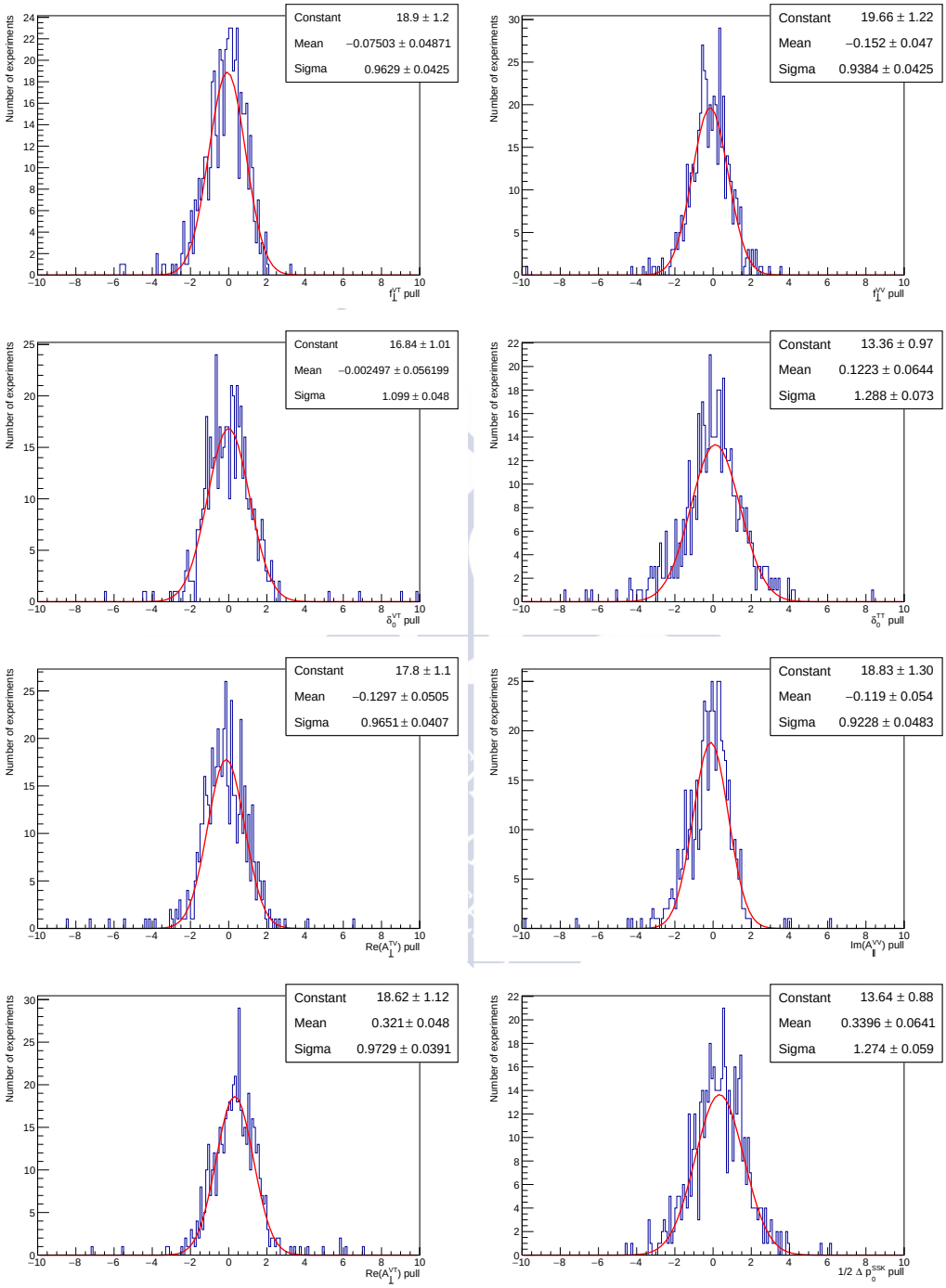



FIGURE A.11: Pull distributions of the fitted parameters.

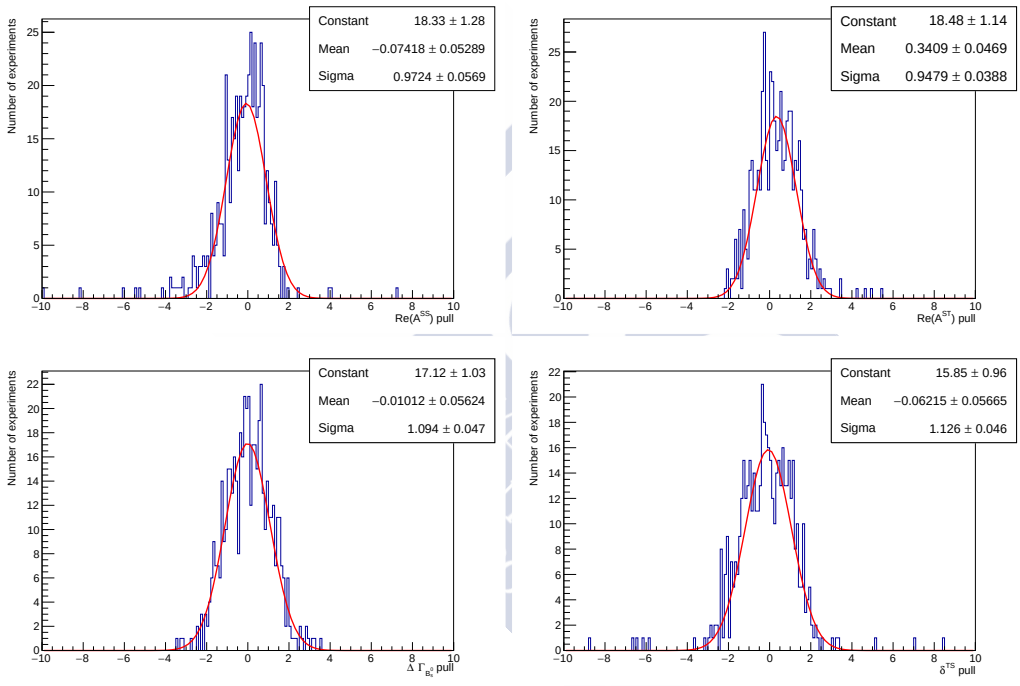



FIGURE A.12: Pull distributions of the fitted parameters.

USC
UNIVERSIDADE
DE SANTIAGO
DE COMPOSTELA

## Appendix B

# Measurement of $\phi_s$: systematic studies on the normalisation weights

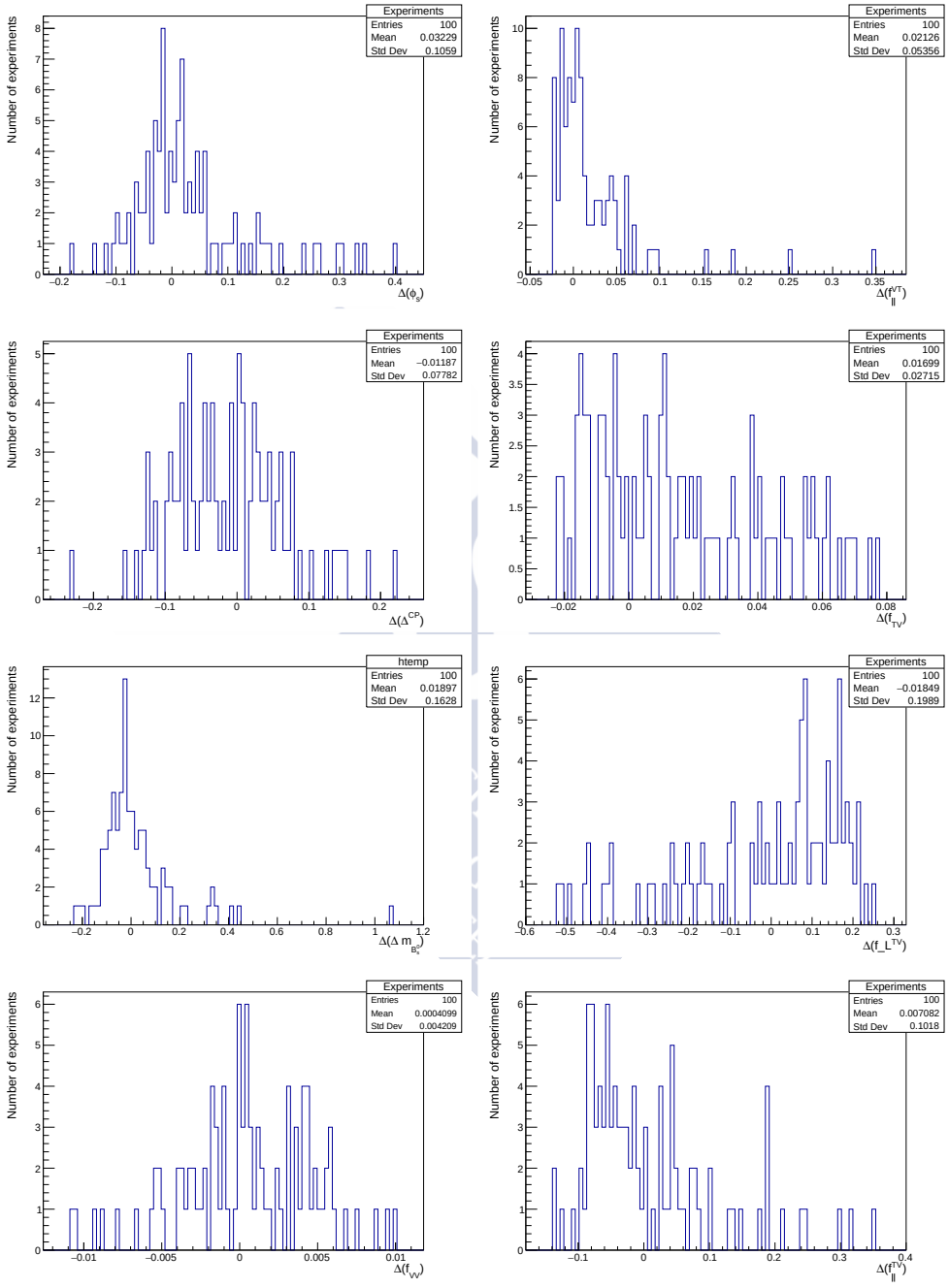



FIGURE B.1: Distributions of the fit parameter deviations when fluctuating the normalisation weights, used to compute systematic uncertainties.

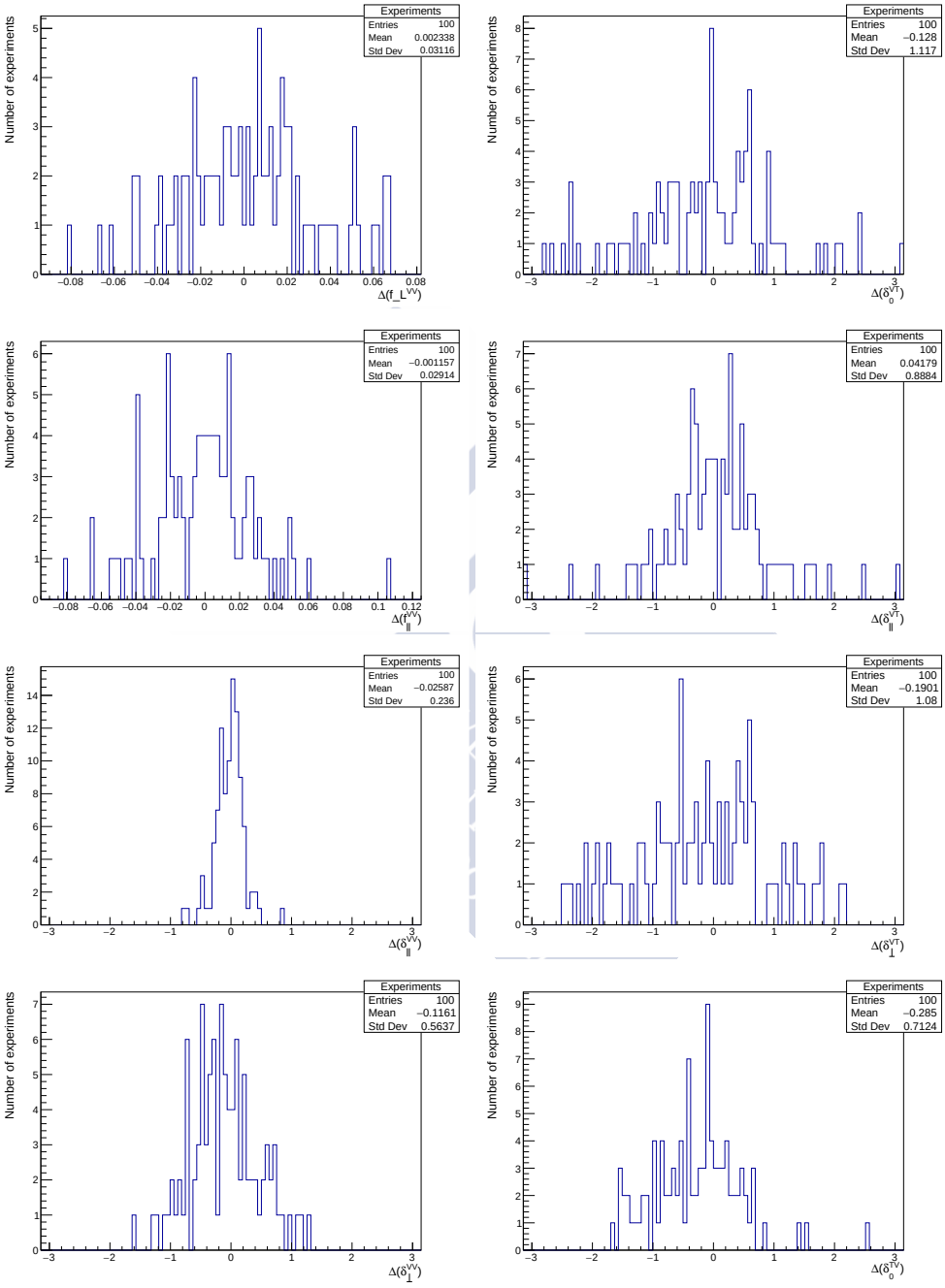



FIGURE B.2: Distributions of the fit parameter deviations when fluctuating the normalisation weights, used to compute systematic uncertainties.

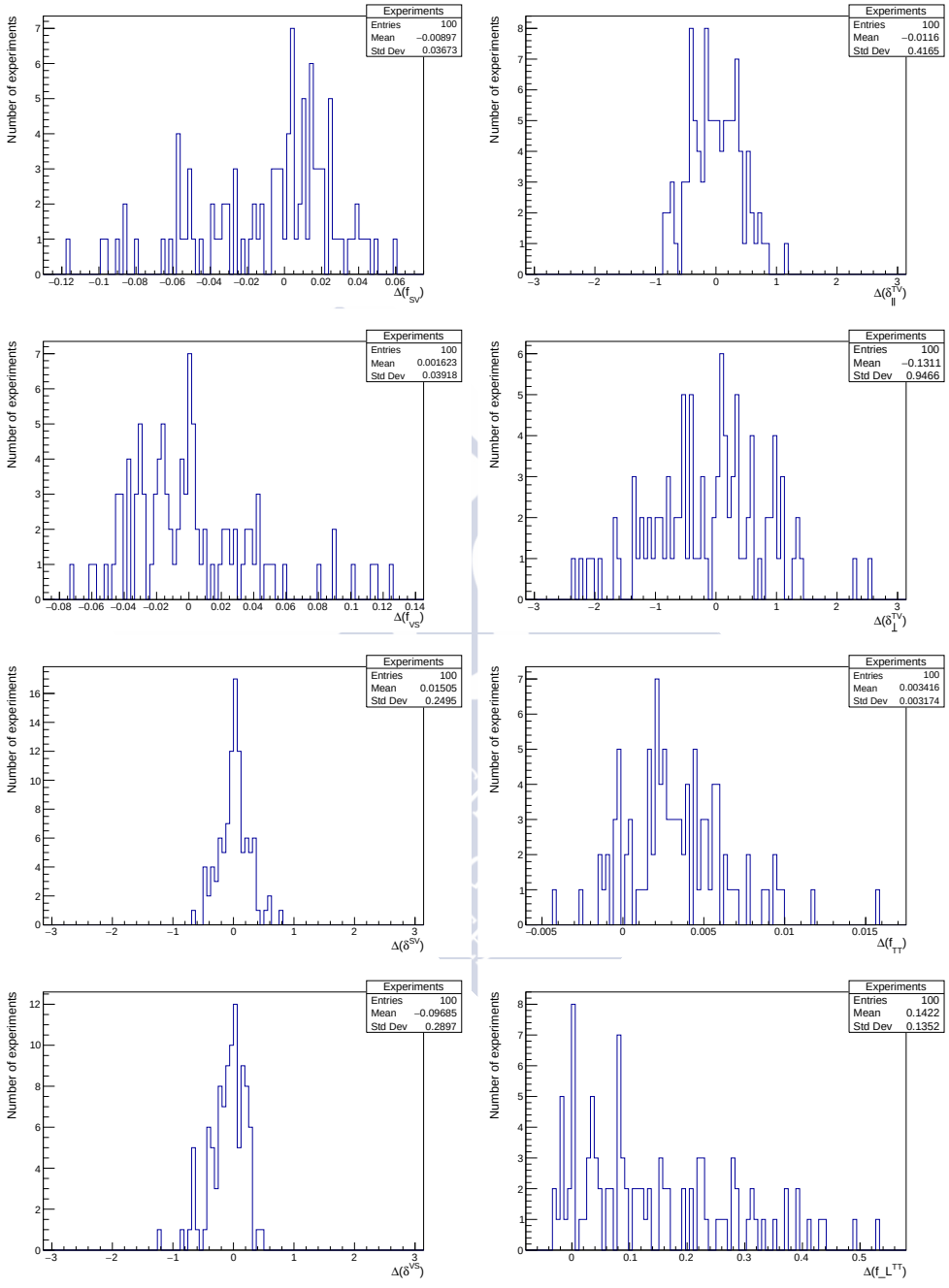



FIGURE B.3: Distributions of the fit parameter deviations when fluctuating the normalisation weights, used to compute systematic uncertainties.

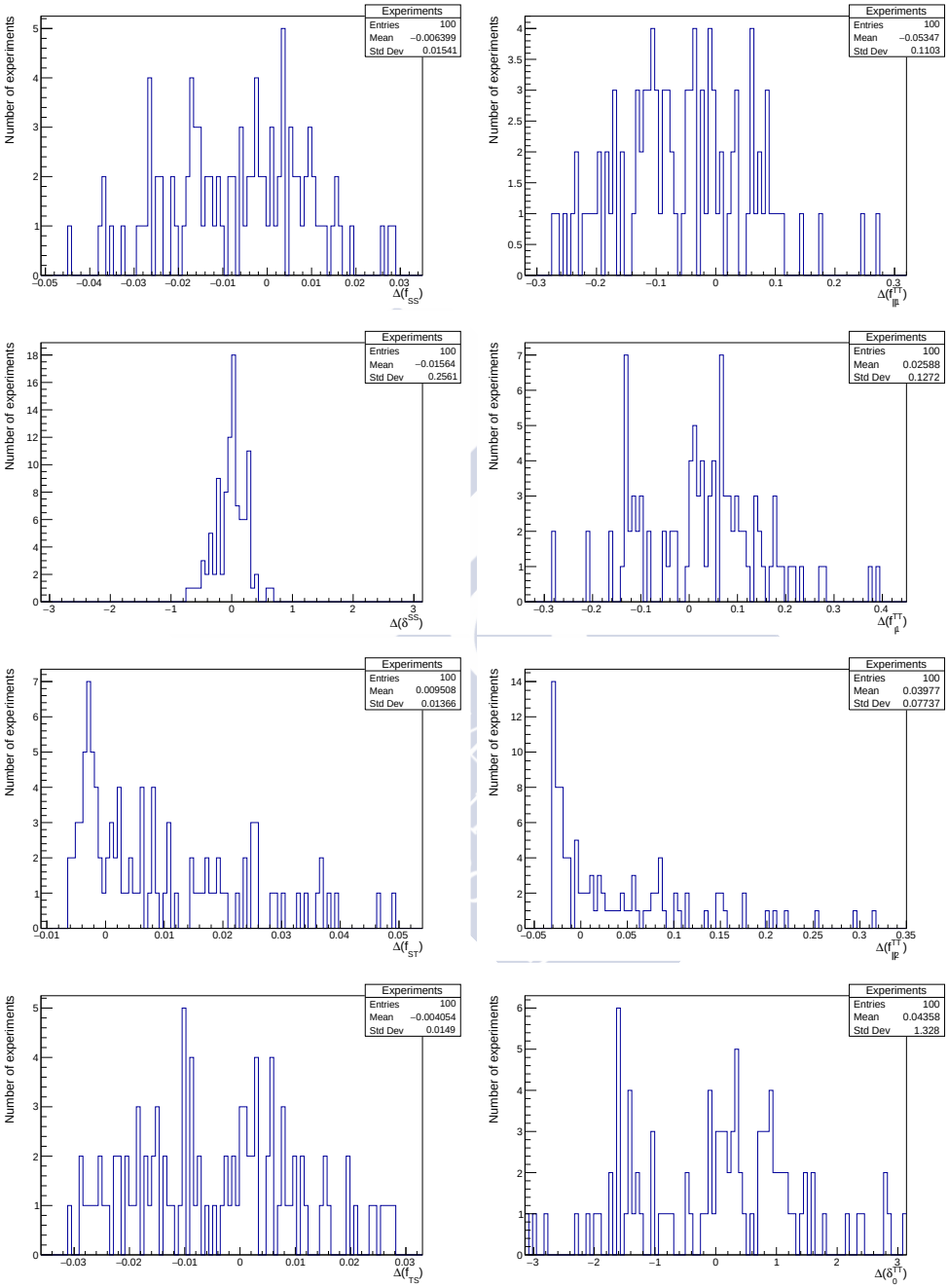



FIGURE B.4: Distributions of the fit parameter deviations when fluctuating the normalisation weights, used to compute systematic uncertainties.

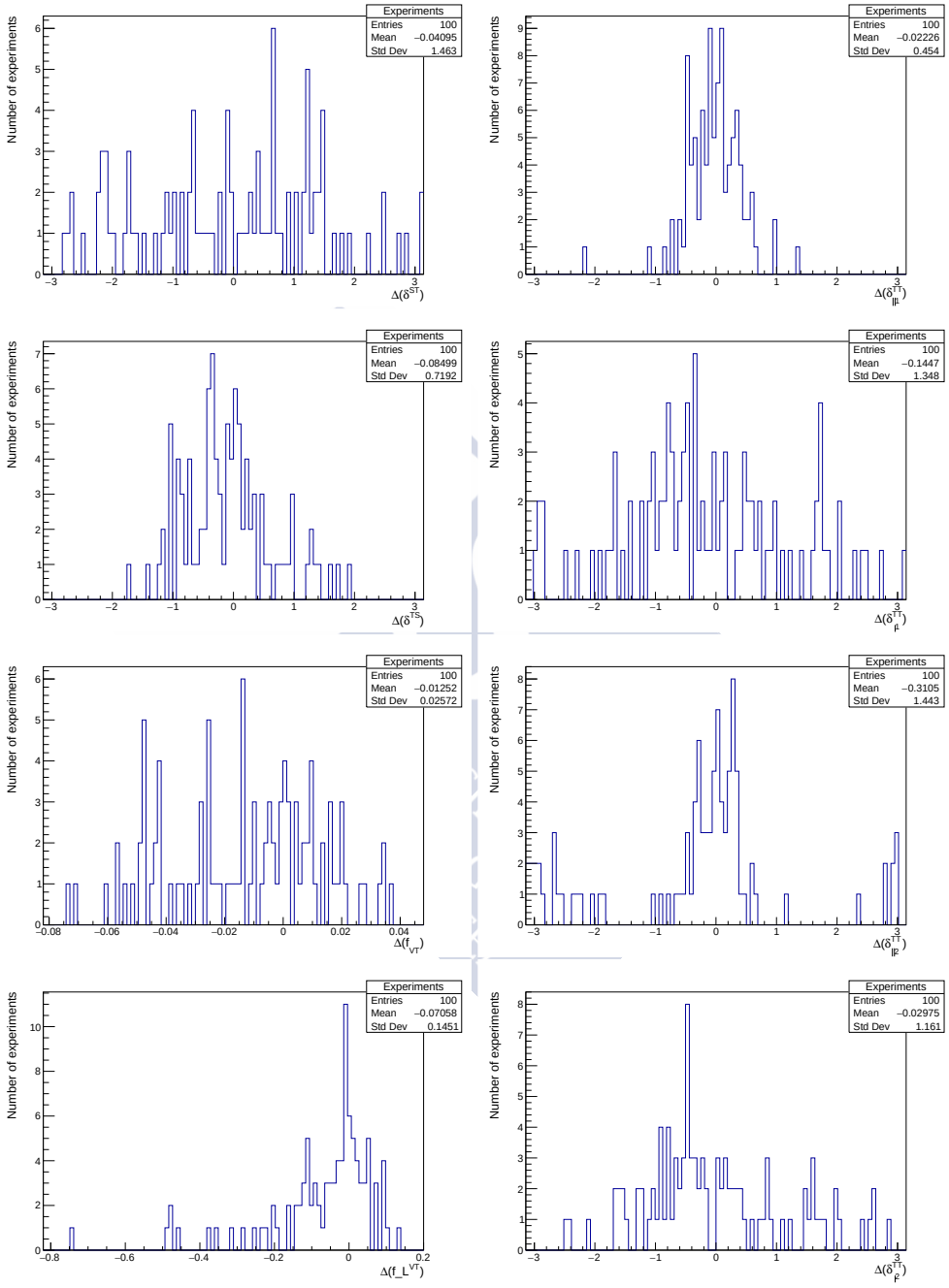



FIGURE B.5: Distributions of the fit parameter deviations when fluctuating the normalisation weights, used to compute systematic uncertainties.

# Bibliography


[1] G. Aad et al. "Observation of a new particle in the search for the Standard Model Higgs boson with the ATLAS detector at the LHC". In: *Physics Letters B* 716.1 (2012), pp. 1 – 29. ISSN: 0370-2693. DOI: http://dx.doi.org/10.1016/j.physletb.2012.08.020. URL: http://www.sciencedirect.com/science/article/pii/S037026931200857X.

[2] S. Chatrchyan et al. "Observation of a new boson at a mass of 125 GeV with the CMS experiment at the LHC". In: *Physics Letters B* 716.1 (2012), pp. 30 –61. ISSN: 0370-2693. DOI: http://dx.doi.org/10.1016/j.physletb.2012.08.021. URL: http://www.sciencedirect.com/science/article/pii/S0370269312008581.

[3] Lyndon Evans and Philip Bryant. "LHC Machine". In: *Journal of Instrumentation* 3.08 (2008), S08001. URL: http://stacks.iop.org/1748-0221/3/i=08/a=S08001.

[4] A Augusto Alves Jr et al. "The LHCb Detector at the LHC". In: *Journal of Instrumentation* 3.08 (2008), S08005. URL: http://stacks.iop.org/1748-0221/3/i=08/a=S08005.

[5] Andrei D Sakharov. "Violation of CP invariance, C asymmetry, and baryon asymmetry of the universe". In: *Soviet Physics Uspekhi* 34.5 (1991), p. 392. URL: http://stacks.iop.org/0038-5670/34/i=5/a=A08.

[6] Y. Amhis et al. "Averages of $b$-hadron, $c$-hadron, and $\tau$-lepton properties as of summer 2014". In: (2014). arXiv: 1412.7515 [hep-ex].

[7] R. Aaij et al. "Precision measurement of *CP* violation in $B_s^0 \to J/\psi K^+K^-$ decays". In: *Phys. Rev. Lett.* 114 (2015), p. 041801. DOI: 10.1103/PhysRevLett.114.041801. arXiv: 1411.3104 [hep-ex].

[8] Georges Aad et al. "Measurement of the CP-violating phase $\phi_s$ and the $B_s^0$ meson decay width difference with $B_s^0 \to J/\psi\phi$ decays in ATLAS". In: (2016). arXiv: 1601.03297 [hep-ex].

[9] Vardan Khachatryan et al. "Measurement of the CP-violating weak phase $\phi_s$ and the decay width difference $\Delta\Gamma_s$ using the $B_s^0 \to J/\psi\phi(1020)$ decay channel in $pp$ collisions at $\sqrt{s} = 8$ TeV". In: *Phys. Lett.* B757 (2016), pp. 97–120. DOI: 10.1016/j.physletb.2016.03.046. arXiv: 1507.07527 [hep-ex].

[10] R. Aaij et al. "Measurement of *CP* violation in $B_s^0 \to \phi\phi$ decays". In: *Phys. Rev.* D90 (2014), p. 052011. DOI: 10.1103/PhysRevD.90.052011. arXiv: 1407.2222 [hep-ex].

[11] Robert Fleischer. "Extracting CKM phases from angular distributions of B(d,s) decays into admixtures of CP eigenstates". In: *Phys. Rev.* D60 (1999), p. 073008. DOI: 10.1103/PhysRevD.60.073008. arXiv: hep-ph/9903540 [hep-ph].

[12] Robert Fleischer and Michael Gronau. "Studying new physics amplitudes in charmless $B_s^0$ decays". In: *Phys. Lett.* B660 (2008), pp. 212–216. DOI: 10.1016/j.physletb.2007.12.028. arXiv: 0709.4013 [hep-ph].

[13] M. Ciuchini, M. Pierini, and L. Silvestrini. "$B_s^0 \to K^{(*)0}\bar{K}^{(*)0}$ decays: The Golden channels for new physics searches". In: *Phys. Rev. Lett.* 100 (2008), p. 031802. DOI: 10.1103/PhysRevLett.100.031802. arXiv: hep-ph/0703137 [HEP-PH].

[14] Sebastien Descotes-Genon, Joaquim Matias, and Javier Virto. "Penguin-mediated $B_{d,s} \to VV$ decays and the $B_s - \bar{B}_s$ mixing angle". In: *Phys. Rev.* D76 (2007). [Erratum: Phys. Rev.D84,039901(2011)], p. 074005. DOI: 10.1103/PhysRevD.76.074005, 10.1103/PhysRevD.84.039901. arXiv: 0705.0477 [hep-ph].

[15] Sebastien Descotes-Genon, Joaquim Matias, and Javier Virto. "An analysis of $B_{d,s}$ mixing angles in presence of New Physics and an update of $B_s \to K^{0*}\bar{K}^{0*}$". In: *Phys. Rev.* D85 (2012), p. 034010. DOI: 10.1103/PhysRevD.85.034010. arXiv: 1111.4882 [hep-ph].

[16] Bhubanjyoti Bhattacharya et al. "Measuring $\beta_s$ with $B_s \to K^{0(*)}\bar{K}^{0(*)}$ – a Reappraisal". In: *Phys. Lett.* B717 (2012), pp. 403–408. DOI: 10.1016/j.physletb.2012.09.054. arXiv: 1203.3435 [hep-ph].

[17] Bhubanjyoti Bhattacharya et al. "Searching for new physics with $\bar{b} \to \bar{s}$ $B_s^0 \to V_1 V_2$ penguin decays". In: *Phys. Rev.* D88.1 (2013), p. 016007. DOI: 10.1103/PhysRevD.88.016007. arXiv: 1306.1911 [hep-ph].

[18] R. Aaij et al. "First observation of the decay $B_s^0 \to K^{*0}\overline{K}^{*0}$". In: *Phys. Lett.* B709 (2012), p. 50. DOI: 10.1016/j.physletb.2012.02.001. arXiv: 1111.4183 [hep-ex].

[19] R. Aaij et al. "Measurement of *CP* asymmetries and polarisation fractions in $B_s^0 \to K^{*0}\overline{K}^{*0}$ decays". In: *JHEP* 07 (2015), p. 166. DOI: 10.1007/JHEP07(2015)166. arXiv: 1503.05362 [hep-ex].

[20] R. Aaij et al. "Test of Lepton Universality Using $B^+ \to K^+\ell^+\ell^-$ Decays". In: *Phys. Rev. Lett.* 113 (15 2014), p. 151601. DOI: 10.1103/PhysRevLett.113.151601. URL: https://link.aps.org/doi/10.1103/PhysRevLett.113.151601.

[21] R. Aaij et al. "Test of lepton universality with $B^0 \to K^{*0}l^+l^-$ decays". In: *Journal of High Energy Physics* 2017.8 (2017), p. 55. ISSN: 1029-8479. DOI: 10.1007/JHEP08(2017)055. URL: https://doi.org/10.1007/JHEP08(2017)055.

[22] Gregory Ciezarek et al. "A challenge to lepton universality in B-meson decays". In: *Nature* 546.7657 (June 2017), pp. 227–233. URL: http://dx.doi.org/10.1038/nature22346.

[23] J. P. Lees et al. "Measurement of an excess of $\overline{B} \to D^{(*)}\tau^-\overline{\nu}_\tau$ decays and implications for charged Higgs bosons". In: *Phys. Rev. D* 88 (7 2013), p. 072012. DOI: 10.1103/PhysRevD.88.072012. URL: https://link.aps.org/doi/10.1103/PhysRevD.88.072012.

[24] R. Aaij et al. "Measurement of the Ratio of Branching Fractions $\mathcal{B}(\overline{B}^0 \to D^{*+}\tau^-\overline{\nu}_\tau)/\mathcal{B}(\overline{B}^0 \to D^{*+}\mu^-\overline{\nu}_\mu)$". In: *Phys. Rev. Lett.* 115 (11 2015), p. 111803. DOI: 10.1103/PhysRevLett.115.111803. URL: https://link.aps.org/doi/10.1103/PhysRevLett.115.111803.

[25] R. Aaij et al. "Measurement of the ratio of the $B^0 \to D^{*-}\tau^+\nu_\tau$ and $B^0 \to D^{*-}\mu^+\nu_\mu$ branching fractions using three-prong $\tau$-lepton decays". In: (2017). arXiv: 1708.08856 [hep-ex].

[26] C. Patrignani et al. "Review of Particle Physics". In: *Chin. Phys.* C40.10 (2016), p. 100001. DOI: 10.1088/1674-1137/40/10/100001.

[27] R. Aaij et al. "Measurement of *CP* violation parameters and polarisation fractions in $B_s^0 \to J/\psi\,\overline{K}^{*0}$ decays". In: *JHEP* 11 (2015), p. 082. DOI: 10.1007/JHEP11(2015)082. arXiv: 1509.00400 [hep-ex].

[28] Diego Martínez Santos et al. "Ipanema-$\beta$: Tools and examples for HEP analysis on GPU". In: (2017). arXiv: 1706.01420 [hep-ex].

[29] Vladimir Gromov et al. "Development and applications of the Timepix3 readout chip". In: *PoS* VERTEX2011 (2011), p. 046.

[30] Michael E. Peskin and Daniel V. Schroeder. *An Introduction to quantum field theory*. Reading, USA: Addison-Wesley, 1995. ISBN: 9780201503975, 0201503972. URL: http://www.slac.stanford.edu/~mpeskin/QFT.html.

[31] Georges Aad et al. "Observation of a new particle in the search for the Standard Model Higgs boson with the ATLAS detector at the LHC". In: *Phys. Lett.* B716 (2012), pp. 1–29. DOI: 10.1016/j.physletb.2012.08.020. arXiv: 1207.7214 [hep-ex].

[32] Serguei Chatrchyan et al. "Observation of a new boson at a mass of 125 GeV with the CMS experiment at the LHC". In: *Phys. Lett.* B716 (2012), pp. 30–61. DOI: 10.1016/j.physletb.2012.08.021. arXiv: 1207.7235 [hep-ex].

[33] Nicola Cabibbo. "Unitary Symmetry and Leptonic Decays". In: *Phys. Rev. Lett.* 10 (1963). [,648(1963)], pp. 531–533. DOI: 10.1103/PhysRevLett.10.531.

[34] Makoto Kobayashi and Toshihide Maskawa. "CP Violation in the Renormalizable Theory of Weak Interaction". In: *Prog. Theor. Phys.* 49 (1973), pp. 652–657. DOI: 10.1143/PTP.49.652.

[35] Ziro Maki, Masami Nakagawa, and Shoichi Sakata. "Remarks on the Unified Model of Elementary Particles". In: *Progress of Theoretical Physics* 28.5 (1962), pp. 870–880. DOI: 10.1143/PTP.28.870. eprint: /oup/backfile/content_public/journal/ptp/28/5/10.1143/ptp.28.870/2/28-5-870.pdf. URL: +http://dx.doi.org/10.1143/PTP.28.870.

[36] A.D. Sakharov. "VIOLATION OF CP INVARIANCE, C ASYMMETRY, AND BARYON ASYMMETRY OF THE UNIVERSE." In: *JETP Lett. (USSR)(Engl. Transl.), 5: 24-7(Jan. 1, 1967).* (1967).

[37] Y. Amhis and others (HFLAV). "Averages of $b$-hadron, $c$-hadron, and $\tau$-lepton properties as of summer 2016". In: (2016). updated results and plots available at http://www.slac.stanford.edu/xorg/hflav/. arXiv: 1612.07233 [hep-ex].

[38] J. Charles et al. "Predictions of selected flavour observables within the Standard Model". In: *Phys. Rev.* D84 (2011), p. 033005. DOI: 10.1103/PhysRevD.84.033005. arXiv: 1106.4041 [hep-ph].

[39] Martti Raidal. "CP asymmetry in $B \to phiK_{(S)}$ decays in left-right models and its implications on $B_s$ decays". In: *Phys. Rev. Lett.* 89 (2002), p. 231803. DOI: 10.1103/PhysRevLett.89.231803. arXiv: hep-ph/0208091 [hep-ph].

[40] Martin Beneke, Johannes Rohrer, and Deshan Yang. "Branching fractions, polarisation and asymmetries of $B \to VV$ decays". In: *Nucl. Phys.* B774 (2007), pp. 64–101. DOI: 10.1016/j.nuclphysb.2007.03.020. arXiv: hep-ph/0612290 [hep-ph].

[41] Bernard Aubert et al. "Observation of $B^0 \to$ K*0 $\bar{K}$* 0 and search for $B^0 \to$ K*0 K*0". In: *Phys. Rev. Lett.* 100 (2008), p. 081801. DOI: 10.1103/PhysRevLett.100.081801. arXiv: 0708.2248 [hep-ex].

[42] R. Aaij et al. "Test of lepton universality using $B^+ \to K^+\ell^+\ell^-$ decays". In: *Phys. Rev. Lett.* 113 (2014), p. 151601. DOI: 10.1103/PhysRevLett.113.151601. arXiv: 1406.6482 [hep-ex].

[43] R. Aaij et al. "Test of lepton universality with $B^0 \to K^{*0}\ell^+\ell^-$ decays". In: *JHEP* 08 (2017), p. 055. DOI: 10.1007/JHEP08(2017)055. arXiv: 1705.05802 [hep-ex].

[44] R. Aaij et al. "Measurement of the ratio of branching fractions $\mathcal{B}(\overline{B}^0 \to D^{*+}\tau^-\overline{\nu}_\tau)/\mathcal{B}(\overline{B}^0 \to D^{*+}\mu^-\overline{\nu}_\mu)$". In: *Phys. Rev. Lett.* 115 (2015), p. 111803. DOI: 10.1103/PhysRevLett.115.111803. arXiv: 1506.08614 [hep-ex].

[45] Heechang Na et al. "$B \to Dl\nu$ form factors at nonzero recoil and extraction of $|V_{cb}|$". In: *Phys. Rev.* D92.5 (2015). [Erratum: Phys. Rev.D93,no.11,119906(2016)], p. 054510. DOI: 10.1103/PhysRevD.93.119906, 10.1103/PhysRevD.92.054510. arXiv: 1505.03925 [hep-lat].

[46] Jon A. Bailey et al. "B→Dl$\nu$ form factors at nonzero recoil and $|V_{cb}|$ from 2+1-flavor lattice QCD". In: *Phys. Rev.* D92.3 (2015), p. 034506. DOI: 10.1103/PhysRevD.92.034506. arXiv: 1503.07237 [hep-lat].

[47] Svjetlana Fajfer, Jernej F. Kamenik, and Ivan Nisandzic. "On the $B \to D^* \tau \bar{\nu}_\tau$ Sensitivity to New Physics". In: *Phys. Rev.* D85 (2012), p. 094025. DOI: 10.1103/PhysRevD.85.094025. arXiv: 1203.2654 [hep-ph].

[48] Vernon D. Barger, J. L. Hewett, and R. J. N. Phillips. "New Constraints on the Charged Higgs Sector in Two Higgs Doublet Models". In: *Phys. Rev.* D41 (1990), pp. 3421–3441. DOI: 10.1103/PhysRevD.41.3421.

[49] J. F. Gunion and Howard E. Haber. "Higgs Bosons in Supersymmetric Models. 1." In: *Nucl. Phys.* B272 (1986). [Erratum: Nucl. Phys.B402,567(1993)], p. 1. DOI: 10.1016/0550-3213(86)90340-8, 10.1016/0550-3213(93)90653-7.

[50] I. Doršner et al. "Physics of leptoquarks in precision experiments and at particle colliders". In: *Phys. Rept.* 641 (2016), pp. 1–68. DOI: 10.1016/j.physrep.2016.06.001. arXiv: 1603.04993 [hep-ph].

[51] Gregory Ciezarek et al. "A Challenge to Lepton Universality in B Meson Decays". In: *Nature* 546 (2017), pp. 227–233. DOI: 10.1038/nature22346. arXiv: 1703.01766 [hep-ex].

[52] R. Aaij et al. "Measurement of form-factor-independent observables in the decay $B^0 \to K^{*0} \mu^+ \mu^-$". In: *Phys. Rev. Lett.* 111 (2013), p. 191801. DOI: 10.1103/PhysRevLett.111.191801. arXiv: 1308.1707 [hep-ex].

[53] Bernat Capdevila et al. "Patterns of New Physics in $b \to s \ell^+ \ell^-$ transitions in the light of recent data". In: *JHEP* 01 (2018), p. 093. DOI: 10.1007/JHEP01(2018)093. arXiv: 1704.05340 [hep-ph].

[54] Wolfgang Altmannshofer and David M. Straub. "Implications of $b \to s$ measurements". In: *Proceedings, 50th Rencontres de Moriond Electroweak Interactions and Unified Theories: La Thuile, Italy, March 14-21, 2015*. 2015, pp. 333–338. arXiv: 1503.06199 [hep-ph]. URL: https://inspirehep.net/record/1353682/files/arXiv:1503.06199.pdf.

[55] Wolfgang Altmannshofer and David M. Straub. "New physics in $b \to s$ transitions after LHC run 1". In: *Eur. Phys. J.* C75.8 (2015), p. 382. DOI: 10.1140/epjc/s10052-015-3602-7. arXiv: 1411.3161 [hep-ph].

[56] T. Hurth, F. Mahmoudi, and S. Neshatpour. "On the anomalies in the latest LHCb data". In: *Nucl. Phys.* B909 (2016), pp. 737–777. DOI: 10.1016/j.nuclphysb.2016.05.022. arXiv: 1603.00865 [hep-ph].

[57] Adam Falkowski, Marco Nardecchia, and Robert Ziegler. "Lepton Flavor Non-Universality in B-meson Decays from a U(2) Flavor Model". In: *JHEP* 11 (2015), p. 173. DOI: 10.1007/JHEP11(2015)173. arXiv: 1509.01249 [hep-ph].

[58] Christoph Niehoff, Peter Stangl, and David M. Straub. "Violation of lepton flavour universality in composite Higgs models". In: *Phys. Lett.* B747 (2015), pp. 182–186. DOI: 10.1016/j.physletb.2015.05.063. arXiv: 1503.03865 [hep-ph].

[59] Rodrigo Alonso, Benjamín Grinstein, and Jorge Martin Camalich. "Lepton universality violation and lepton flavor conservation in $B$-meson decays". In: *JHEP* 10 (2015), p. 184. DOI: 10.1007/JHEP10(2015)184. arXiv: 1505.05164 [hep-ph].

[60] Lorenzo Calibbi, Andreas Crivellin, and Toshihiko Ota. "Effective Field Theory Approach to b→sll(′), B→K(*)$\nu\bar{\nu}$ and B→D(*)$\tau\nu$ with Third Generation Couplings". In: *Phys. Rev. Lett.* 115 (2015), p. 181801. DOI: 10.1103/PhysRevLett.115.181801. arXiv: 1506.02661 [hep-ph].

[61] Andreas Crivellin, Dario Müller, and Toshihiko Ota. "Simultaneous explanation of R(D$^{(*)}$) and b→s$\mu^+$ $\mu^-$: the last scalar leptoquarks standing". In: *JHEP* 09 (2017), p. 040. DOI: 10.1007/JHEP09(2017)040. arXiv: 1703.09226 [hep-ph].

[62] Admir Greljo, Gino Isidori, and David Marzocca. "On the breaking of Lepton Flavor Universality in B decays". In: *JHEP* 07 (2015), p. 142. DOI: 10.1007/JHEP07(2015)142. arXiv: 1506.01705 [hep-ph].

[63] Dario Buttazzo et al. "B-physics anomalies: a guide to combined explanations". In: *JHEP* 11 (2017), p. 044. DOI: 10.1007/JHEP11(2017)044. arXiv: 1706.07808 [hep-ph].

[64] Y. Amhis et al. "Averages of $b$-hadron, $c$-hadron, and $\tau$-lepton properties as of summer 2016". In: (2016). arXiv: 1612.07233 [hep-ex].

[65] R. Aaij et al. "Measurement of the $CP$ asymmetry in $B_s^0 - \overline{B}_s^0$ mixing". In: *Phys. Rev. Lett.* 117.6 (2016). [Addendum: Phys. Rev. Lett.118,no.12,129903(2017)], p. 061803. DOI: 10.1103/PhysRevLett.118.129903,10.1103/PhysRevLett.117.061803. arXiv: 1605.09768 [hep-ex].

[66] D. Aston et al. "A study of K-$\pi$+ scattering in the reaction K-p→K-$\pi$+n at 11 GeV/c". In: *Nuclear Physics B* 296.3 (1988), pp. 493 –526. ISSN: 0550-3213. DOI: http://dx.doi.org/10.1016/0550-3213(88)90028-4. URL: http://www.sciencedirect.com/science/article/pii/0550321388900284.

[67] J. R. Pelaez and A. Rodas. "Pion-kaon scattering amplitude constrained with forward dispersion relations up to 1.6 GeV". In: *Phys. Rev. D* 93 (7 2016), p. 074025. DOI: 10.1103/PhysRevD.93.074025. URL: http://link.aps.org/doi/10.1103/PhysRevD.93.074025.

[68] R. Aaij et al. "Observation of the resonant character of the $Z(4430)^-$ state". In: *Phys. Rev. Lett.* 112 (2014), p. 222002. DOI: 10.1103/PhysRevLett.112.222002. arXiv: 1404.1903 [hep-ex].

[69] K. A. Olive et al. "Review of Particle Physics". In: *Chin. Phys.* C38 (2014), p. 090001. DOI: 10.1088/1674-1137/38/9/090001.

[70] Kenneth M. Watson. "Some General Relations between the Photoproduction and Scattering of $\pi$ Mesons". In: *Phys. Rev.* 95 (1 1954), pp. 228–236. DOI: 10.1103/PhysRev.95.228. URL: https://link.aps.org/doi/10.1103/PhysRev.95.228.

[71] J. G. Körner and G. A. Schuler. "Exclusive semileptonic heavy meson decays including lepton mass effects". In: *Zeitschrift für Physik C Particles and Fields* 46.1 (1990), pp. 93–109. ISSN: 1431-5858. DOI: 10.1007/BF02440838. URL: https://doi.org/10.1007/BF02440838.

[72] Irinel Caprini, Laurent Lellouch, and Matthias Neubert. "Dispersive bounds on the shape of anti-B —> D(*) lepton anti-neutrino form-factors". In: *Nucl. Phys.* B530 (1998), pp. 153–181. DOI: 10.1016/S0550-3213(98)00350-2. arXiv: hep-ph/9712417 [hep-ph].

[73] Dante Bigi, Paolo Gambino, and Stefan Schacht. "A fresh look at the determination of $|V_{cb}|$ from $B \to D^* \ell \nu$". In: *Phys. Lett.* B769 (2017), pp. 441–445. DOI: 10.1016/j.physletb.2017.04.022. arXiv: 1703.06124 [hep-ph].

[74] Benjamin Grinstein and Andrew Kobach. "Model-Independent Extraction of $|V_{cb}|$ from $\bar{B} \to D^* \ell \overline{\nu}$". In: *Phys. Lett.* B771 (2017), pp. 359–364. DOI: 10.1016/j.physletb.2017.05.078. arXiv: 1703.08170 [hep-ph].

[75] Claude Bourrely, Irinel Caprini, and Laurent Lellouch. "Model-independent description of B —> pi l nu decays and a determination of |V(ub)|". In: *Phys. Rev.* D79 (2009). [Erratum: Phys. Rev.D82,099902(2010)], p. 013008. DOI: 10.1103/PhysRevD.82.099902,10.1103/PhysRevD.79.013008. arXiv: 0807.2722 [hep-ph].

[76] *The Large Hadron Collider*. URL: https://home.cern/topics/large-hadron-collider.

[77] *TE-EPC-LPC in LHC*. URL: http://te-epc-lpc.web.cern.ch/te-epc-lpc/machines/lhc/general.stm.

[78] R Aaij et al. "First Evidence for the Decay $B_s^0 \to \mu^+\mu^-$". In: *Phys. Rev. Lett.* 110.2 (2013), p. 021801. DOI: 10.1103/PhysRevLett.110.021801. arXiv: 1211.2674 [hep-ex].

[79] R. Aaij et al. "Measurement of the $B_s^0 \to \mu^+\mu^-$ branching fraction and search for $B^0 \to \mu^+\mu^-$ decays at the LHCb experiment". In: *Phys. Rev. Lett.* 111 (2013), p. 101805. DOI: 10.1103/PhysRevLett.111.101805. arXiv: 1307.5024 [hep-ex].

[80] Vardan Khachatryan et al. "Observation of the rare $B_s^0 \to \mu^+\mu^-$ decay from the combined analysis of CMS and LHCb data". In: *Nature* 522 (2015), pp. 68–72. DOI: 10.1038/nature14474. arXiv: 1411.4413 [hep-ex].

[81] R. Aaij et al. "Measurement of the $B_s^0 \to \mu^+\mu^-$ branching fraction and effective lifetime and search for $B^0 \to \mu^+\mu^-$ decays". In: *Phys. Rev. Lett.* 118.19 (2017), p. 191801. DOI: 10.1103/PhysRevLett.118.191801. arXiv: 1703.05747 [hep-ex].

[82] R Aaij et al. "Observation of $D^0 - \overline{D}^0$ oscillations". In: *Phys. Rev. Lett.* 110.10 (2013), p. 101802. DOI: 10.1103/PhysRevLett.110.101802. arXiv: 1211.1230 [hep-ex].

[83] R. Aaij et al. "Measurement of the CKM angle $\gamma$ from a combination of LHCb results". In: *JHEP* 12 (2016), p. 087. DOI: 10.1007/JHEP12(2016)087. arXiv: 1611.03076 [hep-ex].

[84] R. Aaij et al. "Precision measurement of $CP$ violation in $B_s^0 \to J/\psi K^+K^-$ decays". In: *Phys. Rev. Lett.* 114.4 (2015), p. 041801. DOI: 10.1103/PhysRevLett.114.041801. arXiv: 1411.3104 [hep-ex].

[85] R. Aaij et al. "Measurement of the CP-violating phase $\phi_s$ in $\overline{B}_s^0 \to J/\psi\pi^+\pi^-$ decays". In: *Phys. Lett.* B736 (2014), pp. 186–195. DOI: 10.1016/j.physletb.2014.06.079. arXiv: 1405.4140 [hep-ex].

[86] R. Aaij et al. "Observation of $J/\psi p$ Resonances Consistent with Pentaquark States in $\Lambda_b^0 \to J/\psi K^- p$ Decays". In: *Phys. Rev. Lett.* 115 (2015), p. 072001. DOI: 10.1103/PhysRevLett.115.072001. arXiv: 1507.03414 [hep-ex].

[87] *LHCb Material for Presentations*. URL: https://lhcb.web.cern.ch/lhcb/speakersbureau/html/Material_for_Presentations.html.

[88] R. Aaij et al. "Performance of the LHCb Vertex Locator". In: *JINST* 9 (2014), p. 09007. DOI: 10.1088/1748-0221/9/09/P09007. arXiv: 1405.7808 [physics.ins-det].

[89] R Arink et al. "Performance of the LHCb Outer Tracker". In: *JINST* 9.01 (2014), P01002. DOI: 10.1088/1748-0221/9/01/P01002. arXiv: 1311.3893 [physics.ins-det].

[90] M. Adinolfi et al. "Performance of the LHCb RICH detector at the LHC". In: *Eur. Phys. J.* C73 (2013), p. 2431. DOI: 10.1140/epjc/s10052-013-2431-9. arXiv: 1211.6759.

[91] A. A. Alves Jr. et al. "Performance of the LHCb muon system". In: *JINST* 8 (2013), P02022. DOI: 10.1088/1748-0221/8/02/P02022. arXiv: 1211.1346 [physics.ins-det].

[92] *Antimatter-matters*. URL: http://antimatter-matters.org.

[93] R. Aaij et al. "LHCb Detector Performance". In: *Int. J. Mod. Phys.* A30.07 (2015), p. 1530022. DOI: 10.1142/S0217751X15300227. arXiv: 1412.6352 [hep-ex].

[94] *Mechanical Design Vertex Locator*. URL: https://www.nikhef.nl/pub/departments/mt/projects/lhcb-vertex/index_current.html.

[95] *LHCb International Masterclasses*. URL: http://lhcb-public.web.cern.ch/lhcb-public/en/LHCb-outreach/masterclasses/en/index.html.

[96] *Marcel Merk*. URL: https://www.nikhef.nl/~i93/.

[97] Torbjörn Sjöstrand, Stephen Mrenna, and Peter" Skands. "A brief introduction to PYTHIA 8.1". In: *Comput.Phys.Commun.* 178 (2008), pp. 852–867. DOI: 10.1016/j.cpc.2008.01.036. arXiv: 0710.3820 [hep-ph].

[98] I. Belyaev et al. "Handling of the generation of primary events in Gauss, the LHCb simulation framework". In: *J. Phys. Conf. Ser.* 331 (2011), p. 032047. DOI: 10.1088/1742-6596/331/3/032047.

[99] D. J. Lange. "The EvtGen particle decay simulation package". In: *Nucl. Instrum. Meth.* A462 (2001), pp. 152–155. DOI: 10.1016/S0168-9002(01)00089-4.

[100] Piotr Golonka and Zbigniew Was. "PHOTOS Monte Carlo: A precision tool for QED corrections in $Z$ and $W$ decays". In: *Eur.Phys.J.* C45 (2006), pp. 97–107. DOI: 10.1140/epjc/s2005-02396-4. arXiv: hep-ph/0506026 [hep-ph].

[101] John Allison et al. "Geant4 developments and applications". In: *IEEE Trans.Nucl.Sci.* 53 (2006), p. 270. DOI: 10.1109/TNS.2006.869826.

[102] S. Agostinelli et al. "Geant4: A simulation toolkit". In: *Nucl. Instrum. Meth.* A506 (2003), p. 250. DOI: 10.1016/S0168-9002(03)01368-8.

[103] M Clemencic et al. "The LHCb simulation application, Gauss: Design, evolution and experience". In: *J. Phys. Conf. Ser.* 331 (2011), p. 032023. DOI: 10.1088/1742-6596/331/3/032023.

[104] *Toolkit for Multivariate Data Analysis with ROOT*. URL: http://tmva.sourceforge.net/docu/TMVAUsersGuide.pdf.

[105] Alex Rogozhnikov and contributors. *hep_ml*. https://arogozhnikov.github.io/hep_ml/.

[106] *NVIDIA Accelerated Computing*. URL: https://developer.nvidia.com/cuda-zone.

[107] Andreas Klöckner et al. "PyCUDA and PyOpenCL: A Scripting-Based Approach to GPU Run-Time Code Generation". In: *Parallel Computing* 38.3 (2012), pp. 157–174. ISSN: 0167-8191. DOI: 10.1016/j.parco.2011.09.001.

[108] Carl de Boor. *A Practical Guide to Splines*. Vol. 27. Applied Mathematical Sciences. New York, US-NY: Springer, 1978. ISBN: 3-540-90356-9.

[109] Muriel Pivk and Francois R. Le Diberder. "sPlot: A statistical tool to unfold data distributions". In: *Nucl.Instrum.Meth.* A555 (2005), pp. 356–369. DOI: 10.1016/j.nima.2005.08.106. arXiv: physics/0402083 [physics.data-an].

[110] T. du Pree. "Search for a Strange Phase in Beautiful Oscillations". In: CERN-THESIS-2010-124 (2010).

[111] R. Aaij et al. "A model-independent confirmation of the $Z(4430)^-$ state". In: *Phys. Rev.* D92 (2015), p. 112009. DOI: 10.1103/PhysRevD.92.112009. arXiv: 1510.01951 [hep-ex].

[112] R. Aaij et al. "Measurement of the forward $W$ boson cross-section in $pp$ collisions at $\sqrt{s} = 7\,\text{TeV}$". In: *JHEP* 12 (2014), p. 079. DOI: 10.1007/JHEP12(2014)079. arXiv: 1408.4354 [hep-ex].

[113] Wouter D. Hulsbergen. "Decay chain fitting with a Kalman filter". In: *Nucl.Instrum.Meth.* A552 (2005), pp. 566–575. DOI: 10.1016/j.nima.2005.06.078. arXiv: physics/0503191 [physics].

[114] Avrim Blum, Adam Kalai, and John Langford. "Beating the Hold-out: Bounds for K-fold and Progressive Cross-validation". In: Proceedings of the Twelfth Annual Conference on Computational Learning Theory. COLT '99. Santa Cruz, California, USA: ACM, 1999, pp. 203–208. ISBN: 1-58113-167-4. DOI: 10.1145/307400.307439. URL: http://doi.acm.org/10.1145/307400.307439.

[115] A. Poluektov. "Kernel density estimation of a multidimensional efficiency profile". In: *Journal of Instrumentation* 10.02 (2015), P02011. URL: http://stacks.iop.org/1748-0221/10/i=02/a=P02011.

[116] R. Aaij et al. "LHCb detector performance". In: *Int. J. Mod. Phys.* A30 (2015), p. 1530022. DOI: 10.1142/S0217751X15300227. arXiv: 1412.6352 [hep-ex].

[117] Diego Martínez Santos and Frederic Dupertuis. "Mass distributions marginalized over per-event errors". In: *Nucl. Instrum. Meth.* A764 (2014), pp. 150–155. DOI: 10.1016/j.nima.2014.06.081. arXiv: 1312.5000 [hep-ex].

[118] "Search for hadronic $b \to u$ decays". In: *Phys. Lett.* B241 (1990), pp. 278–282. ISSN: 0370-2693. DOI: 10.1016/0370-2693(90)91293-K. URL: http://www.sciencedirect.com/science/article/pii/037026939091293K.

[119] R. Aaij et al. "Opposite-side flavour tagging of $B$ mesons at the LHCb experiment". In: *Eur. Phys. J. C* 72.arXiv:1202.4979. CERN-PH-EP-2012-039. LHCB-PAPER-2011-027 (2012). Comments: 22 pages, 9 figures, 2022. 28 p. URL: https://cds.cern.ch/record/1427710.

[120] R. Aaij et al. "A new algorithm for identifying the flavour of $B_s^0$ mesons at LHCb". In: *J. Instrum.* 11.arXiv:1602.07252. LHCB-PAPER-2015-056. CERN-EP-2016-030 (2016), P05010. 26 p. URL: https://cds.cern.ch/record/2134228.

[121] Mirco Dorigo. "FT Workshop Intro and Status". 55th Analysis and Software Week. 2014. URL: https://indico.cern.ch/event/257864/contributions/1587682/attachments/453372/628590/FT_Workshop-7-april.pdf.

[122] R. Aaij et al. "Measurement of the $\overline{B}^0$–$B^0$ and $\overline{B}_s^0$–$B_s^0$ production asymmetries in $pp$ collisions at $\sqrt{s} = 7\ TeV$ ". In: *Phys. Lett.* B739 (2014), p. 218. DOI: 10.1016/j.physletb.2014.10.005. arXiv: 1408.0275 [hep-ex].

[123] Sean Benson et al. "Search for CP Violation in the $B_s^0 \to \phi\phi$ Decay with the Full LHCb Run I Dataset". In: (2014). URL: https://cds.cern.ch/record/1669163.

[124] Marc Grabalosa Gandara et al. "First observation of the $B^0 \to \rho^0\rho^0$ decay and amplitude analysis of $B^0 \to (\pi^+\pi^-)(\pi^+\pi^-)$ decays". In: (2013). URL: https://cds.cern.ch/record/1555654.

[125] Till Moritz Karbach, Gerhard Raven, and Manuel Schiller. "Decay time integrals in neutral meson mixing and their efficient evaluation". In: LHCb-INT-2013-043 (). (Private communication.)

[126] *IMinuit - Interactive IPython Friendly Minimizer based on SEAL Minuit*. https://github.com/iminuit/iminuit. 2017.

[127] F. James and M. Winkler. http://www.cern.ch/minuit. CERN. 2004.

[128] E. O. Lebigot. *Uncertainties: a Python package for calculations with uncertainties*. http://pythonhosted.org/uncertainties/.

[129] B Adeva et al. "Analysis of $B_s^0 \to K^{*0}\bar{K}^{*0}$". In: (2012). URL: https://cds.cern.ch/record/1494560.

[130] R Aaij et al. "Flavour tagged time-dependent angular analysis of $B_s^0 \to J/\psi K^+K^-$ decays in the low $K^+K^-$ mass range". In: (2014). URL: https://cds.cern.ch/record/1690588.

[131] R Aaij et al. "Tagged time-dependent analysis of $B_s^0 \to J/\psi K^+K^-$ and $B_s^0 \to J/\psi\pi^+\pi^-$ decays with 1.0 fb$-$1". In: (2013). Linked to LHCb-PAPER-2013-002. URL: https://cds.cern.ch/record/1459106.

[132] Roger Barlow and Christine Beeston. "Fitting using finite Monte Carlo samples". In: *Computer Physics Communications* 77.2 (1993), pp. 219 –228. ISSN: 0010-4655. DOI: https://doi.org/10.1016/0010-4655(93)90005-W. URL: http://www.sciencedirect.com/science/article/pii/001046559390005W.

[133] R. Aaij et al. "First measurement of the $CP$-violating phase $\phi_s^{d\bar{d}}$ in $B_s^0 \to (K^+\pi^-)(K^-\pi^+)$ decays". In: *Submitted to: JHEP* (2017). arXiv: 1712.08683 [hep-ex].